Phosphonium ionic liquids : Versatile nanostructuration and interfacial agents for poly(vinylidene fluoride-chlorotrifluoroethylene)

Jing Yang

N°d'ordre NNT : 2016LYSEI072

THESE de DOCTORAT DE L'UNIVERSITE DE LYON
opérée au sein de
l'Institut National des Sciences Appliquées de Lyon

Ecole DoctoraleN° ED34
Matériaux de Lyon

Spécialité de doctorat : Matériaux Polymères
Discipline : Matériaux

Soutenue publiquement le 20/07/2016, par :

Jing YANG

Phosphonium ionic liquids: versatile nanostructuration and interfacial agents for poly(vinylidene fluoride-chlorotrifluoroethylene)

Devant le jury composé de :

POULIN, Philippe	Directeur de Recherche	CRPP-CNRS	Rapporteur
MIRI, Valérie	Professeur des Universités	Université Lille 1	Rapportrice
BIZET, Stephane	Docteur	ARKEMA	Examinateur
GERARD, Jean-François	Professeur des Universités	INSA-Lyon	Examinateur
DUCHET-RUMEAU, Jannick	Professeur des Universités	INSA-Lyon	Directrice de thèse
PRUVOST, Sébastien	Maître de Conférences HDR	INSA-Lyon	Co-directeur de thèse

N°d'ordre NNT : 2016LYSEI072

THESE de DOCTORAT DE L'UNIVERSITE DE LYON
opérée au sein de
l'Institut National des Sciences Appliquées de Lyon

Ecole DoctoraleN° ED34
Matériaux de Lyon

Spécialité de doctorat : Matériaux Polymères
Discipline : Matériaux

Soutenue publiquement le 20/07/2016, par :

Jing YANG

Phosphonium ionic liquids: versatile nanostructuration and interfacial agents for poly(vinylidene fluoride-chlorotrifluoroethylene)

Devant le jury composé de :

POULIN, Philippe	Directeur de Recherche	CRPP-CNRS	Rapporteur
MIRI, Valérie	Professeur des Universités	Université Lille 1	Rapportrice
BIZET, Stephane	Docteur	ARKEMA	Examinateur
GERARD, Jean-François	Professeur des Universités	INSA-Lyon	Examinateur
DUCHET-RUMEAU, Jannick	Professeur des Universités	INSA-Lyon	Directrice de thèse
PRUVOST, Sébastien	Maître de Conférences HDR	INSA-Lyon	Co-directeur de thèse

Département FEDORA – INSA Lyon – Ecoles Doctorales – Quinquennal 2016-2020

SIGLE	ECOLE DOCTORALE	NOM ET COORDONNEES DU RESPONSABLE
CHIMIE	**CHIMIE DE LYON** **http://www.edchimie-lyon.fr** Sec : Renée EL MELHEM Bat Blaise Pascal 3e etage secretariat@edchimie-lyon.fr Insa : R. GOURDON	M. Stéphane DANIELE Institut de Recherches sur la Catalyse et l'Environnement de Lyon IRCELYON-UMR 5256 Équipe CDFA 2 avenue Albert Einstein 69626 Villeurbanne cedex directeur@edchimie-lyon.fr
E.E.A.	**ELECTRONIQUE, ELECTROTECHNIQUE, AUTOMATIQUE** **http://edeea.ec-lyon.fr** Sec : M.C. HAVGOUDOUKIAN Ecole-Doctorale.eea@ec-lyon.fr	M. Gérard SCORLETTI Ecole Centrale de Lyon 36 avenue Guy de Collongue 69134 ECULLY Tél : 04.72.18 60.97 Fax : 04 78 43 37 17 Gerard.scorletti@ec-lyon.fr
E2M2	**EVOLUTION, ECOSYSTEME, MICROBIOLOGIE, MODELISATION** **http://e2m2.universite-lyon.fr** Sec : Safia AIT CHALAL Bat Darwin - UCB Lyon 1 04.72.43.28.91 Insa : H. CHARLES Safia.ait-chalal@univ-lyon1.fr	Mme Gudrun BORNETTE CNRS UMR 5023 LEHNA Université Claude Bernard Lyon 1 Bât Forel 43 bd du 11 novembre 1918 69622 VILLEURBANNE Cédex Tél : 06.07.53.89.13 e2m2@ univ-lyon1.fr
EDISS	**INTERDISCIPLINAIRE SCIENCES-SANTE** **http://www.ediss-lyon.fr** Sec : Safia AIT CHALAL Hôpital Louis Pradel - Bron 04 72 68 49 09 Insa : M. LAGARDE Safia.ait-chalal@univ-lyon1.fr	Mme Emmanuelle CANET-SOULAS INSERM U1060, CarMeN lab, Univ. Lyon 1 Bâtiment IMBL 11 avenue Jean Capelle INSA de Lyon 696621 Villeurbanne Tél : 04.72.68.49.09 Fax :04 72 68 49 16 Emmanuelle.canet@univ-lyon1.fr
INFOMATHS	**INFORMATIQUE ET MATHEMATIQUES** **http://infomaths.univ-lyon1.fr** Sec :Renée EL MELHEM Bat Blaise Pascal 3e etage infomaths@univ-lyon1.fr	Mme Sylvie CALABRETTO LIRIS – INSA de Lyon Bat Blaise Pascal 7 avenue Jean Capelle 69622 VILLEURBANNE Cedex Tél : 04.72. 43. 80. 46 Fax 04 72 43 16 87 Sylvie.calabretto@insa-lyon.fr
Matériaux	**MATERIAUX DE LYON** **http://ed34.universite-lyon.fr** Sec : M. LABOUNE PM : 71.70 –Fax : 87.12 Bat. Saint Exupéry Ed.materiaux@insa-lyon.fr	M. Jean-Yves BUFFIERE INSA de Lyon MATEIS Bâtiment Saint Exupéry 7 avenue Jean Capelle 69621 VILLEURBANNE Cedex Tél : 04.72.43 71.70 Fax 04 72 43 85 28 Ed.materiaux@insa-lyon.fr
MEGA	**MECANIQUE, ENERGETIQUE, GENIE CIVIL, ACOUSTIQUE** **http://mega.universite-lyon.fr** Sec : M. LABOUNE PM : 71.70 –Fax : 87.12 Bat. Saint Exupéry mega@insa-lyon.fr	M. Philippe BOISSE INSA de Lyon Laboratoire LAMCOS Bâtiment Jacquard 25 bis avenue Jean Capelle 69621 VILLEURBANNE Cedex Tél : 04.72 .43.71.70 Fax : 04 72 43 72 37 Philippe.boisse@insa-lyon.fr
ScSo	**ScSo*** **http://recherche.univ-lyon2.fr/scso/** Sec : Viviane POLSINELLI Brigitte DUBOIS Insa : J.Y. TOUSSAINT viviane.polsinelli@univ-lyon2.fr	Mme Isabelle VON BUELTZINGLOEWEN Université Lyon 2 86 rue Pasteur 69365 LYON Cedex 07 Tél : 04.78.77.23.86 Fax : 04.37.28.04.48

*ScSo : Histoire, Géographie, Aménagement, Urbanisme, Archéologie, Science politique, Sociologie, Anthropologie

献给我的法兰西青春岁月

À mes 4 belles années de thèse en France

“It's not that I'm so smart, it's just that I stay with problems longer.”

---Albert Einstein

Acknowledgements

How time flies! I still remember the 2nd October 2012, the first day I arrived in France. Till now, with this doctoral thesis finished, nearly four years have passed and my journey as a PhD student comes to its end. When I look back these four years in IMP, in Lyon, and in France, I feel so lucky to have such a beautiful journey with so many kind people by my side. Without their help, support and encouragement, my thesis work would not have been possibly finished.

I sincerely thank Prof. Jannick Duchet-Rumeau for having offered me such a precious opportunity to study at IMP under your supervision. With no doubt that I have learned so much from you, especially your solid experience of composite materials, your insight into the polymer science and your vision of a good work. I equally appreciate your patience and kind care along these years. Every time I faced some blocks in my way, you always encouraged me, and told me “don’t worry”. Without you, I even cannot imagine how to overcome the problems time and time again.

I would like to say “thank you” to Dr. Sébastien Pruvost. It was you who has led me and guided me step-by-step from being a fresh PhD student to a conferred one. What's more, it was you who has encouraged me to try my best to speak French, which greatly helped me in adapting myself in France. I value your preciseness about scientific research, being strict to your PhD students, which I realized have helped me achieve my PhD and also are treasures in my future. You are the best supervisor in my heart.

I am grateful to Dr. Sébastien Livi for your kind help during these years. Your rich knowledge in structuration of polymers by adding ionic liquids, your passionate enthusiasm for research, and your constant good mood for work always motivate me to be strong, be positive and be professional with our work.

I wish to express my special thanks to Prof. Daodao Hu. You are the first teacher to initiate me into research. I appreciate your original ideas and valuable advices toward some difficult scientific issues, which always help me to figure out them. I also thank you for your constant encouragement and support.

Thanks to Dr. Vittorio Basso for your kind help with ECE measurement. Great

appreciation also goes to Dr. Annie Rivoire (CTU, TEM), Ruben Vera (Centre Henri Longchambon, XRD), Alain Lapp & François Boue (LLB, SANS), Dr. Françoise Mechin (FT-IR), Guilhem Quintard & Raphaël Brunel (MTS, DMA), Marion Colella (DSC, TGA), Arthur Bouchut (Raman), Alain Rousseau, and Julien Chatard for all your help and advices with my experimental measurements.

Thanks to secretaries and administrators in our lab, with honorable mentions of Prof. Etienne Fleury, Isabelle Polo and Sylvain Baudu for their assistance on the administrative procedure.

I am grateful to all my colleagues in our lab for their kind help and encouragement. Especially, Thibaut Benethuiliere, Sophie Iglesias, Nicolas Laforest, Pauline Sallet, Jean-David Rodier, Jean-Charles Fontanier, Nour Halawani, Benjamin Megevand, Arthur Bouchut, Thomas Salard, Heloise Blache, Constance Robeyns, Laetitia Dentzer, Amélie Gaston, Quentin Charlier, Loriane Desmars, Adeline Crohare, Florence Russo, Biao Zhang, Xibo Yan, Quanyi Yin, Jingping Li, Bo Lu, Luxiao Chai, thanks a lot for your kind accompanying along this beautiful journey.

Here comes to my best friends, Qiang Weng, Clarice Zornio, Luanda Lins, Nguyen Thi Khanh Ly, and Hynek Bens. You are more like my families in my heart, and when I faced problems, all of you always stand with me. Thank you so much, and long live the friendship between us.

I greatly appreciate the care and encouragement provided by my friends in China, especially Yuanying Cao, Jing Wu, Jun Yan and so on.

I would like to express my deep appreciation to Lin Wang for your kind care, your clever idea toward ECE measurements, and especially your every companion with me from police station to hospital.

I would like to say “thank you” to Jing Chen, for the valuable discussion with you, your constructive suggestions on research issues and uncontional support to me.

Finally, I am forever indebted to my family for their everlasting understanding and love.

Jing Yang

July, 2016

List of Abbreviations and Symbols

$[(CF_3SO_2)_2N]^-$	bis(perfluoromethylsulfonyl)imide
$[BF_4]^-$	tetrafluoroborate
[BMIM][PF_6]	1-butyl-3-methylimidazolium hexafluorophosphate
$[CF_3SO_3]^-$	trifluoromethansulfonate
$[MeBuImi]^+[BF4]^-$	1-methyl-2-butyl-imidazolium tetrafluoroborate
$[PF_6]^-$	hexafluorophosphate
$[tbmam]^+[Tf_2N]^-$	tributyl(methyl)ammonium bis(trifluoromethane)sulfonylimide
[VBIM][Cl]	1-vinyl-3-butylimidazolium chloride
$\Delta H_{100\%}$	melting enthalpy for totally crystalline
ΔS	entropy change
λ	wavelengths
χ_c	crystallinity
2θ	diffraction angle
AC	alternating current
ATR-FTIR	attenuated total reflectance Fourier transform infrared
CB	carbon black
CNF	carbon nanofibers
CNTs	carbon nanotubes
CRP	controlled radical polymerization
CTAB	cetyltrimethylammonium bromide
CTE	coefficient of thermal expansions
CuNWs	copper nanowires
CuPc	Cu-phthalocyanine
CVD	chemical vapor deposition
DC	direct-current
DEA	dielectric analysis
DMA	dynamic mechanical analysis
DMF	dimethyl formamide
DSC	differential scanning calorimetry
DTG	differential thermogravimetry
Ea	activation energy

ECE	electrocaloric effect
EMI	electromagnetic interference
FTIR	Fourier transformed infrared
GO	oxidized graphene
HTPB	(1-hexadecyl) triphenylphosphonium bromide
IL-108	tributyl(methyl)phosphonium methylsulfate
IL-C18	octadecyltriphenylphosphonium iodide
IL-C8F13	perfluorooctyltriphenylphosphonium iodide
ILs	ionic liquids
LDH	layered double hydroxide
L_p	long period
M”	imaginary part of dielectric modulus
MAF	mobile amorphous fraction
MEK	methyl ethyl ketone
MW	molecular weight
MWCNTs	multi-walled carbon nanotubes
Ni-NWs	nickel nanowires
P(VDF-CTFE)	poly(vinylidene fluoride-chlorotrifluoroethylene)
P(VDF-HFP)	poly(vinylidene fluoride-hexafluoropropylene)
P(VDF-TrFE)	poly(vinylidene fluoride-trifluoroethylene)
P(VDF-TrFE-CTFE)	poly(vinylidene fluoride-trifluoroethylene-chlorotrifluoroethylene)
PAHs	polycyclic aromatic hydrocarbons
PBAT	poly(butylenes adipate-co-terephthalate)
PC	polycarbonate
PE	polyethylene
PMMA	poly(methyl methacrylate)
PNIPAAm	poly(*N*-isopropylacrylamide)
POM	polarized optical microscope
PTFE	poly(tetrafluoroethylene)
PVA	poly(vinyl alcohol)
PVDF	poly(vinylidene fluoride)
PVDF-NPs	PVDF nanoparticles
RAF	rigid amorphous fraction

rGO	reduced oxidized graphene
RTILs	room temperature ILs
SANS	small angle neutron scattering
SAXS	small angle X-ray scattering
SDD	sample-to-detector distances
SEM	scanning electron microscopy
SI-ATRP	surface-initiated atom transfer radical polymerization
tan δ	dielectric/mechanical loss tangent
T_c	crystallization temperature
TEM	transmission electron microscopy
T_g	glass transition temperature
TGA	thermogravimetric analysis
THF	tetrahydrofuran
T_m	melting temperatures
TPU	thermoplastic polyurethane
VWP	vapor water permeability
xGnP	exfoliated graphite nanoplates
XRD	X-ray diffraction

Phosphonium Ionic Liquids: Versatile Nanostructuration and Interfacial Agents for Poly(vinylidene fluoride-chlorotrifluoroethylene)

Abstract

This thesis work deals with an understanding of the versatile roles of phosphonium ionic liquids (ILs) as nanostructuration and interfacial agents for the fluorinated polymer matrix, *i.e.*, poly(vinylidene fluoride-chlorotrifluoroethylene) (P(VDF-CTFE)). In this context, two phosphonium ILs with different functionalities in steric hindrance and extra dipolar groups are firstly incorporated in P(VDF-CTFE) matrix to prepare polymer films. The crystalline phase structure, dispersion morphology and crystallization behavior are finely characterized with the goal of providing a full and deep understanding of the versatile and tunable nanostructuration effect of phosphonium ILs. Subsequently, in order to elucidate the mechanism of interfacial influence of IL, a fluorinated phosphonium IL with a cation structure combining three phenyls and a short fluorinated chain is added on the surface of graphene oxide (GO) and reduced graphene oxide (rGO), making them as functional nanofillers to be incorporated into P(VDF-CTFE) matrix. Thus, P(VDF-CTFE)/graphene composite films with different filler contents are prepared in order to investigate the mechanism of interfacial interaction and its influence on the composite films, such as crystalline phase structure, crystallization behavior, chain segmental relaxation behavior, dispersion morphology and the final dielectric properties.

Keywords: poly(vinylidene fluoride-chlorotrifluoroethylene); phosphonium ionic liquids; nanostructuration; interfacial agent; graphene; composite films

Les Liquides Ioniques Phosphonium: Des Agents Versatiles pour la Nanostructuration et la Compatibilisation du Poly(fluorure de vinylidène-chlorotrifluoroéthylène)

Résumé

Ce travail de thèse porte sur la compréhension fuie du rôle polyvalent des liquides ioniques (LIs) phosphonium comme agents de nanostructuration et interfaciaux pour la matrice polymère fluorée poly(fluorure de vinylidène-chlorotrifluoroéthylène) (P(VDF-CTFE)). Dans un premier temps, deux LIs phosphonium avec des fonctionnalités différentes générant un encombrement stérique et des fontions dipolaire additionnelles sont tout d'abord incorporés dans la matrice P(VDF-CTFE) pour préparer des films de polymère additivés. La structure de la phase cristalline, la morpholigie issue de la dispersion et le comportement de cristallisation sont finement caractérisés dans le but de fournir une compréhension fuie et complète du rôle joué par le LI sur la nanostructuration. Dans un second temps, le rôle d'agent interfacial du LI est étudié avec un LI phosphonium fluoré comprenant un cation combinant trois phényles et une chaîne fluorée courte. Ce LI est utilisé pour modifier la surface de l'oxyde de graphène (GO) et de l'oxyde de graphène réduit (rGO) afin de rendre ces nanocharges fonctionnelles et les incorporer dans la matrice P(VDF-CTFE). Ainsi, des films composites de P(VDF-CTFE)/graphène avec differentes teneurs en nanocharges sont préparés et une caractérisation fuie de la structure et des propriétés est entreprise afin de mieux compendre les mécanisme d'interaction interfaciale et leurs influences sur les films composites, tels que la structure de la phase cristalline, le comportement de cristallisation, la relaxation des chaînes, la morphologie et les propriétés diélectriques finales.

Mots clés: poly(fluorure de vinylidène-chlorotrifluoroéthylène); liquides ioniques phosphonium; nanostructuration; agent interfacial; graphène; films composites

TABLE OF CONTENTS

General Introduction

General Introduction

The association of ionic liquids (ILs) with polymers has arisen great interests at all levels of the development of a highly functional material, from its synthesis and implementation through to its structuring, which plays a key role in determining the final properties. Recently, great attention has been paid to draw them together with a view to developing an understanding of the relationships between the structure of the ionic liquid and the impact on the properties of the polymer. The unique set of physico-chemical properties of ILs finely tuned from their chemical structure makes them as versatile components for processing of advanced polymer materials, for example, as (1) ionic conducting agents for polymer electrolytes; (2) processing aids as solvents or green composites; (3) plasticizers of polymers; (4) chemically reactive agents able to initiate the polycondensation of epoxy networks; (5) structuration agents to achieve a tunable structure in polymer with enhanced properties; (6) interfacial agents for tailoring the dispersion of fillers in nanocomposites for facilitating the compatibilization of polymer blends.

In terms of one of the most important electroactive fluoropolymers, poly(vinylidene fluoride) (PVDF) and its co(ter)polymers have earned a large range of applications due to pyro/ferro/piezo-properties. Moreover, their semi-crystalline thermoplasticity, excellent thermal stability and chemical resistance make PVDF-based polymers acting as outstanding precursors for polymeric electroactive composites.

This research work, funded by the China Scholarship Council (CSC), is inscribed in this frame. An electroactive fluorinated copolymer poly(vinylidene fluoride-chlorotrifluoroethylene) (PVDF-CTFE) and functional phosphonium ILs or functionalized graphene modified by ILs are used as building elements to prepare P(VDF-CTFE)-based composite films. This thesis will highlight (1) the versatile and tunable nanostructuration effect of ILs on P(VDF-CTFE) matrix; (2) the interfacial effect of ILs on graphene/P(VDF-CTFE) composites.

In this framework, this manuscript is organized in three different chapters. The first bibliographic chapter aims at drawing the context of this work. Thus, this chapter is divided into three main sections. The first section reviews PVDF-based polymer matrix, including synthesis, identification of crystals, methods to form polar

crystalline phases, PVDF-based copolymers or terpolymers and their properties. The second section starts from the chemical structure, synthesis, purification, properties and applications of ILs, and then the progress on the structuration effect of ILs in polymer matrices is addressed. The third section focuses on the structuration of nanofillers on the PVDF-based matrices. After a short introduction of recent processes on the nanofiller-incorporated PVDF-based composites, the process specifically on the PVDF/graphene composites is highlighted. Through comparing the methods to enhance the dispersion of graphene in the matrix, the recent work on the effect of ILs as novel interfacial agents for PVDF/graphene composites is further delivered.

The second chapter aims to investigate the effect of ILs on the P(VDF-CTFE) matrix, which is divided into two parts. The first subsection is relied on one publication in *Macromolecules*, **2015**, *48*, 4581-4590. The objective of this subsection is to promote the current understanding of the fundamental mechanism of the versatile and tuable nanostructuration of ILs on semi-crystalline PVDF-based copolymer to answer some unclear issues such as i) what determines the strength of dipolar interaction between ILs and polymer matrix, ii) how does the dipolar interaction affect the nanostructuration on the matrix, not only the crystalline phase structure but also the dispersion morphology and crystallization behavior, iii) what is the relationship between the nanostructuration effect of ILs and their localization in matrix, and also what governs this localization. Therefore, in this chapter, two phosphonium ionic liquids (ILs), denoted octadecyltriphenylphosphonium iodide (IL-C18) and tributyl(methyl)phosphonium methylsulfate (IL-108) will be used to be incorporated in (P(VDF-CTFE) matrix. The differences in steric hindrance and in functionalities are considered as potential key factors to influence the interaction with P(VDF-CTFE) and diffusion rate of ILs in polymer matrix during the film formation. The crystalline phase structure, dispersion morphology and crystallization behavior are finely characterized with the goal of providing a full and deep understanding of the versatile and tunable nanostructuration effect of phosphonium ILs. The second subsection will pay attention to the electrocaloric effect (ECE) of neat P(VDF-CTFE) by direct measurement and make some reflections on ECE measurements of P(VDF-CTFE)/IL blends.

The third chapter focuses on the investigation of the role of fluorinated IL as a new interfacial agent in the P(VDF-CTFE)/graphene composite films. First, a task-

specific IL, perfluorooctyltriphenylphosphonium iodide (IL-C8F13) is synthesized and modified on the surface of graphene oxide (GO) and reduced graphene oxide (rGO) for making functional nanofillers incorporated into P(VDF-CTFE) matrix. The cation structure of IL combines three phenyls (potential π-π interaction with graphene) and a short fluorinated chain (enhanced miscibility with fluorinated matrix *via* dipolar interaction) to compatibilize graphene filler and P(VDF-CTFE) matrix at the interface between them. Second, two series of P(VDF-CTFE)/GO-IL and P(VDF-CTFE)/rGO-IL composites with different loading contents are prepared with the goal of providing an understanding of the mechanism of interfacial interaction. This chapter will investigate the difference in the interaction model between GO with IL and rGO with IL. Subsequently, the interfacial effect of IL on the properties of P(VDF-CTFE)/graphene composites, such as crystalline phase structure, crystallization behavior, chain segmental relaxation behavior, dispersion morphology and the final dielectric properties will be further studied.

Chapter 1
Reviews on Bibliography

Chapter 1: Reviews on Bibliography

1.1 PVDF and its copolymers

1.1.1 General introduction

Poly(vinylidene fluoride) (PVDF) and its copolymers, having the second largest production volume of fluoro-plastics after poly(tetrafluoroethylene) (PTFE), are distinctive members of the fluoro-polymer family. Due to the small van der Waals radius of F atom (1.32 Å) and strong C-F bond (485 kJ/mol), they exhibit high thermal, chemical, oxidation and aging resistance, and also are inert to various solvents, acids, alkalies and hydrocarbons [1,2,3,4].

Besides the common properties of fluorinated polymers, PVDF and its family of copolymers are arguably the best-known examples of a family of high performance polymers noted for their remarkable piezo, pyro and ferro-electric properties [5,6,7] due to the strong electronegativity of the F atoms and the orientation of dipoles of C-F bonds under electric field. Since Kawai [8] discovered the excellent piezoelectric behavior of PVDF in 1969, more than 30 years' efforts have been made to markedly improve the electroactive properties of PVDF and it copolymers, and up to now, they are still promising electroactive polymers among the best-known synthetic organic materials, being therefore the preferred polymer for the increasing number of possible applications mostly in energy-related fields, such as energy harvesting devices, solid state refrigeration, sonar, infrared imagining devices, capacitors, transducer devices, tactile sensors and actuators, *etc* [3,9,10,11].

This *Section* will highlight the state-of-art on PVDF and its copolymers including synthesis methods, molecular conformations and crystalline structures, methods to form polar crystalline phases and potential applications.

1.1.2 PVDF

1.1.2.1 Synthesis of PVDF

The synthesis of PVDF is usually manufactured by the traditional radical polymerization process. Due to the gaseous monomer VDF (m.p. = -144 ^{o}C and b.p. = -84 ^{o}C), the radical polymerization is carried out in a high pressure vessel, from three routes of polymerization discussed below.

(1) Emulsion or suspension polymerization

In industry, the polymerization process often takes place in aqueous emulsion or suspension under the pressures of 10~300 bar and at the temperatures of 10~130 ^{o}C [1]. Concerning the heterogeneous reaction, the process needs fluorinated surfactants, chain transfer agents, buffers and water- or organo-soluble initiators. Usually, the water-soluble initiators are persulfate salts [12,13], disuccinic acid peroxide [14], hydroxyalkylperoxide or alkylperoxybutyric acid [15]. For organo-soluble initiators, *tert*-butylperoxypivalate [16], di-*tert*-butyl peroxide [17], diisopropylperoxydicarbonate [18,19,20,21] together with water-soluble suspending agents (cellulose derivatives or poly(vinyl alcohol) (PVA)) are often used.

(2) Solution polymerization

The polymerization in chlorofluorinated solvents initiated by organic peroxides such as bis(perfluoropropionyl)peroxide [22], *tert*-butylperoxypivalate [23], bis-4-*tert*-butylperoxycyclohexyldicarbonate [24] can also be performed. In addition, DeSimone *et al.* prepared PVDF by radical polymerization in the green supercritical CO_2 medium, easily producing a clean and dry product after depressurization [25,26].

(3) Controlled radical polymerization (CRP)

Although the examples developed by CRP are relatively scarce, PVDF can also be obtained through CRP methods such as iodine transfer polymerization (ITP), borane-mediated radical polymerization and macromolecular design *via* interchange of xanthates (MADIX). Daikin company is the pioneer to polymerize VDF in the

presence of $C_6F_{13}I$ by ITP, resulting in very low molecular weight (MW) dispersities around 1.2 [27,28]. Moreover, controlled VDF polymerization has been realized at room temperature using a borane/oxygen initiator [29,30]. Recently, Ameduri's group also developed the degenerative chain transfer process involving dithiocarbonates (xanthates), denoted as MADIX, to prepare well-defined PVDF [31,32].

1.1.2.2 Molecular conformations and crystal structures

PVDF is a typical semi-crystalline polymer in which crystalline regions are surrounded by amorphous ones. It has a very simple chemical formula, *i.e.*, $–CH_2–CF_2–$, whose chain flexibility is intermediate between polyethylene (PE) ($–CH_2–CH_2–$) and polytetrafluoroethylene (PTFE) ($–CF_2–CF_2–$). This chemical structure endows PVDF both flexibility and stereochemical constraint to the backbone structure, and thus gives PVDF the ability to adopt different chain conformations, ultimately leading to several crystalline phases. This polymorphism is due to the slightly larger fluorine atoms with respect to the hydrogen atoms. Consequently, this semi-crystalline polymer shows a complex structure and can mainly display five different crystalline phases corresponding to distinct chain conformations: (1) TTTT (*all-trans*) zigzag for the β-phase, (2) TGTG' (*trans-gauche-trans-gauche*) for the α and δ-phases, (3) T_3GT_3G' for the γ and ε-phases [1]. Among them, the most common and stable conformations are α, β and γ-phases which are depicted in Figure 1-1.

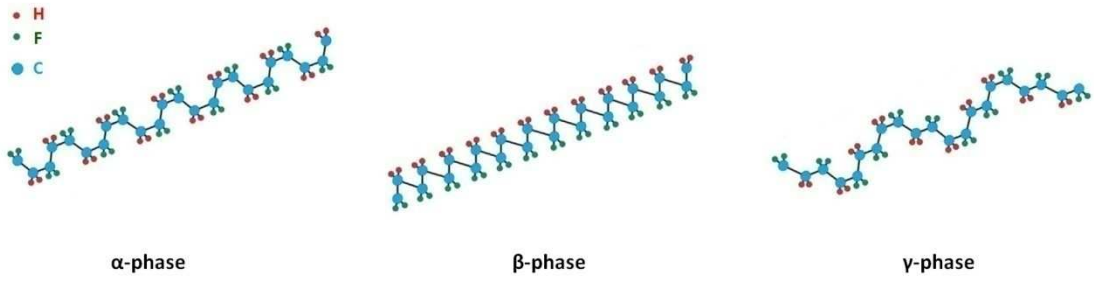

Figure 1-1: Schematic representation of the chain conformations for the α, β and γ-phases of PVDF [3]

Almost all the interesting piezo, pyro and ferro-electric properties of PVDF are related to the strong electrical dipole moment of the PVDF monomer unit ($5\sim8\times10^{-30}$ C·m) due to the higher electronegativity of F atoms compared to those of

H and C atoms [33,34]. Therefore, each bond has a dipole moment perpendicular to the polymer chain. These dipolar moments are then packed in the morphology which can show an overall dipolar contribution only in the polar β and γ-phases butnot in the nonpolar α-phase in which the dipole moments are offset due to the antiparallel packing of the dipoles within the unit cell [35,36]. Since the properties of PVDF are strongly dependent on the crystalline structures, the identification of them is very important.

The β and α-phases were first discovered and clearly identified by Fourier transformed infrared spectroscopy (FTIR) and X-ray diffraction patterns (XRD) [37]. However, it causes some confusion in the distinguishing of the third γ-phase. Some reported results regarding the identification of both β and γ-phases are contradictory due to the similarity of the β and γ-phase specific conformations. The characteristic FTIR bands and XRD peaks typically used for identifying the phases either coincide or are very close to each other, making difficult to distinguish them [38,39,40]. A series of careful and detailed data provided by FTIR, XRD and differential scanning calorimetry (DSC) have already been used toidentify different phases of PVDF [41,42,43,44,45,46,47,48,49]. Moreover, as a complementary method, polarized optical microscope (POM) is a technique to distinguish α- and γ-phase of PVDFthrough the difference in the morphology of spherulites. However, combining all these techniques is sometimes required due to the superposition of the peaks corresponding α, β, and γ-phases if only one method is used. Thus, the combination of the different techniques allows the correct identification of phases. In the following paragraph, the methods to identify the PVDF phases by FTIR, XRD, DSC and POM techniques will be explained in detail.

(1) Fourier transformed infrared (FTIR) spectroscopy

The FTIR spectroscopy gives the wavenumbers of molecular vibrations which are particularly sensitive to the change of the internal rotational angles, *i.e.*, chain conformation [50]. Consequently, as a semi-crystalline polymer, the changes of macromolecular conformation of PVDF may occur in two cases: (1) regular

changesthroughout the whole chain with a new chain conformation; (2) random changes along the polymer chain. The former one gives rise to a new crystalline phase with totally different infrared absorption bands, whereas the latter one should lead to the same absorption bands observed for the amorphous phase but with a varying intensity. So the spectra of PVDF provide rich information allowing distinguishing among different crystalline forms and also amorphous regions of PVDF. However, β and γ-phases have some superpositions in FTIR spectra [42]. And also, due to the preparation methods, the same film can involve one or more than one crystalline phase, the identification of crystalline phases by FTIR usually causes some qualitative problems [43].

First, the most easily confirmed crystalline phase by FTIR is α-phase since it presents a large number of characteristic bands exclusively belonging to it, such as the vibration absorption bands at 489, 614, 766, 795, 855 and 976 cm^{-1} (Table 1-1) [42]. Second, as mentioned above, β and γ-phases have some absorption peaks locating closely to each other, and even the same wavenumbers due to the similar polymer chain conformation [42]. For example, the band at 512cm^{-1} is assigned to the γ-phase, which is very close to one at 510 cm^{-1} for the β-phase [41]. Moreover, some authors classify the strong peak at 840 cm^{-1} as a characteristic of the β-phase [41,47] while others consider it attributed to both of them [48]. Until recently, it has been widely accepted that the band at 840 cm^{-1} is common to both polymorphs but it is a strong band only for the β-phase, whereas a shoulder localized at 833 cm^{-1} is attributed to γ-PVDF band (Figure 1-2) [42,43]. However, fortunately, there are still some distinguishable FTIR absorption bands for β and γ-phases, respectively. For instance, the bands at 431, 776, 812, 833 and 1234 cm^{-1} are exclusively of the γ-phase, while the ones at 445 and 1279 cm^{-1} are characteristic for β-phase. All the data can be used to identify them and all the characteristic bands of each crystalline phase are summarized in Table 1-1.

Table 1-1: FTIR absorption bands of α, β, and γ-phases of PVDF

Crystalline phase	Wavenumber (cm^{-1})
α	408, 532, 614, 766, 795, 855, 976
β	510, 840
γ	431, 512, 776, 812, 833, 840, 1234

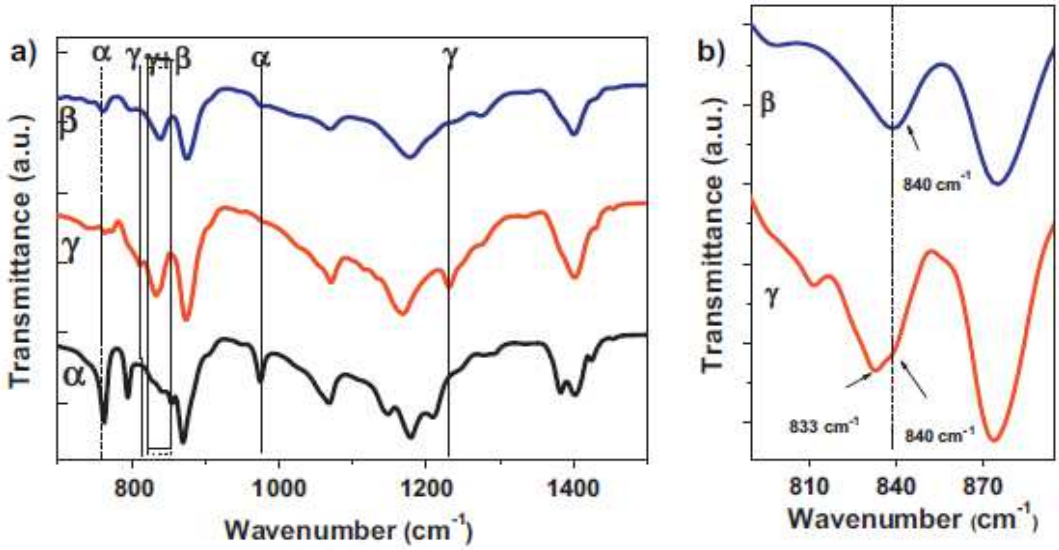

Figure 1-2: ATR FTIR spectra of crystalline identification of α, β, and γ-phases (a) and a detail of the β, and γ-characteristic region commonly used in the literature for distinguishing them (b) [3]

However, there are still several problems in determining crystalline phases for specific samples only using FTIR technique because it is difficult to obtain an ideal single type of crystalline phase of PVDF and also that the FTIR spectrum is strongly dependent on molar mass distribution, head-to-head and tail-to-tail defects, crystalline nature, orientation and thickness of samples, *etc* [51]. Furthermore, it could lead to some confusion between β and γ-phases when only FTIR results are used. Thus, some additional techniques such as XRD and DSC have been explored for the phase identification.

(2) X-ray diffraction (XRD)

XRD is an useful tool to study the crystalline phases of PVDF [41,52,53]. The

positions of the diffraction peaks are the fingerprints of each crystalline phase. Nevertheless, the γ-phase is still the one that has some identification problems because of the lack of characteristic diffractogram of this phase since until recently no samples containing exclusively the γ-phase had been processed [41,45]. However, we can identify the diffraction peaks exclusively belonging to the γ-phase through the comparison of the diffractograms of exclusive α-phase samples and mixed α and γ-phase ones [41]. More recently, samples of PVDF with completed γ-phase have been obtained by the incorporation of clays [38] and thus the XRD diffraction peaks could be confirmed.

In the XRD patterns, all α, β and γ-phases have an intense peak around $2\theta = 20^{o}$, but only α and γ-phase present other peaks close to $2\theta = 18^{o}$ which makes them easily distinguishable from the β-phase [45]. In this way, the β-phase displays a well defined peak at $2\theta = 20.26^{o}$ which is related to the sum of the (110) and (200) planes [41,45]. In the same region, α-phase presents more characteristic peaks at $2\theta = 17.66^{o}$, $18.30^{o}$and 19.90^{o}corresponding to (100), (020) and (110) planes, respectively. In addition, α-phase also shows a peak at $2\theta = 26.56^{o}$ assigned to the (021) diffraction plane [41,45,54]. Finally, γ-phase presents a superposition of peaks at $2\theta = 18.50^{o}$ and 19.20^{o} associated to (020) and (002) planes, respectively, and a more intense peak can be detected at $2\theta = 20.04^{o}$ corresponding to the (110) crystalline plane. Similarly to α-phase, γ-phase presents a weaker peak inthe region of 26.80^{o} attributed to the (022) plane. The diffraction 2θ angles and crystal planes for each crystalline phase of PVDF are summarized in Table 1-2 and Figure 1-3. To conclude, FTIR spectra can cause some confusion between β and γ-phases, while XRD results lead to some difficulties in distinguishing α and γ-phase. Thus, combining both techniques is an ideal strategy to determine all the main crystalline phases of PVDF. However, for PVDF copolymers or terpolymers, the existence of comonomer in the PVDF crystal or in the amorphous zone is complex, which could disturb the position of β-crystal planes. Thus, in some cases, more techniques are required to identify the crystalline phases of PVDF.

Table 1-2: Diffraction 2θ angles and planes of each phase of PVDF

Crystalline phase	2θ (°) and (crystal plane)
α	17.66 (100), 18.30 (020), 19.90 (110), 26.56 (021)
β	20.26 (110) (200)
γ	18.50 (020), 19.20 (002), 20.04 (110), 26.80 (022)

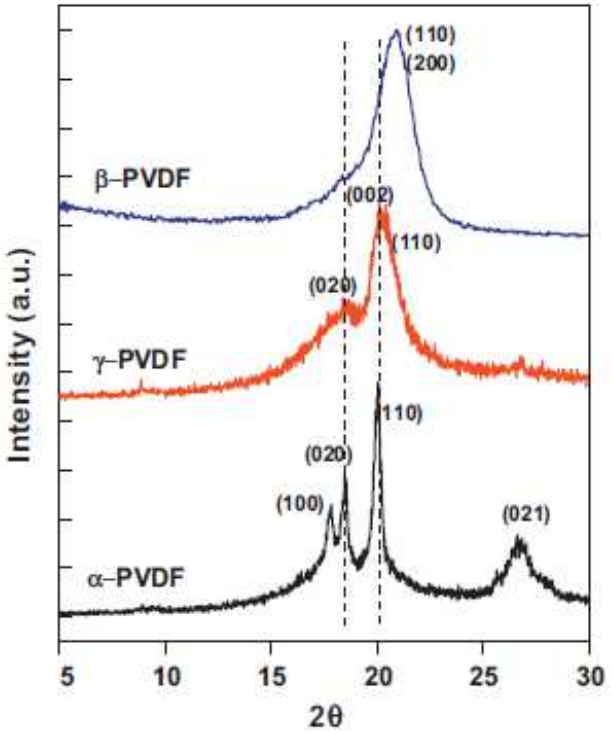

Figure 1-3: XRD patterns of crystalline identification of α, β, and γ-phases of PVDF commonly used in the literature for distinguishing them [3]

(3) Differential scanning calorimetry

Being a thermo-analytical technique, DSC is a complementary identification method of the crystalline phases of PVDF because the differentiated melting peaks are a signature on the DSC thermogram. Besides the crystalline phases, there are other morphological factors influencing the characteristics of the DSC peaks including defects and crystal size, thus the existing literature reported no work defining a melting temperature for the characteristic phase but a temperature range. Prest and

Luca *et al*. finds that the melting temperature of the α-phase of PVDF is 172 °C while Gregorio and Cestarini [55] report that it occurs at 167 °C. For the β-phase, a melting temperature similar to the one for α-phase is found [41], and therefore, DSC can not be used to distinguish these two phases, but only to calculate the crystallinity [38,56]. However, the melting temperature of γ-phase is dramatically different from those of α and β-phases. For example, the melting temperature of the γ-phase obtained by crystallization from the melt is around 179-180 °C, which is about 8 °C higher than one of the α-phase [41]. Specially, when the γ-phase is obtained from the transformation of α-phase to γ-phase, the melting temperature is about 18 °C higher than that of α-phase, *i.e.*, around 189-190 °C [41,43]. In this way, DSC technique is particularly interesting to assess the existence of γ-phase of PVDF. However, note that DSC should be just a complementary technique to FTIR or XRD as its characteristic peaks are not only dependent on the crystalline phase, butalsocanbe affected by crystalline defects which are particularly promoted by the presence of fillers in polymer composites. Typical DSC thermograms of different PVDF crystals are shown in Figure 1-4.

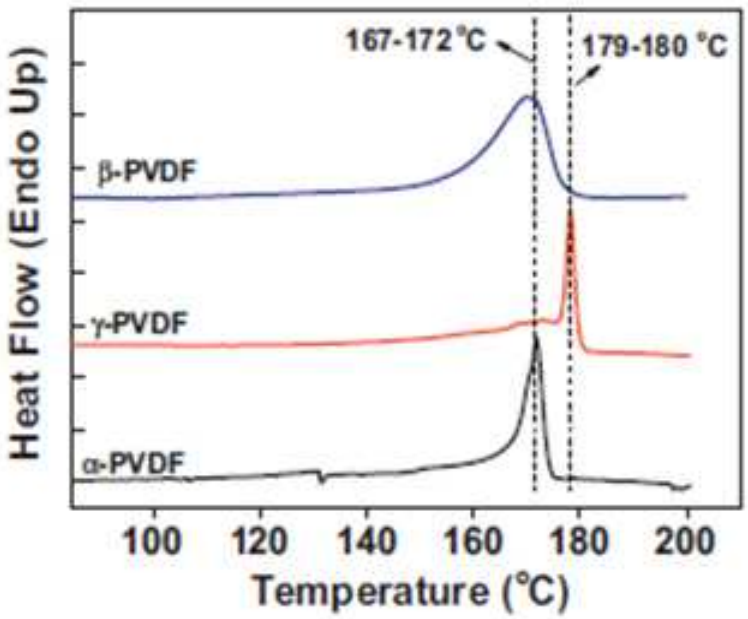

Figure 1-4: DSC thermograms for crystalline identification of α, β, and γ-phases of PVDF commonly found in the literature [3]

(4) Polarized optical microscope (POM)

The crystalline morphology observed by POM is a complementary method to differentiate α-crystal from γ-one. Typically, α-crystals show strongly birefringent spherulites as well as closely spaced concentric rings from twisting lamellae, while very darker and less birefringent γ-spherulites are usually observed in the POM image (see Figure 1-5 for a typical comparison) [39].

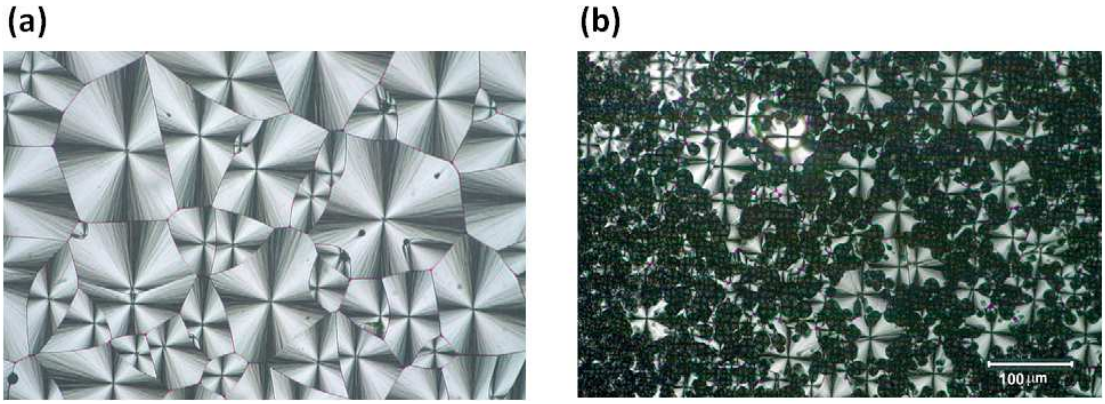

Figure 1-5: Typical POM images of pure α-crystal (a) and dominant γ-crystal (b) of PVDF

In conclusion, the experimental techniques mentioned above allow the identification of the most investigated phases of PVDF. On the one hand, FTIR gives a clear determination of α-phase, but the β and γ-phase bands are very similar. On the other hand, XRD shows superimposed diffraction peaks for α and γ-phases, but allows identifying the β-phase. So, the combination of these two techniques can correctly identify the crystalline phases of PVDF, and also, DSC can be used to confirm the results, especially to check the existence of the γ-phase. It is necessary to combine at least two of the techniques to correctly and fully identify a specific crystalline phase of PVDF.

1.1.2.3 Methods to form polar crystalline phases

As mentioned before, the electroactive properties of PVDF are related to the strong electrical dipole moment of PVDF, so the highly polar β and γ-phases have demonstrated excellent performances and different strategies have been developed to promote the formation of electroactive polar phases of PVDF, mainly focusing on the development of processing methods and the inclusion of fillers. Generally, the

strategies of producing polar β and γ-phases can be divided into (1) "from melting", (2) "from α-phase", (3) "from solvent casting", (4) "from addition of fillers", (5) "from copolymerization". In this sub-section, we will summarize the first four methods described in literatures in Table 1-3, and the last one will be highlighted in the following section concerning the PVDF-based copolymers (*subsection 1.1.3*).

Table1-3: Strategies of producing polar β and γ-phases of PVDF in literatures

Strategy	Preparation	Results	Ref
From melting	Pressure quenching at high pressure (800 MPa)	Pure β-phase film	[57]
	Non-isothermal crystallization at ultra-high cooling rate (30~3000 K/s)	Pure β-phase film when cooling rate increases up to 2000 K/s	[58]
	Isothermal melting crystallization at extremely high temperatures (~170 °C for 20 h)	34.8% of γ-phase film	[59,60]
From α-phase	Stretching mechanism	The maximum β-phase (74%) achieved at 90 °C and stretch ratio R = 4.5~5	[61]
	Annealed at around m.p. of PVDF	Formation of γ-phase	[62]
From solvent casting	Under high electric field	Pure β-phase	[63]
	Electrospinning	Submicron to nano-scale fibers with high content of β-phase (~80%) without post-treatment	[64,65]
	Spin-coating	Spin speed and humidity control the formation of β-phase (0~75%)	[66,67,68]
	Langmuir-Blodgett deposition	Direct formation of ultra-thin β-phase films without any post-processing	[69,70]
	From polar solvents (DMF, DMAc) at temperature below 70 °C	High degree of porosity and fragility, high content of polar β-phase	[71,72]
Adding fillers	$BaTiO_3$	~90% of β-phase	[73]
	Organically modified clays	>90% of β-phase	[74,75,76]
	Ferrite	Formation of β-phase	[77]

	Palladium nanoparticles (by heat-controlled spin coating)	Formation of β-phase	[78]
	Gold nanoparticles and nanoshells (by solution mixing)	Formation of β-phase	[79]
	Carbon nanotubes (solution sonication and mechanical treatment)	Formation of β-phase	[80]
	KBr powder isothermally crystallization (165 ^{o}C, 45 min)	γ-phase-rich films	[81]
	Montmorillonite clay	Total crystallization on γ-phase	[82]
	zeolite	Total crystallization on γ-phase	[83]

1.1.3 PVDF-based copolymers

Generally, copolymerization is a very powerful method to make effective systematic changes in polymers' structure and properties, thanks to the strong ability to modify the symmetry of the polymeric chain and to modulate both intra- and inter-molecular interactions. Thus, different PVDF copolymers have been prepared to improve the PVDF properties, creating a family of PVDF-based copolymers. It is well known that the introduction of bulky comonomers such as trifluoroethylene (TrFE), chlorotrifluoroethylene (CTFE), or hexafluoropropylene (HFP) as crystalline defect into the PVDF backbone actually imposes a large steric hindrance, which decreases the energy barrier of phase transformation and thus facilitates the *trans*-conformation of the polymer backbone, inducing more polar crystalline phases. [84,85]. In this section, four most used PVDF copolymers will be introduced and their chemical structures are shown in Figure 1-6.

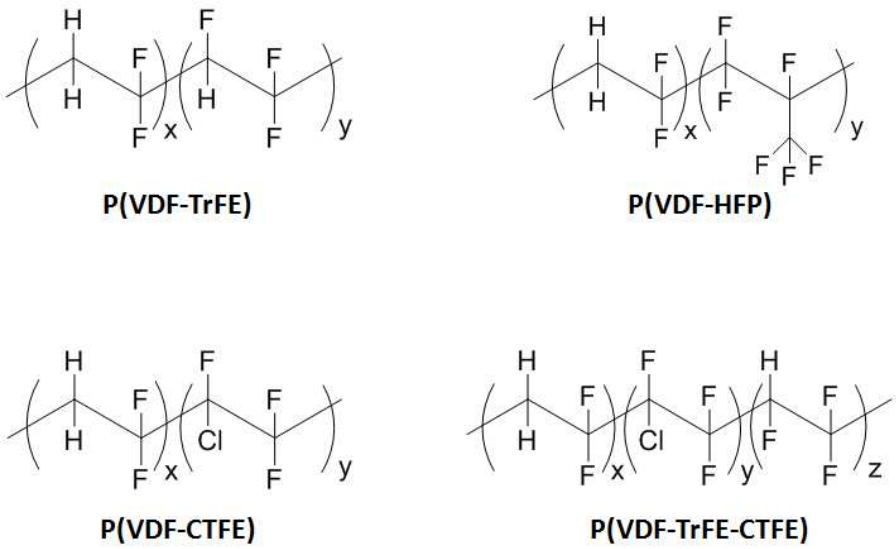

Figure 1-6: Chemical structures of PVDF-based copolymers

(1) Poly(vinylidene fluoride-trifluoroethylene) (P(VDF-TrFE))

P(VDF-TrFE) always presents the polar β-phase when the molar content of VDF is between 50 and 80%. The addition of the third fluoride in the TrFE unit with a large steric hindrance contributes the *all-trans* conformation, and thus induces the polar β-phase which is independent on the general processing methods such as from melting or solution casting [10]. Moreover, P(VDF-TrFE) has a remnant polarization (~110 $mC \cdot m^{-2}$) higher than pure PVDF due to the higher degree of crystallinity and the preferred orientation of well-grown crystallites, which also generates a larger electromechanical coupling factor, *k*, meaning a higher efficiency during the mutually conversion between mechanical to electrical energy [86]. Furthermore, P(VDF-TrFE) also shows the Curie temperature (T_{Curie}) below the melting temperature (T_m), which is different from PVDF. In this way, it allows to study the ferroelectric (FE)—paraelectric (PE) phase transition [87,88]. The T_{Curie} of P(VDF-TrFE) varies from 55 to 128 ^oC with VDF molar ratio included between 55 and 88%. The corresponding enthalpy change, ΔH_{Curie} = 67 J/g [86], which has the potential to be used in cooling devices. In addition to the production of films, P(VDF-TrFE) copolymer can be processed to thin nano-films by spin-coating with controlled thickness, which is ideal for the production of microstructures [89,90]. On the other hand, P(VDF-TrFE) can also be processed under the form of membranes with a controlled microporosity

which is, for instance, relevant to be used for the lithium-ion battery applications [91,92].

(2) Poly(vinylidene fluoride-hexafluoropropylene) (P(VDF-HFP))

P(VDF-HFP) copolymer contains a second amorphous phase linked to HFP within the PVDF homopolymer. Since P(VDF-HFP) is chemically inert and shows lower crystallinity compared with PVDF due to the presence of the bulky CF_3 groups, polymer electrolytes of rechargeable lithium batteries and membranes for organophilic pervaporation are always in progress [93].

The ferroelectric properties of P(VDF-HFP) is strongly dependent on the film-formation processing. The slowly-cooled films do not display a hysteresis upon displacement *versus* electric field (D-E), giving thus a proof of the lack of ferroelectricity. However, the solution-casted and quenched samples present a typical ferroelectric behavior [93]. The highest value of remnant polarization (P_r) is 80 $mC \cdot m^{-2}$ for solution-casted samples with 5% of HFP and the value decreases with increasing the HFP content. Finally, the piezoelectric coefficient (d_{31}) of P(VDF-HFP) (30 $pC \cdot N^{-1}$) being higher than pure PVDF one makes it a kind of promising material used in the piezo- and ferroelectric applications such as transducers, microelectromechanical devices and actuators [93,94,95].

(3) Poly(vinylidene fluoride-chlorotrifluoroethylene) (P(VDF-CTFE))

In P(VDF-CTFE), it has been widely accepted that the comonomer CTFE is critical in determining the copolymer physicochemical properties [1]. First, the P(VDF-CTFE) copolymers containing small contents of CTFE (< 30 mol%) give rise to a monoclinic crystalline structure in which the comonomer CTFE is not able to accommodate within the VDF unit cell, *i.e.*, not cocrystallizable with VDF units but in the amorphous phase. However, those containing 30-75 mol% of CTFE are totally amorphous, and those containing higher than 75 mol% of CTFE lead to a hexagonal crystalline structure. Second, the introduction of the bulky comonomer CTFE, as the crystalline defect into the PVDF backbone, actually imposes a large steric hindrance

which decreases the energy barrier of phase transformation and thus facilitates the trans-conformation of the polymer backbone [84,85]. However, a theoretical work by Ranjan et *al.* [96] indicates that for P(VDF-CTFE) with CTFE contents lower than 17 mol%, the non-polar α-phase is the more thermodynamically stable form than thepolar β-phase. For neat PVDF, the total energy of α-phase is 23 meV per carbon atom lower than that of β-phase. With increasing the CTFE content in the copolymer, this difference in the energy between α-phase and β-phase decreases, so the transformation to β-phase becomes progressively easier untill a critical value is approached (17 mol%) at which the energy difference decreases down to zero. Above 17 mol% of CTFE in the copolymer, the β-phase is preferred and can be obtained easily. Therefore, the comonomer CTFE indeed influences the formation of polar β- and/or γ-phase only when the content of CTFE in the copolymer increases up to a critical value inducinga steric hindrance reducing the energy barrier of phase transformation.

This copolymer also presents piezoelectric properties, higher electrostrictive response and higher dielectric constant than pure PVDF. These behaviors can be explained by the introduction of bulky CTFE which makes the structure looser, leading to an easier orientation of dipoles under external electric field [97].

(4) Poly(vinylidene fluoride-trifluoroethylene-chlorotrifluoroethylene) (P(VDF-TrFE-CTFE))

Furthermore, a terpolymer P(VDF-TrFE-CTFE) is obtained by introducing CTFE in the P(VDF-TrFE) copolymer with different content [1,98]. An increase of CTFE concentration slightly moves T_{Curie} at lower temperature, and leads toa similar level of electroactive strain (~1%) [99]. Similarly to high-energy electron irradiation, the introduction of bulky CTFE also creates the defects in the PVDF-TrFE ferroelectric structure, and thus a so-called relaxor ferroelectric behavior can be observed [100,101]. This particular property of P(VDF-TrFE-CTFE) terpolymer endows it multifunctional due to the unique relaxor ferroelectric behavior in comparison with normal ferroelectric one, such as high electrostrictive strain (~4%

under 150 MV/m) and high dielectric constant (~60 at 1 kHz) [102].

1.1.4 Conclusion

In summary, the family of PVDF and its co(ter)polymers ispromising forthe advanced applications due to their high dielectric constant, piezo-, pyro-, and ferro-electric effects. The finely controlled processing condition to promote more electroactive crystalline phases of PVDF is a key pursuit to meet the requirements in different applications such as energy storage, filtration, sensor, actuators, *etc*. Combining different experimental techniques such as FTIR, XRD and DSC, the main characteristics of the electroactive phases can be well identified. Recent advances in the development of promoting more polar crystalline phases dynamically advance the applications of PVDF and its co(ter)polymers. PVDF-based polymer materials mean a dynamic, interesting and promising field that should achieve fruitful applications in near future.

1.2 Structuration of ILs on PVDF-based polymers

1.2.1 State-of-art of ILs

Since the first and startling discovery that a pure salt (ethylammonium nitrate, EAN) was liquid at ambient temperature by Walden in 1914 [103], the term "ionic liquids (ILs)" has been widely accepted and also emerged as "green" and environment friendly solvents for their use in both academic and industrial fields. In the past decades, more and more ILs have been used for diverse applications such as organic synthesis, catalysis, electrochemical devices, solvent extraction of a variety of compounds and more recent energy field [104,105] due to the particularly significant properties which are summarized in Table 1-4. ILs are a subset of molten salts with melting points (T_m) below 100 ^oC. Some authors also distinguish ILs (T_m < 100 ^oC) from room temperature ILs (RTILs) (T_m < 25 ^oC). In this sub-section, a general introduction of ILs including *chemical structure*, *synthesis and purification* and *applications* will be presented below.

Table 1-4: Physico-chemical properties of ILs

Molecular size	Cation and/or anion quite large
T_m	Preferable < 100 ^oC
Liquids range	Often > 200 ^oC
Thermal stability	Usually high
Viscosity	Normally < 100 cp, workable
Dielectric constant	Implied < 30
Polarity	Moderate
Specific conductivity	Usually < 10 $mScm^{-1}$, "Good"
Molar conductivity	< 10 Scm^2mol^{-1}
Electrochemical window	> 2 V, even 4.5 V
Solvent and/or catalyst	Excellent for many organic reactions
Vapor pressure	Usually negligible

1.2.1.1 Chemical structure

ILs exist as liquids at ambient temperatures due to their particular chemical structures. The cation and anion structures should be chosen precisely to overcome the usually strong crystal lattice energy, which in general can be achieved within a relatively large number of combinations of ion structures by balancing ion-ion interactions and symmetry. The available number of cation-anion potential combinations is about 10^{12} ILs formed from bulky and asymmetrical structure in order to induce a low T_m [106]. For example, the alkyl chain in cation should be long enough to reduce the Coulomb force and disrupt the lattice packing.However, the chain length also should not be too long otherwise the $T_m$will be increased despite the enhanced structure asymmetry [105].

Up to now, the chemical structures of cations and anions used for ILs have been developed and the most representative cations and anions are gathered in Figure 1-7 [105].

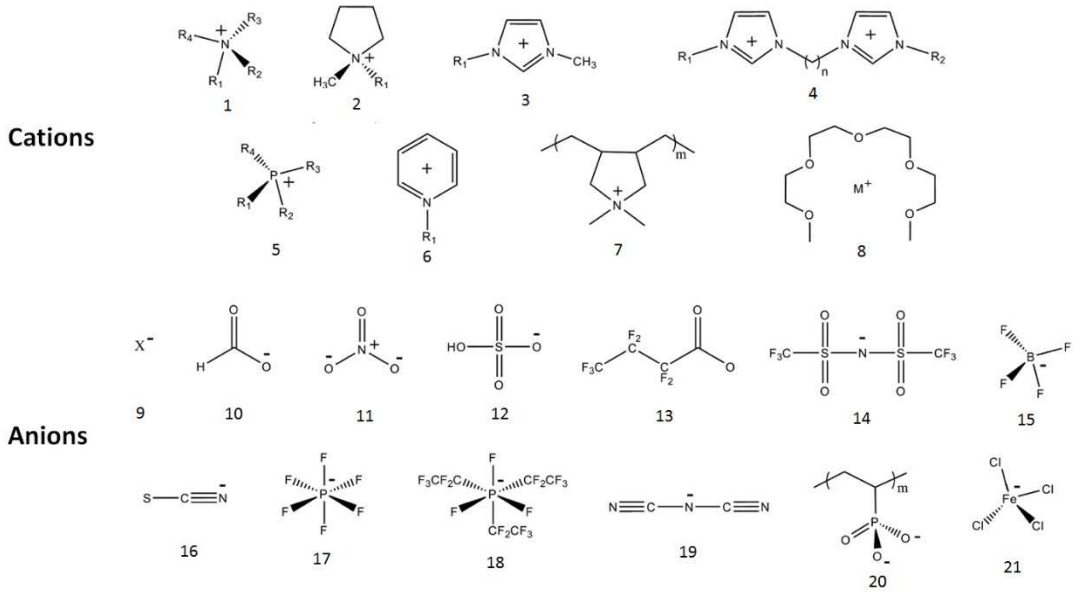

Figure 1-7: The chemical structures of representative cations and anions used in ILs: ammonium (1), pyrrolidinium (2), 1-methyl-3-alkylimidazolium (3), 1,3-bis[3-methylimidazolium-1-yl]alkane (4), phosphonium (5), pyridinium (6), poly(diallyldimethylammonium) (7), metal (M^+) tetraglyme (8), halides (9), formate (10), nitrate (11), hydrogen sulfate (12), heptafluorobutyrate (13), bis(perfluoromethylsulfonyl)imide (14), tetrafluoroborate (15), thiocyanate (16), hexafluorophosphate (17), tris(pentafluoroethyl)trifluorophosphate (18), dicyanamide (19), poly(phosphonic acid) (20), and tetrachloroferrate (21) [105]

The chemical profiles of cation and anion in ILs play a key role in the physico-chemical properties of ILs. First, for cations, the length of alkyl substituent chains and the symmetry significantly influence the T_m. It is reported that the T_m of ILs increases with the size and asymmetry of the cation. Moreover, the increase in the branching on the alkyl chain also enhances the T_m [107]. Second, the anions are also responsible for the change of T_m and for the thermal stability [108]. The ILs with fluorinated anion are usually more thermally stable. For example, 1-methyl-2-butyl-imidazolium tetrafluoroborate has a better thermal stability than the same salt in the presence of a bromide anion. In addition, the chemical nature of anion also affects the solubility of ILs. For example, 1-methyl-2-butyl-imidazolium tetrafluoroborate $[MeBuImi]^+[BF_4]^-$ is soluble in water while the same cation with the anion hexafluorophosphate $[PF_6]^-$ is totally insoluble in water. Finally, some fluorinated anions have the limitation of hydrolysis to form HF when heated in water. For example, tetrafluoroborate $[BF_4]^-$ and hexafluorophosphate $[PF_6]^-$ anions are the most commonly used in electrolytes and batteries. They have significant limitations due to the formation of HF during the hydrolysis. In order to solve this issue, other alternative anions such as trifluoromethansulfonate $[CF_3SO_3]^-$ and bis(perfluoro-methylsulfonyl)imide $[(CF_3SO_2)_2N]^-$ by C-F bonds which are inert to hydrolysis have been developed.

1.2.1.2 Synthesis and purification

Although the combination of cation and anion is almost infinite, the synthesis of ILs can be generally split into two steps: (1) quaternizing a cation, (2) exchange of the anion to produce the final product. The synthetic paths of typical imidazolium, pyridinium and phosphonium ILs which are the most commonly used ILs are represented in Figure 1-8.

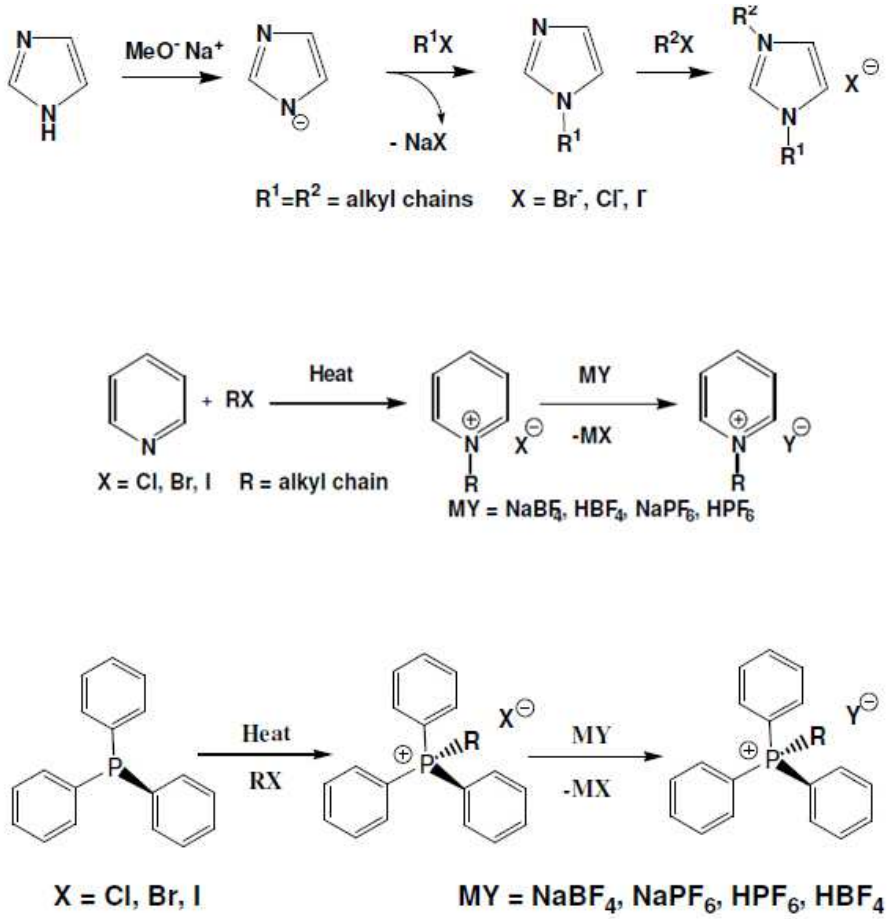

Figure 1-8: Typical paths for the preparation of imidazolium, pyridinium and phosphonium ILs

There are also some other routes such as solvent and halide-free pathways, microwave or sonochemical methods as well as using cheap industrial products as starting materials, *e.g.*, the detergent sodium octylsulfate [104].

The impurities in the final IL products could be tertiary amines, alkyl halides or alkyl sulfates or their side-reaction byproducts, and residual halide or sulfate after metathesis. The purification methods include extraction by polar solvent (*e.g.*, ethyl acetate), extraction of the aqueous solution of ILs with an immiscible organic solvent (*e.g.*, dichloromethane), flash column chromatography, treatment with activated charcoal, *etc*.

1.2.1.3 Applications

ILs offer a variety of physico-chemical properties that make them very attractive to a broad field of applications.

(1) Promoting solvents in organic reactions

ILs are found to be promising solvents in many organic reactions such as Diels-Alder, Bailis-Hillman, Heck reaction, esterification, isomerization reactions and also coupling reactions [109]. It is well-known that pressure, temperature and concentrations of reactants govern the reaction process. However, it has been found that the viscosity can also play an important role in the kinetics of reaction. For example, the rates of Diels-Alder reaction increase with the viscosity up to ~1cP. There are reports showing that the rate of reaction is faster in the ILs possessing higher viscosities than in the media with lower viscosities [110], which means that the high viscosity favors the reaction kinetics. In another study, the rate constants for a diffusion-controlled reaction involving neutral reactants were measured in ILs with different viscosities at varying temperatures. The overall bimolecular rate constant was found to increase with an increase of the viscosities of ILs [110].

(2) Electrochemical devices

Many applications of ILs as electrochemical devices such as super capacitors, lithium ion batteries, polymer-electrolyte fuel cells and dye-sensitized solar cells in which the ILs act as the electrolyte were developed [111,112]. Two main advantages of ILs used in electrochemical devices are non-volatility and prevention of electrolytes from drying during the operation. It is well-known that the transport properties governed by viscosity, conductivity and diffusion must be considered for processing an effective electrochemical device. However, the fundamental requirement for an IL to be used in electrochemistry is a wide electro chemical window. While the aqueous system possesses about 1.23 V of the electrochemical window, and propylene carbonate and acetonitrile can offer an electrochemical window as high as 4 V, many ILs exhibit an electrochemical window in the range of 4~5 V, and even as high as 6 V for the most common and popular ILs such as [BMIM][BF_4] and [BMP][$CFSO_3$]. Moreover, ILs have been observed to be useful for electric double layer capacitors [113,114]. For instance, many ILs composed of [EMIM] cation with a variety of anions have been found effective. Another IL

[BMIM][BF_4] with a quite high electrochemical window is also very useful for this application.

(3) Extraction technology

The use of ILs to separate toxic metal ions and organic molecules in the field of nuclear waste has been reported [115,116,117,118,119]. Many of works have focused on the extraction of radioactive metals such as lanthanides and actinides [120]. Others have focused on the behavior of uranium in ILs. In mostof cases, the family of imidazolium ILs is the most often used.For example, Visser*et al.* [121], Chun *et al.* [122], and Luo *et al.* [123] have studied the use of imidazolium IL containing PF_6^- anion to extract Na^+, Cs^+, Li^+ and K^+. Other authors have also used imidazolium IL associated to a TF_2N^- anion to extract strontium [124]. In addition, the distribution coefficients for the IL extraction systems are higher than those based on organic solvents. The successful extraction of organic acids from aqueous solutions into an IL, 1-butyl-3-methylimidazolium hexafluorophosphate has been reported [125]. The solvation of ionic species in the ILs is more favored thermodynamically than in conventional solvent extractions.

(4) Multi-functional additives within polymer matrices

Besides the conventional applications of ILs mentioned above, the last decade witnessed the increasing development of ILs as multi-functional additives within polymer-based materials for a wide range of applications of advanced materials. The particular set of physico-chemical properties of ILs finely tuned from the chemical structures gives rise to ideal components for the processing of advanced polymer materials [126]. A successful **"wedding"** between polymers and ILs has been proven in a variety of applications, opening a promising field in the material science through combining the innovations of both polymer and ILs communities together. For example, ILs can be seen as (1) ionic conducting agents for polymer electrolytes; (2) processing aids as solvents or green composites; (3) plasticizers of polymers; (4) chemically reactive agents able to initiate the polycondensation of networks; (5) structuration agents to achieve a tunable structure in polymer with enhanced

properties; (6) interfacial agents for tailoring the dispersion of fillers in nanocomposites, and the pore size in the foams or for enhancing the compatibilization of polymer blends. Among them, the role of ILs as *structuration agents* and *interfacial agents* has been paid less attention. The use of ILs as building elements or compatibilizers and the achievement of a controlled nanoscale structuration with interesting properties combining ILs into polymer matrices should open promising new horizons for the use of ILs in many potential industrial applications. These two aspects are the key points of this thesis, so the following sections will review the recent achievements about them in the literature.

1.2.2 ILs as structuration agents in polymer matrices: a new application

The idea of "*functionalization via structuration*" is a critical guideline for every researcher in the designing and development of new polymer materials with significantly unprecedented and improved physicochemical properties. For many years, in order to design new advanced polymer materials with improved thermal, mechanical and barrier properties, mostly used methods are the incorporation of nanofillers or block copolymers, such as silica [127], layered silicates [128,129], carbon nanotubes (CNTs) [130,131], amphiphilic block copolymers[132,133,134,135], *etc*.

More recently, a great deal of research has focused on the use of ILs as structuration agents to finely influence the morphology and thus the final properties of polymeric materials through the chemical nature control of the cation and counter anion of ILs. Pioneering works in this field were obtained on different polymer matrices such as polytetrafluoroethylene (PTFE) [136,137], poly(butylenes adipate-*co*-terephthalate) (PBAT) [138], and epoxy resin [139,140,141,142,143,144,145], and will be presented in the following paragraphs.

In the PTFE matrix, pyridium, imidazolium and phosphonium ILs were incorporated as functional building elements to generate a nanostructured phase, leading to excellent mechanical properties [136,137]. The influence of the chemical structure of ILs on the structuration of ionic clusters in PTFE matrix is shown in

Figure 1-9(a). Imidazolium and pyridinium ILs give rise to the aggregates of ionic clusters, while phosphonium IL displays a homogeneous so-called “spider-web” morphology at the nanoscale. The interaction between the polymer matrix and the anion-cation combination is the key parameter that controls the microphase separation which generates the formation of multiple structures. Moreover, it was highlighted that 1 wt% of the iodide phosphonium IL generated a significant increase of the mechanical behavior of the PTFE/IL composite film with an increase of +160% in Young’s modulus as well as an incredible increase of +190% of the strain at break (Figure 1-9(b)). In these reports, the authors demonstrated that the chemical nature of the cations and anions of ILs play a significant role in the distribution and the structuration of ionic domains in the polymer matrix.

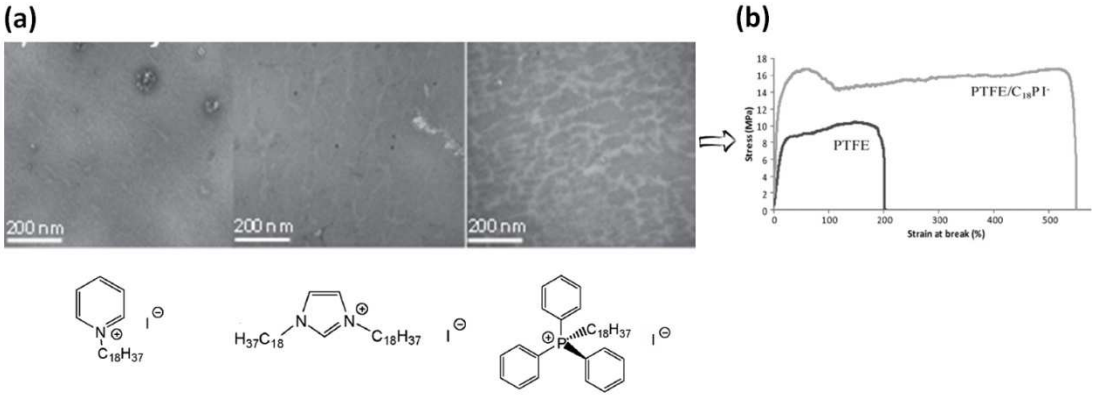

Figure 1-9: TEM images (a) showing the effect of chemical nature of cation on the morphologies of PTFE/IL films and the mechanical property (b) of PTFE/phosphonium IL [136]

Recently, the authors developed a simple and scalable method to prepare PBAT films containing ILs by melt blending which could be used for food-packaging applications [138]. In this report, a very low amount of tetraalkylphosphonium ILs combined with chloride, bistriflimide and bis-2,4,4-(trimethylpentyl)phosphinate anions have been introduced in PBAT matrix. The formation of ionic clusters in PBAT is shown in Figure 1-10(a). Moreover, the hydrophobic nature of the ILs due to the long alkyl chains on the phosphonium cation contributes to the significant decreasing of the vapor water permeability (VWP) in the range of 40 to 70% (Figure 1-10(b)). This behavior can be explained by the good distribution of ILs in the PBAT matrix,

which involves the creation of so-called “tortuous path” that postpones the diffusion of the water molecules in the polymer matrix.

(a)

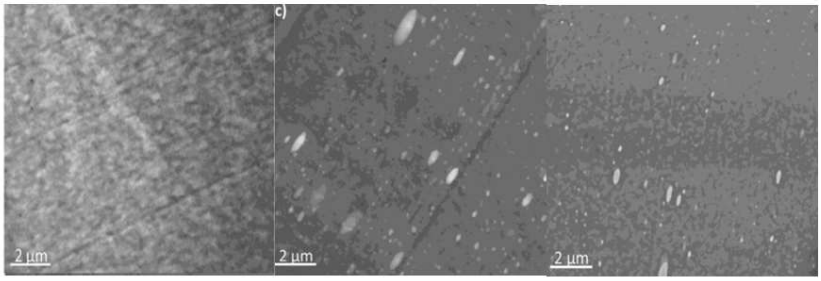

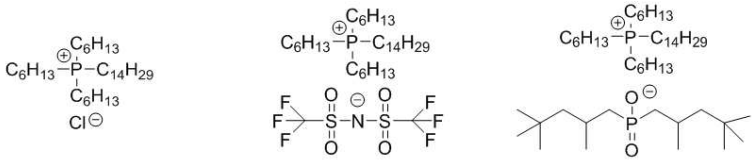

(b)

Sample	Water sorption C_{eq} (g per 100 g)	Water diffusion D (cmq s^{-1})	Water permeability (cc(STP) cm^{-3} atm^{-1}) (cm^2 s^{-1})
PBAT	2.37	2.26×10^{-8}	3.32×10^{-8}
PBAT/IL-TMP	0.84	2.50×10^{-8}	1.30×10^{-8}
PBAT/IL-TFSI	0.47	3.80×10^{-8}	1.10×10^{-8}
PBAT/IL-Cl	1.45	2.10×10^{-8}	1.90×10^{-8}

Figure 1-10: TEM images (a) showing the effect of chemical nature of anion on the morphologies of PBAT/IL films and their water permeability (b) [138]

It is well-known that the use of amphiphilic block copolymers as modifiers in thermosets, *e.g.*, epoxy networks, gives rise to the phase separation or self-assembly structures, which is mainly ascribed to the miscibility of the sub-chains of the block copolymers [146,147]. Besides PTFE and PBAT matrices, the same authors have demonstrated that ILs can also act as functional additives for the preparation of nanostructured epoxy resin [139,140,141,142,143,144,145]. For example, in this report, the effect of the concentration of phosphonium IL coupled with the dicyanamide anion on the morphologies of the epoxy networks is demonstrated by TEM in Figure 1-11. It is clearly shown that a miscibility limit is reached when 30 phr of phosphonium salt is inserted in the epoxy prepolymers, resulting in the formation of ionic clusters with a size of 20-30 nm during the curing and post-curing steps.

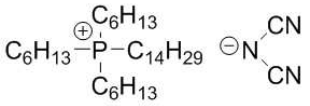

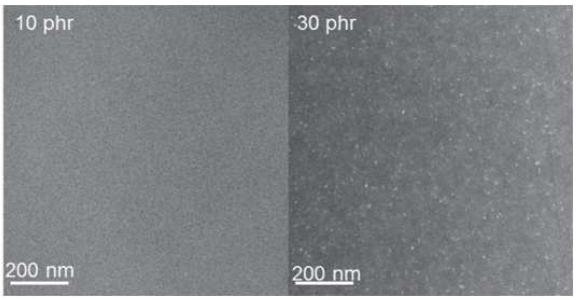

Figure 1-11: TEM images showing the effect of concentration of phosphonium IL on the morphologies of cured epoxy networks [143]

More recently, Li's group also paid a lot of efforts to investigate the effect of ILs on the properties of polymer matrices. An IL, tributyl(methyl)ammonium bis(trifluoromethane)sulfonylimide ($[tbmam^+][Tf_2N^-]$), was integrated into polycarbonate (PC) to fabricate optically transparent anti-electrostatic composites by melt processing [148] (Figure 1-12(a)). DSC and DMA indicated the depression of the glass transition temperatures of the PC/IL composites, compared with that of neat PC (Figure 1-12(b)), demonstrating the interaction between PC and the IL. TEM showed that the IL was highly compatible with PC at low IL loadings (see Figure 1-12(c)). This resulted in enhanced anti-electrostatic properties with a surface resistivity of 6.35×10^{10} ($\Omega \cdot sq^{-1}$) for 3 wt% of loading, and a significantly improved elongation at break of the PC/IL composites (see Fig 1-12(d)). The PC/IL composites maintained the high transmittance of PC (see Figure 1-12(e)). In addition, the PC/IL composites with high clearance and anti-electrostatic properties could be achieved by large-scale continuous melt extrusion, indicating that the method to fabricate both optically transparent and anti-electrostatic composites issuitable for the industrial applications.

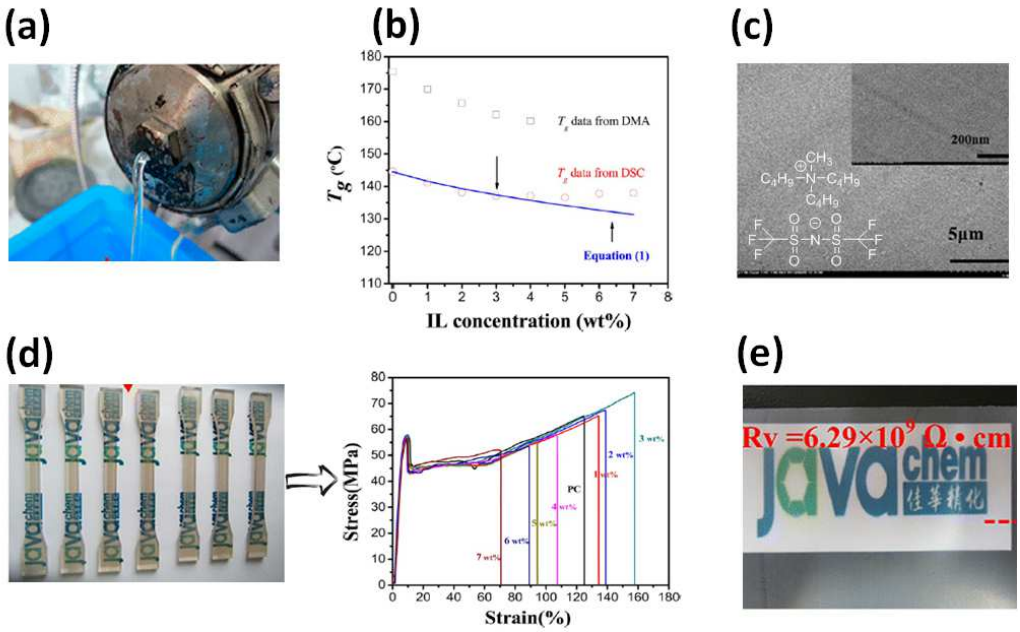

Figure 1-12: PC/[tbmam$^+$][Tf_2N^-] composite films prepared by melt processing (a); and T_g of composites as a function of IL loading by DSC and DMA(b); TEM image of PC/[tbmam$^+$][Tf_2N^-] composite (3 wt%) (c); stress-strain curves of neat PC and PC/IL composites (d); transparent film and antistatic property (e) [148]

The authors also developed antibacterial, anti-electrostatic, and hydrophilic nanofibers by electrospinning based on a blend containing thermoplastic polyurethane (TPU) and an IL, 1-butyl-3-methylimidazolium hexafluorophosphate [BMIM][PF_6] [149]. The effect of the IL on the morphology and the physical properties of the TPU nanofibers was investigated. Nanofibers with a 'bead-on-string' morphology were obtained by electrospinning from a neat TPU solution. The incorporation of the IL, at levels as low as 1 wt%, largely suppressed the formation of beads during electrospinning, and homogeneous nanofibers were obtained (see Figure 1-13). The as-spun TPU/IL composite nanofibers showed significant activity against both Escherichia coli (*E coli*) and Staphylococcus aureus (*S. aureus*), with antibacterial activities efficiencies of 99.99% and 99.9%, respectively. Moreover, nonwoven fabrics derived from the electro-spun TPU/IL composite nanofibers exhibit better stretchability, elasticity, and higher electrical conductivity compared to those made using neat TPU without IL. Additionally, the incorporation of the IL leads to a hydrophilic surface for the TPU/IL composite nanofibers compared to hydrophobic neat TPU nanofibers. These multifunctional nanofibers with excellent antibacterial,

anti-electrostatic, and mechanical properties and improved hydrophilicity are promising candidates for biomedical and wastewater treatment applications.

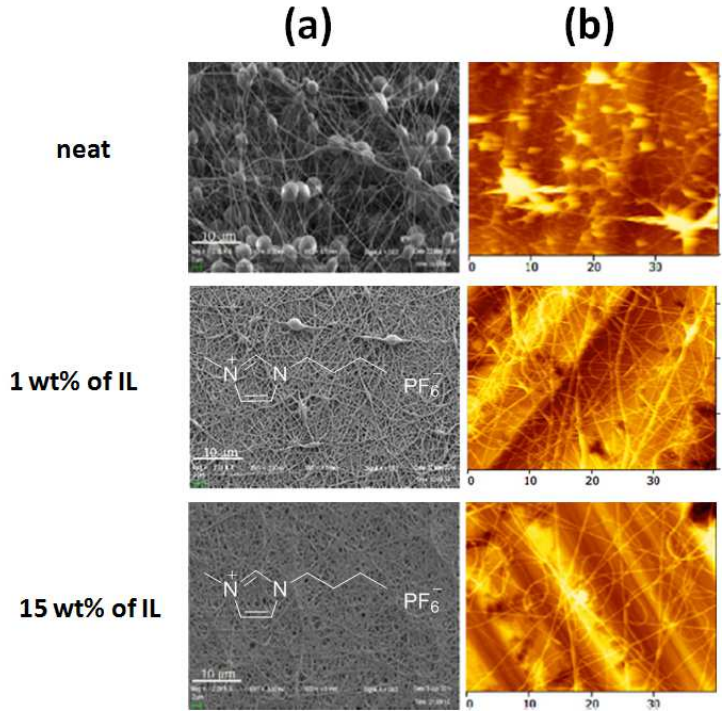

Figure 1-13: SEM (a) and AFM (b) of neat TPU and its composites with IL [149]

As a family of multi-functional polymer materials, PVDF and its copolymers also attracted increasing attentions to be as a matrix for preparing the IL/PVDF composites and study the effect of ILs on the properties thereof. Since the concerned polymer matrix in this thesis is P(VDF-CTFE), the examples of PVDF/IL composites in the literature will be highlighted in the following *sub-section 1.2.3* in detail.

1.2.3 Examples of PVDF /IL composites

Wang *et al.* [150] prepared β-phase-dominant PVDF/IL (1-ethyl-3-methyl-imidazolium nitrate) thin films spin-coated from a solution. IL promotes the formation of ferroelectric β-phase as shown in FT-IR spectra (Figure 1-14(a)) and much smaller crystalline regions as shown in SEM images (Figure 1-14(b)). The ferroelectric properties show a remanent polarization of 60 mC/m^2 and a quasi-static pyroelectric coefficient of 19 μC/(m^{2}K) at 30 ^{o}C. It is suggested that the IL promotes the formation of the β-phase through dipolar interactions between PVDF chain-macromolecules and the IL which is identified as Coulomb attraction between hydrogen atoms in PVDF

chains and anions in IL. The strong crystallinity increase could also be ascribed to the same dipolar interactions.

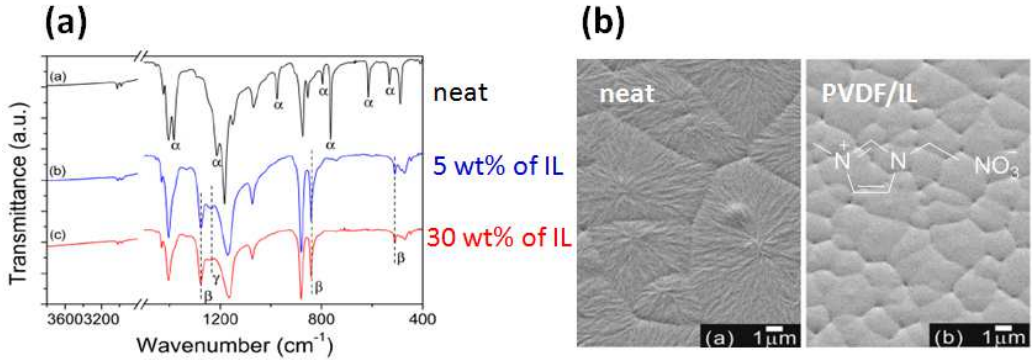

Figure 1-14: FTIR (a) and SEM (b) of neat PVDF and its composites with IL [150]

Xing *et al.* [151] in Li's group also systematically investigated the crystalline structure, miscibility, and physical properties of PVDF/IL (1-butyl-3-methylimidazolium hexafluorophosphate) ([BMIM][PF_6]) blend film by hot pressing(see Figure 1-15(a)). It was found that the incorporation of IL into the PVDF leads to drastically increased γ-crystal of PVDF (see Fig 1-15(b)) by the interaction between the >CF_2 and cationic ions. Dynamic mechanical analysis (DMA) and small angle X-ray scattering (SAXS) results indicate that the IL molecules are inserted into the gallery of PVDF lamellae. A small amount of ILs induces the appearance of the crystal-amorphous interface relaxation of PVDF, originating from the enrichment of IL distribution near the crystal-amorphous interface (see Figure 1-15(c)). The obtained PVDF/IL blends exhibit excellent mechanical performance with significantly increased ductility and good optical transmittance (see Figure 1-15(d)). In addition, the incorporation of IL into PVDF enhances the electrical conductivity of PVDF films greatly.

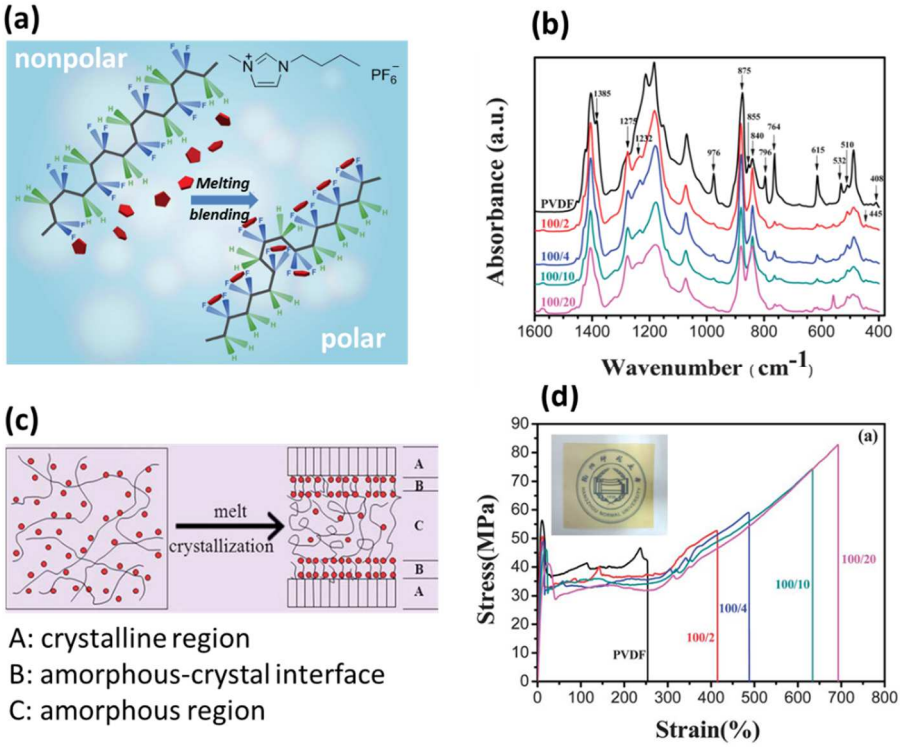

Figure 1-15: PVDF/[BMIM][PF_6] composites prepared by hot pressing (a); FT-IR spectra of neat PVDF and PVDF/[BMIM][PF_6] composites (b); schematic presentation of composite from melting to crystal state (c); Stress–strain curves of neat PVDF and composites (d) [151]

Furthermore, the same authors prepared the nanofibers of PVDF/[BMIM][PF_6] composites by the aid of electrospinning technique [152] (see Figure 1-16(a) for the fiber-like morphology). The extremely high β-phase content (almost 100%) of fibers as shown in FI-IR spectra (Figure 1-16(b)), their excellent anti-electrostatic properties, their improved stretchability, and hydrophobicity make them a promising candidate for micro- and nanoscale electronic device applications.

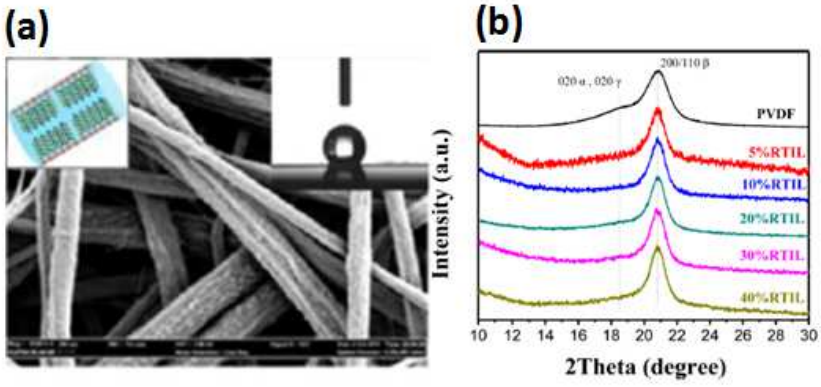

Figure 1-16: SEM (a) and FTIR (b) of PVDF/[BMIM][PF_6] nanofibers [152]

PVDF nanoparticles (PVDF-NPs), another form of matrix morphology, have also been used by Yamamoto *et al* [153]. The pristine PVDF-NPs (~230 nm of diameter) consist of 46% α-phase and 54% amorphous PVDF. They were assembled on a quartz substrate by means of vertical deposition method to form colloidal thin films (see Figure 1-17(a)). The films were then immersed into an acetonitrile solution containing 2 wt % IL, *i.e.*, imidazolium nitrate, subsequently air-dried, and thermally annealed at 140 °C that is below the T_m of the PVDF/IL blends. After annealing, the PVDF-NPs are partially transformed into β-phase crystals with the volume percentages of α-, β-, and amorphous phases of 22, 32, and 46%, respectively (see FT-IR spectra in Figure 1-17(b)). The post-annealed colloidal films still maintained the face-centered-cubic assembling structure of PVDF NPs, thus displaying the greenish structural color and selective reflection.

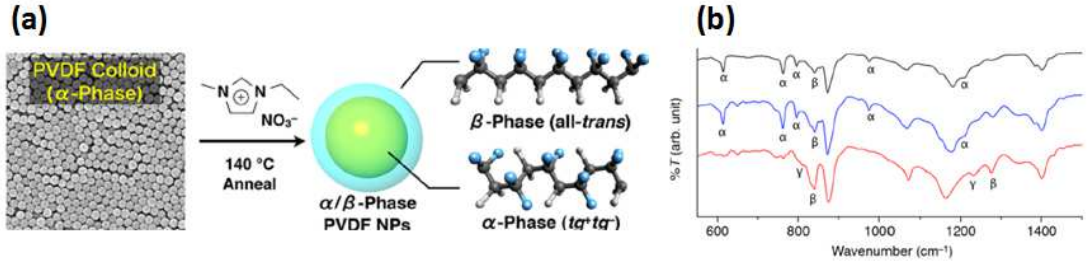

Figure 1-17: Preparation process (a) and FTIR spectra (b) of PVDF-NPs/IL [153]

More recently, Li's group [154,155] innovatively grafted an unsaturated IL, 1-vinyl-3-butylimidazolium chloride ([VBIM][Cl]), onto the PVDF backbone (PVDF-*g*-IL) by electron beam irradiation at room temperature (see Figure 1-18(a)). In this way, organic conductive nano-domains with diameters of 20-30 nm are homogeneously dispersed in the PVDF matrix due to the microphase separation of the PVDF-*g*-IL segments from the neat PVDF only when the IL content exceeds 3 wt%. (see TEM image in Figure 1-18(b)).

The authors schematically demonstrated the formation of such organic conductive nano-domains in Fiugre 1-18(c): (1) the semi-crystalline PVDF with distinct amorphous and crystalline phase (state I) was melt-blended with unsaturated IL (state II) in which IL is miscible with PVDF only in the amorphous phase due to

the interaction between PVDF and IL; (2) such blend was then exposed to electron beam irradiation at room temperature, resulting in chemical grafting onto the amorphous PVDF chains by radical reaction (PVDF-*g*-IL) (state III); (3) however, the resulting PVDF-*g*-IL segments are not miscible with PVDF in melting state (state IV), leading to the microphase separation of PVDF-*g*-IL segments from the neat PVDF chains. The PVDF-*g*-IL segments and counterpart Cl^- anions migrate from the bulk PVDF to form the nano-domains; (4) thus, the nano-structured PVDF/IL composites with the conductive nano-domains are achieved during cooling process from the melt (state V).

Such nanostructured PVDF composites exhibit dominant non-polar α-phase, better Young's modulus (1.76 GPa) and ductility (328.4% of strain at break), and improved dielectric permittivity (increased by 124% at 10^2 Hz and by 38.6% at 10^3 Hz compared to neat PVDF) as well as low dielectric loss (~1 at 10^2 Hz and ~0.5 at 10^3 Hz), making the composites promising for potential use in dielectric capacitors.

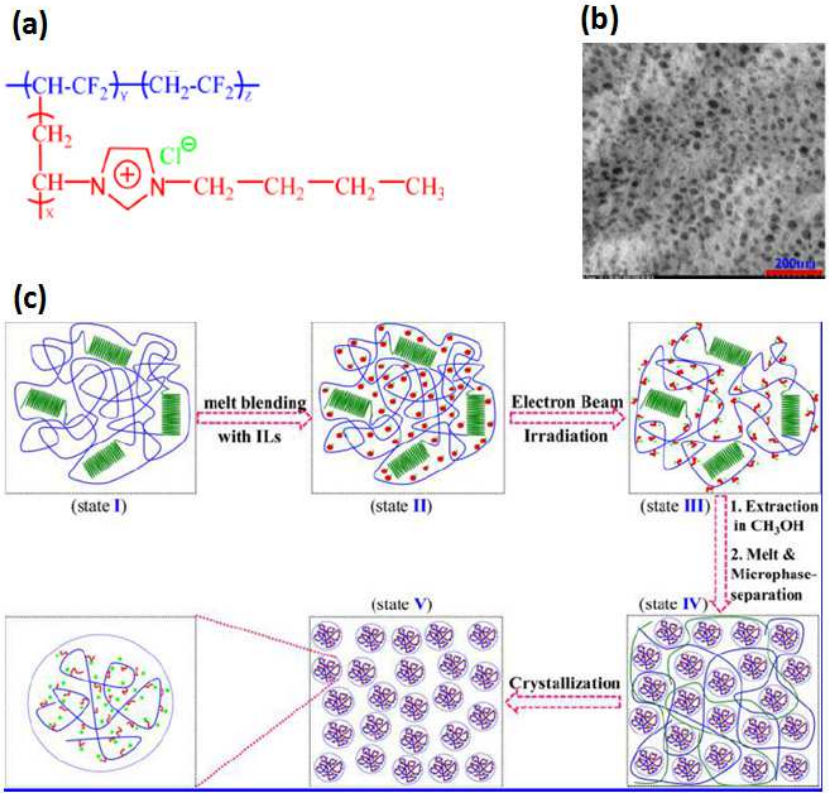

Figure 1-18: Chemical structure (a) and TEM image (b) of IL-grafted PVDF (PVDF-*g*-IL); synthesis route for processing a nanostructured PVDF composite (c) [155]

1.2.4 Conclusions

The unique physico-chemical properties of ILs well adjusted by their infinite cation-anion combinations provide a powerful and multi-functional tool to develop advanced polymer/IL composite materials. As one of the functions in polymer matrix, the structuration effects of ILs have been investigated recently. However, due to the just growing of this field, the mechanism for the structuration is quite elusive and most of works only focus on the formation of polar crystalline phase. From current understanding, dipolar interactions between PVDF chains and ILs contribute to the formation of polar crystalline phase. In essence, the understanding of the fundamental mechanism of the versatile nanostructuration of ILs on semicrystalline PVDF-based polymer is still superficial. For example, we should investigate the the effects of IL chemical structures on dipolar interactions, the influence of the localization of ILs in the matrix on the nanostructuration and the governing factor thereof, *etc*. As one of the research targets of this thesis, all of these issues will be investigated in the subsequent *Chapter 2*.

1.3 Structuration of nanofillers on PVDF-based polymer

As stated in *Section 1.1*, the family of PVDF and its co(ter)polymers is one of ferroelectric polymers, showing a great potential for applications in micro-electromechanical devices, actuator, supercapacitors, batteries and optoelectronic devices [156,157,158]. These applications require relatively high electric constants (high-ε_r) of materials, which has been realized by incorporating nanofillers in PVDF-based polymers matrices.

1.3.1 Nanofillers incorporated in PVDF-based matrix

Conventionally, ferroelectric metal oxides ceramics with high-ε_r such as $BaTiO_3$ [159,160,161,162], $Ba_{0.6}Sr_{0.4}TiO_3$ [163,164], ZrO_2 [165] are incorporated in PVDF matrix, usually leading to a relatively high dielectric permittivity around 100 and a low dielectric loss (<0.1 at 1 kHz). $CaCu_3Ti_4O_{12}$ ceramic powders are also added into P(VDF-TrFE) matrix [166]. The dielectric constant of the composites at 100 Hz reaches more than 610 at RT and 1210 at 70 ^oC with low dielectric loss (0.1~0.4). The dielectric properties of as-prepared composites are a good compromise of the ceramic fillers and the polymer host. Nevertheless, a relatively high ceramic loading amount (>50 vol %) is frequently required to achieve high-ε_r due to the giant difference between the dielectric constants of ceramic fillers and polymeric materials, resulting in many shortcomings such as high weight, low flexibility, poor processability, and high defect density [167,168].

In order to solve the limitations of ceramic filler-based composites, recent promising works have been reported based on percolation theory, in which a small volume fraction of conductive fillers was added into the polymer matrix to achieve a high dielectric constant while preserving the mechanical flexibility of the polymer [168, 169, 170,171,172,173,174,175]. The dielectric properties of as-prepared composites display a sharp change when the content of conductive fillers reaches a certain percolation threshold (f_c) which is usually much lower than 50 vol %. With the increase of dielectric constant, one issue that simultaneously occurs is the increase of

dielectric loss. When the filler content approaches the percolation threshold, the dielectric loss is normally high and the breakdown strength is also reduced. Although the dielectric strength of conductive filler-based composite remains unclear, the giant ability to increase dielectric constant of these materials still constantly stimulates us to find a balancing solution to prepare conductive filler-based composites with high permittivity but low loss [176].

Nan *et al.* reported the preparation of high-ε_r PVDF-based composites filled with conductive nickel powders [177]. The percolation volume fraction was evaluated to be 17 vol% and the effective ε_r of the composites near the threshold increased to 400 at 100 Hz with a low dielectric loss (tan δ = 0.18). Panda *et al.* [173] reported that, for PVDF/Ni composites, a high effective dielectric constant of 2050 (tan δ = 10) at 100 Hz was observed near the f_c = 27 vol%.

A metal coordination compound, tetrameric Cu-phthalocyanine (CuPc), is shown to possess a very high relative dielectric constant ($\varepsilon_r = 10^4 \sim 10^5$) [178]. Thus, Zhang *et al.* prepared P(VDF-TrFE)/CuPc composites which exhibit large ε_r values of 225 and low loss factor of 0.4 at low field with 40 wt% of loading content [179].

Carbon black (CB) was also added into P(VDF-TrFE-CTFE) matrix to prepare the percolative P(VDF-TrFE-CTFE)/carbon black nanocomposites *via* a simple solution blending method [180]. The dielectric properties, mechanical properties, and breakdown strength were comprehensively investigated for electrostrictive applications. The nanocomposites exhibit excellent mechanical properties and dielectric properties with a dielectric permittivity of 140 and a low dielectric loss of 0.05 at 100 Hz with an f_c = 4.68 wt%. However, the breakdown strength decreased simultaneously due to the enhanced local electric field induced by the thin insulating layer between CB fillers, which could limit the practical applications.

Dang *et al.* exploited carbon nanotubes (CNTs) as nanofillers incorporated in PVDF-based matrices. For the PVDF/CNTs composites, they possess a dielectric constant of ~600 and a dielectric loss (tan δ) of ~2 at 1 kHz with f_c = 8 vol% over a wide temperature range (from 0 ~ 50 ^oC) [168]. Although it should be noted that the

value of dielectric loss was still high, such a high dielectric permittivity suggests potential applications as novel dielectric materials over a broad temperature range. For P(VDF-TrFE-CTFE)/CNTs composites, the dielectric constant increased from 57 to 102 (tan $\delta \approx 0.36$) at 100 Hz by inclusion of only 2 wt % (1.2 vol%) carbon nanotube [181]. Lonjon and Lacabanne *et al.* prepared highly electrical conductive nickel nanowires (Ni-NWs)/P(VDF-TrFE) nanocomposites. For a very low percolation threshold (0.75 vol%), a very high electrical conductivity (100 S/m) was found [182]. More recently, the authors have got the very good magnetoelectric properties for this composite. Combining the Ni-NWs magnetism and the P(VDF-TrFE) piezoelectricity, the magnetoelectric coefficient has reached the value of 237 V/(m Oe) which is the highest one found in the literature for composites with a polymer matrix [183]. Bretas *et al.* [184] prepared the copper nanowires (CuNWs)/PVDF nanocomposites and multi-walled carbon nanotubes (MWCNTs)/PVDF nanocomposites by melt compression to compare their dielectric properties. It was observed that the CuNWs/PVDF nanocomposites had higher dielectric permittivity, lower dielectric loss and thus significantly lower dissipation factor (tan δ) than the MWCNTs/PVDF ones at room temperature. This behavior was ascribed to a higher conductivity of the fresh core of the CuNWs relative to the MWCNT, which provided the composites with a larger amount of mobile charge carriers participating in the interfacial polarization. Moreover, the presence of oxide layers on the CuNWs surfaces diminished the conductive network formation leading to a low dielectric loss.

Since the discovery of graphene materials with exciting physico-chemical properties, the 2D graphene nanosheets have emerged as being even a better conductive filler than CNTs due to the ultrahigh aspect ratio, excellent electrical conductivity and relatively low product cost [185,186]. In 2009, Ansari and Giannelis reported the functional graphene sheet/PVDF conductive nanocomposites with a low percolation threshold (2 wt%). These composites showed an unusual resistance/temperature behavior, *i.e.*, the resistance decreased with temperature,

indicating a negative temperature coefficient (NTC) behavior [187]. In the same year, Fan *et al.* [188] prepared composites of PVDF/exfoliated graphite nanoplates (xGnP) by a solution-cast and hot-pressing method. The dielectric constant was more than 200 obtained near the percolation threshold (1.01 vol%) at 100 Hz with a low dielectric loss (tan δ = 0.48), respectively, which are 20 times higher than that of the PVDF matrix.

Since then, the strategy of the inclusion of graphene in the PVDF-based matrix is attracting more and more attention to develop advanced PVDF-based electroactive materials. The reported literatures will be reviewed in the following *sub-section 1.3.2* after a general introduction on graphene.

1.3.2 Graphene as an effective conductive filler in PVDF matrix

1.3.2.1 State-of-art of graphene

(1) Discovery, structure and properties of graphene

Graphene is the basic structural unit of some carbon allotropes including diamond, graphite, carbon nanotubes and fullerenes (see Figure 1-19). It is believed to be composed of benzene rings stripped of their hydrogen atoms. The rolling up of graphene along a given direction can produce a carbon nanotube. A zero-dimensional fullerene can also be obtained by wrapping-up graphene [189,190]. In 1940, it was established theoretically that graphene is the building element of graphite [191]. In 2004, Geim and co-workers first successfully separated and identified single layers of graphene and other 2-D crystals in a simple tabletop experiment [192], which were previously considered to be thermodynamically unstable and could not exist under ambient conditions [193,194].

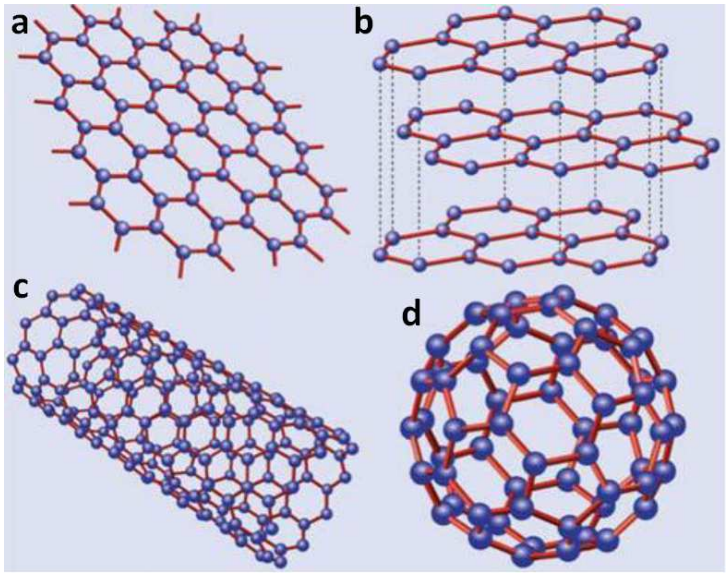

Figure 1-19: Structrues of graphene (a), graphite (b), CNTs (c) and fullerene (d) [190]

The structure of graphene can be seen as less than 10 layers of graphite [195]. Hence, the monolayer graphene is a single-atom-thick sheet of sp^2 carbon atoms, while bilayer graphene is two sheets. Because graphene has a structure analogous to benzene and polycyclic aromatic hydrocarbons (PAHs), the chemical profiles of graphene could be deduced to be similar. Breaking and formation of conjugated sp^2 C-C bonds (basal plane) or sp^2 C-H bonds (edge) are important in this chemistry. To synthesize graphene, various forms of carbon are transformed into the monolayer hexagonal symmetrical conjugated sp^2 structure. To chemically modify graphene, these sp^2 bonds are broken, and new bonds are made to exogenic functional groups. However, modification of the flat, rigid structure of graphene is challenging because of the necessity for overcoming the high-energy barriers associated with intralayer conjugation and interlayer van der Waals forces, thereby usually requiring high temperature or energetic species to complete the reactions, while under moderate reaction conditions, the yields of the reactions are usually low [196].

Regarded as the “thinnest material in the universe”, graphene has tremendous potential applications due to the remarkable properties such as high thermal conductivity, superior mechanical properties and excellent electronic transport properties [185]. These intrinsic properties of graphene have generated enormous interest for its possible implementation in a myriad of devices [197] such as new

generations of high speed and radio frequency logic devices, thermally and electrically conducting reinforced nanocomposites, ultra-thin carbon films, electronic circuits, sensors, and transparent and flexible electrodes for displays and solar cells [185].

In the field of advanced nanocomposite materials, graphene, as a nanofiller, has shown some advantages over other conventional nanofillers (*e.g.*, Na-MMT, layered double hydroxide (LDH), CNT, carbon nanofibers (CNF), expanded graphite (EG), *etc.*) thanks to its high surface area, aspect ratio, tensile strength, thermal conductivity and electrical conductivity, electromagnetic interference (EMI) shielding ability, flexibility, transparency, and low coefficient of thermal expansions (CTE) [198]. Table 1-5 summarizes the mechanical, thermal and electrical properties of graphene compared with CNTs, steel, plastic, rubber and fiber. The tensile strength of graphene is similar to or slightly higher than CNTs, but much higher than steel, Kevlar, HDPE and natural rubber. The thermal conductivity of graphene is higher than other materials. The electrical conductivity of graphene is also higher than the most of fillers except for steel.

Table 1-5: Properties of graphene, CNTs, nano-sized steel and polymers [185]

Materials	Tensile strength	Thermal conductivity (W/mK) at RT	Electrical conductivity (S/m)
Graphene	130±10 GPa	$(4.48\pm0.44)\times10^3$ ~ $5.30\pm0.48)\times10^3$	7200
CNTs	60~150 GPa	3500	3000~4000
Nano-sized steel	1769 MPa	5~6	1.35×10^6
HDPE	18~20 MPa	0.46~0.52	Insulator
Natural rubber	20~30 MPa	0.13~0.142	Insulator
Kevlar fiber	3620 MPa	0.04	Insulator

(2) Synthesis of graphene

Generally, graphene can be prepared by six methods [199]: (1) chemical vapor deposition (CVD) and epitaxial growth, such as the decomposition of ethylene on

nickel surfaces [200]; (2) micromechanical exfoliation of graphite, which is also known as the 'scotch tape' or 'peel-off' method [192,201]; (3) epitaxial growth on electrically insulating surfaces, such as SiC; (4) reduction of graphene oxide [202]; (5) solvothermal reaction between ethanol and sodium followed by a thermal treatment step [203]; (6) from anthracite coal in supercritical fluids [204]. For most of early studies, the mechanical exfoliation method has some shortcomings such as low yield, no control over graphene's spatial structure. Therefore, for a short time, graphene represented a precious material that was only available in picogram quantities. Chemical oxidation and exfoliation of graphene oxide followed by its reduction give rise to a large quantity of graphene sheets, which increases the yield dramatically compared to the mechanically exfoliated method [205,206,207]. However, the harsh oxidization process in this technique interrupts the conjugation of graphene, thus requiring additional chemical steps to convert the graphene oxide back to its pristine form, which is never completely attainable [208]. More recently, the solvothermal method has attracted more attentions due to the possibility of scale-up for the industrial applications [203]. Moreover, in 2016, Poulin's group firstly reported a green and scalable method to synthesize aspect ratio controlled graphenic materials from anthracite coal under supercritical enviroments [204]. By this way, there are no convential requirements such as strong acid treatments, complicated synthetic conditions, long reaction time, sonication, or extensive post treatment purification procedures, which opens a novel door to the large scale production of graphic materials.

(3) Surface modification of graphene

Pristine graphene is not suitable for intercalation by large species, such as polymer chains, because graphene as a bulk material has a pronounced tendency to aggregate in a polymer matrix [207,209]. It is likely that oxidation followed by chemical functionalization will favor the dispersion and stabilize graphene to prevent aggregation [209,210]. Thus, the surface modification of graphene is a particularly attractive target because it can improve the solubility and processability as well as

enhance the interactions with organic polymers [211,212]. Generally, the strategies of modification can be divided into three ones: (1) chemical modification from graphite oxide (GO); (2) electrochemical modification; (3) π-π interaction.

Chemical modification. This method is initiated from the preparation of GO from naturally existed graphite by the modified Hummers method [205]. There are four kinds of oxygen functionalities known to exist in GO: (1) epoxide (-O-), (2) hydroxyl (-OH), (3) carbonyl (-C=O), and (4) carboxyl (-COOH). The major components are epoxide and hydroxyl which are located on the basal plane of GO, while the minor ones are carbonyl and carboxyl distributed at the edges of GO (see Figure 1-20) [213].

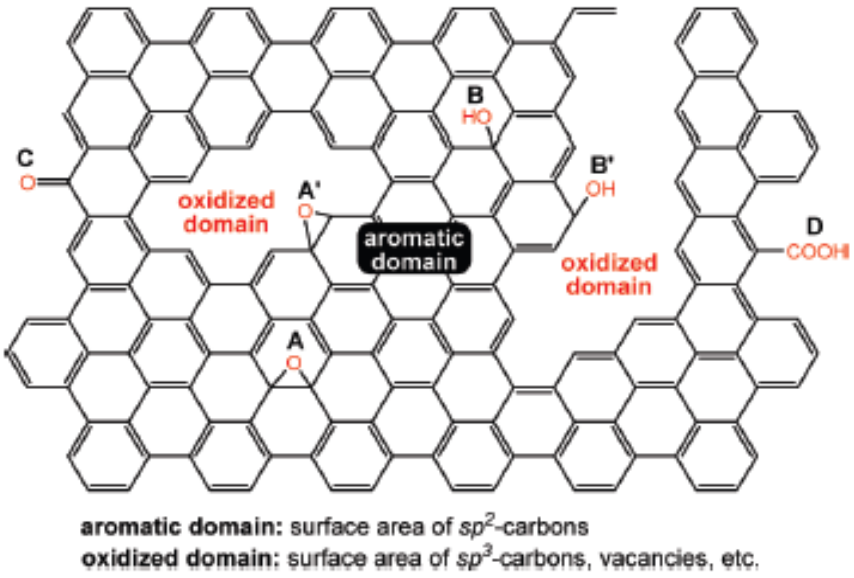

Figure 1-20: Schematic illustration of oxygen-containing groups in GO [213]

After the oxidation, there are several ways to obtain “soluble” graphene, such as reduction of GO in a stabilization medium (see Figure 1-21) [214], covalent modification by the amidation of the carboxylic groups [211,212], non-covalent functionalization of reduced graphene oxide [215,216,217], nucleophilic attack to epoxy groups [218] and diazonium salt coupling [219].

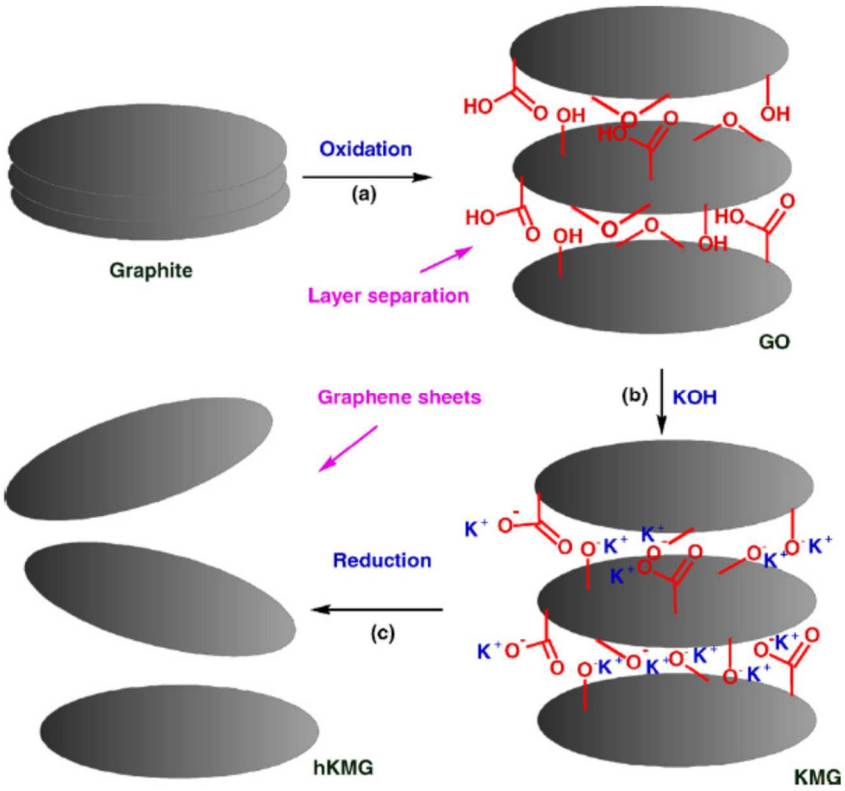

Figure 1-21: Simple route for the preparation of a homogeneous aqueous suspension of graphene sheets from graphite stack: (a) graphite stack is oxidized to separate the individual layers of graphene oxide (GO), (b) GO is dispersed in water and treated with aqueous KOH solution to obtain KOH modified oxidized graphene (KMG) and finally (c) KMG is reduced using hydrazine to produce hydrazine reduced KOH modified graphene (hKMG) in the form of stable aqueous dispersion of individual graphene sheets [214]

Electrochemical modification. Figure 1-22 shows a schematic representation of the experimental set-up of electrochemical modification to produce a colloidal suspension of graphene [220]. A graphite electrode was used as the cathode, and then immersed in a phase-separated mixture of water and imidazolium-based ionic liquids. A constant potential of 10~20 V was applied across the electrodes. After 30 min of electrochemical reaction, ionic liquid functionalized graphene (GNPIL) sheets originating from the graphite anode precipitated. Ultrasonication of dried GNPIL in DMF gave rise to a homogeneous dispersion (1 mg/mL). The average length and width of the GNPIL were 700 and 500 nm, respectively, evidenced from the TEM images. AFM image revealed the thickness of GNPIL to be ~1.1 nm.

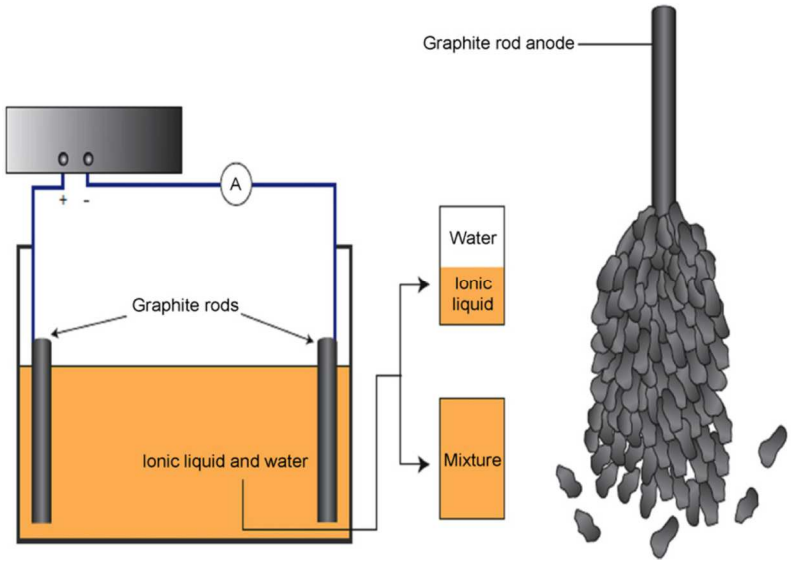

Figure 1-22: Experimental set-up (left) diagram for the electrochemical modification of graphene by ionic liquids and exfoliation of the graphite anode (right) to graphene. Electrochemical treatment (10~20 V) of graphite produces a colloidal suspension of chemically modified graphene in water and imidazolium based ionic liquids [220]

π-π interaction. Recently, Liu *et al.* [221] reported a modification technique of graphene by the π-π interaction between the π-orbitals of graphene and poly(*N*-isopropylacrylamide) (PNIPAAm). The authors dissolved pyrene-terminated PNIPAAm in water followed by the addition of a graphene aqueous solution. Water dispersible graphene was produced by sonicating the resulting mixture in an ice-water bath.

1.3.2.2 Examples of graphene/PVDF-based matrices composites

As mentioned above, graphene is a promising nanofiller incorporated in the polymer matrix to develop advanced composite materials. This field has blossomed over the last decade and attracted increasing attentions. Concerning the PVDF-based matrix which is a family of multifunctional polymer materials, the literatures about graphene/PVDF-based matrices composites are summarized in Table 1-6. Dependent on the different forms of graphene, unmodified GO or rGO and chemical modified GO or rGO are the two main kinds shown successively.

Table 1-6: Reported works on graphene/PVDF-based composites in literatures

Matrix	Form of graphene	Note	Ref
PVDF/nylon 6 blend	GO	Compatibilize immiscible PVDF/nylon 6 blend	[222]
PVDF	Exfoliated graphite nanoplates (xGnP)	High dielectric permittivity, low percolation threshold	[188]
PVDF	Porous graphene sandwich	Semiconductor-conductor-semiconductor structure gives high dielectric properties	[223]
P(VDF-HFP)	rGO	Spin-assistant gives homogeneous dispersion and good alignment of rGO with high dielectric constant and low loss	[224]
P(VDF-HFP)	Graphene sheets	Superhydrophobic microspheres *via* gelation	[225]
P(VDF-TrFE-CFE)	rGO	Comparison between hydrothermal and hydrazine reduction methods: N-doping by hydrazine gives high dielectric constant and low loss	[226]
PVDF	rGO	Increased dielectric constant and enhanced remnant polarization to be used for energy harvesting	[227]
PVDF	rGo	High dielectric permittivity and low percolation threshold	[228]
PVDF	rGO	Piezoelectric property	[229]
PVDF	GO	Microfiltration tubes for Cu^{2+} removal	[230]
PVDF	GO	Enhanced ferroelectric and pyroelectric properties	[231]
PVDF	GO	Promotes β-phase, increases dynamic mechanical properties and thermal stability, excellent optical transparency and modified wettability	[232]

PVDF	GO	Graphene as nucleating agents for α-phase, decreased electrical volume resistivity	[233]
PVDF	rGO	Isolated monolayer rGO via in situ thermal reduction prevent aggregation	[234]
PVDF	Functionalized graphene sheets (FGS) *vs.* exfoliated graphite (EG)	Differences in electrical, mechanical, thermal properties and the effect of temperature on the electrical conductivity is due to higher aspect ratio of FGS which leads to contact resistance predominating over tunneling resistance	[235]
PVDF	Graphene nano-ribbons	First-principles computational approaches	[236]
PVDF	rGO	Melt-compounding by two-screw mixer, better dispersion and distribution throughout the matrix	[237]
PVDF	rGO	Crystallization, rheological behavior and mechanical properties	[238]
PVDF	Graphite nano-sheets (GNS)	Crystallization behavior and phase-transformation mechanism	[239]
PVDF	rGO	Thermally reduced, excellent electrical conductivity and a low percolation threshold	[240]
PVDF	rGO	Structure, thermal stability and electrical properties	[241]
PVDF	rGO	High dielectric constant and low percolation threshold	[242]
PVDF	PVA modified rGO	Improved dielectric properties	[243]
P(VDF-CTFE)	SiO_2 coated rGO	Suppression of energy dissipation and enhancement of breakdown strength	[244]

PVDF	Noncovalently functionalized rGO by quaternary phosphorus salt, (1-hexadecyl) triphenylphosphonium bromide(HTPB)	Excellent electric property, improved dielectric property and dominant polar crystalline forms	[245]
PVDF	Noncovalently functionalized GO by ionic surfactant cetyltrimethylammonium bromide(CTAB)	Role of strong ion-dipole interaction between GO and CTAB in nucleation of γ-phase	[246]
PVDF	Polyaniline-functionalized rGO/$BaTiO_3$	High permittivity, low dielectric loss, and low percolation threshold	[247]
PVDF	Au (or Ag) modified GO *via*(3-mercaptopropyl)triethoxysilane	Effectively immobilize metal nanoparticles onto a graphene surface, and that better distribution and size control of metal nanoparticles, significantly increased AC conductivity	[248]
PVDF	Stable dispersion of rGO in ILs	Improved thermostability	[249]
PVDF	PMMA modified GO via traditional polymerization	Crystalline structure	[250]
PVDF	GO modified by phenyl isocyanate	Phase structure and tribological property	[251]

1.3.2.3 Methods to enhance the dispersion of graphene

The distribution of graphene layers in the polymer matrix as well as interfacial bonding between the graphene layers and polymer matrix is the key to improve physico-chemical properties of the nanocomposites. Interfacial bonding between graphene and the host polymer dictates the final properties of the graphene reinforced polymer nanocomposite. However, pristine graphene is not compatible with organic polymers and does not form homogeneous composites due to the lack of active chemical groups. Oppositely, GO sheets are heavily oxygenated graphene (bearing hydroxyl, epoxide, diol, ketone and carboxyl functional groups) that make change the van der Waals interactions significantly and be more compatible with organic

polymers [252,253,254,255,256,257]. There are also some additional carbonyl and carboxyl groups located at the edge of the sheets, which makes graphene oxide sheets strongly hydrophilic, allowing them to readily swell and disperse in polar solvents such as water, DMF, DMAc, *etc* [258,259]. Therefore, GO has attracted considerable attention as a nanofiller for polymer nanocomposites. However, unlike graphene, GO is electrically insulating, which makes it unsuitable for the synthesis of conducting nanocomposites. To a certain extent, this issue can be solved by the chemical reduction of GO. Thus, in order to avoid the reagglomeration during the reduction, the surface modification of graphene by so-called interfacial agents (compatibilizer between graphene and polymer matrix) is an essential step for obtaining a molecular level dispersion of individual graphene in a polymer matrix even after the reduction process. In this way, two requirements are well met: (1) restoring the graphitic network of sp^2 bonds, (2) displaying a fine dispersion of graphene. Furthermore, the process method to prepare graphene/polymer composites is another key to determine the distribution of graphene in the matrix. In this sub-section, both *"through process"* and *"through interfacial agents"* will be explained as follows.

(1) Through process

***In situ* intercalation polymerization.** In this way, graphene or modified graphene is first dispersed within the liquid monomer. Comparing to the polymer chains, graphene sheets can form a homogeneous mixture with small size monomers more easily. Thanks to the *in situ* polymerization initiated by heat or radiation, the dispersion of graphene in polymer matrices can be predicted to be enhanced. This way has been exploited for polystyrene (PS)/graphene [260,261,262] and poly(methyl methacrylate) (PMMA)/expanded graphite [263].

Polymer intercalation in cosolvent. This way is based on a cosolvent system in which the polymer is solubilized and graphene or modified graphene layers are allowed to be homogeneously dispersed [264]. Graphene or modified graphene can be dispersed easily in a suitable solvent, such as water, chloroform, tetrahydrofuran (THF), dimethyl formamide (DMF) or toluene, due to the weak forces that stack the

layers together. The polymer then adsorbs onto the delaminated sheets. After the solvent evaporation, the graphene sheets reassemble to sandwich the polymer to form the nanocomposites [187]. The driving force for polymer intercalation from solution is the entropy gained by the desorption of solvent molecules, which compensates for the decrease in conformational entropy of the intercalated polymer chains. The main advantage of this method is that it allows the synthesis of intercalated nanocomposites based on polymers with low or even no polarity.

Polymer intercalation in melting state. In this technique, no solvent is required and graphene or modified graphene is mixed with the polymer matrix in the molten state. Typically, a thermoplastic polymer is mechanically mixed with graphene or modified graphene at elevated temperatures using conventional methods, such as extrusion and injection molding [265,266]. During the melting blending, the polymer chains are intercalated between graphene layers, producing a well homogeneous dispersed nanocomposites. This method is popular for preparing thermoplastic polymer/graphene nanocomposites, especially for those polymers which are unsuitable for adsorption or *in situ* polymerization.

(2) Through interfacial agents

As we mentioned above, the graphene/PVDF composites are prepared from the GO as the starting material. The resulting oxygenated graphene sheets covered with hydroxyl, epoxy and carboxyl groups offer tremendous possibilities for further functionalization. Thus, it is possible to obtain judicious incorporation of graphene in the polymer matrix by a uniform dispersion and fine interface control.

The covalent modification of the surface of GO was one of the commonly used methods. It is reported that PMMA chains have been grafted from the GO or rGO surface *via* surface-initiated atom transfer radical polymerization (SI-ATRP) [267] (see Figure 1-23), yielding homogeneous nanocomposites with well-dispersed GO or rGO platelets [268,269]. It has been proven that PVDF and PMMA are completely miscible in melt state [270,271]. Thus, PMMA chains covalently anchored on the graphene surface act as the so-called interfacial agents, providing strong

interfacial interactions between graphene and PVDF host and leading to a steady and homogeneous distribution of graphene throughout the composites.

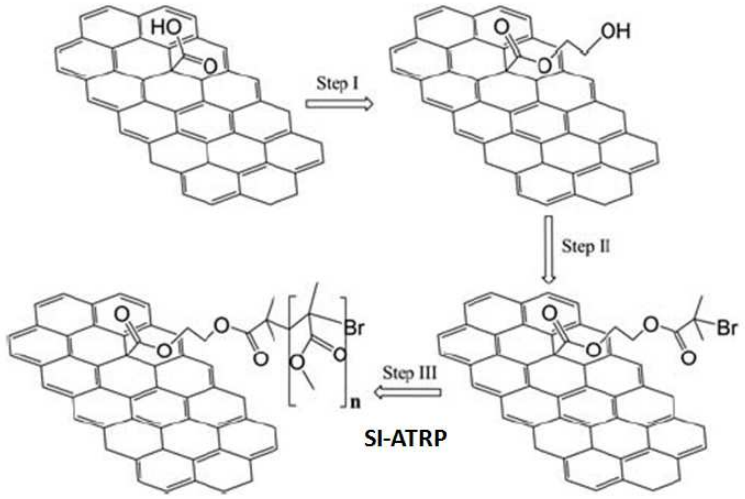

Figure 1-23: Reaction pathway to covalently modify GO by SI-ATRP [268]

Poly (vinyl alcohol) (PVA) was also reported to be covalently bonded to the surface of GO through esterification between the hydroxyl groups of PVA and carboxyl acid groups of GO (see Figure 1-24(a)) [243]. The PVA functionalized graphene surface can not only prevent the agglomeration of original rGO but also enhance the interactions between PVDF and rGO-PVA through the intermolecular hydrogen bonds between PVA and PVDF. The values of percolation threshold for rGO/PVDF and rGO-PVA/PVDF were determined to be 0.61 vol % and 2.24 vol %, respectively. The effect of PVA interfacial engineering on the enhancement of rGO fillers was highlighted in this work. Compared with the rGO/PVDF composites, higher dielectric permittivity combined with lower loss factor are achieved for rGO-PVA/PVDF nanocomposites in a frequency range of 1×10^2 to 1×10^3 Hz. At 1×10^2 Hz, the rGO-PVA/PVDF nanocomposite shows a high dielectric constant of 230, which is 2.3 times higher than one measured on of rGO/PVDF nanocomposite (see Figure 1-24(b)).

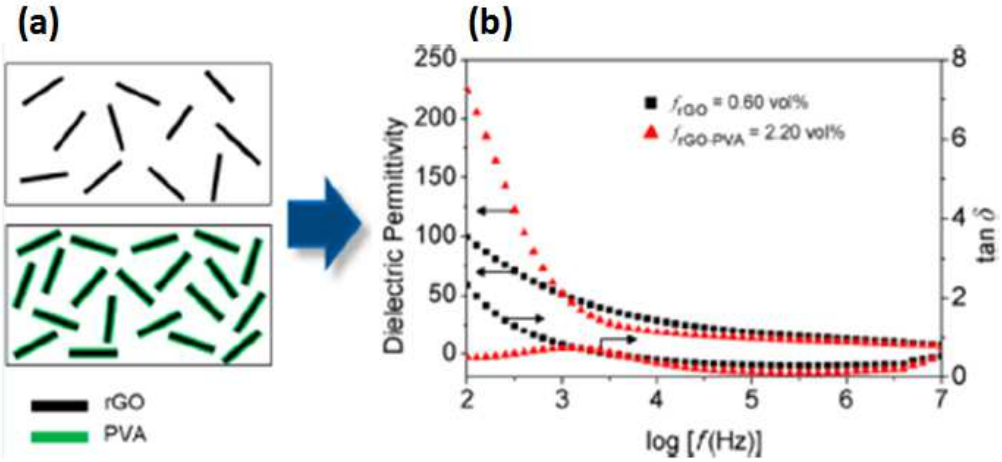

Figure 1-24: rGO-PVA/PVDF nanocomposite (a); frequency dependence of dielectric permittivity and loss factor of rGO/PVDF and rGO-PVA/PVDF nanocomposites with the filler volume fraction near the percolation threshold (b) [243]

Han *et al.* reported homogeneous percolative composites based on P(VDF-CTFE) as matrix and tetraethyl orthosilicate-modified rGO nanosheets as fillers [244]. The resulting composites exhibit a higher electrical resistivity and breakdown strength which show superior dielectric performance compared to the composites containing unmodified rGO. He *et al.* covalently linked the (3-mercaptopropyl)triethoxysilanemolecule onto the surface of GO as interfacial agent to attach the Ag or Au nanoparticles to the surface of graphene nanosheets [248]. The resulting metalliccoating PVDF/graphene-Ag nanocomposites were obtained by solution casting, and the composite materials showed significantly increased AC conductivity with only 2 wt% of filler loading, which is promising in composite reinforcement, sensors, and electronic devices [248].

More recently, ILs as novel interfacial agents have been non-covalently bonded on the surface of graphene. Li *et al.* modified the surface of GO with an ammonium-based IL (cetyltrimethylammonium bromide, CTAB) [246]. The resulting PVDF/GO composites show nearly pure γ-crystals due to ion-dipole interactions during melt crystallization (see Figure 1-25). It is also reported that CTAB-treated GO can induce the nucleation and growth of γ-phase preferentially in the early stage, and enhancethe α to γ transformation in the later stage.

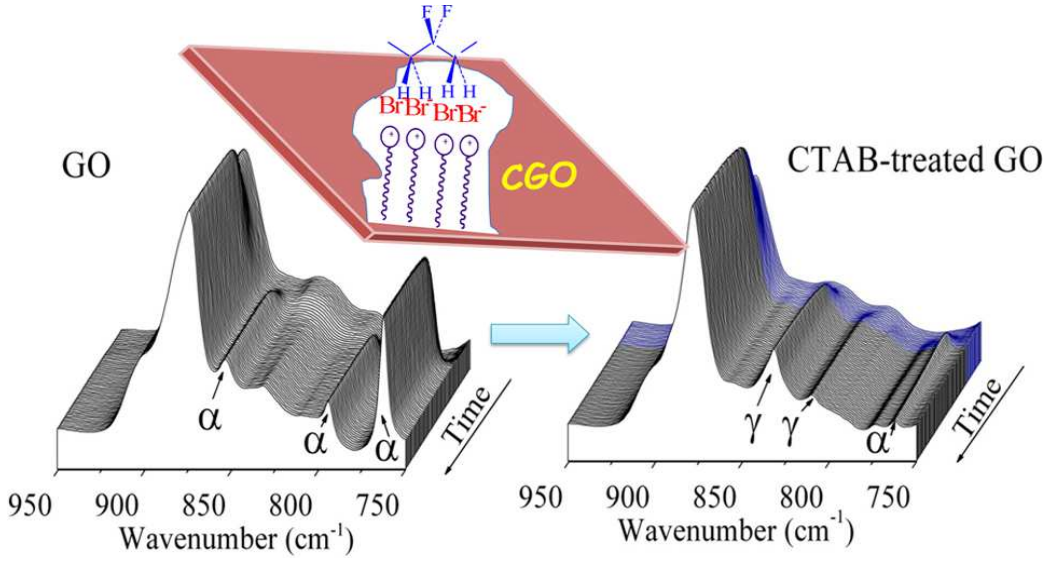

Figure 1-25: CTAB modified GO and formation of γ-crystal of PVDF [246]

By using another imidazolium based IL, Maity *et al.*have processed the PVDF/IL-functionalized GO (GO-IL) composites by solution-casting from DMF (see Figure 1-26(a)) [272]. The GO-IL is found to be homogeneously dispersed in the PVDF matrix with a dendritic morphology due to interfacial interactions of GO-IL with PVDF chains (see TEM image in Figure 1-26(b)). Both FT-IR (Figure 1-26(c)) and XRD Figure 1-26(d) spectra indicate the formation of polar β-crystal. The composites exhibit a gradual increase of melting, crystallization, glass transition (T_g) and other relaxation temperatures increasing with GO-IL concentration. Moreover, the authors demonstrate that the GO sheets are randomly distributed at low GO-IL concentration but they are unidirectional at higher concentration. With the incorporation of GO-IL fillers, there is a clear increase of conductivity even at low loading content of fillers. The author attributed the conductivity to the electron conductivity of graphene rings through the three dimensional network in the composites. It is also reported that a sharp increase of DC-conductivity of composite to ~10^{-2} S/cm occurs at the percolation threshold (0.1 wt%), and the dielectric permittivity increases from 7.5 for PVDF to 13.5 at 100 Hz for the composites with 3 wt% of GO-IL.

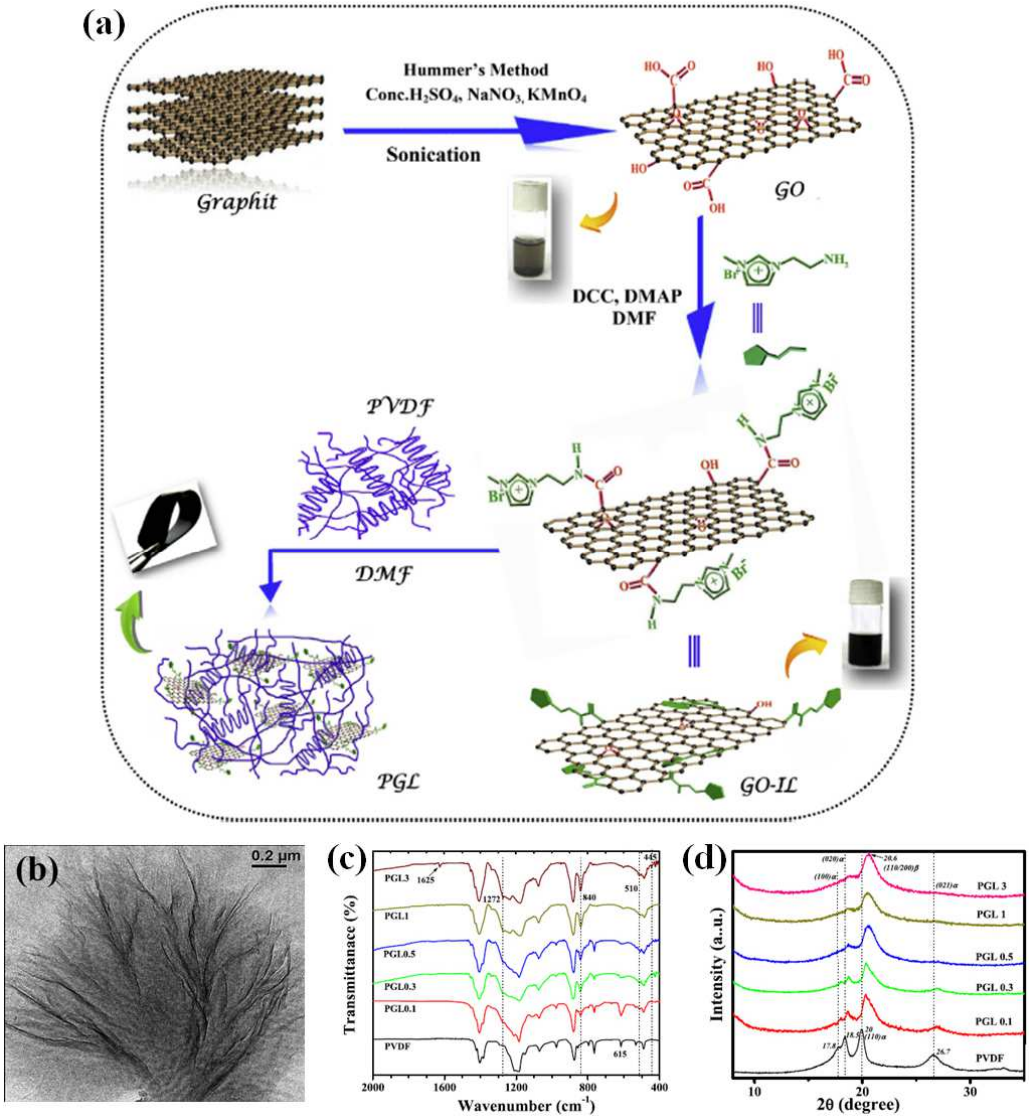

Figure 1-26: Preparation of GO-IL and P(VDF-CTFE)/GO-IL composite (PGL) (a); TEM image of PGL-1 (1 wt%) (b); FT-IR (c) and XRD (d) spectra of neat PVDF and PGL composites containing different amounts of GO-IL: PGL0.1 (0.1 wt%), PGL0.3 (0.3 wt%), PGL0.5 (0.5 wt%), PGL0.5 (0.5 wt%), PGL1 (1 wt%), PGL3 (3 wt%) [272]

Moreover, phosphonium ILs have been increasingly a hot issue at present due to their higher thermal and chemical stability compared to imidazolium and pyridinium counterparts. Recently, a phosphonium IL, (1-hexadecyl)triphenyl-phosphonium bromide (HTPB), was introduced for the non-covalent functionalization of graphene [245]. Thanks to the modification of graphene surface with IL, an excellent dispersion of graphene in DMAc even after reduction from GO and later in PVDF matrix has been achieved (see Figure 1-27a). As a result, the films exhibit improved dielectric property with a very low percolation threshold of 0.662 wt%,

e.g.,the dielectric constant of the composite films at 1000 Hz with lower than 0.86 wt% of HTPB-rGO shows an obvious increase (more than 3 times of neat PVDF), while the dielectric loss remains quite low (all lower than 0.07) (see Figure 1-27b & c). Moreover, the phosphonium ionic liquid can also be an effective inducer of polar β or γ-phases (see Figure 1-27d). Therefore, these PVDF/graphene films with good electric and dielectric property as well as dominant polar crystals promise a wide range of potential applications in electronic devices.

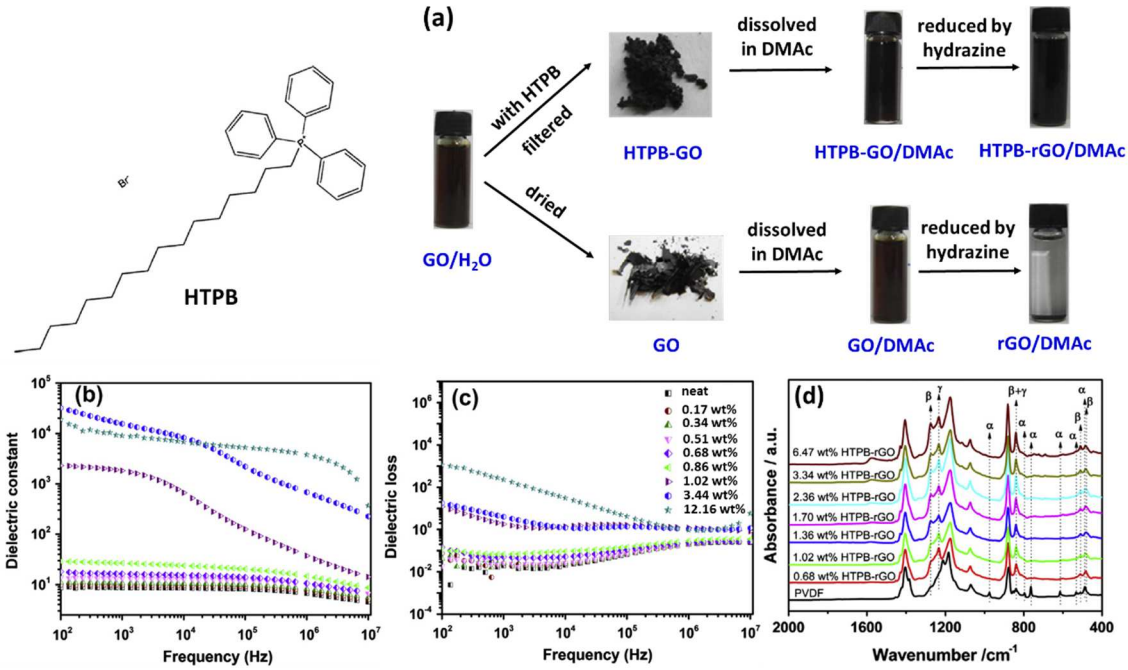

Figure 1-27: IL-modified rGO with excellent dispersion in DMAc (a); dielectric constant *vs.* frequency (b); dielectric loss *vs.* frequency (c) and FTIR spectra (d) of neat PVDF and PVDF/HTPB-rGO composites films [245]

1.3.3 Conclusions

Graphene has been considered as one of promising carbon nanofillers in polymer matrices due to its high surface area, aspect ratio, thermal conductivity and electrical conductivity. Graphene-based polymer nanocomposites represent one of the most technologically promising developments with a variety of applications. Concerning the PVDF-based matrices, both unmodified and modified graphene materials have been incorporated by solvent or melting process to obtain nanocoposites with well dispersed morphology. Among them, the use of ILs as

interfacial agents to modify the surface of graphene is just unfolding and many parameters, such as designing of IL structure, experimental conditions, processing method, should be paid more attention, and more importantly, most of the works at present concerning GO or rGO modified by ILs in PVDF-based nanocomposites mainly focus on the improvement of final dielectric properties with the addition of GO-IL or rGO-IL, few of them deeply investigate the interactions between ILs and graphene before and after the reduction treatment, which will be presented in *Chapter 3*.

1.4 References

[1] Ameduri B. From vinylidene fluoride (VDF) to the applications of VDF-containing polymers and copolymers: recent developments and future trends. *Chemical Reviews*, 2009, 109(12): 6632-6686.
[2] Voet V S D, Brinke G, Loos K. Well-defined copolymers based on poly(vinylidene fluoride): From preparation and phase separation to application. *Journal of Polymer Science Part A: Polymer Chemistry*, 2014, 52(20): 2861-2877.
[3] Martins P, Lopes A C, Lanceros-Mendez S. Electroactive phases of poly(vinylidene fluoride): determination, processing and applications. *Progress in Polymer Science*, 2014, 39(4): 683-706.
[4] Ameduri B, Boutevin B, Kostov G. Fluoroelastomers: synthesis, properties and applications. *Progress in Polymer Science*, 2001, 26(1): 105-187.
[5] Lovinger A J. Ferroelectric polymers. *Science*, 1983, 220(4602): 1115-1121.
[6] Furukawa T. Ferroelectric properties of vinylidene fluoride copolymers. *Phase Transitions: A Multinational Journal*, 1989, 18(3-4): 143-211.
[7] Nalwa H S, ed. *Ferroelectric Polymers*. Dekker, New York, 1995.
[8] Kawai H. The piezoelectricity of poly(vinylidene fluoride). *Japanese Journal of Applied Physics*, 1969, 8(7): 975.
[9] Zhang Q M, Bharti V, Kavarnos G. Poly(vinylidene fluoride) (PVDF) and its copolymers. *Encyclopedia of Smart Materials*, 2002.
[10] Fukada E. History and recent progress in piezoelectric polymers. *IEEE Transactions on Ultrasonics, Ferroelectrics, and Frequency Control*, 2000, 47(6): 1277-1290.
[11] Chang Y M, Lee J S, Kim K J. Heartbeat monitoring technique based on corona-poled PVDF film sensor for smart apparel application. *Solid State Phenomena*. 2007, 124: 299-302.
[12] Blaise J, Grimaud E. (Elf Atochem S.A.) *U.S. Patent* 4,025,709,1977.
[13] Bacque X, Lasson P. (Solvay S.A.) *Eur. Pat. Appl.* 387,938, 1990.
[14] Iserson, H. (Pennwalt Corp.) *U.S. Patent* 3,245,971, 1966.
[15] Baxter, J. A.; Eddy, C. O.; Stevens, H. C. (PPG Industries, Inc) *U.S.Patent* 3,642,755, 1972.
[16] Lasson, P. (Solvay S.A.)*European Patent* 0,417,585, 1990.
[17] Brinati, G.; Arcella, V.; Albano, M. (Ausimont S.p.A.) *U.S. Patent* 5,583,190, 1996.
[18] Amagi, Y.; Bannai, N. (Kureha Chemical Co) *U.S. Patent* 3,553,785, 1971.
[19] Dohany, J. E. (Pennwalt Corp.) *U.S. Patent* 3,781,265, 1973.
[20] Dumoulin, J. (Solvay & Cie) *U.S. Patent* 4,542,194, 1985.
[21] Ihara, K.; Noda, Y.; Amano, T. (Daikin Industries, Ltd.) *Japanese Patent* 01,129,005, 1989.
[22] Carlson, D. P. (E.I. du Pont de Nemours & Co., Inc.) *German Patent* 1,806, 426, 1969; *French Patent* 1 590 301, 1970.
[23] Guiot J, Ameduri B, Boutevin B. Radical homopolymerization of vinylidene

fluoride initiated by tert-butyl peroxypivalate. Investigation of the microstructure by ^{19}F and ^{1}H NMR spectroscopies and mechanisms. *Macromolecules*, 2002, 35(23): 8694-8707.

[24] Moggi, G.; Caratto, A.; Bonardelli, P.; Monti, C. (Montefluos S.p.A.) *U.S. Patent* 4,739,024, 1988.

[25] Ahmed T S, DeSimone J M, Roberts G W. Continuous precipitation polymerization of vinylidene fluoride in supercritical carbon dioxide: modeling the molecular weight distribution. *Chemical Engineering Science*, 2004, 59(22): 5139-5144.

[26] Du L, Kelly J Y, Roberts G W, et al. Fluoropolymer synthesis in supercritical carbon dioxide. *The Journal of Supercritical Fluids*, 2009, 47(3): 447-457.

[27] Boyer C, Valade D, Sauguet L, et al. Iodine transfer polymerization (ITP) of vinylidene fluoride (VDF). Influence of the defect of VDF chaining on the control of ITP. *Macromolecules*, 2005, 38(25): 10353-10362.

[28] Boyer C, Valade D, Lacroix-Desmazes P, et al. Kinetics of the iodine transfer polymerization of vinylidene fluoride. *Journal of Polymer Science Part A: Polymer Chemistry*, 2006, 44(19): 5763-5777.

[29] Wang Z, Zhang Z, Chung T C M. High dielectric VDF/TrFE/CTFE terpolymers prepared by hydrogenation of VDF/CTFE copolymers: synthesis and characterization. *Macromolecules*, 2006, 39(13): 4268-4271.

[30] Zhang Z, Chung T C M. The structure-property relationship of poly (vinylidene difluoride)-based polymers with energy storage and loss under applied electric fields. *Macromolecules*, 2007, 40(26): 9391-9397.

[31] Girard E, Marty J D, Ameduri B, et al. Direct synthesis of vinylidene fluoride-based amphiphilic diblock copolymers by RAFT/MADIX polymerization. *ACS Macro Letters*, 2012, 1(2): 270-274.

[32] Patil Y, Ameduri B. First RAFT/MADIX radical copolymerization of tert-butyl 2-trifluoromethacrylate with vinylidene fluoride controlled by xanthate. *Polymer Chemistry*, 2013, 4(9): 2783-2799.

[33] Salimi A, Yousefi A A. Analysis method: FTIR studies of β-phase crystal formation in stretched PVDF films. *Polymer Testing*, 2003, 22(6): 699-704.

[34] Giannetti E. Semi-crystalline fluorinated polymers. *Polymer International*, 2001, 50(1): 10-26.

[35] El Mohajir B E, Heymans N. Changes in structural and mechanical behaviour of PVDF with processing and thermomechanical treatments. 1. Change in structure. *Polymer*, 2001, 42(13): 5661-5667.

[36] Martins P, Costa C M, Benelmekki M, et al. On the origin of the electroactive poly(vinylidene fluoride) β-phase nucleation by ferrite nanoparticles via surface electrostatic interactions. *Cryst. Eng. Comm.*, 2012, 14(8): 2807-2811.

[37] Bachmann M A, Gordon W L, Koenig J L, et al. An infrared study of phase-III poly(vinylidene fluoride). *Journal of Applied Physics*, 1979, 50(10): 6106-6112.

[38] Lopes A C, Costa C M, Tavares C J, et al. Nucleation of the electroactive γ phase and enhancement of the optical transparency in low filler content

poly(vinylidene)/clay nanocomposites. *The Journal of Physical Chemistry C*, 2011, 115(37): 18076-18082.

[39] Ince-Gunduz B S, Alpern R, Amare D, et al. Impact of nanosilicates on poly(vinylidene fluoride) crystal polymorphism: Part 1. Melt-crystallization at high supercooling. *Polymer*, 2010, 51(6): 1485-1493.

[40] Ince-Gunduz B S, Burke K, Koplitz M, et al. Impact of nanosilicates on poly(vinylidene fluoride) crystal polymorphism: part 2. Melt-crystallization at low supercooling. *Journal of Macromolecular Science, Part A: Pure and Applied Chemistry*, 2010, 47(12): 1208-1219.

[41] Gregorio R. Determination of the α, β, and γ crystalline phases of poly(vinylidene fluoride) films prepared at different conditions. *Journal of Applied Polymer Science*, 2006, 100(4): 3272-3279.

[42] Boccaccio T, Bottino A, Capannelli G, et al. Characterization of PVDF membranes by vibrational spectroscopy. *Journal of Membrane Science*, 2002, 210(2): 315-329.

[43] Imamura R, Silva A B, Gregorio R. γ→β Phase Transformation Induced in Poly (vinylidene fluoride) by Stretching. *Journal of Applied Polymer Science*, 2008, 110(5): 3242-3246.

[44] Bormashenko Y, Pogreb R, Stanevsky O, et al. Vibrational spectrum of PVDF and its interpretation. *Polymer Testing*, 2004, 23(7): 791-796.

[45] Esterly D M, Love B J. Phase transformation to β-poly(vinylidene fluoride) by milling. *Journal of Polymer Science Part B: Polymer Physics*, 2004, 42(1): 91-97.

[46] Gregorio Jr R, Ueno E M. Effect of crystalline phase, orientation and temperature on the dielectric properties of poly(vinylidene fluoride) (PVDF). *Journal of Materials Science*, 1999, 34(18): 4489-4500.

[47] Lanceros-Mendez S, Mano J F, Costa A M, et al. FTIR and DSC studies of mechanically deformed β-PVDF films. *Journal of Macromolecular Science, Part B*, 2001, 40(3-4): 517-527.

[48] Gregorio R, Capitao R C. Morphology and phase transition of high melt temperature crystallized poly(vinylidene fluoride). *Journal of Materials Science*, 2000, 35(2): 299-306.

[49] Benz M, Euler W B. Determination of the crystalline phases of poly(vinylidene fluoride) under different preparation conditions using differential scanning calorimetry and infrared spectroscopy. *Journal of Applied Polymer Science*, 2003, 89(4): 1093-1100.

[50] Cortili G, Zerbi G. Further infra-red data on polyvinylidene fluoride. *Spectrochimica Acta Part A: Molecular Spectroscopy*, 1967, 23(7): 2216-2218.

[51] Wang Z Y, Fan H Q, Su K H, et al. Structure and piezoelectric properties of poly(vinylidene fluoride) studied by density functional theory. *Polymer*, 2006, 47(23): 7988-7996.

[52] He L, Sun J, Wang X, et al. Facile and effective promotion of β crystalline phase in poly(vinylidene fluoride) via the incorporation of imidazolium ionic liquids. *Polymer International*, 2013, 62(4): 638-646.

[53] Priya L, Jog J P. Polymorphism in intercalated poly(vinylidene fluoride)/clay nanocomposites. *Journal of Applied Polymer Science*, 2003, 89(8): 2036-2040.
[54] Buckley J, Cebe P, Cherdack D, et al. Nanocomposites of poly(vinylidene fluoride) with organically modified silicate. *Polymer*, 2006, 47(7): 2411-2422.
[55] Gregorio Jr R, Cestari M. Effect of crystallization temperature on the crystalline phase content and morphology of poly(vinylidene fluoride). *Journal of Polymer Science Part B: Polymer Physics*, 1994, 32(5): 859-870.
[56] Martins P, Costa C M, Lanceros-Mendez S. Nucleation of electroactive β-phase poly (vinilidene fluoride) with $CoFe_2O_4$ and $NiFe_2O_4$ nanofillers: a new method for the preparation of multiferroic nanocomposites. *Applied Physics A*, 2011, 103(1): 233-237.
[57] Scheinbeim J, Nakafuku C, Newman B A, et al. High-pressure crystallization of poly(vinylidene fluoride). *Journal of Applied Physics*, 1979, 50(6): 4399-4405.
[58] Gradys A, Sajkiewicz P, Adamovsky S, et al. Crystallization of poly(vinylidene fluoride) during ultra-fast cooling. *Thermochimica Acta*, 2007, 461(1): 153-157.
[59] Prest Jr W M, Luca D J. The formation of the γ phase from the α and β polymorphs of polyvinylidene fluoride. *Journal of Applied Physics*, 1978, 49(10): 5042-5047.
[60] Prest Jr W M, Luca D J. The morphology and thermal response of high-temperature–crystallized poly(vinylidene fluoride). *Journal of Applied Physics*, 1975, 46(10): 4136-4143.
[61] Salimi A, Yousefi A A. Analysis method: FTIR studies of β-phase crystal formation in stretched PVDF films. *Polymer Testing*, 2003, 22(6): 699-704.
[62] Prest Jr W M, Luca D J. The formation of the γ phase from the α and β polymorphs of polyvinylidene fluoride. *Journal of Applied Physics*, 1978, 49(10): 5042-5047.
[63] Davis G T, McKinney J E, Broadhurst M G, et al. Electric-field-induced phase changes in poly (vinylidene fluoride). *Journal of Applied Physics*, 1978, 49(10): 4998-5002.
[64] Ribeiro C, Sencadas V, Ribelles J L G, et al. Influence of processing conditions on polymorphism and nanofiber morphology of electroactive poly(vinylidene fluoride) electrospun membranes. *Soft Materials*, 2010, 8(3): 274-287.
[65] Zheng J, He A, Li J, et al. Polymorphism control of poly(vinylidene fluoride) through electrospinning. *Macromolecular Rapid Communications*, 2007, 28(22): 2159-2162.
[66] Benz M, Euler W B, Gregory O J. The role of solution phase water on the deposition of thin films of poly(vinylidene fluoride). *Macromolecules*, 2002, 35(7): 2682-2688.
[67] Ramasundaram S, Yoon S, Kim K J, et al. Direct Preparation of Nanoscale Thin Films of Poly(vinylidene fluoride) Containing β-Crystalline Phase by Heat-Controlled Spin Coating. *Macromolecular Chemistry and Physics*, 2008, 209(24): 2516-2526.
[68] Cardoso V F, Minas G, Costa C M, et al. Micro and nanofilms of poly(vinylidene fluoride) with controlled thickness, morphology and electroactive crystalline phase for

sensor and actuator applications. *Smart Materials and Structures*, 2011, 20(8): 087002.
[69] Jiang Y, Ye Y, Yu J, et al. A study on ferroelectric PVDF ultrathin films prepared by LB technique. *Integrated Ferroelectrics*, 2007, 88(1): 21-26.
[70] Chen S, Li X, Yao K, et al. Self-polarized ferroelectric PVDF homopolymer ultra-thin films derived from Langmuir–Blodgett deposition. *Polymer*, 2012, 53(6): 1404-1408.
[71] Sencadas V, Gregorio Filho R, Lanceros-Mendez S. Processing and characterization of a novel nonporous poly(vinylidene fluoride) films in the β phase. *Journal of Non-Crystalline Solids*, 2006, 352(21): 2226-2229.
[72] Gregorio Jr R, Ueno E M. Effect of crystalline phase, orientation and temperature on the dielectric properties of poly(vinylidene fluoride) (PVDF). *Journal of Materials Science*, 1999, 34(18): 4489-4500.
[73] Ye H J, Shao W Z, Zhen L. Crystallization kinetics and phase transformation of poly(vinylidene fluoride) films incorporated with functionalized $BaTiO_3$ nanoparticles. *Journal of Applied Polymer Science*, 2013, 129(5): 2940-2949.
[74] Patro T U, Mhalgi M V, Khakhar D V, et al. Studies on poly(vinylidene fluoride)-clay nanocomposites: effect of different clay modifiers. *Polymer*, 2008, 49(16): 3486-3499.
[75] Shah D, Maiti P, Gunn E, et al. Dramatic Enhancements in Toughness of Polyvinylidene Fluoride Nanocomposites via Nanoclay-Directed Crystal Structure and Morphology. *Advanced Materials*, 2004, 16(14): 1173-1177.
[76] Priya L, Jog J P. Poly(vinylidene fluoride)/clay nanocomposites prepared by melt intercalation: crystallization and dynamic mechanical behavior studies. *Journal of Polymer Science Part B: Polymer Physics*, 2002, 40(15): 1682-1689.
[77] Martins P, Moya X, Phillips L C, et al. Linear anhysteretic direct magnetoelectri effect in $Ni_{0.5}Zn_{0.5}Fe_2O_4$/poly(vinylidene fluoride-trifluoroethylene) nanocomposites. *Journal of Physics D: Applied Physics*, 2011, 44(48): 482001.
[78] Mandal D, Kim K J, Lee J S. Simple Synthesis of Palladium Nanoparticles, β-Phase Formation, and the Control of Chain and Dipole Orientations in Palladium-Doped Poly(vinylidene fluoride) Thin Films. *Langmuir*, 2012, 28(28): 10310-10317.
[79] Wang W, Zhang S, Srisombat L, et al. Gold Nanoparticle and Gold Nanoshell Induced Polymorphism in Poly(vinylidene fluoride). *Macromolecular Materials and Engineering*, 2011, 296(2): 178-184.
[80] Yu S, Zheng W, Yu W, et al. Formation mechanism of β-phase in PVDF/CNT composite prepared by the sonication method. *Macromolecules*, 2009, 42(22): 8870-8874.
[81] Miyazaki T, Takeda Y, Akasaka M, et al. Preparation of isothermally crystallized γ-form poly (vinylidene fluoride) films by adding a KBr powder as a nucleating agent. *Macromolecules*, 2008, 41(7): 2749-2753.
[82] Lopes A C, Costa C M, Tavares C J, et al. Nucleation of the electroactive γ phase and enhancement of the optical transparency in low filler content poly(vinylidene)/clay nanocomposites. *The Journal of Physical Chemistry C*, 2011, 115(37): 18076-18082.

[83] Lopes A C, Caparros C, Ribelles J L G, et al. Electrical and thermal behavior of γ-phase poly(vinylidene fluoride)/NaY zeolite composites. *Microporous and Mesoporous Materials*, 2012, 161: 98-105.
[84] Buckley G S, Roland C M, Casalini R, et al. Electrostrictive Properties of Poly(vinylidenefluoride-trifluoroethylene-chlorotrifluoroethylene). *Chemistry of Materials*, 2002, 14(6): 2590-2593.
[85] Zhu L, Wang Q. Novel ferroelectric polymers for high energy density and low loss dielectrics. *Macromolecules*, 2012, 45(7): 2937-2954.
[86] Koga K, Ohigashi H. Piezoelectricity and related properties of vinylidene fluoride and trifluoroethylene copolymers. *Journal of Applied Physics*, 1986, 59(6): 2142-2150.
[87] Lovinger A J, Furukawa T, Davis G T, et al. Crystallographic changes characterizing the Curie transition in three ferroelectric copolymers of vinylidene fluoride and trifluoroethylene: 2. Oriented or poled samples. *Polymer*, 1983, 24(10): 1233-1239.
[88] Furukawa T, Johnson G E, Bair H E, et al. Ferroelectric phase transition in a copolymer of vinylidene fluoride and trifluoroethylene. *Ferroelectrics*, 1981, 32(1): 61-67.
[89] Cardoso V F, Costa C M, Minas G, et al. Improving the optical and electroactive response of poly(vinylidene fluoride–trifluoroethylene) spin-coated films for sensor and actuator applications. *Smart Materials and Structures*, 2012, 21(8): 085020.
[90] Kim D W, Kim J H, Kim J N, et al. Characterization of Metal-Ferroelectric-Semiconductor Structure Using Ferroelectric Polymer Polyvinylidene Fluoride-trifluoroethylene (PVDF-TrFE) (51/49). *Integrated Ferroelectrics*, 2008, 98(1): 121-127.
[91] Ferreira A, Silva J, Sencadas V, et al. Poly(vinylidene fluoride-trifluoroethylene) (72/28) interconnected porous membranes obtained by crystallization from solution. *Materials Research Society Symposium Proceedings*, 2011, 1312: 125-130.
[92] Costa C M, Rodrigues L C, Sencadas V, et al. Effect of degree of porosity on the properties of poly(vinylidene fluoride–trifluorethylene) for Li-ion battery separators. *Journal of Membrane Science*, 2012, 407: 193-201.
[93] Neese B, Wang Y, Chu B, et al. Piezoelectric responses in poly(vinylidene fluoride/hexafluoropropylene) copolymers. *Applied Physics Letters*, 2007, 90, 242917.
[94] Künstler W, Wegener M, Seiß M, et al. Preparation and assessment of piezo-and pyroelectric poly(vinylidene fluoride-hexafluoropropylene) copolymer films. *Applied Physics A*, 2001, 73(5): 641-645.
[95] Huan Y, Liu Y, Yang Y, et al. Influence of extrusion, stretching and poling on the structural and piezoelectric properties of poly(vinylidene fluoride-hexafluoropropylene) copolymer films. *Journal of applied polymer science*, 2007, 104(2): 858-862.
[96] Ranjan V, Yu L, Nardelli M B, et al. Phase equilibria in high energy density PVDF-based polymers. *Physical Review Letters*, 2007, 99(4): 047801.
[97] Li Z, Wang Y, Cheng Z Y. Electromechanical properties of poly(vinylidene fluoride-chlorotrifluoroethylene) copolymer. *Applied Physics Letters*, 2006, 88(6):

062904.
[98] Bauer F. Relaxor fluorinated polymers: novel applications and recent developments. *IEEE Transactions on Dielectrics and Electrical Insulation*, 2010, 17(4): 1106-1112.
[99] Yu Z, Ang C, Cross L E, et al. Dielectric and electroactive strain properties of poly(vinylidene fluoride-trifluoroethylene-chlorotrifluoroethylene) terpolymers. *Applied Physics Letters*, 2004, 84(10): 1737-1739.
[100] Bauer F. Review on the properties of the ferrorelaxor polymers and some new recent developments. *Applied Physics A*, 2012, 107(3): 567-573.
[101] Bauer F, Capsal J F, Larcher Q, et al. Advances in relaxor ferroelectric terpolymer: new applications. *IEEE International Symposium on Application of Ferroelectrics*, 2011: 1-4.
[102] Xu H, Cheng Z Y, Olson D, et al. Ferroelectric and electromechanical properties of poly(vinylidene fluoride-trifluoroethylene-chlorotrifluoroethylene) terpolymer. *Applied Physics Letters*, 2001, 78(16): 2360-2362.
[103] Walden, P. *Bulletin de l'academie imperial des Sciences de St.-Peterbourg* 1914, 405.
[104] Pinkert A, Marsh K N, Pang S, et al. Ionic liquids and their interaction with cellulose. *Chemical Reviews*, 2009, 109(12): 6712-6728.
[105] Hayes R, Warr G G, Atkin R. Structure and Nanostructure in Ionic Liquids. *Chemical Reviews*, 2015, 115(13): 6357-6426.
[106] Forsyth S A, Pringle J M, MacFarlane D R. Ionic liquids-an overview. *Australian Journal of Chemistry*, 2004, 57(2): 113-119.
[107] Chiappe C, Pieraccini D. Ionic liquids: solvent properties and organic reactivity. *Journal of Physical Organic Chemistry*, 2005, 18(4): 275-297.
[108] Awad W H, Gilman J W, Nyden M, et al. Thermal degradation studies of alkyl-imidazolium salts and their application in nanocomposites. *Thermochimica Acta*, 2004, 409(1): 3-11.
[109] Khupse N D, Kumar A. Ionic liquids: New materials with wide applications. *Indian Journal of Chemistry*, 2010, 49(5): 635-648.
[110] Aggarwal A, Lancaster N L, Sethi A R, et al. The role of hydrogen bonding in controlling the selectivity of Diels–Alder reactions in room-temperature ionic liquids. *Green Chemistry*, 2002, 4(5): 517-520.
[111] Lu W, Fadeev A G, Qi B, et al. Use of ionic liquids for π-conjugated polymer electrochemical devices. *Science*, 2002, 297(5583): 983-987.
[112] Wang P, Dai Q, Zakeeruddin S M, et al. Ambient temperature plastic crystal electrolyte for efficient, all-solid-state dye-sensitized solar cell. *Journal of the American chemical society*, 2004, 126(42): 13590-13591.
[113] Hagiwara R, Lee J S. Ionic liquids for electrochemical devices. *Electrochemistry*, 2007, 75(1): 23-34.
[114] Frackowiak E, Lota G, Pernak J. Room-temperature phosphonium ionic liquids for supercapacitor application. *Applied Physics Letters*, 2005, 86(16): 164104.
[115] Zhou D, Spinks G M, Wallace G G, et al. Solid state actuators based on

polypyrrole and polymer-in-ionic liquid electrolytes. *Electrochimica Acta*, 2003, 48(14): 2355-2359.
[116] Dai S, Shin Y S, Toth L M, et al. Comparative UV-Vis studies of uranyl chloride complex in two basic ambient-temperature melt systems: The observation of spectral and thermodynamic variations induced via hydrogen bonding. *Inorganic Chemistry*, 1997, 36(21): 4900-4902.
[117] Dai S, Toth L M, Del Cul G D, et al. Solubilities of uranium (IV) dioxide in magnesium chloride, calcium chloride, and aluminum chloride melts: A comparative study. *The Journal of Physical Chemistry*, 1996, 100(1): 220-223.
[118] Ionic Liquids Industrial Applications for Green Chemistry, American Chemical Society, Washington, DC, (2002); 58-68.
[119] Dai S, Ju Y H, Barnes C E. Solvent extraction of strontium nitrate by a crown ether using room-temperature ionic liquids. *J. Chem. Soc., Dalton Trans.*, 1999 (8): 1201-1202.
[120] Zhao H, Xia S, Ma P. Use of ionic liquids as 'green' solvents for extractions. *Journal of Chemical Technology and Biotechnology*, 2005, 80(10): 1089-1096.
[121] Visser A E, Swatloski R P, Reichert W M, et al. Task-specific ionic liquids incorporating novel cations for the coordination and extraction of Hg^{2+} and Cd^{2+}: synthesis, characterization, and extraction studies. *Environmental Science & Technology*, 2002, 36(11): 2523-2529.
[122] Chun S, Dzyuba S V, Bartsch R A. Influence of structural variation in room-temperature ionic liquids on the selectivity and efficiency of competitive alkali metal salt extraction by a crown ether. *Analytical Chemistry*, 2001, 73(15): 3737-3741.
[123] Luo H, Dai S, Bonnesen P V, et al. Extraction of cesium ions from aqueous solutions using calix[4]arene-bis(tert-octylbenzo-crown-6) in ionic liquids. *Analytical Chemistry*, 2004, 76(11): 3078-3083.
[124] Luo H, Dai S, Bonnesen P V. Solvent extraction of Sr^{2+} and Cs^{+} based on room-temperature ionic liquids containing monoaza-substituted crown ethers. *Analytical Chemistry*, 2004, 76(10): 2773-2779.
[125] Huddleston J G, Rogers R D. Room temperature ionic liquids as novel media for 'clean'liquid–liquid extraction. *Chemical Communications*, 1998 (16): 1765-1766.
[126] Livi S, Duchet-Rumeau J, Gérard J F, et al. Polymers and ionic liquids: A successful wedding. *Macromolecular Chemistry and Physics*, 2015, 216(4): 359-368.
[127] Yokoyama R, Suzuki S, Shirai K, et al. Preparation and properties of biocompatible polymer-grafted silica nanoparticle. *European Polymer Journal*, 2006, 42(12): 3221-3229.
[128] Vermogen A, Masenelli-Varlot K, Séguéla R, et al. Evaluation of the structure and dispersion in polymer-layered silicate nanocomposites. *Macromolecules*, 2005, 38(23): 9661-9669.
[129] Gilman J W, Jackson C L, Morgan A B, et al. Flammability properties of polymer-layered-silicate nanocomposites. Polypropylene and polystyrene nanocomposites. *Chemistry of Materials*, 2000, 12(7): 1866-1873.
[130] Li L, Li B, Hood M A, et al. Carbon nanotube induced polymer crystallization:

The formation of nanohybrid shish–kebabs. *Polymer*, 2009, 50(4): 953-965.
[131] Bose S, Khare R A, Moldenaers P. Assessing the strengths and weaknesses of various types of pre-treatments of carbon nanotubes on the properties of polymer/carbon nanotubes composites: A critical review. *Polymer*, 2010, 51(5): 975-993.
[132] Guo Q, Liu J, Chen L, et al. Nanostructures and nanoporosity in thermoset epoxy blends with an amphiphilic polyisoprene-block-poly(4-vinyl pyridine) reactive diblock copolymer. *Polymer*, 2008, 49(7): 1737-1742.
[133] Yang X, Yi F, Xin Z, et al. Morphology and mechanical properties of nanostructured blends of epoxy resin with poly(ε-caprolactone)-block-poly(butadiene-co-acrylonitrile)-block-poly(ε-caprolactone) triblock copolymer. Polymer, 2009, 50(16): 4089-4100.
[134] Xu Z, Zheng S. Morphology and thermomechanical properties of nanostructured thermosetting blends of epoxy resin and poly(ε-caprolactone)-block-polydimethylsiloxane-block-poly(ε-caprolactone) triblock copolymer. *Polymer*, 2007, 48(20): 6134-6144.
[135] Maiez-Tribut S, Pascault J P, Soule E R, et al. Nanostructured epoxies based on the self-assembly of block copolymers: a new miscible block that can be tailored to different epoxy formulations. *Macromolecules*, 2007, 40(4): 1268-1273.
[136] Livi S, Gérard J F, Duchet-Rumeau J. Ionic liquids: structuration agents in a fluorinated matrix. *Chemical Communications*, 2011, 47(12): 3589-3591.
[137] Livi S, Duchet-Rumeau J, Gérard J F. Nanostructuration of ionic liquids in fluorinated matrix: influence on the mechanical properties. *Polymer*, 2011, 52(7): 1523-1531.
[138] Livi S, Bugatti V, Soares B G, et al. Structuration of ionic liquids in a poly (butylene-adipate-co-terephthalate) matrix: its influence on the water vapour permeability and mechanical properties. *Green Chemistry*, 2014, 16(8): 3758-3762.
[139] Soares B G, Silva A A, Pereira J, et al. Preparation of epoxy/Jeffamine networks modified with phosphonium based ionic liquids. *Macromolecular Materials and Engineering*, 2015, 300(3): 312-319.
[140] Soares B G, Silva A A, Pereira J, et al. Preparation of epoxy/Jeffamine networks modified with phosphonium based ionic liquids. *Macromolecular Materials and Engineering*, 2015, 300(3): 312-319.
[141] Livi S, Silva A A, Thimont Y, et al. Nanostructured thermosets from ionic liquid building block–epoxy prepolymer mixtures. *RSC Advances*, 2014, 4(53): 28099-28106.
[142] Nguyen T K L, Livi S, Pruvost S, et al. Ionic liquids as reactive additives for the preparation and modification of epoxy networks. *Journal of Polymer Science Part A: Polymer Chemistry*, 2014, 52(24): 3463-3471.
[143] Livi S, Silva A A, Thimont Y, et al. Nanostructured thermosets from ionic liquid building block–epoxy prepolymer mixtures. *RSC Advances*, 2014, 4(53): 28099-28106.
[144] Soares B G, Livi S, Duchet-Rumeau J, et al. Synthesis and Characterization of

Epoxy/MCDEA Networks Modified with Imidazolium-Based Ionic Liquids. *Macromolecular Materials and Engineering*, 2011, 296(9): 826-834.
[145] Soares B G, Silva A A, Livi S, et al. New epoxy/Jeffamine networks modified with ionic liquids. *Journal of Applied Polymer Science*, 2014, 131(3), 39834.
[146] Hillmyer M A, Lipic P M, Hajduk D A, et al. Self-assembly and polymerization of epoxy resin-amphiphilic block copolymer nanocomposites. *Journal of the American Chemical Society*, 1997, 119(11): 2749-2750.
[147] Meng F, Zheng S, Li H, et al. Formation of ordered nanostructures in epoxy thermosets: a mechanism of reaction-induced microphase separation. *Macromolecules*, 2006, 39(15): 5072-5080.
[148] Xing C, Zheng X, Xu L, et al. Toward an optically transparent, antielectrostatic, and robust polymer composite: morphology and properties of polycarbonate/ionic liquid composites. *Industrial & Engineering Chemistry Research*, 2014, 53(11): 4304-4311.
[149] Xing C, Guan J, Chen Z, et al. Novel multifunctional nanofibers based on thermoplastic polyurethane and ionic liquid: towards antibacterial, anti-electrostatic and hydrophilic nonwovens by electrospinning. *Nanotechnology*, 2015, 26(10): 105704.
[150] Wang F, Lack A, Xie Z, et al. Ionic-liquid-induced ferroelectric polarization in poly(vinylidene fluoride) thin films. *Applied Physics Letters*, 2012, 100(6): 062903.
[151] Xing C, Zhao M, Zhao L, et al. Ionic liquid modified poly(vinylidene fluoride): crystalline structures, miscibility, and physical properties. *Polymer Chemistry*, 2013, 4(24): 5726-5734.
[152] Xing C, Guan J, Li Y, et al. Effect of a room-temperature ionic liquid on the structure and properties of electrospun poly(vinylidene fluoride) nanofibers. *ACS Applied Materials & Interfaces*, 2014, 6(6): 4447-4457.
[153] Okada D, Kaneko H, Kato K, et al. Colloidal Crystallization and Ionic Liquid Induced Partial β-Phase Transformation of Poly(vinylidene fluoride) Nanoparticles. *Macromolecules*, 2015, 48(8): 2570-2575.
[154] Xing C, Wang Y, Zhang C, et al. Immobilization of Ionic Liquids onto the Poly(vinylidene fluoride) by Electron Beam Irradiation. *Industrial & Engineering Chemistry Research*, 2015, 54(38): 9351-9359.
[155] Xing C, You J, Li Y, et al. Nanostructured Poly(vinylidene fluoride)/Ionic Liquid Composites: Formation of Organic Conductive Nanodomains in Polymer Matrix. *The Journal of Physical Chemistry C*, 2015, 119(36): 21155-21164.
[156] Zhang Q M, Li H, Poh M, et al. An all-organic composite actuator material with a high dielectric constant. *Nature*, 2002, 419(6904): 284-287.
[157] Zhang Q M, Bharti V, Zhao X. Giant electrostriction and relaxor ferroelectric behavior in electron-irradiated poly(vinylidene fluoride-trifluoroethylene) copolymer. *Science*, 1998, 280(5372): 2101-2104.
[158] Naber R C G, Tanase C, Blom P W M, et al. High-performance solution-processed polymer ferroelectric field-effect transistors. *Nature Materials*, 2005, 4(3): 243-248.

[159] Kim P, Doss N M, Tillotson J P, et al. High energy density nanocomposites based on surface-modified BaTiO3 and a ferroelectric polymer. *ACS Nano*, 2009, 3(9): 2581-2592.
[160] Yang K, Huang X, Huang Y, et al. Fluoro-polymer@$BaTiO_3$ hybrid nanoparticles prepared via RAFT polymerization: toward ferroelectric polymer nanocomposites with high dielectric constant and low dielectric loss for energy storage application. *Chemistry of Materials*, 2013, 25(11): 2327-2338.
[161] Li J, Claude J, Norena-Franco L E, et al. Electrical energy storage in ferroelectric polymer nanocomposites containing surface-functionalized $BaTiO_3$ nanoparticles. *Chemistry of Materials*, 2008, 20(20): 6304-6306.
[162] Gao L, He J, Hu J, et al. Large Enhancement in Polarization Response and Energy Storage Properties of Poly(vinylidene fluoride) by Improving the Interface Effect in Nanocomposites. *The Journal of Physical Chemistry C*, 2014, 118(2): 831-838.
[163] Li K, Wang H, Xiang F, et al. Surface functionalized $Ba_{0.6}Sr_{0.4}TiO_3$/ poly(vinylidene fluoride) nanocomposites with significantly enhanced dielectric properties. *Applied Physics Letters*, 2009, 95(20): 202904.
[164] Shaohui L, Jiwei Z, Jinwen W, et al. Enhanced energy storage density in poly(vinylidene fluoride) nanocomposites by a small loading of suface-hydroxylated Ba0.6Sr0.4TiO3 nanofibers. *ACS Applied Materials & Interfaces*, 2014, 6(3): 1533-1540.
[165] Chen X Z, Li X, Qian X S, et al. A nanocomposite approach to tailor electrocaloric effect in ferroelectric polymer. *Polymer*, 2013, 54(20): 5299-5302.
[166] Arbatti M, Shan X, Cheng Z Y. Ceramic–polymer composites with high dielectric constant. *Advanced Materials*, 2007, 19(10): 1369-1372.
[167] Shen Y, Lin Y, Li M, et al. High dielectric performance of polymer composite films induced by a percolating interparticle barrier layer. *Advanced Materials*, 2007, 19(10): 1418-1422.
[168] Dang Z M, Wang L, Yin Y I, et al. Giant dielectric permittivities in functionalized carbonnanotube/electroactivepolymer nanocomposites. *Advanced Materials*, 2007, 19(6): 852-857.
[169] Zhang S, Zhang N, Huang C, et al. Microstructure and electromechanical properties of carbon nanotube/poly(vinylidene fluoride-trifluoroethylene-chlorofluoroethylene) composites. *Advanced Materials*, 2005, 17(15): 1897-1901.
[170] Wei T, Jin C Q, Zhong W, et al. High permittivity polymer embedded with Co/ZnO core/shell nanoparticles modified by organophosphorus acid. *Applied Physics Letters*, 2007, 91, 222907.
[171] Dang Z M, Wu J P, Xu H P et al. Dielectric properties of upright carbon fiber filled poly(vinylidene fluoride) composite with low percolation threshold and weak temperature dependence. *Applied Physics Letters*, 2007, 91, 072912.
[172] Chen Q, Du P, Jin L, et al. Percolative conductor/polymer composite films with significant dielectric properties. *Applied Physics Letters*, 2007, 91, 022912.
[173] Panda M, Srinivas V, Thakur A K. On the question of percolation threshold in

polyvinylidene fluoride/nanocrystalline nickel composites. *Applied Physics Letters*, 2008, 92(13): 132905.
[174] Li Y J, Xu M, Feng J Q, et al. Dielectric behavior of a metal-polymer composite with low percolation threshold. *Applied Physics Letters*, 2006, 89(7): 072902.
[175] Shen Y, Yue Z, Li M, et al. Enhanced Initial Permeability and Dielectric Constant in a DoublePercolating $Ni_{0.3}Zn_{0.7}Fe_{1.95}O_4$–Ni–Polymer Composite. *Advanced Functional Materials*, 2005, 15(7): 1100-1103.
[176] Wang Q, Zhu L. Polymer nanocomposites for electrical energy storage. *Journal of Polymer Science Part B: Polymer Physics*, 2011, 49(20): 1421-1429.
[177] Dang Z M, Lin Y H, Nan C W. Novel ferroelectric polymer composites with high dielectric constants. *Advanced Materials*, 2003, 15(19): 1625-1629.
[178] Nalwa H S, Ed.; *Handbook of Low and High Dielectric Constant Materials and Their Applications*; Academic Press: London, 1999.
[179] Zhang Q M, Li H, Poh M, et al. An all-organic composite actuator material with a high dielectric constant. *Nature*, 2002, 419(6904): 284-287.
[180] Yin X, Capsal J F, Guyomar D. A comprehensive investigation of poly(vinylidene fluoride-trifluoroethylene-chlorofluoroethylene) terpolymer nanocomposites with carbon black for electrostrictive applications. *Applied Physics Letters*, 2014, 104(5): 052913.
[181] Zhang S, Zhang N, Huang C, et al. Microstructure and electromechanical properties of carbon nanotube/poly(vinylidene fluoride-trifluoroethylene-chlorofluoroethylene) composites. *Advanced Materials*, 2005, 17(15): 1897-1901.
[182] Lonjon A, Laffont L, Demont P, et al. New highly conductive nickel nanowire-filled P (VDF-TrFE) copolymer nanocomposites: elaboration and structural study. The *Journal of Physical Chemistry C*, 2009, 113(28): 12002-12006.
[183] Nguyen T H L, Laffont L, Capsal J F, et al. Magnetoelectric properties of nickel nanowires-P(VDF-TrFE) composites. *Materials Chemistry and Physics*, 2015, 153: 195-201.
[184] da Silva A B, Arjmand M, Sundararaj U, et al. Novel composites of copper nanowire/PVDF with superior dielectric properties. *Polymer*, 2014, 55(1): 226-234.
[185] Kuilla T, Bhadra S, Yao D, et al. Recent advances in graphene based polymer composites. *Progress in Polymer Science*, 2010, 35(11): 1350-1375.
[186] Kim H, Abdala A A, Macosko C W. Graphene/polymer nanocomposites. *Macromolecules*, 2010, 43(16): 6515-6530.
[187] Ansari S, Giannelis E P. Functionalized graphene sheet—Poly(vinylidene fluoride) conductive nanocomposites. *Journal of Polymer Science Part B: Polymer Physics*, 2009, 47(9): 888-897.
[188] He F, Lau S, Chan H L, et al. High dielectric permittivity and low percolation threshold in nanocomposites based on poly(vinylidene fluoride) and exfoliated graphite nanoplates. *Advanced Materials*, 2009, 21(6): 710-715.
[189] Neto A H C, Guinea F, Peres N M R, et al. The electronic properties of graphene. *Reviews of Modern Physics*, 2009, 81(1): 109-162.
[190] Neto A C, Guinea F, Peres N M. Drawing conclusions from graphene. *Physics*

World, 2006, 19(11): 33-37.
[191] Wallace P R. The band theory of graphite. *Physical Review*, 1947, 71(9): 622-634.
[192] Novoselov K S, Geim A K, Morozov S V, et al. Electric field effect in atomically thin carbon films. *Science*, 2004, 306(5696): 666-669.
[193] Statistical physics. Part I. 3rd ed. Oxford, England: Pergamon Press; 1980.
[194] Mermin N D. Crystalline order in two dimensions. *Physical Review*, 1968, 176(1): 250-254.
[195] Geim A K, Novoselov K S. The rise of graphene. *Nature Materials*, 2007, 6(3): 183-191.
[196] Sun Z, James D K, Tour J M. Graphene chemistry: synthesis and manipulation. *The Journal of Physical Chemistry Letters*, 2011, 2(19): 2425-2432.
[197] Allen M J, Tung V C, Kaner R B. Honeycomb carbon: a review of graphene. *Chemical Reviews*, 2009, 110(1): 132-145.
[198] Miranda R, de Parga A L V. Graphene: Surfing ripples towards new devices. *Nature Nanotechnology*, 2009, 4(9): 549-550.
[199] Li D, Mueller M B, Gilje S, et al. Processable aqueous dispersions of graphene nanosheets. *Nature Nanotechnology*, 2008, 3(2): 101-105.
[200] Eizenberg M, Blakely J M. Carbon monolayer phase condensation on Ni(111). *Surface Science*, 1979, 82(1): 228-236.
[201] Lu X, Yu M, Huang H, et al. Tailoring graphite with the goal of achieving single sheets. *Nanotechnology*, 1999, 10(3): 269-272.
[202] Berger C, Song Z, Li X, et al. Electronic confinement and coherence in patterned epitaxial graphene. *Science*, 2006, 312(5777): 1191-1196.
[203] Speyer L, Fontana S, Cahen S, et al. Multi-scale characterization of graphenic materials synthesized by a solvothermal-based process: Influence of the thermal treatment. *Solid State Sciences*, 2015, 50: 42-51.
[204] Sasikala S P, Henry L, Yesilbag Tonga G, et al. High Yield Synthesis of Aspect Ratio Controlled Graphenic Materials from Anthracite Coal in Supercritical Fluids. *ACS Nano*, 2016, 10, 5293-5303.
[205] Hummers Jr W S, Offeman R E. Preparation of graphitic oxide. *Journal of the American Chemical Society*, 1958, 80(6): 1339-1339.
[206] Li D, Mueller M B, Gilje S, et al. Processable aqueous dispersions of graphene nanosheets. *Nature Nanotechnology*, 2008, 3(2): 101-105.
[207] Stankovich S, Dikin D A, Piner R D, et al. Synthesis of graphene-based nanosheets via chemical reduction of exfoliated graphite oxide. *Carbon*, 2007, 45(7): 1558-1565.
[208] Gao W, Alemany L B, Ci L, et al. New insights into the structure and reduction of graphite oxide. *Nature Chemistry*, 2009, 1(5): 403-408.
[209] Geng Y, Wang S J, Kim J K. Preparation of graphite nanoplatelets and graphene sheets. *Journal of Colloid and Interface Science*, 2009, 336(2): 592-598.
[210] Pradhan S K, Nayak B B, Sahay S S, et al. Mechanical properties of graphite flakes and spherulites measured by nanoindentation. *Carbon*, 2009, 47(9): 2290-2299.

[211] Worsley K A, Ramesh P, Mandal S K, et al. Soluble graphene derived from graphite fluoride. *Chemical Physics Letters*, 2007, 445(1): 51-56.
[212] Niyogi S, Bekyarova E, Itkis M E, et al. Solution properties of graphite and graphene. *Journal of the American Chemical Society*, 2006, 128(24): 7720-7721.
[213] Gao X, Jang J, Nagase S. Hydrazine and thermal reduction of graphene oxide: reaction mechanisms, product structures, and reaction design. *The Journal of Physical Chemistry C*, 2009, 114(2): 832-842.
[214] Park S, An J, Piner R D, et al. Aqueous suspension and characterization of chemically modified graphene sheets. *Chemistry of Materials*, 2008, 20(21): 6592-6594.
[215] Bai H, Xu Y, Zhao L, et al. Non-covalent functionalization of graphene sheets by sulfonated polyaniline. *Chem. Commun.*, 2009 (13): 1667-1669.
[216] Salavagione H J, Gomez M A, Martínez G. Polymeric modification of graphene through esterification of graphite oxide and poly(vinyl alcohol). *Macromolecules*, 2009, 42(17): 6331-6334.
[217] Stankovich S, Piner R D, Chen X, et al. Stable aqueous dispersions of graphitic nanoplatelets via the reduction of exfoliated graphite oxide in the presence of poly (sodium 4-styrenesulfonate). *Journal of Materials Chemistry*, 2006, 16(2): 155-158.
[218] Bourlinos A B, Gournis D, Petridis D, et al. Graphite oxide: chemical reduction to graphite and surface modification with primary aliphatic amines and amino acids. *Langmuir*, 2003, 19(15): 6050-6055.
[219] Lomeda J R, Doyle C D, Kosynkin D V, et al. Diazonium functionalization of surfactant-wrapped chemically converted graphene sheets. *Journal of the American Chemical Society*, 2008, 130(48): 16201-16206.
[220] Liu N, Luo F, Wu H, et al. Onestep ionic liquid assisted electrochemical synthesis of ionic liquid functionalized graphene sheets directly from graphite. *Advanced Functional Materials*, 2008, 18(10): 1518-1525.
[221] Liu J, Yang W, Tao L, et al. Thermosensitive graphene nanocomposites formed using pyrene‐terminal polymers made by RAFT polymerization. *Journal of Polymer Science Part A: Polymer Chemistry*, 2010, 48(2): 425-433.
[222] Yang J, Feng C, Dai J, et al. Compatibilization of immiscible nylon 6/poly (vinylidene fluoride) blends using graphene oxides. *Polymer International*, 2013, 62(7): 1085-1093.
[223] Chu L, Xue Q, Sun J, et al. Porous graphene sandwich/poly (vinylidene fluoride) composites with high dielectric properties. *Composites Science and Technology*, 2013, 86: 70-75.
[224] Tong W, Zhang Y, Yu L, et al. Novel Method for the Fabrication of Flexible Film with Oriented Arrays of Graphene in Poly(vinylidene fluoride-co-hexafluoropropylene) with Low Dielectric Loss. *The Journal of Physical Chemistry C*, 2014, 118(20): 10567-10573.
[225] Zhang L, Zha D, Du T, et al. Formation of superhydrophobic microspheres of poly(vinylidene fluoride–hexafluoropropylene)/graphene composite via gelation. *Langmuir*, 2011, 27(14): 8943-8949.

[226] Almadhoun M N, Hedhili M N, Odeh I N, et al. Influence of stacking morphology and edge nitrogen doping on the dielectric performance of graphene–polymer nanocomposites. *Chemistry of Materials*, 2014, 26(9): 2856-2861.
[227] Rahman M A, Chung G S. Synthesis of PVDF-graphene nanocomposites and their properties. *Journal of Alloys and Compounds*, 2013, 581: 724-730.
[228] Cui L, Lu X, Chao D, et al. Graphene−based composite materials with high dielectric permittivity via an in situ reduction method. *Physica Status Solidi (a)*, 2011, 208(2): 459-461.
[229] Xue J M, Wu L K, Hu N, et al. Evaluation of piezoelectric property of reduced graphene oxide (rGO)–poly(vinylidene fluoride) nanocomposites. *Nanoscale*, 2012, 4(22): 7250-7255.
[230] Ji T, Sun M, Zou L, et al. Fabrication of graphene oxide-filled poly(vinylidene fluoride) microfiltration tubes and the applications in a separation of citral solution and a removal of Cu^{2+} ions. *Materials Letters*, 2014, 120: 30-32.
[231] Jiang Z Y, Zheng G P, Han Z, et al. Enhanced ferroelectric and pyroelectric properties of poly(vinylidene fluoride) with addition of graphene oxides. *Journal of Applied Physics*, 2014, 115(20): 204101.
[232] Yu J, Jiang P, Wu C, et al. Graphene nanocomposites based on poly(vinylidene fluoride): structure and properties. *Polymer Composites*, 2011, 32(10): 1483-1491.
[233] Jang J W, Min B G, Yeum J H, et al. Structures and physical properties of graphene/PVDF nanocomposite films prepared by solution-mixing and melt-compression. *Fibers and Polymers*, 2013, 14(8): 1332-1338.
[234] Tang H, Ehlert G J, Lin Y, et al. Highly efficient synthesis of graphene nanocomposites. *Nano Letters*, 2011, 12(1): 84-90.
[235] Ansari S, Giannelis E P. Functionalized graphene sheet-poly(vinylidene fluoride) conductive nanocomposites. *Journal of Polymer Science Part B: Polymer Physics*, 2009, 47(9): 888-897.
[236] Lee Y L, Kim S, Park C, et al. Controlling half-metallicity of graphene nanoribbons by using a ferroelectric polymer. *ACS Nano*, 2010, 4(3): 1345-1350.
[237] El Achaby M, Arrakhiz F Z, Vaudreuil S, et al. Preparation and characterization of melt-blended graphene nanosheets–poly(vinylidene fluoride) nanocomposites with enhanced properties. *Journal of Applied Polymer Science*, 2013, 127(6): 4697-4707.
[238] Cao J, Wang Y, Ke K, et al. Crystallization, rheological behavior and mechanical properties of poly(vinylidene fluoride) composites containing graphitic fillers: a comparative study. *Polymer International*, 2012, 61(6): 1031-1040.
[239] Zhang Y Y, Jiang S L, Yu Y, et al. Crystallization behavior and phasetransformation mechanism with the use of graphite nanosheets in poly(vinylidene fluoride) nanocomposites. *Journal of Applied Polymer Science*, 2012, 125, E314-E319.
[240] Li M, Gao C, Hu H, et al. Electrical conductivity of thermally reduced graphene oxide/polymer composites with a segregated structure. *Carbon*, 2013, 65: 371-373.
[241] Han P, Fan J, Zhu L, et al. Structure, Thermal Stability and Electrical Properties of Reduced Graphene/Poly(vinylidene fluoride) Nanocomposite Films. *Journal of*

nanoscience and nanotechnology, 2012, 12(9): 7290-7295.
[242] Fan P, Wang L, Yang J, et al. Graphene/poly(vinylidene fluoride) composites with high dielectric constant and low percolation threshold. *Nanotechnology*, 2012, 23(36): 365702.
[243] Wang D, Bao Y, Zha J W, et al. Improved dielectric properties of nanocomposites based on poly(vinylidene fluoride) and poly(vinyl alcohol)-functionalized graphene. *ACS Applied Materials & Interfaces*, 2012, 4(11): 6273-6279.
[244] Han K, Li Q, Chen Z, et al. Suppression of energy dissipation and enhancement of breakdown strength in ferroelectric polymer–graphene percolative composites. *Journal of Materials Chemistry C*, 2013, 1(42): 7034-7042.
[245] Wang J, Wu J, Xu W, et al. Preparation of poly(vinylidene fluoride) films with excellent electric property, improved dielectric property and dominant polar crystalline forms by adding a quaternary phosphorus salt functionalized graphene. *Composites Science and Technology*, 2014, 91: 1-7.
[246] Li Y, Xu J Z, Zhu L, et al. Role of ion–dipole interactions in nucleation of gamma poly(vinylidene fluoride) in the presence of graphene oxide during melt crystallization. *The Journal of Physical Chemistry B*, 2012, 116(51): 14951-14960.
[247] Wang D, Zhou T, Zha J W, et al. Functionalized graphene–$BaTiO_3$/ferroelectric polymer nanodielectric composites with high permittivity, low dielectric loss, and low percolation threshold. *Journal of Materials Chemistry A*, 2013, 1(20): 6162-6168.
[248] He F A, Fan J T, Song F, et al. Fabrication of hybrids based on graphene and metal nanoparticles by in situ and self-assembled methods. *Nanoscale*, 2011, 3(3): 1182-1188.
[249] Zhang B, Ning W, Zhang J, et al. Stable dispersions of reduced graphene oxide in ionic liquids. *J. Mater. Chem.*, 2010, 20(26): 5401-5403.
[250] Mohamadi S, Sharifi‐Sanjani N. Investigation of the crystalline structure of PVDF in PVDF/PMMA/graphene polymer blend nanocomposites. *Polymer Composites*, 2011, 32(9): 1451-1460.
[251] Thangavel E, Ramasundaram S, Pitchaimuthu S, et al. Structural and tribological characteristics of poly(vinylidene fluoride)/functionalized graphene oxide nanocomposite thin films. *Composites Science and Technology*, 2014, 90: 187-192.
[252] Becerril H A, Mao J, Liu Z, et al. Evaluation of solution-processed reduced graphene oxide films as transparent conductors. *ACS Nano*, 2008, 2(3): 463-470.
[253] Dikin D A, Stankovich S, Zimney E J, et al. Preparation and characterization of graphene oxide paper. *Nature*, 2007, 448(7152): 457-460.
[254] Vickery J L, Patil A J, Mann S. Fabrication of Graphene Polymer Nanocomposites with HigherOrder Three Dimensional Architectures. *Advanced Materials*, 2009, 21(21): 2180-2184.
[255] McAllister M J, Li J L, Adamson D H, et al. Single sheet functionalized graphene by oxidation and thermal expansion of graphite. *Chemistry of Materials*, 2007, 19(18): 4396-4404.
[256] Bourlinos A B, Gournis D, Petridis D, et al. Graphite oxide: chemical reduction

to graphite and surface modification with primary aliphatic amines and amino acids. *Langmuir*, 2003, 19(15): 6050-6055.
[257] Stankovich S, Dikin D A, Piner R D, et al. Synthesis of graphene-based nanosheets via chemical reduction of exfoliated graphite oxide. *Carbon*, 2007, 45(7): 1558-1565.
[258] Nethravathi C, Rajamathi J T, Ravishankar N, et al. Graphite oxide-intercalated anionic clay and its decomposition to graphene-inorganic material nanocomposites. *Langmuir*, 2008, 24(15): 8240-8244.
[259] Szabó T, Szeri A, Dékány I. Composite graphitic nanolayers prepared by self-assembly between finely dispersed graphite oxide and a cationic polymer. *Carbon*, 2005, 43(1): 87-94.
[260] Ye L, Meng X Y, Ji X, et al. Synthesis and characterization of expandable graphite–poly(methyl methacrylate) composite particles and their application to flame retardation of rigid polyurethane foams. *Polymer Degradation and Stability*, 2009, 94(6): 971-979.
[261] Zheng W, Lu X, Wong S C. Electrical and mechanical properties of expanded graphitereinforced highdensity polyethylene. *Journal of Applied Polymer Science*, 2004, 91(5): 2781-2788.
[262] Liang J, Wang Y, Huang Y, et al. Electromagnetic interference shielding of graphene/epoxy composites. *Carbon*, 2009, 47(3): 922-925.
[263] Chen G, Wu D, Weng W, et al. Exfoliation of graphite flake and its nanocomposites. *Carbon*, 2003, 41(3): 619-621.
[264] Stankovich S, Dikin D A, Dommett G H B, et al. Graphene-based composite materials. *Nature*, 2006, 442(7100): 282-286.
[265] Kalaitzidou K, Fukushima H, Drzal L T. A new compounding method for exfoliated graphite–polypropylene nanocomposites with enhanced flexural properties and lower percolation threshold. *Composites Science and Technology*, 2007, 67(10): 2045-2051.
[266] Wang W P, Pan C Y. Preparation and characterization of polystyrene/graphite composite prepared by cationic grafting polymerization. *Polymer*, 2004, 45(12): 3987-3995.
[267] Braunecker W A, Matyjaszewski K. Controlled/living radical polymerization: features, developments, and perspectives. *Progress in Polymer Science*, 2007, 32(1): 93-146.
[268] Gonçalves G, Marques P A A P, Barros-Timmons A, et al. Graphene oxide modified with PMMA via ATRP as a reinforcement filler. *Journal of Materials Chemistry*, 2010, 20(44): 9927-9934.
[269] Layek R K, Samanta S, Chatterjee D P, et al. Physical and mechanical properties of poly(methyl methacrylate)-functionalized graphene/poly(vinylidine fluoride) nanocomposites: Piezoelectric β polymorph formation. *Polymer*, 2010, 51(24): 5846-5856.
[270] Mijovic J, Sy J W, Kwei T K. Reorientational dynamics of dipoles in poly(vinylidene fluoride)/poly(methyl methacrylate) (PVDF/PMMA) blends by

dielectric spectroscopy. *Macromolecules*, 1997, 30(10): 3042-3050.
[271] Sy J W, Mijovic J. Reorientational dynamics of poly(vinylidene fluoride)/ poly(methyl methacrylate) blends by broad-band dielectric relaxation spectroscopy. *Macromolecules*, 2000, 33(3): 933-946.
[272] Maity N, Mandal A, Nandi A K. Interface engineering of ionic liquid integrated graphene in poly(vinylidene fluoride) matrix yielding magnificent improvement in mechanical, electrical and dielectric properties. *Polymer*, 2015, 65: 154-167.

Chapter 2
Effect of Ionic Liquids as Nanostructuration Agents on P(VDF-CTFE) Matrix

Chapter 2: Effect of Ionic Liquids as Nanostructuration Agents on P(VDF-CTFE) Matrix

2.1 Understanding of versatile and tunable nanostructuration of ionic liquids on fluorinated copolymer P(VDF-CTFE)

2.1.1 Introduction

In the development of advanced polymer materials with significantly unprecedented and improved physico-chemical properties, the concept of "functionalization *via* structural design" is a critical guideline to tailor the matter structuration at nanoscale [1]. Since the first use of a small amount of ionic liquids (ILs) in polytetrafluoroethylene (PTFE) matrix to achieve a tunable nanostructuration on the morphologies and mechanical properties was innovatively discovered in our group [2,3], increasing interest has been developed to prepare functional polymer materials with tailored nanostructures by the aid of ILs as nanostructuration agents. The attractiveness of ILs arises from their simple synthetic route and low-content requirement over the mostly used amphiphilic block copolymers [4,5,6,7], silica [8], layered silicates [9,10], carbon nanotubes (CNTs) [11,12], *etc*. For example, imidazolium [13,14] and phosphonium [14,15,16,17,18] ILs were used as functional additives to achieve diglycidylether of bisphenol A (DGEBA)-based epoxy networked polymeric materials which display a structuration at nanoscale with dramatic mechanical properties. More recently, phosphonium ILs were used as nanostructuration agents to develop a biopolymer matrix poly(butylene adipate-*co*-terephthalate (PBAT) with significantly improved water vapor permeability and mechanical properties [19]. Therefore, a virgin application of ILs as efficient nanostructuration agents has been exploited to achieve nanostructured polymeric materials with tunable properties, more frequently used as "green" solvents for organic synthesis, catalysis, fuel cells, electrochemistry, *etc* [20].

In terms of one of the most important electroactive fluoropolymers, poly(vinylidene fluoride) (PVDF) and its co(ter)polymers have earned a large range of applications due to pyro-/ferro-/piezo properties [21]. Among the most frequent α, β and γ crystalline phases, polar β- and γ-ones present superior electrical properties than nonpolar α-one due to the relative large spontaneous polarization per unit cell.The electroactive performance of PVDF-based materials is found to be tightly associated with the nanostructure, thus the tunable nanostructuration on PVDF-based matrices is a key issue for versatile applications. Recently, few works report the effect of imidazolium ILs on the structures and properties of PVDF matrix. As been reviewed in *Chapter 1* detailedly, Wang *et al*. [22] prepared β-phase-dominant PVDF/IL (1-ethyl-3-methylimidazolium nitrate) thin films spin-coated from a solution. IL promotes the formation of ferroelectric β-phase and much smaller crystalline regions. The ferroelectric properties show a remanent polarization of 60 mC/m^2 and a quasi-static pyroelectric coefficient of 19 $\mu C/m^2K$ at 30 ^oC. Xing *et al.* [23] systematically investigated the crystalline structures, miscibility and physical properties of PVDF/IL (1-butyl-3-methylimidazolium hexafluorophosphate) blend films. It was found that the IL displays drastic effects on both structure and properties of PVDF, generating a multifunctional film. Moreover, by the aid of electrospinning technique, the resulting nanofibers of PVDF/IL blends exhibiting extremely high β-phase content were obtained [24]. The synergistic effect of ILs combined with CNTs influencing the structure of PVDF crystalline regions has also been illustrated [25,26]. The resulting materials exhibit improved mechanical and electronic conductivity properties due to the anchored ILs on the surface of CNTs. The latest case is that PVDF nanoparticles with α-phase were partly transformed into β-one by adding imidazolium nitrate IL and subsequent thermal annealing below the melting temperature [27]. Although the influence of IL on the structure of PVDF (mainly focusing on the formation of polar crystalline phase) has been observed above, the mechanism for the structuration is quite elusive. From current understanding, dipolar interactions between PVDF chain-molecules and ILs contribute the formation of polar crystalline phase. Moreover, in order to obtain more β-crystals, the long tangible

template, IL-covalently modified CNTs, was suggested to be the second factor to provide long enough sequences and stabilize the high-energy of all-*trans* conformation of PVDF. In essence, understanding of the fundamental mechanism of the versatile nanostructuration of ILs on semi-crystalline PVDF-based polymer is still superficial, such as *i)* what determines the strength of dipolar interaction, *ii)* how does the dipolar interaction affect the nanostructuration on the matrix, not only the crystalline phase structure but also the dispersion morphology and crystallization behavior, *iii)* what is the relationship between the nanostructuration effect of ILs and their localization in the matrix, and also what governs this localization.

If we consider the advantages of phosphonium ILs over imidazolium and pyridinium counterparts which are widely used in polymer/IL blends, we can say that they *i)* are thermally more stable, which is desirable for polymer processing at temperatures greater than 200-300 ^{o}C; *ii)* have no acidic proton, which avoids the formation of carbene; *iii)* exhibit a higher electrochemical stability, leading them to be used as electrolytes with excellent electrochemical performance [28,29]. In this work, two phosphonium ILs, denoted octadecyltriphenyl-phosphonium iodide (IL-C18) and tributyl(methyl)phosphonium methylsulfate (IL-108) (Scheme 2.1-1), are incorporated in a PVDF copolymer poly(vinylidene fluoride-*co*-chlorotrifluoroethylene) (P(VDF-CTFE)) to prepare two series of blend films with different IL amounts *via* solution casting from methyl ethyl ketone (MEK) solution. The differences in steric hindrance and extra dipolar groups are considered as potential key factors to influence the interaction with P(VDF-CTFE) and the diffusion rate of ILs in polymer matrix during the film formation. The crystalline phase structure, dispersion morphology and crystallization behavior are finely characterized with the goal of providing a full and deep understanding of the versatile and tunable nanostructuration effect of phosphonium ILs. We propose that the essence of structuring mechanism is closely related to the chemical structure of IL. Thus, such a fundamental understanding of the nanostructuration of ILs will help to design and tune this unique class of PVDF-based materials with the help of ILs.

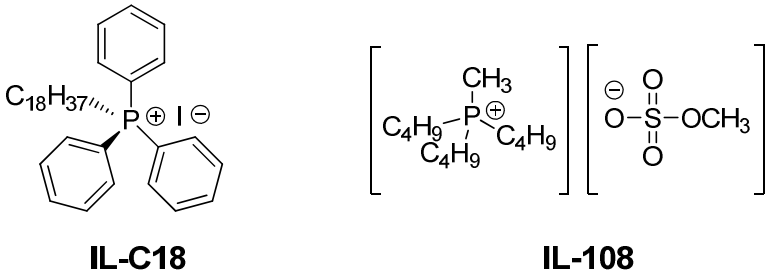

IL-C18 **IL-108**

Scheme 2.1-1: Molecular structures of two phosphonium ILs used in this work

2.1.2 Experimental Section

Materials and blend films preparation

P(VDF-CTFE) copolymer containing 8 wt%%, *i.e.*, 4.6 mol%, of CTFE was purchased from Arkema. IL-108 is commercially available CYPHOS-IL108 from Cytec (USA). The synthesis of IL-C18 was described elsewhere [2]. The solvent methyl ethyl ketone (MEK) (chemically pure) was purchased from CARLO ERBA (France) and used as received.

The solution of P(VDF-CTFE) with a mass concentration of 12% in MEK was first prepared at 60 ^{o}C. Different amounts of ILs (IL-C18 or IL-108) were added into the solution to generate different compositions, *i.e.*, the ratio of IL over P(VDF-CTFE) were 2 wt%, 5 wt% and 10 wt%. After adequately stirring at 60 ^{o}C, the films were solution-casted from the mixture on a stainless steel substrate *via* doctor-blade, followed by drying at 80 ^{o}C in air-circulation oven for three hours to remove any residual solvent,and the solvent of MEK has been thoroughly eliminated by the drying process above, which can be verified by NMR results shown in Figure 2.1-S1 of Annexe.The obtained films (around 15-30 μm) were peeled from the substrate and marked as P(VDF-CTFE)/IL-C18 or P(VDF-CTFE)/IL-108 for different compositions.

Characterizations

The X-ray diffraction (XRD) data was collected using a Bruker D8 Advance X-ray diffractometer. A bent quartz monochromator (before the sample) was used to select the Cu $K_{\alpha 1}$ radiation (λ = 0.15406 nm) and run under operating conditions of 45 mA and 33 kV in a Bragg-Brentano geometry. The angle range scanned is $1^{o} < 2\theta <$

30°at a scanning speed of 2°/min with a step interval of 0.02°.

Fourier transform infrared (FTIR) spectra were recorded at room temperature on a Nicolet iSO10 Thermo Scientific spectrometer. Note that the resulting films under the conditions we used are too thick to obtain perfect absorption peaks in the characteristic range of 1100~1500 cm^{-1} (some flat peaks are visible, data not shown) if only transmission mode is used. Thus, both transmission and attenuated total reflectance (ATR) modes (a diamond crystal was used) were performed to determine each characteristic band. All spectra were recorded at 2 cm^{-1} resolution and 32 scans from 4000 to 400 cm^{-1} for transmission mode and 4000 to 650 cm^{-1} for ATR mode. Although two modes were used, all characteristic absorption peaks are in agreement with each other.

Differential scanning calorimetry (DSC) analyses were conducted on a thermoanalyzer system, model Q20 (TA Co. Ltd, USA) under a nitrogen atmosphere at a rate of 10 °C/min. Four scans (heating/cooling/heating/cooling, separated by a 10 min isotherm) were realized for each sample between -70 °C to 180 °C. All nonisothermal crystallization temperatures (T_c) from the first cooling run and melting temperatures (T_m) from the second heating run reported here correspond to the summit point of each peak. The crystallinity (χ_c) is obtained from the enthalpy change in the second heating run. The values are calculated by considering $\Delta H_{100\%}$ (melting enthalpy for totally crystalline PVDF) to be 104.9 J/g [30].

Transmission electron microscopy (TEM) was performed at the Center of Microstructures (Université de Lyon) using a Philips CM 120 field emission scanning electron microscope with an accelerating voltage of 80 kV. The samples were cut using an ultramicrotome equipped with a diamond knife, to obtain 60 nm thick ultrathin sections. Then, the stained sections by RuO_4 were set on copper grids for observation.

Small angle neutron scattering (SANS) experiments were carried on the small angle spectrometer PAXY spectrometer of Léon Brillouin Laboratory (Saclay, France). Three sample-to-detector distances (SDD) and neutron wavelengths (λ) were

used to cover magnitudes of the scattering vector modulus q from 0.03 to 4.2 nm^{-1} (λ = 1.2 nm, SDD = 6.75 m, λ = 1.2 nm, SDD = 3 m, and λ = 0.5 nm, SDD = 1 m). The resulting level of the scattering intensity at the high q values is of the order of magnitude of the experimental background, notably the incoherent contributions of the polymer phase and ionic liquids are subtracted.

Dynamic mechanical analysis (DMA) was investigated by a Rheometrics Solid Analyzer RSA II at 0.01 wt% tensile strain and a frequency of 10 Hz. The heating rate was 3 K/min for the temperature range from -80 °C to 120 °C under nitrogen atmosphere.

Dielectric analysis (DEA) measurements were carried out using a Novocontrol Alpha-A analyzer (BDS Novocontrol). Samples for DEA tests were cut out from the films as 25×25 mm^2. Gold electrodes of circular size with diameter 10 mm were deposited by sputtering. The applied voltage is 1 V RMS. The temperature of the sample was controlled with a stability of ΔT=0.1 °C (Novocontrol Quatro system controller BDS 1330). Two cycles were carried out for the frequency domain $10^6$to 10^{-1}Hz and for temperature from -80 to 100 °C in a step of 2 °C/min.

Uniaxial tensile tests were carried out using a MTS 2/M electromechanical testing machine at 22±1 °C and 30±5% relative humidity at a crosshead speed of 5 mm/min. The strain was calculated from the crosshead displacement. The tensile tests were performed at least 3 samples. A cookie cutter was used to obtain dumbbell-shaped specimens.

2.1.3 Results and discussion

2.1.3.1 Identification of crystalline phase

The XRD pattern of neat P(VDF-CTFE) in Figure 2.1-1 presented three diffraction peaks at 2θ = 17.9°, 19.9° and 27.2°, which shows remarkable similarities with PVDF corresponding to the α-crystal planes with Miller indices (100), (110) and (021), respectively. The P(VDF-CTFE) copolymers containing small content of CTFE (< 30 mol%) give rise to a monoclinic crystalline structure in which the comonomer

CTFE is not able to accommodate within the VDF unit cell, *i.e.*, not cocrystallizable with VDF units but in the amorphous phase [21]. Concerning the low content of CTFE (8 wt%, *i.e.*, 4.6 mol%) in this work, the crystalline nature of P(VDF-CTFE) copolymer is due to the PVDF-like crystal, exhibiting the same 2θ values as PVDF homopolymer and relatively broad diffraction peaks. The corresponding FTIR spectra in both ATR mode (in the range of 1600 to 650 cm^{-1}) (Figure 2.1-2A) and transmission (in the range of 700 to 400 cm^{-1}) mode (Figure 2.1-2B) also indicate only all characteristic absorption peaks of α-phase at 408, 532, 615, 761, 796, 854, 974 and 1383 cm^{-1} [23,31,32], suggesting that the neat P(VDF-CTFE) exclusively exists in the α-phase which is the most common polymorph produced from the solution casting.

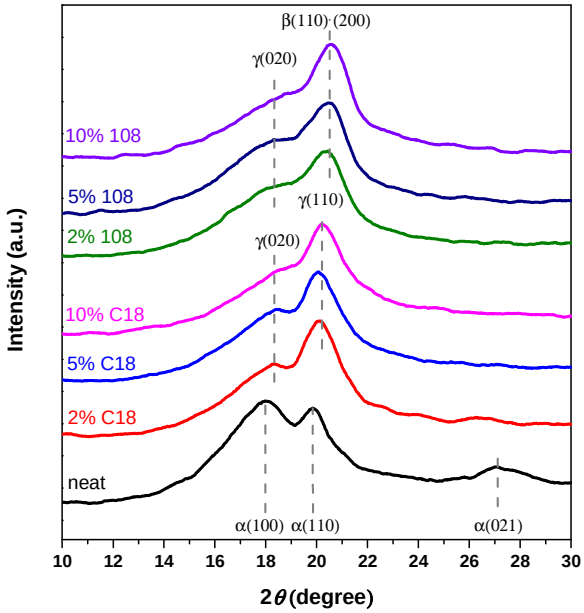

Figure 2.1-1: XRD patterns of neat P(VDF-CTFE) and P(VDF-CTFE)/ILs blends

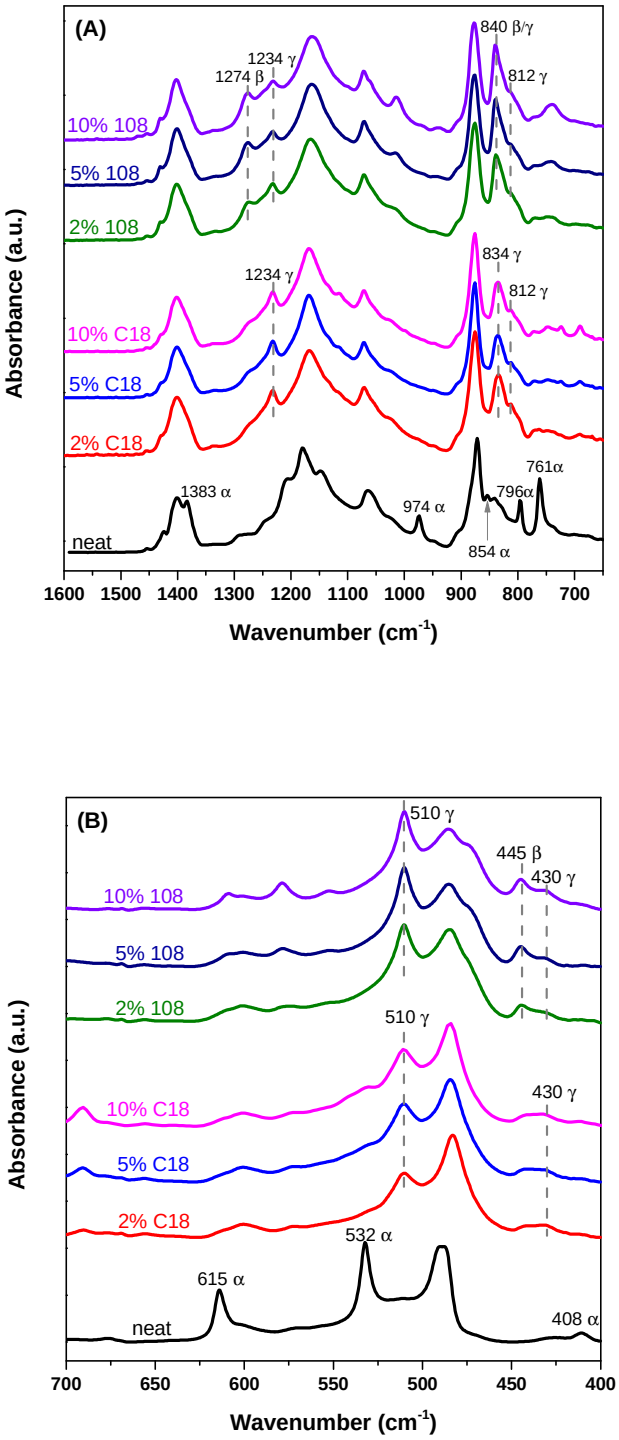

Figure 2.1-2: FTIR spectra of neat P(VDF-CTFE) and P(VDF-CTFE)/ILs blends in ATR mode (A) and transmission mode (B)

As IL-C18 is added in P(VDF-CTFE) with the quantity from 2 wt% to 10 wt%, the characteristic diffraction peaks of α-phase were not traced, but two new peaks are

observed at 2θ =18.5^o and 20.1^o, corresponding to γ(020) and γ(110) crystal planes. The FTIR spectra also show the complete removal of α-phase and the obvious appearance of new bands of γ-phase at 430, 510, 812, 834 and 1234 cm^{-1}, confirming almost entire transformation of α-phase to γ-phase.

With adding IL-108 in P(VDF-CTFE), the diffraction peaks uniquely assigned to α-phase are not observed but only two major peaks at 2θ = 18.5^o and 20.5^o are measured for all blends regardless of the amount of IL, assigned to γ (020) and/or β (110) (200) planes, respectively [33,34].The corresponding FTIR spectra display no characteristic bands of α-phase but γ-phase at 430, 510, 812, 1234 cm^{-1} and new typical bands of β-phase at 445 and 1274 cm^{-1} as well as band at 840 cm^{-1} ascribed to β- or γ-phase [23,31], suggesting that all nonpolar α-phase is converted to a mixture of polar β- and γ-phase. Note that the introduction of the bulky comonomer CTFE, as the crystalline defect into the PVDF backbone, actually imposes a large steric hindrance and makes polymer chains loose, which decreases the energy barrier of phase transformation and thus facilitates the *trans*-conformation of the polymer backbone [35,36]. However, a theoretical work by Ranjan *et al.* [37] indicates that for those P(VDF-CTFE) containing CTFE lower than 17 mol%, the non-polar α-phase is the more thermodynamically stable form (with lower energy) than polar β-phase. With increasing the CTFE content in the copolymer, this difference in the energy between α-phase and β-phase decreases, so the transformation to β-phase becomes progressively easier till a critical value is approached (17 mol%) at which the energy difference decreases down to zero. Above 17 mol% of CTFE in the copolymer, the β-phase is preferred and can be obtained easily. Due to the low content of CTFE in our case, the effect of CTFE on the formation of polar phases is negligible, and that's why only α-phase is obtained in the neat P(VDF-CTFE). Thus, the obvious phase transformation behavior from non-polar α-phase to β- and/or γ-phase is only due to the incorporation of phosphonium ILs.

Combining XRD and FTIR results, it is significant to show that tiny amount of both phosphonium ILs can transform the nonpolar α-phase to polar phases very

efficiently (only 2 wt% of ILs is enough to induce 100% of crystalline phase transformation) and IL-108 can even induce some all-*trans* β-phase with longer TTTT sequence than that γ-phase with shorter TTT sequence. It is therefore an easy and efficient method to prepare polar phase films with large spontaneous polarization profile applying to a wide range of electroactive polymeric materials fields. This use of phosphonium ILs supplies a promising andefficient strategy comparing withmost of recent endeavors such as incorporating pristine CNTs [34], IL-modified CNTs [25,26], poly(methyl methacrylate) (PMMA) functionalized multi-walled carbon nanotubes (MWNT) [38], ester functionalized MWNT [39], organically modified montmorillonite (OMMT) [40] mesoporous SiO_2 nanorods [41], and imidazolium ILs combining electrospinning technique [24] with the aid of electrical poling and uniaxial stretching, *etc.*, avoiding using expensive nanofillers, complicated chemically modification as well as the sophisticated electrospinning instruments.

2.1.3.2 Dispersion morphology: nanostructuration effect

The dispersion of ILs in P(VDF-CTFE) matrix can be well reflected by signals of SANS which are sensitive to the different nuclei density fluctuation among different phases in the semi-crystalline matrix. Figure 2.1-3 shows the SANS profiles focusing on the modest-*q* regime of films with different IL incorporations.

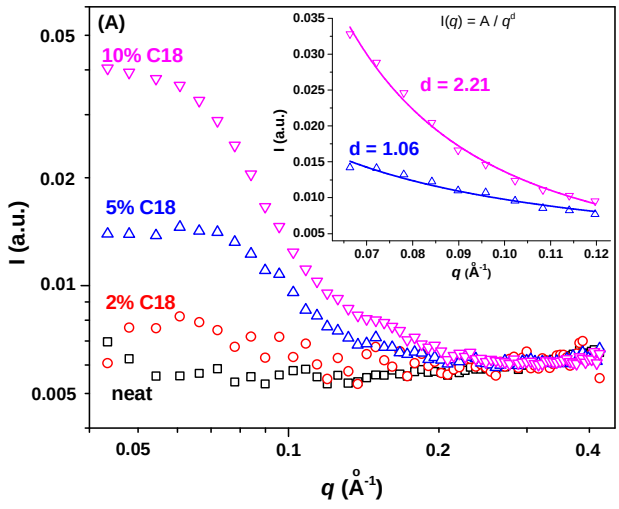

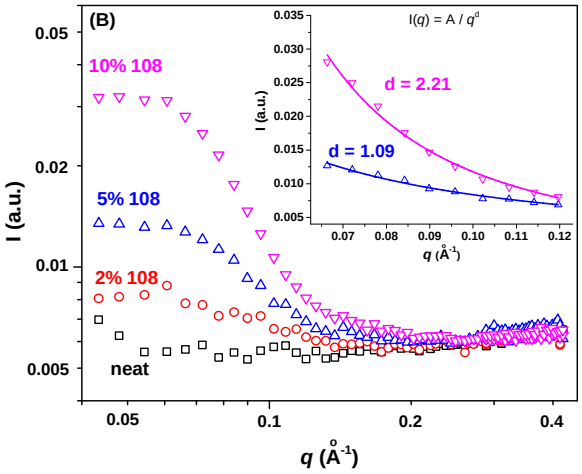

Figure 2.1-3: SANS patterns of neat P(VDF-CTFE) and blends with IL-C18 (A) and IL-108 (B). Insets display the Porod fitting in the modest-*q* range

It is well-known that the crystalline phase has higher nuclei density while the amorphous phase exhibits lower one. The scattering intensity is proportional to the density difference between them. However, very weak and random nuclei density fluctuations exist in neat P(VDF-CTFE) and in those blends containing 2 wt% of ILs, potentially due to,on the one hand,the limited contrast between crystalline and amorphous phase of P(VDF-CTFE) and, on the other hand,that 2 wt% is not sufficient to enhance the contrast, respectively [42]. We thus can consider them as a "homogeneous" system. However, the scattering intensity is subjected to increase when more ILs (from 5 wt% to 10 wt%) are incorporated in P(VDF-CTFE) matrix. We thus can conclude that the nuclei density difference has increased large enough to be seen as a "heterogeneous" system due to the incorporation of phosphonium ILs in matrix. Moreover, these Porod regimes in the range of 0.07 $Å^{-1} < q < 0.12 Å^{-1}$ for blends with 5 wt% and 10 wt% ILs are fitted with $I(q) = A/q^d$, represented by solid lines in the insets of Figure 2.1-3, where d is the Porod exponent yielding information about the so-called "fractal dimension", *i.e.*, estimation of the geometric form of scattering objects [43,44]. For P(VDF-CTFE)/ILs containing 5 wt% of ILs, d values stay around 1 which indicates the formation of 1D rod-like scattering objects, whereas they increase up to around 2 when 10 wt% of ILs are incorporated, reflecting the clearly

detected 2D scattering objects like lamellae. The regular geometric scattering objects as well as the evolution from 1D to 2D profile with increasing IL amount indicates the regular assembly of ILs in semi-crystalline matrix. It has been accepted widely that a semi-crystalline polymer can be considered as a heterogeneous mixture consisting of crystalline phase and amorphous phase. The disordered chains in the amorphous phase present different mobility depending on the location in regard with crystalline phase, *i.e.*, the rigid amorphous fraction (RAF) confined between crystalline lamellae and the mobile amorphous fraction (MAF) with fully "free" disordered chain conformation. RAF is an intermediate nanophase existing at the interface between crystalline phase and MAF as a result of the immobilization of a polymer chain due to the covalently coupling of crystals occurring across the crystalline phase boundaries [45]. First, due to the long-range disordered isotropic nature of MAF, the dispersion of ILs in the MAF cannot induce the observed regular scattering objects. Second, XRD diffractograms show no change of crystalline diffraction peaks with increasing the amount of ILs, indicating no dispersion of ILs in crystalline phase co-crystallized with P(VDF-CTFE). Thus, the most reasonable explanation to the evolution of 1D to 2D scattering objects is the regularly assembled structure of ILs in the RAF of matrix. These detected regularly geometric scattering objects by nuclei density fluctuation are actually seen as the low-dimensional arrangements of ILs assembled in the confined RAF between crystallites. Therefore, the 2D lamellar crystallite of P(VDF-CTFE) permits a so-called "template" confinement effect on the diffusion and dispersion of ILs in the RAF. The localization of ILs in the RAF will be further confirmed in the following microstructural characterization section.

The dispersion morphologies of ILs in the matrix are visually evaluated by TEM in Figure 2.1-4. Two types of phosphonium ILs display different dispersion degrees at nanoscale. P(VDF-CTFE)/IL-108 presents a homogeneous and co-continuous morphology of highly dispersed ILs in matrix without aggregates at nanoscale revealed by RuO_4 marking, which is similar to the neat copolymer. For P(VDF-CTFE)/IL-C18, the image obtained by RuO_4 staining for locating phenyl

groups in IL-C18 obviously shows enriched IL-C18 aggregation displayed by black domains with well-ranged grid-like morphology at relatively larger scale. The origin of different dispersion morphologies is likely due to the interaction between them.

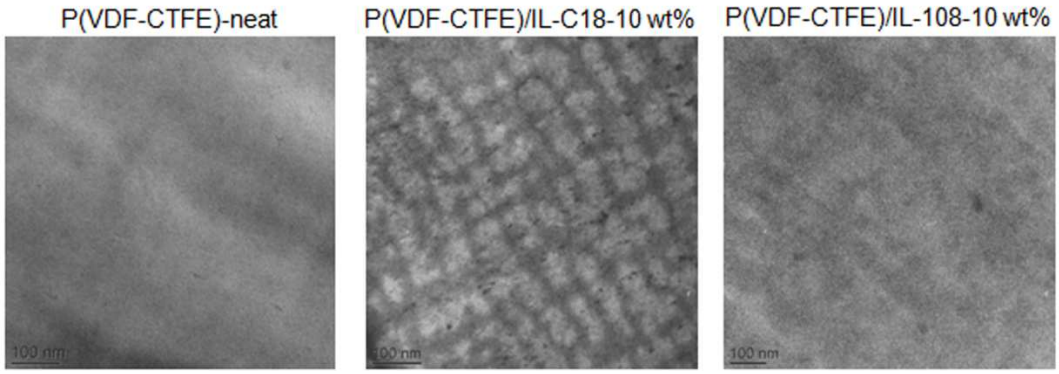

Figure 2.1-4: TEM images of P(VDF-CTFE)-neat and P(VDF-CTFE)/ILs-10 wt% blends

2.1.3.3 Interaction between P(VDF-CTFE) and phosphonium ILs

In view of molecular level, we further investigate the interactions between P(VDF-CTFE) and two types of phosphonium ILs. The dipolar interaction has been identified as Coulomb attraction between dipoles in PVDF and ions in IL [22,23]. Therefore, the driven force governing the nanostructuration effect of ILs on P(VDF-CTFE) matrix is the dipolar interaction between dipoles in P(VDF-CTFE) (C-F and C-Cl) and ions in phosphonium ILs. For both phosphonium ILs, the dipolar interaction can be confirmed by FTIR spectra shown in Figure 2.1-5, and schematically presented in Scheme 2.1-2(a).

The amorphous peak of $-CF_2-CH_2-$ bending vibration in neat copolymer is located at 871 cm^{-1} [23,39], and it is independent on the crystalline phase transformation [46]. This peak shows a blue shift (moving to higher wavenumber) in all blends, and the peak positions for P(VDF-CTFE)/IL-C18-10 wt% and P(VDF-CTFE)/IL-108-10 wt% are at 876 cm^{-1} and 877 cm^{-1}, respectively. The blue shift could be ascribed to a higher energy required for the $-CF_2-CH_2-$ bending vibration because the dipoles in polymer matrix (C-F) are involved in the dipolar interaction with cations of phosphonium ILs. Note that IL-C18 has a bigger volume of phosphonium cation with three rigid phenyls and a long C18 alkyl chain substituent

than that of IL-108, which to some extent hinders the accessibility between dipoles and thus dilute such dipolar interaction.

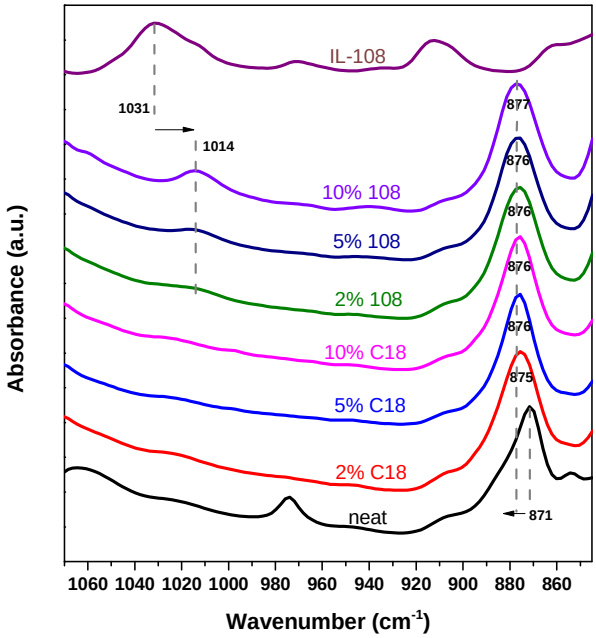

Figure 2.1-5: ATR FTIR spectra of neat P(VDF-CTFE), IL-108 and P(VDF-CTFE)/ILs blends

Moreover, unlike IL-C18, IL-108 has extra S=O dipoles in its anion, inducing the additional dipolar interaction with those dipoles in copolymer matrix. As shown in Figure 2.1-5, IL-108 displays an absorption band at 1031 cm^{-1} attributed to symmetric $–SO_3$ stretching vibrations [47]. It is clear to see a red shift (moving to lower wavenumber) to 1014 cm^{-1} for all blends containing IL-108. This red shift reflects lower vibration energy needed for S=O dipole when it is involved in the dipolar interactions with P(VDF-CTFE) matrix because the electrostatic interaction of $CH_3OSO_3^-$ with phosphonium cation in the IL-108 was to some extent weakened and replaced by the inter-molecular dipolar interaction of the phosphonium cation with P(VDF-CTFE) dipoles with lower energy requirement for bending vibration. This additional dipolar interaction with P(VDF-CTFE) only for IL-108 is presented in Scheme 2.1-2(b).

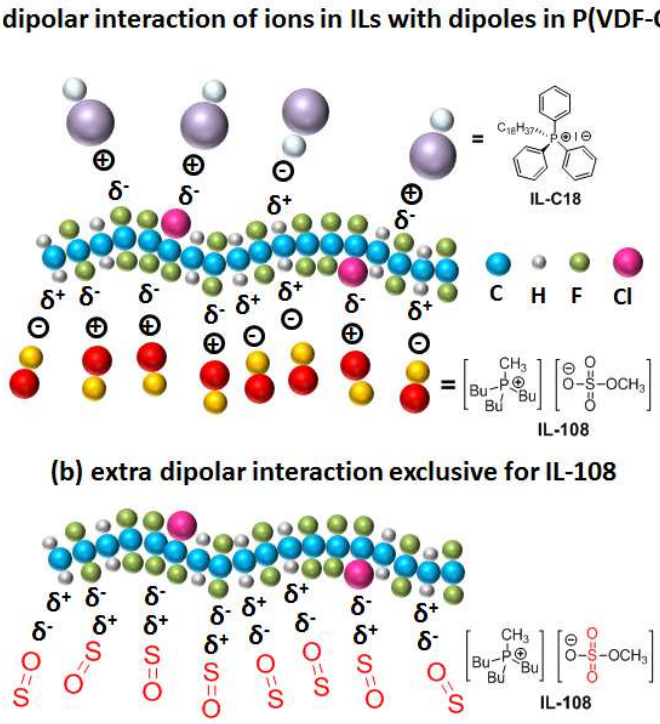

Scheme 2.1-2: Schematic presentation of dipolar interaction between P(VDF-CTFE) and ILs

Thus, in view of the chemical structures of two phosphonium ILs used, we propose that the origin of the difference in the interaction strength between P(VDF-CTFE) and ILs (IL-108 > IL-C18) is two-fold: *i)* accessibility between ions in ILs and dipoles in P(VDF-CTFE); *ii)* existence of more extra dipolar groups in the structure of ILs.

Concerning the different interaction strengths of P(VDF-CTFE) with IL-C18 and IL-108, it thus well explains why IL-108 can even induce some β-phase comparing with IL-C18: the stronger interaction capability of IL-108 with P(VDF-CTFE) can finely stabilize the TTTT conformation requiring higher energy [34], consequently engendering more favorable β-phase. In addition, the stronger interaction also promotes more homogeneously dispersion of IL-108 in the P(VDF-CTFE) matrix without aggregates at nanoscale comparing with that of IL-C18 with larger nano-aggregates shown in TEM images (Figure 2.1-4). Therefore, the strength of affinity between phosphonium ILs and P(VDF-CTFE) matrix due to the chemical nature of ILs determines the resulting crystalline phase structure and dispersion morphology, and should have a significant effect on the crystallization behavior of

semi-crystalline matrix with respect of the polymer high-ordered crystalline structure generated in the growth of crystalline lamellae.

2.1.3.4 Crystallization behavior

T_c, T_m and χ_c of P(VDF-CTFE)/ILs blends as a function of the IL amount are shown in Figure 2.1-6 (all DSC traces are shown in Figure 2.1-S2 of Annexe). Note that the blend film containing 2 wt% of either IL-108 or IL-C18 displays an abrupt enhancement in T_c and T_m compared with those of neat P(VDF-CTFE). The T_c-increment behavior is due to the nucleation effect of ILs to accelerate the crystallization of polar γ- and/or β-phase which exhibit 6-7 °C higher T_m than non-polar α-phase [48,49], subsequently leading to T_m-increment in the second heating run. For a given IL, one can also obviously see the T_c, T_m and χ_c depressions as increasing the amount of ILs in the blends. For a given amount of IL, it is evident to see the different potentials to reduce T_c, T_m and χ_c (IL-108 > IL-C18).

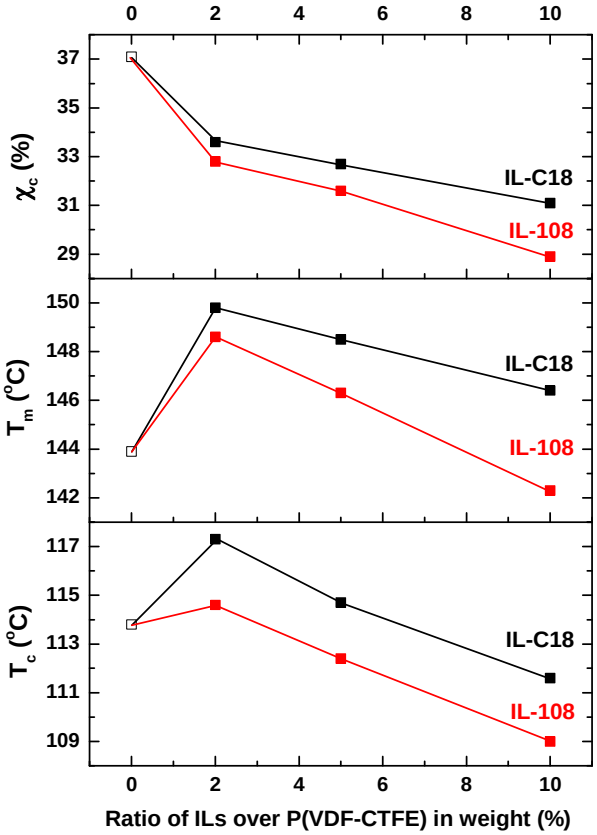

Figure 2.1-6: T_c, T_m and χ_c as a function of ILs amount in P(VDF-CTFE)/ILs blends

The depression effect of phosphonium ILs on crystallization behavior from the solution for preparing blend films can be further explored by the evolution of the size of lamellar crystallites calculated by using Debye-Bueche equation fitting with SANS data [42]:

$$I(q) = \frac{I_0}{(1 + q^2\xi^2)^2}$$

where ξ is the correlation length related to the crystallite size and I_0 is the zero-angle scattering intensity. The low-q regime is best fitted, represented by solid line in Figure 2.1-7, and the calculated values of ξ are compared in Table 2.1-1.

Table 2.1-1. Summary of SANS analyses

Sample	Correlation length (ξ) (Å)	Long period (L_p) (Å)
P(VDF-CTFE)-neat	159.2±15.2	---
P(VDF-CTFE)/IL-C18-5 wt%	133.6±17.0	65.6
P(VDF-CTFE)/IL-C18-10 wt%	130.1±18.4	80.5
P(VDF-CTFE)/IL-108-5 wt%	100.3±13.2	74.6
P(VDF-CTFE)/IL-108-10 wt%	97.5±15.4	87.1

The same depression behavior of crystallite size can be illustrated by the ξ values. For neat P(VDF-CTFE), the ξ value is 159.2 Å, while the incorporation of both phosphonium ILs decreased the ξ value. Moreover, it is striking to see a more dramatic decrease of crystallite size by IL-108 than that by IL-C18 with the same IL amount (*e.g.* ξ = 130.1 Å for 10 wt% of IL-C18 *versus* ξ = 97.5 Å for 10 wt% of IL-108). Accompanying the decrease of lamellar crystallite size, the distance between them (*i.e.*, interlamellar spacing) should also increase, which can be estimated by the average long period (L_p) defined as the center-to-center distance of the lamellar crystallites equaling to sum of the thickness of the lamellar crystallite and the rigid amorphous domain between them [42,50]. The values of L_p (shown in Table 2.1-1) are calculated by using the Bragg's law, $L_p = 2\pi/q_{max}$, where q_{max} is the peak value found in the Lorentz-corrected plot (Iq^2 vs. q) in Figure 2.1-8. However, one cannot observe the L_p peaks for neat copolymer and blends containing 2 wt% of ILs because of the limited contrast as mentioned above. The opposite variations of L_p and ξ values are

observed for all blends with 5 wt% and 10 wt% of ILs: decreasing the crystallites size leads to increasing the distance between them.

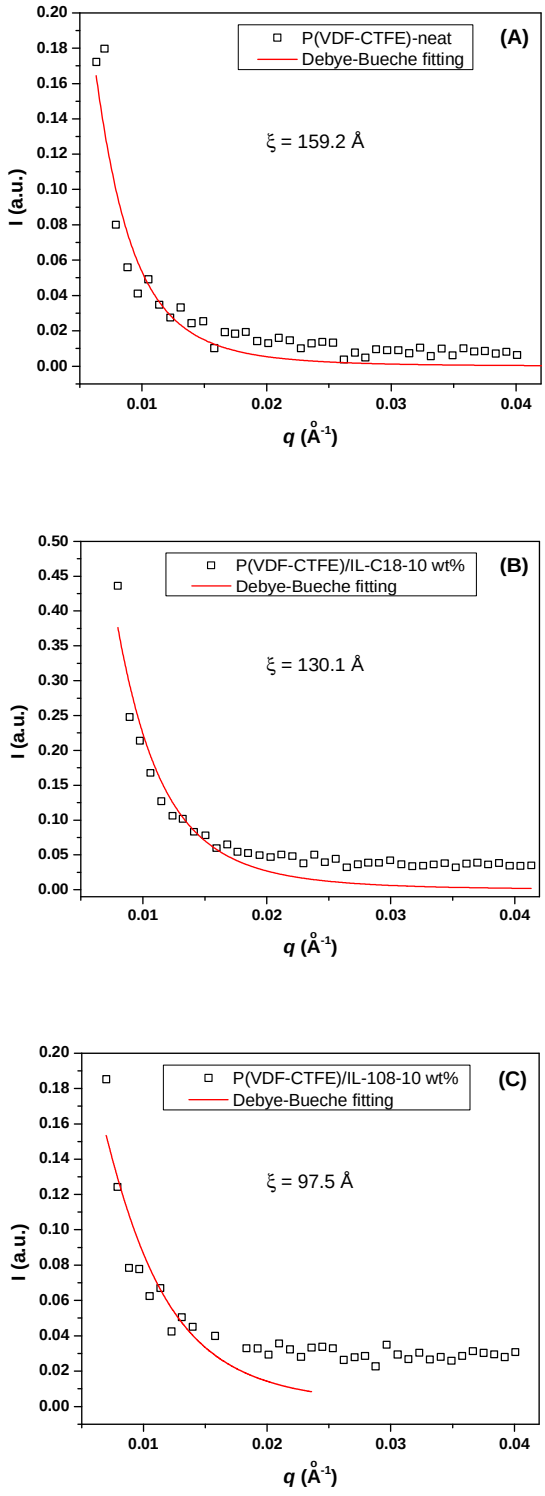

Figure 2.1-7: Debye-Bueche fitting of neat P(VDF-CTFE) (A), blends with 10 wt% of IL-C18 (B) and IL-108 (C)

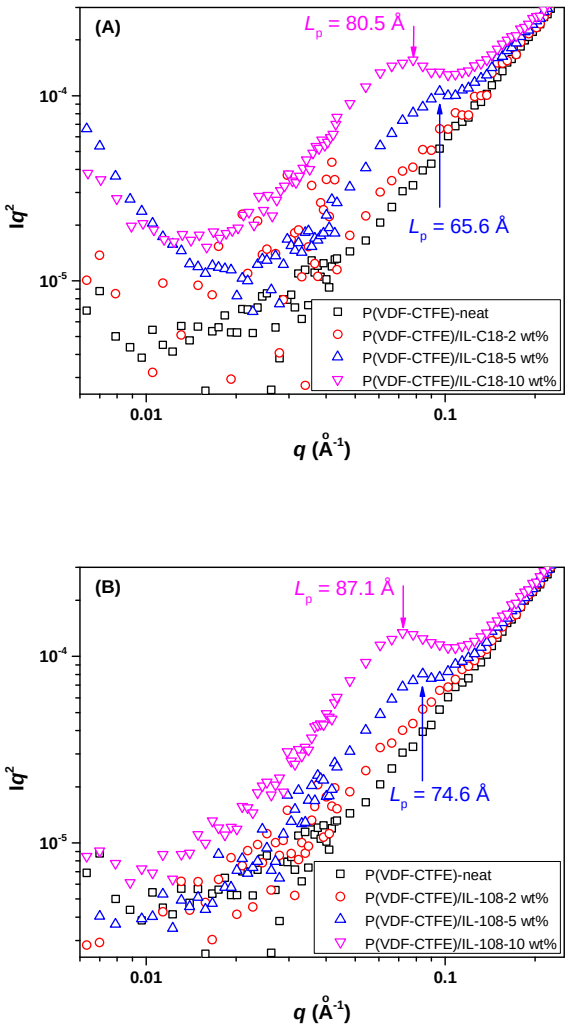

Figure 2.1-8: Lorentz-corrected scattering patterns of neat P(VDF-CTFE) and blends with IL-C18 (A) and IL-108 (B)

It is well-known that the crystallization behavior of the growth of lamellar structure for a semi-crystalline polymer/filler blend is actually reassigning fillers in the matrix and consequently perturbing the dispersion of fillers from either solution or melt. For our P(VDF-CTFE)/ILs blends, this so-called redispersion of phosphonium ILs upon crystallization either from solution (SANS analyses based on as-prepared films) or melt (DSC analyses after the first heating run up to above melting temperature) is necessarily related to two factors: *i)* the diffusion ability of ILs in the matrix; *ii)* the interaction strength between them, which are all governed by the chemical structures of ILs. First, for both phosphonium ILs, we have shown no coexistence of ILs and P(VDF-CTFE) in the crystalline phase, so the most reasonable

explanation to the effect of depressing crystalline phase is that ILs are able to migrate in the RAF confined between lamellar crystallites to affect the chain-folding, which agrees to the Porod fitting results in SANS analyses. Those ILs existing in the RAF definitely act as obstacles for the formation of crystallites and thus reduce the crystal growth rate, exhibiting a lower T_c in the nonisothermal crystallization and then producing a relatively imperfect crystalline phase comparing with neat P(VDF-CTFE) with a lower T_m, reduced χ_c and crystallite size. Second, the affinity of both ILs with P(VDF-CTFE) which has been confirmed above restrains the process of regularly folding chain to form crystalline phase because any chain segment movement to change the configuration is restricted by neighboring ILs due to the interaction between them. In addition, the different degrees of depression on the crystallization behavior of P(VDF-CTFE) matrix by using two types of phosphonium ILs (IL-108 > IL-C18) are thus due to the difference in the ability of diffusion motion of ILs and in the interaction strength when blend films are formed from the solution containing polymer, ILs and solvent. In view of the chemical structure, three benzenic rings and a long C18-alkyl chain of IL-C18 cause bulky spatial distribution and that makes difficulty in diffusion motion in the matrix. Oppositely, IL-108 with smaller volume than IL-C18 diffuses faster to reside in the RAF in greater magnitude, consequently depressing the crystallization much more. Combining to the stronger dipolar interaction of IL-108 with matrix than that of IL-C18 due to the chemical structure, the depression effect on crystallization behavior is thus very dependent on the chemical structures of ILs.

2.1.3.5 Microstructural characterization: localization of ILs

The versatile and tunable nanostructuration effect of phosphonium ILs on crystalline phase structure, dispersion morphology and crystallization behavior of P(VDF-CTFE) matrix has been in-depth investigated. We suggested that the localization of ILs in the RAF between lamellar crystallites contributes the structuring actions, so the further insight into the microstructure to understand the localization of ILs in the matrix is not only a direct proof to interpret the IL structuring mechanism,

but also important to forecast electroactive properties dependent on the tunable microstructures. The dynamics of amorphous segmental relaxation in both non-confined and confined environments are the most effective means to indentify the MAF and RAF of amorphous phase in semi-crystalline polymers such as poly(phenylene sulfide) [51], poly(ether ether ketone) [52], polycarbonate [53], polylactides [54].

Figure 2.1-9 shows the DEA curves for dielectric loss tangent (tan δ) and the imaginary part of dielectric modulus (M") as a function of temperature. In this work, the electric modulus formalism is used to analyze the segemental chain relaxation behavior. It is because that when conductivity dominates the dielectric loss spectra and thus hides the intrinsic relaxation contribution, the dielectric modulus formalism is usually adopted and given as:

$$M^* = 1 / \varepsilon^* = M' + j\,M'' = \varepsilon' / (\varepsilon'^2 + \varepsilon''^2) + j\varepsilon''/ (\varepsilon'^2 + \varepsilon''^2)$$

where M', M", ε' and ε" are the real and imaginary part of the complex dielectric modulus (M*) and complex permittivity (ε*).

In Figure 2.1-9A, a single dissipation peak centered at -28 °C of neat matrix corresponds to T_α associate with the glass transition temperature (T_g) of MAF of P(VDF-CTFE). For a given IL, the T_α (MAF) decreases with the increasing ILs amounts. For a given amount of IL, blends with IL-108 display a lower value of T_α (MAF) than IL-C18 (see Table 2.1-2 for each T_α value).

Table 2.1-2: Temperature values of amorphous relaxation peaks by DEA and DMA

Sample	T_α (MAF)			T_α (RAF)	
	DEA [a] (°C)	DEA [b] (°C)	DMA [c] (°C)	DEA [b] (°C)	DMA [c] (°C)
P(VDF-CTFE)-neat	-28	-31	-45	56	NA
P(VDF-CTFE)/IL-C18-2 wt%	-32	-33	-47	50	NA
P(VDF-CTFE)/IL-C18-5 wt%	---	---	-53	---	21
P(VDF-CTFE)/IL-C18-10 wt%	-44	-44	NA	28	18
P(VDF-CTFE)/IL-108-2 wt%	-36	-35	-47	48	NA
P(VDF-CTFE)/IL-108-5 wt%	---	---	NA	---	12
P(VDF-CTFE)/IL-108-10 wt%	-62	NA	NA	9	6

a: dielectric tan δ *vs.* T (Figure 2.1-9A); b: dielectric M" *vs.* T (Figure 2.1-9B); c: dynamic mechanical tan δ *vs.* T (Figure 2.1-10)

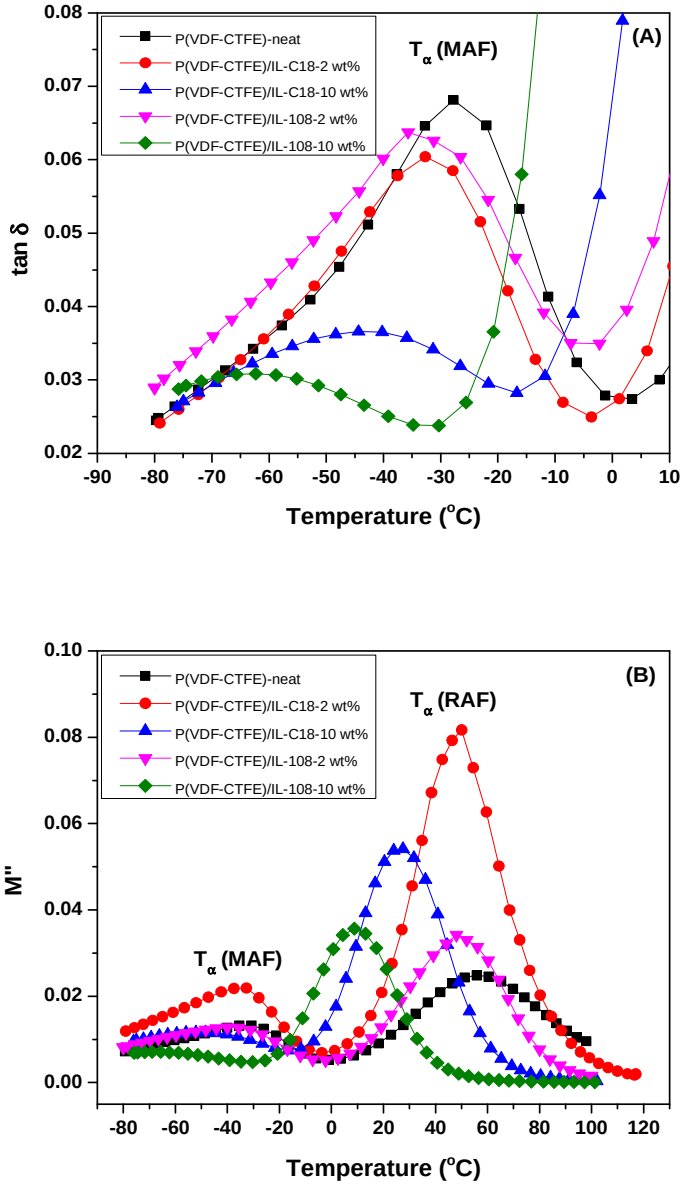

Figure 2.1-9: The dielectric loss tangent (tan δ) (A) and the imaginary part of the dielectric modulus (M") (B) as a function of temperature of neat P(VDF-CTFE) and blends with ILs (*f*= 1 kHz, the second heating run without the thermal history). Note that the peak position from the first heating run is the same as the one from the second heating run

The change of T_α (MAF) verifies the localization of both phosphonium ILs in the MAF through the dipolar interactions with P(VDF-CTFE) chains. On the one hand, the interaction of ILs with polymer chains by incorporating small molecular ILs in the MAF of P(VDF-CTFE) weakens the original inter-chain affinity to enhance the motion freedom with increased free volume. On the other hand, the already confirmed effect of ILs on the depression of crystalline phase gives rise to a lower crystallinity

and smaller crystallite size, and thus makes more amorphous room for the free volume. Combining these two factors, the increment of free volume in the MAF contributes the T_α depression. Moreover, the stronger interaction with matrix and depression behaviors on crystallinity and crystallite size allow IL-108 to induce a lower T_α than IL-C18 with the same IL amounts. The T_α-depression behavior actually indicates the plasticizer effect of ILs on the matrix, which can be further confirmed by the macroscopic mechanical property *via* the strain-stress tests, and the results are summarized in Table 2.1-3.

Table 2.1-3: Data summary of strain-stress tests

Sample	Young's modulus (MPa)	Yield strength (MPa)	Elongation at break (%)
P(VDF-CTFE)-neat	866±1.53	31±7.32	23±0.08
P(VDF-CTFE)/IL-C18-10 wt%	318±20.33	13±0.72	122±0.83
P(VDF-CTFE)/IL-108-10 wt %	276±38.31	15±0.26	838±1.55

Comparing the results of neat P(VDF-CTFE) and blends containing 10 wt% of ILs, it is noticeable that the incorporation of IL reduced the Young's modulus, suppressed the yield strength and improved the elongation at break. It is also significant to find a dramatic enhancement of elongation at break up to 838% for P(VDF-CTFE)/IL-108-10 wt% film, whereas only 122% for P(VDF-CTFE)/IL-C18-10 wt% one. In Figure 2.1-9B, besides the T_α (MAF) relaxation with the same depression behavior, another relaxation peaks centering at relatively high temperature are visible. These relaxations are due to T_α in the RAF confined between crystalline lamellae because a higher temperature is required to acquire sufficient energy to mobilize these so-called constrained chains in the RAF [54,55]. Incorporating both phosphonium ILs also leads to the same T_α (RAF) variations as T_α (MAF) due to the increment of free volume in the RAF (see Table 2.1-2 for each T_α value).

These two relaxations occurring in the MAF and RAF can also be seen in DMA curves in Figure 2.1-10. All temperature values of relaxation peaks are summarized in Table 2.1-2.

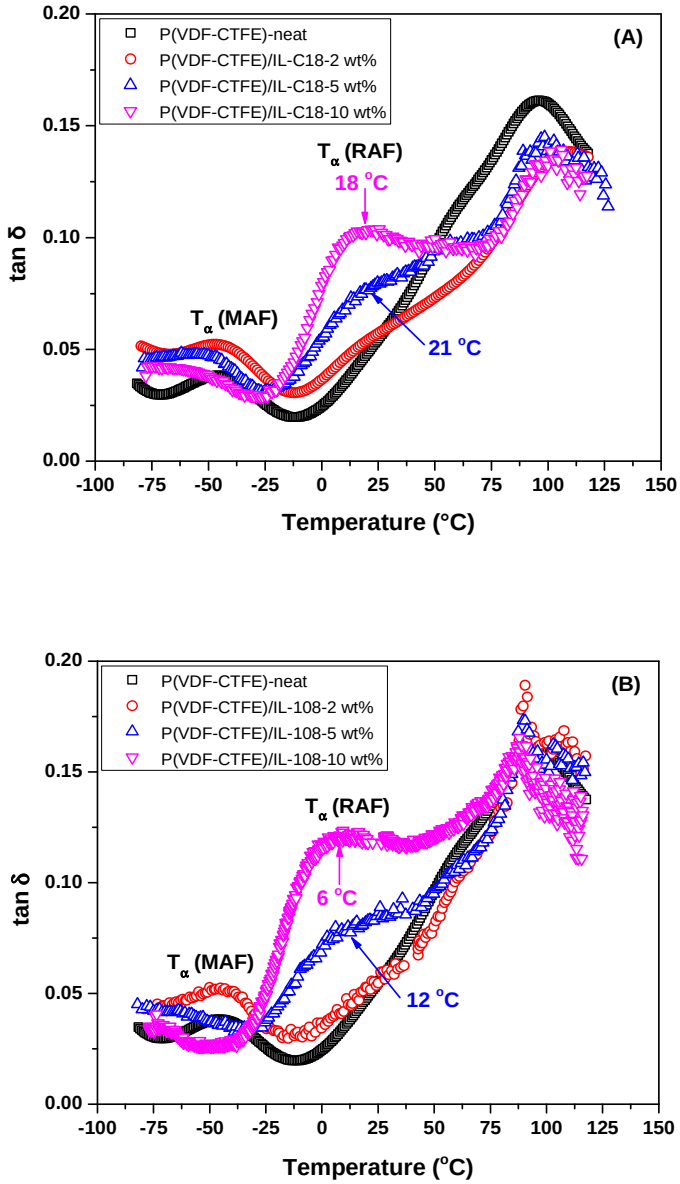

Figure 2.1-10. The dynamic mechanical loss tangent (tan δ) as a function of temperature for neat P(VDF-CTFE) and all blends with IL-C18 (A) and IL-108 (B). Note: the relaxation peaks from 75 to 100 °C is ascribed to imperfections in the crystalline phase [23,56], which can also be verified by the presence in the 1st heating run (Figure 2.1-S2A) and absence in the 2nd heating run (Figure 2.1-S2C) from the DSC thermograms in Annexe

A loss tan δ peak centered at -45 °C for neat matrix is due to the "liquid-like" chain relaxation in the MAF. This T_α (MAF) peak also shows a depression behavior for blends containing either IL-C108 or IL-108. But it is more unclear to see the T_α (MAF) peaks when the amount of ILs in blends increases up to 10 wt% for IL-C18 and 5 wt% for IL-108. It could be ascribed to the more miscible nature of the mixture of ILs and P(VDF-CTFE) chains in the MAF through the strong dipolar interaction

which is more tardy to the dynamic changes of stress. The second T_α (RAF) relaxation peaks are not shown for neat P(VDF-CTFE) and blends containing 2 wt% of both ILs because of the very weak intensity in dynamic mechanical spectroscopy [23]. With gradually adding both ILs from 5 wt% to 10 wt%, the RAF relaxation peaks are more visible and shift to lower temperature. Moreover, IL-108 induces lower values of T_α (RAF) than IL-C18 with the same IL amount. The depression behaviors of two T_αs corresponding to relaxations in the MAF and RAF of P(VDF-CTFE) are consistent with the DEA results.

The T_α (RAF)-depression behavior unambiguously proves the localization of both phosphonium ILs in the RAF. In fact, the realization of nanostructuration of ILs on the matrix has a close link to the mobility of polymer chains in the constrained RAF, which is analogous to the reported case by Miri *et al.*: strain-induced plastic deformation of polyamide 6 (PA6) *via* partial transformation to a less ordered and less stable state within crystalline phase [57]. Herein, on the one hand, as already mentioned above, the crystalline lamellae of P(VDF-CTFE) is the "template" that guides those ILs diffusing into the RAF constrained within the regular 2D crystalline lamella, inducing orderly assembled ILs with 1D to 2D geometric evolution with increasing the IL amount. On the other hand, the regular 1D or 2D assembled structure of ILs in turn works as a so-called "template" to affect the polymer chain-folding to stabilize more *trans*-configuration, consequently inducing more polar γ- and/or β-crystalline phase. Actually, these regularly assembled structures of ILs in the RAF can be seen as those long tangible templates which can provide a long arrangement of surface functional groups that anchor the interaction with PVDF chains, such as IL-modified CNTs [25,26], OMMT [40], mesoporous SiO_2 nanorods [41]. Meanwhile, these so-called "templates" in the RAF are also like obstacles to depress T_c, T_m, crystallinity and crystallite size during crystallization through dipolar interactions with P(VDF-CTFE). Thus, the synergistic influence of mutual "templates" above synchronously occurring upon crystallization of film formation from solution endues the ILs efficient and versatile nanostructuration ability on the semi-crystalline

fluorinated matrix. In addition, the differences in the diffusion and interacting abilities of ILs due to the chemical structure govern the localization state of ILs in the RAF, and thus tailor the nanostructuration on the semi-crystalline fluorinated matrix. IL-108 with faster migration rate and stronger affinity with P(VDF-CTFE) is sure to be located in the RAF more than IL-C18 with larger distance between lamellae (confirmed by increased L_p values with the same IL amount), and thus induces and stabilizes more *trans*-sequence (β-phase) and also depresses the crystallization in a higher degree.

2.1.4 Conclusions

In conclusion, phosphonium ILs were found to be versatile and tunable nanostructuration agents on a semi-crystalline fluorinated copolymer P(VDF-CTFE), including crystalline phase structure, dispersion morphology and crystallization behavior. A fundamental mechanism of nanostructuration was elaborated in-depth. We propose that the nanostructuration effect is strongly dependent on the diffusion abilities of ILs and the dipolar interaction strengths of ILs with P(VDF-CTFE) due to the difference in the chemical structures. Through the dipolar interaction, those ILs migrating into the RAF are constrained as a regular assembly templated by the 2D crystalline lamella. Simultaneously, this regular arrangement of ILs coupling with the strong dipolar interaction with P(VDF-CTFE) chains in the RAF in turn affects the chain folding to induce more *trans*-sequence for polar crystalline phases and also restrains the crystallization to reduce T_c, T_m, crystallinity and crystallite size. The synergistic effect of these mutual "templates" makes it possible for the nanostructuration of ILs. Since the diffusion ability and the dipolar interaction of IL with polymer matrix can be finely tuned by changing the chemical structures of cation and/or anion, the nanostructuration can also be easily tuned to require different applications. IL-108 shows a higher extent to be located in the RAF as well as stronger interaction with polymer matrix than IL-C18 due to the smaller steric hindrance and extra dipolar groups in the chemical structure, consequently inducing more polar β-phase, more homogeneous dispersion morphology and depressing the

crystallization much more. Therefore, tailoring the chemical structures of phosphonium ILs based on the varied cation/anion combinations and small amount (from 2 wt%) in the PVDF-based matrix provides a facile and efficient pathway to adjust the profiles of blends through the tunable nanostructuration of ILs, which supplies potential possibilities for applications of PVDF-based materials. For example, *i)* the nanostructuration mechanism of ILs on the semicrystalline fluorinated polymer matrix could give some guidelines to comprehensions of structuration of semicrystalline polymers by other fillers; *ii)* phosphonium ILs are efficient plasticers for PVDF-based polymers; *iii)* considering that ILs can induce a transformation of non-polar crystalline phases to polar ones and a formation of nanostructures within P(VDF-CTFE) matrix, we expect that these blends with ILs could be used as materials with the electrocaloric effect (ECE), which will be introduced in the following *sub-section* 2.2.

2.1.5 References

[1] Livi S, Duchet-Rumeau J, Gérard J F, et al. Polymers and ionic liquids: A successful wedding. *Macromolecular Chemistry and Physics*, 2015, 216(4): 359-368.
[2] Livi S, Gérard J F, Duchet-Rumeau J. Ionic liquids: structuration agents in a fluorinated matrix. *Chemical Communications*, 2011, 47(12): 3589-3591.
[3] Livi S, Duchet-Rumeau J, Gérard J F. Nanostructuration of ionic liquids in fluorinated matrix: influence on the mechanical properties. *Polymer*, 2011, 52(7): 1523-1531.
[4] Guo Q, Liu J, Chen L, et al. Nanostructures and nanoporosity in thermoset epoxy blends with an amphiphilic polyisoprene-block-poly(4-vinyl pyridine) reactive diblock copolymer. *Polymer*, 2008, 49(7): 1737-1742.
[5] Yang X, Yi F, Xin Z, et al. Morphology and mechanical properties of nanostructured blends of epoxy resin with poly(ε-caprolactone)-block-poly(butadiene-co-acrylonitrile)-block-poly(ε-caprolactone) triblock copolymer. *Polymer*, 2009, 50(16): 4089-4100.
[6] Xu Z, Zheng S. Morphology and thermomechanical properties of nanostructured thermosetting blends of epoxy resin and poly(ε-caprolactone)-block-polydimethylsiloxane-block-poly(ε-caprolactone) triblock copolymer. *Polymer*, 2007, 48(20): 6134-6144.
[7] Maiez-Tribut S, Pascault J P, Soule E R, et al. Nanostructured epoxies based on the self-assembly of block copolymers: a new miscible block that can be tailored to different epoxy formulations. *Macromolecules*, 2007, 40(4): 1268-1273.
[8] Yokoyama R, Suzuki S, Shirai K, et al. Preparation and properties of biocompatible polymer-grafted silica nanoparticle. *European Polymer Journal*, 2006, 42(12): 3221-3229.
[9] Vermogen A, Masenelli-Varlot K, Séguéla R, et al. Evaluation of the structure and dispersion in polymer-layered silicate nanocomposites. *Macromolecules*, 2005, 38(23): 9661-9669.
[10] Gilman J W, Jackson C L, Morgan A B, et al. Flammability properties of polymer-layered-silicate nanocomposites. Polypropylene and polystyrene nanocomposites. *Chemistry of Materials*, 2000, 12(7): 1866-1873.
[11] Li L, Li B, Hood M A, et al. Carbon nanotube induced polymer crystallization: The formation of nanohybrid shish–kebabs. *Polymer*, 2009, 50(4): 953-965.
[12] Bose S, Khare R A, Moldenaers P. Assessing the strengths and weaknesses of various types of pre-treatments of carbon nanotubes on the properties of polymer/carbon nanotubes composites: A critical review. *Polymer*, 2010, 51(5): 975-993.
[13] Soares B G, Livi S, Duchet-Rumeau J, et al. Synthesis and Characterization of Epoxy/MCDEA Networks Modified with Imidazolium-Based Ionic Liquids. *Macromolecular Materials and Engineering*, 2011, 296(9): 826-834.
[14] Soares B G, Silva A A, Livi S, et al. New epoxy/jeffamine networks modified with ionic liquids. *Journal of Applied Polymer Science*, 2014, 131(3): 39834.
[15] Soares B G, Silva A A, Pereira J, et al. Preparation of epoxy/Jeffamine networks

modified with phosphonium based ionic liquids. *Macromolecular Materials and Engineering*, 2015, 300(3): 312-319.
[16] Silva A A, Livi S, Netto D B, et al. New epoxy systems based on ionic liquid. *Polymer*, 2013, 54(8): 2123-2129.
[17] Livi S, Silva A A, Thimont Y, et al. Nanostructured thermosets from ionic liquid building block–epoxy prepolymer mixtures. *RSC Advances*, 2014, 4(53): 28099-28106.
[18] Nguyen T K L, Livi S, Pruvost S, et al. Ionic liquids as reactive additives for the preparation and modification of epoxy networks. *Journal of Polymer Science Part A: Polymer Chemistry*, 2014, 52(24): 3463-3471.
[19] Livi S, Bugatti V, Soares B G, et al. Structuration of ionic liquids in a poly(butylene-adipate-co-terephthalate) matrix: its influence on the water vapour permeability and mechanical properties. *Green Chemistry*, 2014, 16(8): 3758-3762.
[20] Huddleston J G, Visser A E, Reichert W M, et al. Characterization and comparison of hydrophilic and hydrophobic room temperature ionic liquids incorporating the imidazolium cation. *Green Chemistry*, 2001, 3(4): 156-164.
[21] Ameduri B. From vinylidene fluoride (VDF) to the applications of VDF-containing polymers and copolymers: recent developments and future trends. *Chemical Reviews*, 2009, 109(12): 6632-6686.
[22] Wang F, Lack A, Xie Z, et al. Ionic liquid-induced ferroelectric polarization in poly(vinylidene fluoride) thin films. *Applied Physics Letters*, 2012, 100(6): 062903.
[23] Xing C, Zhao M, Zhao L, et al. Ionic liquid modified poly(vinylidene fluoride): crystalline structures, miscibility, and physical properties. *Polymer Chemistry*, 2013, 4(24): 5726-5734.
[24] Xing C, Guan J, Li Y, et al. Effect of a room-temperature ionic liquid on the structure and properties of electrospun poly(vinylidene fluoride) nanofibers. ACS *Applied Materials & Interfaces*, 2014, 6(6): 4447-4457.
[25] Xing C, Zhao L, You J, et al. Impact of ionic liquid-modified multiwalled carbon nanotubes on the crystallization behavior of poly(vinylidene fluoride). *The Journal of Physical Chemistry B*, 2012, 116(28): 8312-8320.
[26] Mandal A, Nandi A K. Ionic liquid integrated multiwalled carbon nanotube in a poly (vinylidene fluoride) matrix: Formation of a piezoelectric β-polymorph with significant reinforcement and conductivity improvement. *ACS Applied Materials & Interfaces*, 2013, 5(3): 747-760.
[27] Okada D, Kaneko H, Kato K, et al. Colloidal Crystallization and Ionic Liquid Induced Partial β-Phase Transformation of Poly(vinylidene fluoride) Nanoparticles. *Macromolecules*, 2015, 48(8): 2570-2575.
[28] Fraser K J, MacFarlane D R. Phosphonium-based ionic liquids: an overview. *Australian Journal of Chemistry*, 2009, 62(4): 309-321.
[29] Atefi F, Garcia M T, Singer R D, et al. Phosphonium ionic liquids: design, synthesis and evaluation of biodegradability. *Green Chemistry*, 2009, 11(10): 1595-1604.
[30] Nakagawa K, Ishida Y. Annealing effects in poly(vinylidene fluoride) as revealed

by specific volume measurements, differential scanning calorimetry, and electron microscopy. *Journal of Polymer Science: Polymer Physics Edition*, 1973, 11(11): 2153-2171.

[31] Ince-Gunduz B S, Alpern R, Amare D, et al. Impact of nanosilicates on poly(vinylidene fluoride) crystal polymorphism: Part 1. Melt-crystallization at high supercooling. *Polymer*, 2010, 51(6): 1485-1493.

[32] Gregorio R. Determination of the α, β, and γ crystalline phases of poly(vinylidene fluoride) films prepared at different conditions. *Journal of Applied Polymer Science*, 2006, 100(4): 3272-3279.

[33] Yee W A, Kotaki M, Liu Y, et al. Morphology, polymorphism behavior and molecular orientation of electrospun poly(vinylidene fluoride) fibers. *Polymer*, 2007, 48(2): 512-521.

[34] Yu S, Zheng W, Yu W, et al. Formation mechanism of β-phase in PVDF/CNT composite prepared by the sonication method. *Macromolecules*, 2009, 42(22): 8870-8874.

[35] Buckley G S, Roland C M, Casalini R, et al. Electrostrictive Properties of Poly(vinylidenefluoride-trifluoroethylene-chlorotrifluoroethylene).*Chemistry of Materials*, 2002, 14(6): 2590-2593.

[36] Zhu L, Wang Q. Novel ferroelectric polymers for high energy density and low loss dielectrics. *Macromolecules*, 2012, 45(7): 2937-2954.

[37] Ranjan V, Yu L, Nardelli M B, et al. Phase equilibria in high energy density PVDF-based polymers. *Physical Review Letters*, 2007, 99(4): 047801.

[38] Mandal A, Nandi A K. Physical properties of poly(vinylidene fluoride) composites with polymer functionalized multiwalled carbon nanotubes using nitrene chemistry. *Journal of Materials Chemistry*, 2011, 21(39): 15752-15763.

[39] Manna S, Nandi A K. Piezoelectric β polymorph in poly(vinylidene fluoride)-functionalized multiwalled carbon nanotube nanocomposite films. *The Journal of Physical Chemistry C*, 2007, 111(40): 14670-14680.

[40] Ramasundaram S, Yoon S, Kim K J, et al. Preferential formation of electroactive crystalline phases in poly(vinylidene fluoride)/organically modified silicate nanocomposites. *Journal of Polymer Science Part B: Polymer Physics*, 2008, 46(20): 2173-2187.

[41] Yuan D, Li Z, Thitsartarn W, et al. β phase PVDF-hfp induced by mesoporous SiO_2 nanorods: synthesis and formation mechanism. *Journal of Materials Chemistry C*, 2015, 3(15): 3708-3713.

[42] Yin W, Dadmun M. A new model for the morphology of P3HT/PCBM organic photovoltaics from small-angle neutron scattering: rivers and streams. *ACS Nano*, 2011, 5(6): 4756-4768.

[43] Hammouda B. A new Guinier–Porod model. *Journal of Applied Crystallography*, 2010, 43(4): 716-719.

[44] Hammouda, B. *Probing Nanoscale Structures-The SANS Toolbox*, http://www.ncnr.nist.gov/staff/hammouda/the_SANS_toolbox.pdf, p229.

[45] Wunderlich B. Reversible crystallization and the rigid–amorphous phase in

semicrystalline macromolecules. *Progress in Polymer Science*, 2003, 28(3): 383-450.
[46] Sousa R E, Ferreira J C C, Costa C, et al. Tailoring poly(vinylidene fluoride-co-chlorotrifluoroethylene) microstructure and physicochemical properties by exploring its binary phase diagram with dimethylformamide. *Journal of Polymer Science Part B: Polymer Physics*, 2015, 53(11): 761-773.
[47] Zhang Q G, Wang N N, Yu Z W. The hydrogen bonding interactions between the ionic liquid 1-ethyl-3-methylimidazolium ethyl sulfate and water. *The Journal of Physical Chemistry B*, 2010, 114(14): 4747-4754.
[48] Lovinger A J. Crystallization and morphology of melt-solidified poly (vinylidene fluoride). *Journal of Polymer Science: Polymer Physics Edition*, 1980, 18(4): 793-809.
[49] Gregorio R, Capitao R C. Morphology and phase transition of high melt temperature crystallized poly(vinylidene fluoride). *Journal of Materials Science*, 2000, 35(2): 299-306.
[50] Russell T P, Ito H, Wignall G D. Neutron and X-ray scattering studies on semicrystalline polymer blends. *Macromolecules*, 1988, 21(6): 1703-1709.
[51] Lu S X, Cebe P, Capel M. Effects of molecular weight on the structure of poly(phenylene sulfide) crystallized at low temperatures. *Macromolecules*, 1997, 30(20): 6243-6250.
[52] Nogales A, Ezquerra T A, Batallan F, et al. Restricted dynamics in poly(ether ether ketone) as revealed by incoherent quasielastic neutron scattering and broad-band dielectric spectroscopy. *Macromolecules*, 1999, 32(7): 2301-2308.
[53] Laredo E, Grimau M, Müller A, et al. Influence of aging and crystallinity on the molecular motions in bisphenol−A polycarbonate. *Journal of Polymer Science Part B: Polymer Physics*, 1996, 34(17): 2863-2879.
[54] Zuza E, Ugartemendia J M, Lopez A, et al. Glass transition behavior and dynamic fragility in polylactides containing mobile and rigid amorphous fractions. *Polymer*, 2008, 49(20): 4427-4432.
[55] Wang Y, Gómez Ribelles J L, Salmerón Sánchez M, et al. Morphological contributions to glass transition in poly(L-lactic acid). *Macromolecules*, 2005, 38(11): 4712-4718.
[56] Mijovic J, Sy J W, Kwei T K. Reorientational dynamics of dipoles in poly(vinylidene fluoride)/poly(methyl methacrylate)(PVDF/PMMA) blends by dielectric spectroscopy. *Macromolecules*, 1997, 30(10): 3042-3050.
[57] Miri V, Persyn O, Seguela R, et al. On the deformation induced order–disorder transitions in the crystalline phase of polyamide 6. *European Polymer Journal*, 2011, 47(1): 88-97.

2.1.6 Annexe

1. No residual MEK solvent in the resulting film by the solvent-casting method used in this work

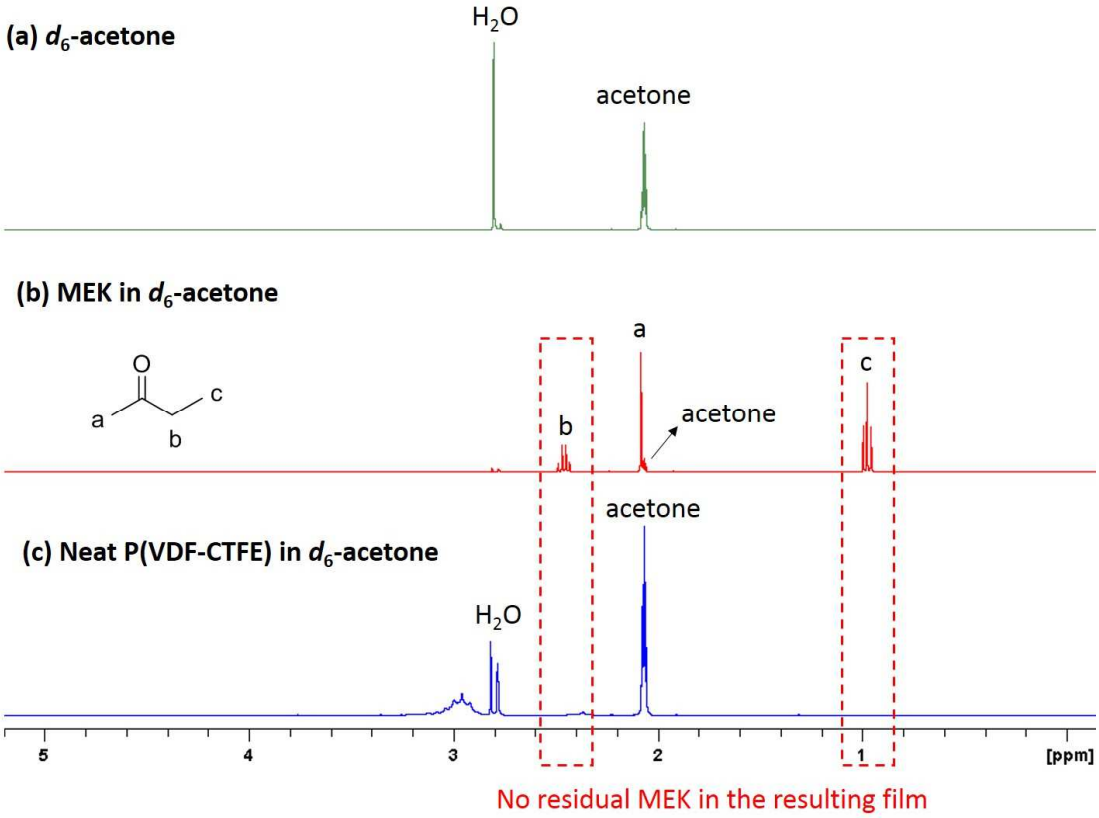

Figure 2.1-S1: ^{1}H NMR spectra of deuterated acetone (d_6-acetone) solvent (a), the solvent MEK in d_6-acetone (b) and neat P(VDF-CTFE) film in d_6-acetone.

2. DSC thermograms of neat P(VDF-CTFE) and P(VDF-CTFE)/ILs blends

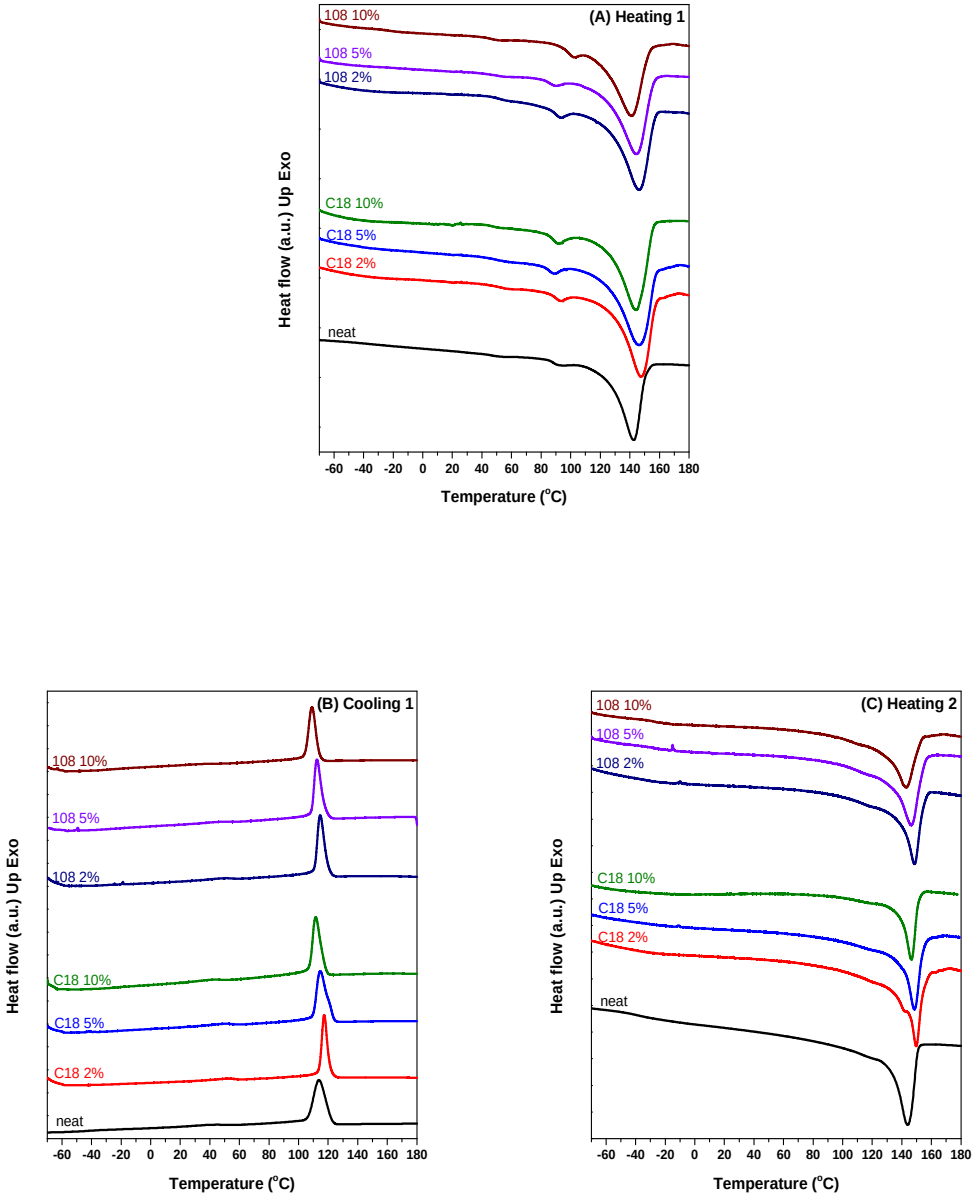

Figure 2.1-S2: DSC thermograms during heating/cooling/heating cycles

Table 2.1-S1: Summary of data from the DSC traces in Figure 2.1-S2

Sample	Heating 1			Cooling 1	Heating 2		
	T_m (°C)	ΔH (J/g)	χ_c	T_c (°C)	T_m (°C)	ΔH (J/g)	χ_c
P(VDF-CTFE)-neat	142.8	40.0	38.3%	113.8	143.9	38.8	37.1%
P(VDF-CTFE)/IL-C18-2 wt%	147.6	42.4	40.6%	117.3	149.8	35.1	33.6%
P(VDF-CTFE)/IL-C18-5 wt%	146.4	40.8	39.0%	114.7	148.5	34.2	32.7%
P(VDF-CTFE)/IL-C18-10 wt%	144.5	38.3	36.7%	111.6	146.4	32.5	31.1%
P(VDF-CTFE)/IL-108-2 wt%	146.3	40.4	38.7%	114.6	148.6	34.3	32.8%
P(VDF-CTFE)/IL-108-5 wt%	144.3	37.6	36.0%	112.4	146.3	33.0	31.6%
P(VDF-CTFE)/IL-108-10 wt%	141.2	32.3	30.9%	109.0	142.3	30.2	28.9%

2.2 The electrocaloric effect (ECE) of P(VDF-CTFE) film by direct measurement and reflections on the ECE measurements of P(VDF-CTFE)/IL blends

2.2.1 Introduction

The phosphonium ILs have shown a versatile nanostructuration effect on the P(VDF-CTFE) matrix in the previous *subsection 2.1*. In the view of universal guidance of "structure determining property", it is verty interesting to investigate the electroactive properties of neat P(VDF-CTFE) and the blends containing ILs to understand how does nanostructuration tuned by ILs influence the properties. Therefore, as one of important electroactive properties of PVDF-based materials, the electrocaloric effect (ECE) is promising to the next generaion of refrigeration systems, *i.e.*, solid state refrigerator. ECE can be described as a phenomenon in which the increase of net polarization with application of an external electric field on the material causes a decrease in entropy, and in turn, an adiabatic increase of its temperature. ECE is reversible, and when the external field is removed, the entropy increases and the temperature decreases to its initial value. Since increasing efforts have been made to improve this effect of dielectrics, dielectrics with enhanced ECE have been potentially used in friendly environment solid state refrigeration devices [1].

PVDF-based co(ter)polymers have been attracting increasing attentions as promising alternatives to conventional ECE ceramic materials due to their flexibility, easy processing as thin films, relatively high dielectric constant and breakdown strength [2,3]. Among all the PVDF-based co(ter)polymers, the copolymer P(VDF-TrFE) with the addition of trifluoro-ethylene (TrFE,-CHF-CF_2-), and the terpolymer P(VDF-TrFE-CTFE) synthesized by the introduction of the third monomer chlorofluoroethylene (CFE,-CFCl-CH_2-) or chlorotrifluoroethylene (CTFE, -CClF-CF_2-) are the two mostly investigated fluorinated polymers for ECE.

The largest ECE for P(VDF-TrFE) films takes place at the temperatures around ferroelectric-paraelectric transition (T_C) using the indirect measurement by

simulation, where an isothermal entropy change (ΔS) of more than 55 J/kgK, and an adiabatic temperature change (ΔT) of more than 12 ^{o}C were observed [2]. Moreover, by direct measurement, a great ECE can be induced in the irradiated P(VDF-TrFE) copolymer near first-order ferroelectric-paraelectric transition [4]. It has been reported that the giant ECE of P(VDF-TrFE) occurs at T_C, because at T_C the polymer chains configuration changes from a low temperature polar all-trans configuration to a high temperature disordered one [5,6]. More recently, Basso *et al.* have reported an enhanced entropy change for P(VDF-TrFE) by applying a negative electric field to positively poled state, which is interesting for improving the ECE at the same electric field change by decreasing the maximum applied electric field and reducing the impact of electrical conductivity [7]. However, it should be noted that the largest entropy change for P(VDF-TrFE) is around its T_c about 80 ^{o}C [8], and the relatively high temperature imposes some limits to its applications.

Terpolymer P(VDF-TrFE-CTFE) displays the so called *relaxor* behavior because the presence of the bulk chlorine atoms coming from the third monomer (CTE or CTFE) hinders the formation of the long range ferroelectric order and induces the emerging of nanodomains with a short range polar order at nanoscale, resulting in a reduction of the spontaneous polarization (even no remanent polarization at zero electric field) and thus narrow single hysteresis loops [9,10]. And further, P(VDF-TrFE-CTFE) shows a relaxor transition at near room temperature [2], and displays a relatively wide temperature range from -10 ^{o}C to 40 ^{o}C in which the permittivity increases from 10 to 50 and is frequency-dependent [11,12]. Neese *et al.* reported a similar level of ECE near room temperature for P(VDF-TrFE-CTFE) [2], and they also demonstrated that ECE in the relaxor ferroelectric terpolymer is weaker than that in the normal ferroelectric copolymer because polarization response from the nanopolar regions does not generate much entropy change [4]. It is reported that terpolymer films show temperature dependence of ECE critically according to the film preparation conditions, *e.g.*, the unaxially stretched terpolymer films show pronounced temperature dependence of ECE, while the non-stretched films exhibit a temperature independent ECE between 5 ^{o}C and 45 ^{o}C [11]. Recently, Basso *et*

*al.*have conducted a direct accurate determination of ECE in the transition region of terpolymers from -5 °C to 60 °C by heat flux calorimetry using Peltier cell heat flux sensors. They found that the isothermal entropy change ΔS can reach 4.2 $Jkg^{-1}K^{-1}$ at 31 °C with an adiabatic temperature change ΔT of 1.1 K [13]. Furthermore, an interesting work firstly showed that ECE was enhanced in P(VDF-TrFE-CTFE)/ZrO_2 nanocomposites (ΔT of the nanocomposites with 3 vol% ZrO_2 is 120% of that of the neat terpolymer) because of the interface effects between polymer matrix and nanofillers enhancing polarization responses and then providing additional electrocaloric entropy changes [14].

However, no work on ECE has been reported for copolymer poly (vinylidene fluoride-*co*-chlorotrifluoroethylene) (P(VDF-CTFE)) which represents also an important copolymer in PVDF-based co(ter)polymer family. In this work, we investigated the entropy change for P(VDF-CTFE) in the temperature range from room temperature to 70 °C at two different electric fields (100 MV/m and 150 MV/m). More importantly, we analysized the factors responsible for the relatively low breakdown strength for P(VDF-CTFE)/IL blends which impose detrimental effects on ECE measurements of composite samples. Further, we propose some perspectives of ECE measurements for both P(VDF-CTFE)/IL blends and P(VDF-CTFE)/graphene composites, which are very important aspects for improving our work in the future.

2.2.2 Experimental section

2.2.2.1 Materials and preparation of P(VDF-CTFE) films

P(VDF-CTFE) copolymer containing 8 wt% of CTFE was purchased from Arkema. Twelve wt % of P(VDF-CTFE) solution in MEK was first prepared at 60 °C and the polymer solution was magnetically stirred at 60 °C for several hours to assure the total dissolution of polymers in solvent. Afterwards, the solution was cast onto clean stainless steel substrate via doctor blade, followed by a drying process at 80 °C in an air-circulation oven for 3 h to evaporate any residual solvent. The obtained films have typical thicknesses of around 15-30 μm. For ECE measurement, film samples were cut into the size of 3 cm × 4 cm, and circular gold electrodes with diameters of

10 mm and lateral contacts were deposited by sputtering.

2.2.2.2 ECE measurement system

In the work of Basso *et al.*, a direct measuring system has been developed on the principle of differential detection of heat flow using Peltier cell heat flux sensors [13]. The charging electric power to the sample is offered by a Trek amplifier (10 kV, 40 mA) driven by an Agilent 33500 waveform generator. The electric current is measured by an SRS570 amplifier. The voltage at the measuring Peltier cells is measured by a Keithley 2000 multimeter. All the instruments are computer controlled.

The experimental setup is composed of a thermal bath and a couple of heat flux sensors connected differentially (shown in Figure 2.2-1). The thermal bath is made by a 25 × 25 mm^2 copper block (B) to ensure temperature uniformity. The temperature of the copper block is measured by a copper constantan thermocouple (C) with an accuracy of ± 0.1K and can be finely adjusted in the range between -20 °C and 80 °C by regulating the electric current supplied at two power Peltier cells (A) (of size 30 × 30 mm^2, in thermal series) placed below the copper block. Two miniaturized Peltier cells (D) are used as a differential heat flux sensor. The differential configuration is essential for the purpose of subtracting the large net heat flow, which traverses both cells, generated by the temperature regulation system.

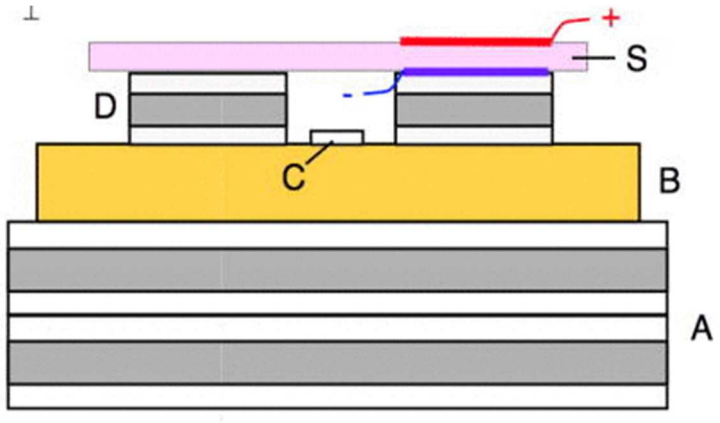

Figure 2.2-1: Scheme of the calorimeter in ECE measuring system. (A) Power Peltier cells; (B) copper block; (C) thermometer; (D) miniaturized Peltier heat flow sensors; (S) sample [13]

2.2.2.3 The treatment of ECE experiment data: the determination of ΔS and ΔP (polarization change)

The electric field applied on the film is calculated by E = V/d, where V is the applied voltage and d is the film thickness measured at zero field (note that the effect of electric field on the film thickness is negligible). The electric current density is j = i/A, with i being the current and A being the electrode area. Figure 2.2-2 shows an example of the measured signals. In the example, the increase of electric field from zero to 100 MV/m or 150 MV/m takes place within 0.25 s, and the final electric field is kept for 10 s allowing for heat flux relaxation. The waiting time is repeated when the electric field is removed.

In all our experiments, one can observe a peak for both j and q_s followed by a plateau level at constant electric field. The peaks are due to the changing of the capacitor and to the ECE, respectively. The plateau shown only under applied field is due to the nonzero electric conductivity of the sample.

The polarization change ΔP was computed by subtracting the direct current (DC) conduction component which is proportional to the electrical field through the equation, $j_{dc} = \sigma E$ (σ is the DC conductivity of the sample), from the measured current density j: $\Delta P = \int (j - \sigma E)dt - \varepsilon_0 E$. Similarly, the entropy change ΔS was calculated by subtracting the Joule heating contribution presented as $q_{s,dc} = -\nu\sigma E^2$, where $\nu = d \times A$ is the volume and by making the integration: $\Delta S = \left(\frac{1}{T}\right) \int ((q_s / \nu) + \sigma E^2)dt$.

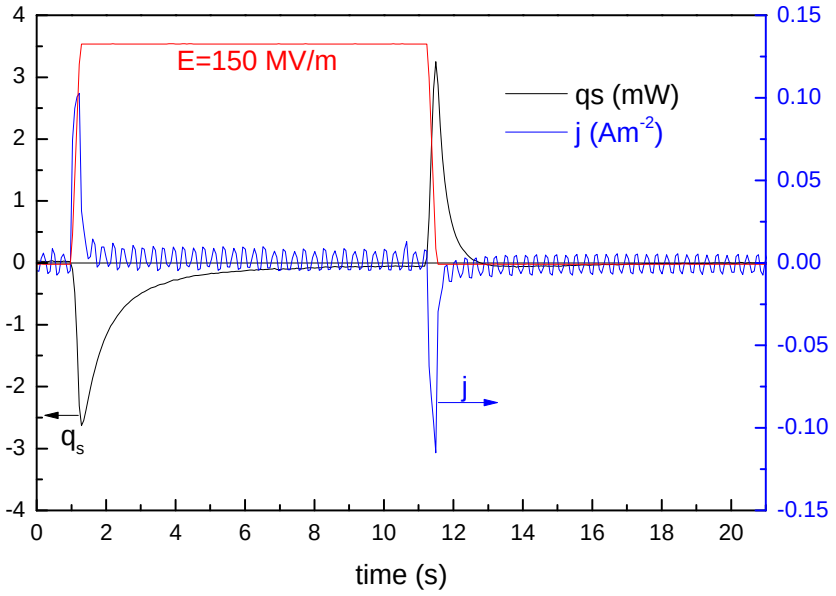

Figure 2.2-2: Example of the measured signals in an ECE experiment for P(VDF-CTFE) copolymer at room temperature and 150 MV/m: electric field E, electric current density j, heat current q_s exchanged by the sample with the thermal bath through the Peltier sensors

2.2.2.4 Loop experiments with unipolar electric field

The polarization-depolarization loops measurements with unipolar electric field applied along the same direction were performed after ECE experiments. The applied waveform includes four steps: increasing the field in 0.25 s, waiting Δt, decreasing the field in 0.25 s and waiting Δt. In fact, Δt = 0 s, because the polarization slowly relaxed with time, and the unipolar loop experiments are excluding the long time relaxation processes to trace the P(E) hysteresis loop. Unipolar loop experiments are performed by repeating three times the waveform.

2.2.3 Results and discussion

2.2.3.1 The calibration of heat flux sensors

The heat flux sensors were calibrated by using the Joule heating of a strain gauge resistor (R=119.5 Ohm) with similar size and thickness as the polymer sample. The measured voltage V_p is proportional to the heat current q_s through the Peltier cell and be expressed as $V_p = S_p \bullet q_s$. The constant S_p was determined in the stationary state

as the ratio $S_p=V_p/q_s$ where q_s is given by the Joule heat current $q_s = -Ri_R^2$. The resulting calibration curve as a function of temperature is shown in Figure 2.2-3.

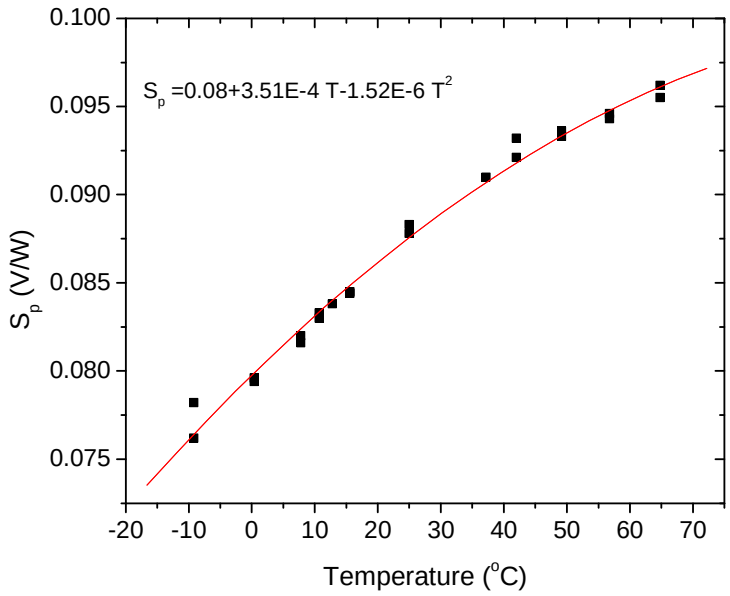

Figure 2.2-3: The calibration curve of the Peltier heat flow sensors. The inset displays the fitting relationship between S_p and temperature

2.2.3.2 The ECE of P(VDF-CTFE) film

Figure 2.2-4 shows ΔP_{ECE} (from ECE experiments) and ΔP_{loop} (from the uniloop experiments, and all the unipolar P-E loops of neat P(VDF-CTFE) are presented in Figure 2.2-S1 in Annexe) as a function of temperature at 100 MV/m and 150MV/m. It is obvious to see the more enhanced polarization change either from ECE measurements or from the uniloop experiments at 150 MV/m than at 100 MV/m, and the polarization changes exhibit increasing tendency with the temperature. Note that the valule of ΔP_{ECE} is slightly higher than that of ΔP_{loop}, because for ECE experiment there exists waiting time of 10 seconds (ΔT =10 s) which allows the polarization slowly relaxing with time due to both the thermal relaxation of the polar nanoregions and the polarization of the electrodes because of the migration of ionic impurities [13], while for loop experiments, ΔT = 0 s and there is no time for polarization relaxing.

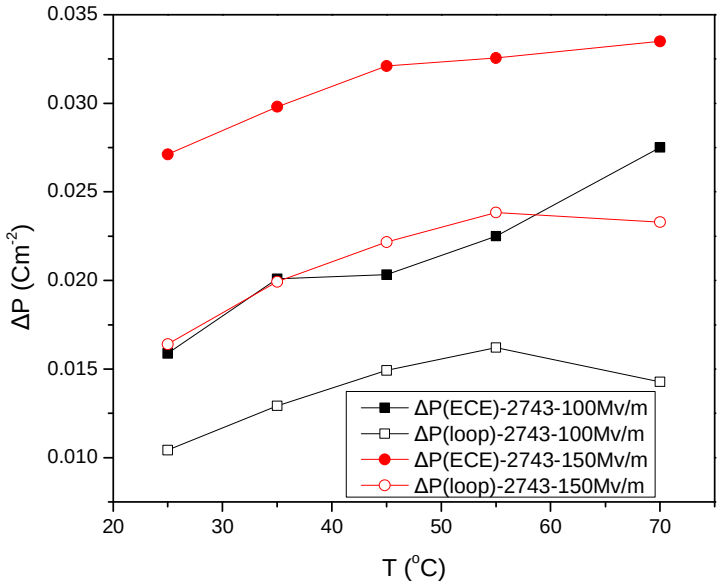

Figure 2.2-4: The polarization changes of P(VDF-CTFE) film as a function of temperature at 100 MV/m and 150 MV/m. Full symbols are corresponding to ΔP from ECE experiments, while open symbols are related to ΔP_{loop} from the unipolar loop experiments

Figure 2.2-5 presents the entropy change ΔS of P(VDF-CTFE) film as a function of temperature at electric fields of 100 MV/m and 150 MV/m. It is interesting to find that ΔS of P(VDF-CTFE) increases with the temperature, and the value of |ΔS| of P(VDF-CTFE) can attain 4.8 $JKg^{-1}K^{-1}$ at 70 °C and 150 MV/m, which is comparable with that of 4.2 $JKg^{-1}K^{-1}$ measured at 31 °C and 50 MV/m reported by Basso *et al.* [13], making copolymer P(VDF-CTFE) as a new important ECE material.

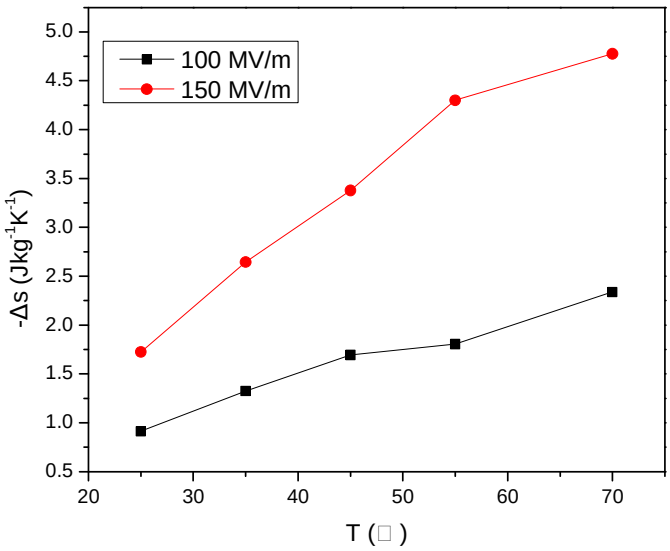

Figure 2.2-5: The entropy change ΔS of P(VDF-CTFE) film as a function of temperature at electric fields of 100 MV/m and 150 MV/m

2.2.3.3 Reflections on the ECE measurements of P(VDF-CTFE)/IL blends

On the one hand, we have already demonstrated that neat P(VDF-CTFE) films from MEK are very interesting materials with electrocaloric effects, and their entropy change ΔS at 70 °C and 150 MV/m can even reach to 4.8 $Jkg^{-1}K^{-1}$, which imposes potential applications on solid state refrigeration. On the other hand, the natural high ionic conductance profile of ILs [15,16] and high dielectric constants [17,18] due to nonvanishing electrical dipole moments and their complicated ion pairs and dipolar ion complexes in the bulk state [17] facilitates them to work as promising additives to enhance dielectric constant for PVDF-based composites with high dielectric performances. Combining the advantages from both P(VDF-CTFE) and ILs, we hope that P(VDF-CTFE)/IL blends could exhibit interesting electrocaloric effects. However, P(VDF-CTFE)/IL blends showed relatively higher AC conductivity and dielectric loss compared to neat copolymer, and the blend films brokedown when the electric fieldreached to 100 MV/m, which is not advantageous to improve the ECE of polymer materials with ILs. It is potentially ascribed to the fact that ILs present a free state in polymer matrix under AC or DC electric field because the dipolar interaction between

ILs and P(VDF-CTFE) resulting from a physical blending cannot restrain their movements in domains, subsequently generating great conductivity and dielectric loss. This behavior is a negative factor for the dielectric applications because a large amount of heat energy can be produced from the movement of free ILs under electric field, and thus decreasing the breakdown strength of blends. More recently, Li *et al.* reported that, organic conductive nanodomains can be formed and movements of ILs can be confined within domains by grafting IL molecules onto the amorphous PVDF chains with electron-beam irradiation [19]. Such blends containing confined ILs exhibit improved dielectric properties compared to neat PVDF.

Based on these analyses above, a continuous work should be focused on how to improve ECE for PVDF/IL blends. For example, there are several possibilities that could be considered: (1) fixing the ILs onto the polymer chains; (2) trapping ILs into so-called domains by chemical bonding; (3) adding the third filler to pin the movement of ILs in polymer blends. All possible solutions aim to improve the dielectric constant but restrain the dielectric loss, and simultaneously maintain the breakdown strength of polymer matrix.

2.2.4 Conclusion

In conclusion, we investigated ECE of P(VDF-CTFE) neat film in the temperature range from room temperature to 70 ^{o}C by direct measurement using Peltier cell heat flux sensors. The entropy change of P(VDF-CTFE) can reach up to 4.8 $JKg^{-1}K^{-1}$ at 70 ^{o}C and 150 MV/m, which makes copolymer P(VDF-CTFE) as a promising ECE material. Further work should be paid much more intentions to investigate the ECE of P(VDF-CTFE)/IL blends.

2.2.5 References

[1] Valant M. Electrocaloric materials for future solid-state refrigeration technologies. *Progress in Materials Science*, 2012, 57(6): 980-1009.
[2] Neese B, Chu B, Lu S G, et al. Large electrocaloric effect in ferroelectric polymers near room temperature. *Science*, 2008, 321(5890): 821-823.
[3] Neese B, Lu S G, Chu B, et al. Electrocaloric effect of the relaxor ferroelectric poly(vinylidene fluoride-trifluoroethylene-chlorofluoroethylene) terpolymer. *Applied Physics Letters*, 2009, 94(4): 2910.
[4] Li X, Qian X S, Gu H, et al. Giant electrocaloric effect in ferroelectric poly(vinylidenefluoride-trifluoroethylene) copolymers near a first-order ferroelectric transition. *Applied Physics Letters*, 2012, 101(13): 132903.
[5] Furukawa T. Ferroelectric properties of vinylidene fluoride copolymers. *Phase Transitions: A Multinational Journal*, 1989, 18(3-4): 143-211.
[6] Su R, Tseng J K, Lu M S, et al. Ferroelectric behavior in the high temperature paraelectric phase in a poly(vinylidene fluoride-co-trifluoroethylene) random copolymer. *Polymer*, 2012, 53(3): 728-739.
[7] Basso V, Gerard J F, Pruvost S. Doubling the electrocaloric cooling of poled ferroelectric materials by bipolar cycling. *Applied Physics Letters*, 2014, 105(5): 052907.
[8] Gregorio R, Botta M M. Effect of crystallization temperature on the phase transitions of P(VDF/TrFE) copolymers. *Journal of Polymer Science B Polymer Physics Edition*, 1998, 36(3): 403-414.
[9] Bauer F. Review on the properties of the ferrorelaxor polymers and some new recent developments. *Applied Physics A*, 2012, 107(3): 567-573.
[10] Bokov A A, Ye Z G. Recent progress in relaxor ferroelectrics with perovskite structure. *Frontiers of Ferroelectricity*. Springer US, 2006: 31-52.
[11] Li X, Qian X, Lu S G, et al. Tunable temperature dependence of electrocaloric effect in ferroelectric relaxor poly(vinylidene fluoride-trifluoroethylene-chlorofluoro-ethylene terpolymer. *Applied Physics Letters*, 2011, 99(5): 052907.
[12] Zhu H, Pruvost S, Cottinet P J, et al. Energy harvesting by nonlinear capacitance variation for a relaxor ferroelectric poly(vinylidene fluoride-trifluoroethylene-chloro-fluoroethylene) terpolymer. *Applied Physics Letters*, 2011, 98(22): 222901.

[13] Basso V, Russo F, Gerard J F, et al. Direct measurement of the electrocaloric effect in poly(vinylidene fluoride-trifluoroethylene-chlorotrifluoroethylene) terpolymer films. *Applied Physics Letters*, 2013, 103(20): 202904.
[14] Chen X Z, Li X, Qian X S, et al. A nanocomposite approach to tailor electrocaloric effect in ferroelectric polymer. *Polymer*, 2013, 54(20): 5299-5302.
[15] Huddleston J G, Visser A E, Reichert W M, et al. Characterization and comparison of hydrophilic and hydrophobic room temperature ionic liquids incorporating the imidazolium cation. *Green Chemistry*, 2001, 3(4): 156-164.
[16] Davis Jr J H, Fox P A. From curiosities to commodities: ionic liquids begin the transition. *Chemical Communications*, 2003 (11): 1209-1212.
[17] Wu J, Stark J P W. Measurement of low frequency relative permittivity of room temperature molten salts by triangular waveform voltage. *Measurement Science and Technology*, 2006, 17(4): 781.
[18] Wakai C, Oleinikova A, Ott M, et al. How polar are ionic liquids? Determination of the static dielectric constant of an imidazolium-based ionic liquid by microwave dielectric spectroscopy. *The Journal of Physical Chemistry B*, 2005, 109(36): 17028-17030.
[19] Xing C, You J, Li Y, et al. Nanostructured Poly(vinylidene fluoride)/Ionic Liquid Composites: Formation of Organic Conductive Nanodomains in Polymer Matrix. *The Journal of Physical Chemistry C*, 2015, 119(36): 21155-21164.

2.2.6 Annexe

Unipolar P-E (Polarization-Electric field) loop curves of neat P(VDF-CTFE) copolymer at different temperatures.

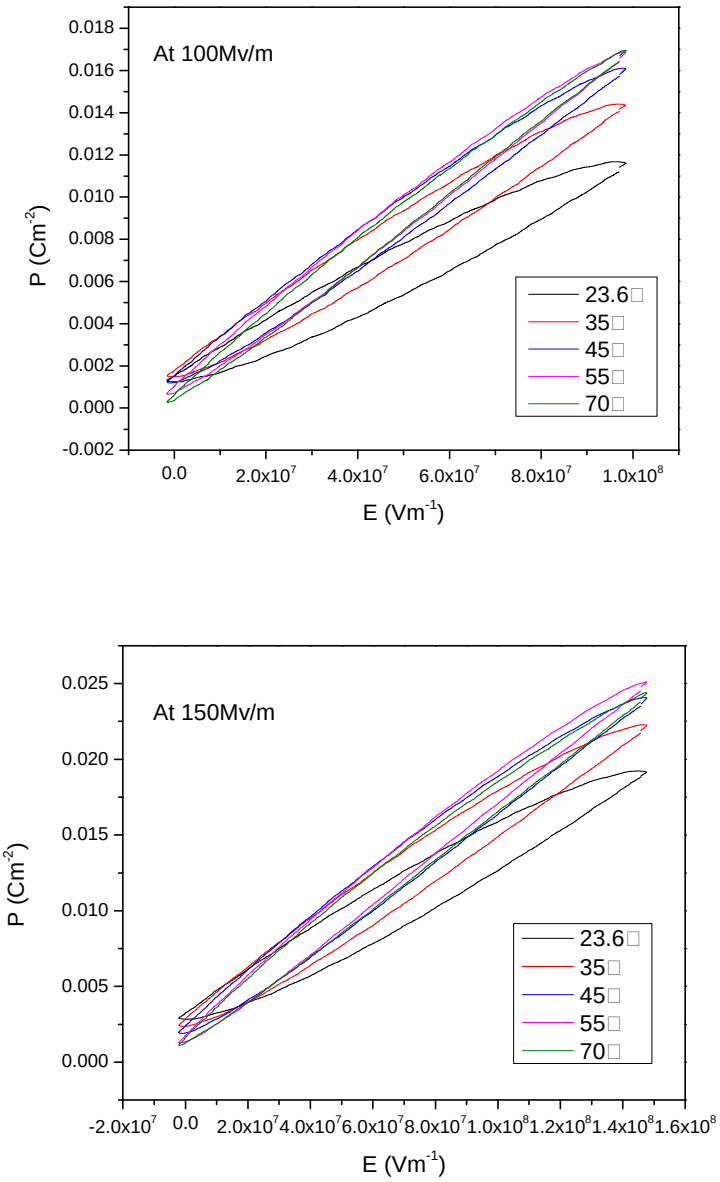

Figure 2.2-S1: Unipolar P-E (Polarization-Electric field) loop curves of neat P(VDF-CTFE) copolymer at different temperatures and 100 MV/m and 150 MV/m

Chapter 3
The Role of Fluorinated IL as a New Interfacial Agent in P(VDF-CTFE)/Graphene Composite Films

Chapter 3: The Role of Fluorinated IL as a New Interfacial Agent in P(VDF-CTFE)/Graphene Composite Films

3.1 Introduction

It is well-known that the incorporation of nanofillers into a polymer matrix can endow the composites extended functions and applications originated from the functional fillers while retaining excellent processing and manufacturing abilities due to the flexibility inherent in polymer matrices. As introduced in *Chapter 1*, graphene, a monolayer of sp^2 hybridized carbon atoms arranged in a hexagonal lattice, has potential applications for developing nanocomposites, sensors, supercapacitors, and optoelectronic devices, *etc.* due to its intriguing properties such as excellent electrical conductivity, ultrahigh aspect ratio and relatively low production cost [1,2]. Therefore, a great deal of research has been under the spotlight to prepare graphene/polymer nanocomposites [3]. Through the synergistical effect from both graphene and polymer, these nanocomposites could exhibit outstanding structural performances and multifunctional properties if the well-controlled and expected structuration and interfacial organization can be achieved. However, pristine graphene can not be used directly as the nanofiller for polymer composites due to the lack of functional groups on the surface for bonding with polymer matrix. It is difficult to prevent the macroscopic aggregation of graphene sheets to restore the graphite-like one due to the inherent affinity between graphene layers *via* π-π stacking. Therefore, a fine control of dispersion and distribution of graphene nanofillers in the polymer matrix and the interface tuning is utmost necessary and significant to obtain enhanced performance of graphene/polymer nanocomposites [4].

As a continuous and systematic work of this thesis, in *Chapter 3*, we will focus on the preparation of P(VDF-CTFE)/graphene nanocomposites, and expect to obtain

enhanced properties thanks to the combining of merits of both graphene nanofillers and electroactive PVDF-based matrix. However, the naturally poor compatibility between nonpolar graphene and polar PVDF-based matrix is a negative factor to from a homogeneous distribution, which gives rise to adverse excessive aggregation of graphene and vacancies at interfaces. In contrast, surface functional oxidized graphene (GO) with heavily oxygenated groups such as hydroxyl, epoxide, carbonyl and carboxyl allows being more compatible and homogeneously dispersed in the more or rather polar polymer matrix. However, GO is usually incompatible with most organic solvents which are good solvents for the polymer matrix. Moreover, unlike graphene, GO is considered electrically insulator, which is undesired to be used as the conductive filler in the composites. Thus, a routine way to obtain conductive graphene filler in the matrix is the chemical reduction of GO to produce reduced oxidized graphene (rGO), recovering the graphitic sp^2 network, but the aggregation issue should also be avoided during the reduction process [5].

Therefore, the key strategy to enhance the dispersion of graphene in the PVDF-based matrix is the surface functionalization, endowing the so-called interfacial agent on the surface of graphene to tune the interfacial bonding between graphene and polymer matrix with controlled and reinforced properties. The resulting interface tailored by the interfacial agents is thus the linking region between polymer matrix and nanofiller, resulting in the improvement of compatibility between polymer phase and filler phase upon the composites.

In this framework, there are several works to show the well-dispersed GO or rGO in PVDF-based matrix by either covalent or non-covalent surface modification of graphene. It was reported that PMMA chains have been grafted from the GO or rGO surface *via* surface-initiated atom transfer radical polymerization (SI-ATRP). The covalently anchored PMMA chains on the surface of graphene act as the so-called interfacial agents, providing strong interfacial interactions between graphene and PVDF host and thus leading to a homogeneous distribution of graphene throughout the matrix [6]. PMMA covalently modified graphene layers become thinner for the

exfoliation during composite formation. Graphene sheets promoted the formation of piezoelectric β-crystal of PVDF. The thermal stability of nanocomposites is significantly increased and the T_g increase is really large (21 ^oC). The mechanical properties are also enhanced, for example, the storage modulus shows an increase of 124%, a stress at break of 157% and a Young's modulus of 321% for 5% of PMMA modified graphene loading content.

It is reported that poly(vinyl alcohol) (PVA) was used as a modifier to be covalently bonded to the surface of GO through esterification reaction [7]. Thanks to the PVA functionalized graphene surface, the agglomeration of original rGO was prevented, and simutaneously interactions between PVDF and rGO-PVA were enhanced through the intermolecular hydrogen bonds between PVA and PVDF. The effect of PVA interfacial engineering on the enhancement of rGO fillers was highlighted in this work. In comparison with the rGO/PVDF composites, a higher dielectric permittivity coupled with a lower loss factor were achieved for rGO-PVA/PVDF nanocomposites in the frequency range of 1×10^2 to 1×10^3 Hz. And a high dielectric constant of 230 which is 2.3 times higher than rGO/PVDF nanocomposite one was obtained for rGO-PVA/PVDF nanocomposites at 1×10^2 Hz.

Han *et al.* reported the tetraethyl orthosilicate-modified rGO nanosheets as fillers incorporated in P(VDF-CTFE) matrix [8]. The presence of SiO_2 layers breaks the connectivity of the fillers and reduces the Ohmic conduction. Thus, the dielectric loss of the P(VDF-CTFE) composites containing r-GO@SiO_2 has been significantly reduced compared to that of r-GO-based ones. For example, at the percolation threshold, the loss tangent of the 1.49 vol% r-GO@SiO_2 composite is 0.4, which is almost one order of magnitude smaller than that of the 0.51 vol% r-GO composite at 1 kHz. Remarkably, the dielectric loss of r-GO@SiO_2 based composites decreases to a level as low as that of the neat polymer at a relatively high frequency even after the percolation threshold.

More recently, ILs have also been used as modifiers of the surface of graphene, subsequently producing homogenously dispersed polymer composites with excellent

properties, which expands the functions of ILs in the polymer composite materials. As we have already investigated the nanostructuration ability of phosphonium ILs on the P(VDF-CTFE) matrix in *Chapter 2*, it is also very interesting for us to study the interfacial tunability of ILs on the graphene/P(VDF-CTFE) nanocomposites in *Chapter 3*. In this context, recent progresses on the ILs-modified graphene as nanofillers for the PVDF-based matrix are reviewed as follows.

An ammonium-based IL, (cetyltrimethylammonium bromide, CTAB), was non-covalently functionalized on the surface of graphene [9]. It is found that ILs showed an efficient interfacial reinforcement between PVDF matrix and GO fillers, resulting in nearly pure γ-crystals due to the introduction of strong ion-dipole interactions between PVDF and GO.

A phosphonium IL, (1-hexadecyl)triphenylphosphonium bromide (HTPB), has also been used as an interfacial agent to tune the interface property [10]. Through the non-covalent modification by HTPB, the modified graphene even after the reduction from GO (HTPB-rGO) still retains an excellent dispersion in the cosolvent of PVDF, *i.e.*, DMAc, without any macroscopic aggregation. This interfacial tunability induced by HTPB provides an efficient way to prepare graphene/PVDF nanocomposites with well dispersed graphene sheets inside the matrix. Thus, the resulting HTPB-rGO/PVDF composite films exhibit an improved dielectric property at a very low percolation threshold (0.662 wt%). The dielectric constant of HTPB-rGO/PVDF (lower than 0.86 wt%) at 1 kHz is more than 3 times of that of neat PVDF, while the dielectric loss is still very low (loss factor for all composites are lower than 0.07). Moreover, the interfacial agent HTPB can also efficiently induce polar β or γ-phase through the interfacial interactions with the matrix to influence the chain segemental configuration of PVDF.

Unlike the non-covalent functionalization above, imidazolium IL with functional amino-group was covalently bonded on the surface of GO to fabricate the PVDF/GO-IL composites through amidation reaction between -COOH on the edge of sureface of GO and -NH_2 of IL [11]. Due to the interfacial interactions of PVDF chains and GO-

IL provided from the interfacial agent IL, the GO-IL is found to be homogeneously dispersed in the PVDF matrix with a dendritic morphology, leading to an increased dielectric constant. The resulting PVDF/GO-IL composite films showed an obviously enhanced conductivity even at a low content of GO-IL incorporated. It is suggested that electron conductivity of graphene sheets connected by the 3D network in the composites is the reason of the improved conductivity. In addition, the DC-conductivity of composite displayed a sharp increase up to ~10^{-2} S/cm occuring at the percolation threshold (0.1 wt%) (see Figure 3-1a), and the dielectric permittivity increases up to 13.5 at 100 Hz for the composites loading 3 wt% of GO-IL compared to the value of 7.5 for the neat PVDF (see Figure 3-1b).

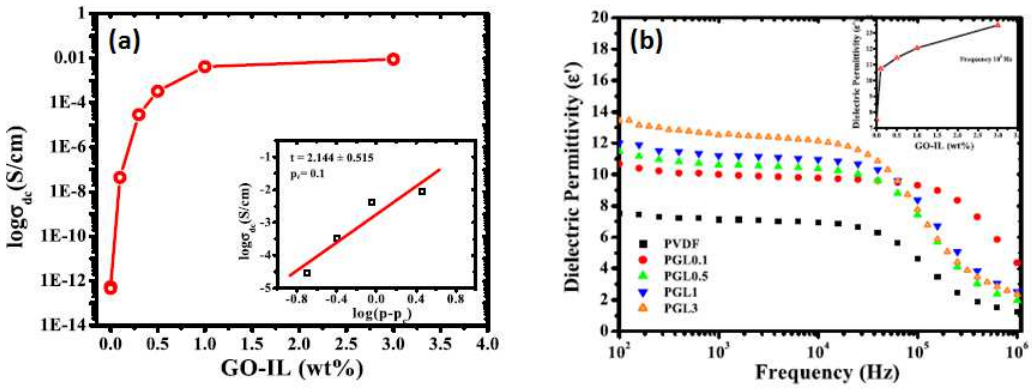

Figure 3-1: DC conductivity of composite films as a function of GO-IL loading amount (a); dielectric permittivity of composite films with different loading amounts as a function of frequency (b) [11]

Although a few works above have demonstrated that ILs used as interfacial agents can dramatically improve the dispersion of GO in PVDF matrix, some issues of the role of ILs as interfacial agents in polymer composites still need to be paid more attension as follows, which is also the goal of *Chapter 3*.

First, for most reported ILs used as modifier, the commercial origin of ILs is short of chemical structure design. They only focused on the use of monofunctional cation with imidazolium or phenyls structure which could form π-π interactions with graphene. However, an ideal interfacial compatibilizer is preferred to have difunctional moieties, being binding both graphene and polymer matrix to realize the interfacial reinforcement. In view of this consideration, a task-specific IL, perfluorooctyltriphenylphosphonium iodide (IL-C8F13) (Scheme 3-1) will be

synthesized and modified on the surface of GO (GO-IL) and rGO (rGO-IL) as functional nanofillers incorporated into P(VDF-CTFE) matrix in this work. The cation structure of IL combines three phenyls (potential π-π interaction with graphene) and a short fluorinated chain (enhanced miscibility with fluorinated matrix *via* dipolar interaction [12]) to compatibilize graphene fillers and P(VDF-CTFE) matrix at the interface between them.

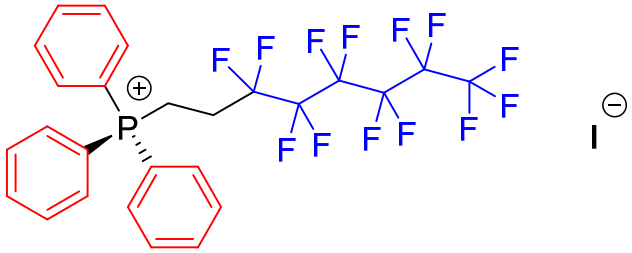

IL-C8F13

Scheme 3-1: Chemical structure of IL-C8F13 used in this work

Second, the usual strategy starting from GO to IL-modified GO, and finally reduced to rGO-IL used as nanofillers in polymer matrix [13] paid less attention on the change of functional environment between graphene and IL during the reduction process, which is a key factor to influence the interfacial interactions. Thus, the difference in the interaction model of GO with IL and rGO with IL is investigated in this work.

Third, it will be required to investigate the interfacial effect of IL on the properties of P(VDF-CTFE) composites, such as crystalline phase structure, crystallization behavior, dispersion morphology, chain segmental relaxation behavior, subsequently influencing the final dielectric properties of composites. The different influences above provided from the different interaction models of GO and rGO with matrix should also be compared.

Consequently, basd on the considerations above, concretely in this work, P(VDF-CTFE)/graphene composites with different contents of nanofillers will be prepared with the goal of providing a deep understanding of the mechanism of interfacial interactions, which could facilitate the development of graphene/PVDF-based

nanocomposites with tunable and enhanced properties through the versatile ILs as interfacial agents.

3.2 Preparation of GO and rGO and modification by IL

3.2.1 Experimental section

3.2.1.1 Raw materials

Graphite powder with the size ≤ 20 μm was purchased from Aldrich. IL-C8F13 was synthesized following the report described elsewhere [14], and the detail is shown in the subsection 3.2.1.2. H_2SO_4, $NaNO_3$, $KMnO_4$ were purchased from CARLO ERBA (France) and used as received.

3.2.1.2 Synthesis of IL-C8F13

Fluorinated phosphonium IL (IL-C8F13) was prepared by the nucleophilic substitution reaction (see Figure 3-2). In a typical synthesis, triphenylphosphine (20 mmol, 5 g) and 1*H*,1*H*,2*H*,2*H*-perfluorooctyl iodide (9.48 g, 20 mmol) were mixed in toluene (20 mL) at room temperature. The stirred suspension was heated under reflux for 24 h at 120 °C and a white precipitate was formed. After cooling to room temperature, the reaction mixture was filtered then washed repeatedly with petroleum ether and dried under vacuum to produce white powder (yield = 65%).

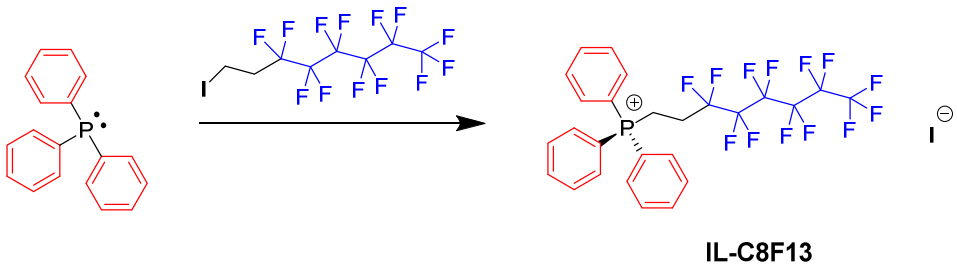

Figure 3-2: Synthesis of IL-C8F13

3.2.1.3 Preparation of GO and rGO

GO was prepared by a modified Hummers method [15]. In a typical synthesis, graphite powder (1 g) and $NaNO_3$ (0.75 g) were charged in a flask, concentrated H_2SO_4 (96%) (34 mL) was added into it at 0 °C. The mixture was allowed to stir

overnight at RT. $KMnO_4$ (5 g) was slowly added into the flask in 3 h at 0 ^oC, and then stirred at 0 ^oC for 2 h until the color became dark green. The flask was shifted to an oil bath and the mixture was allowed to stir at 38 ^oC for 3 days until it became pasty brownish. The temperature was slowly increased to 60 ^oC and allowed to stir for 4 h. The mixture was diluted with de-ionized water (40 mL) at 0 ^oC, and the reaction was ended by adding 7 mL of H_2O_2 (30%) solution at 0 ^oC until the color became dark yellow. The mixture was centrifuged for 10 min, the solid was washed by HCl solution (5%). After 10 cycles of centrifugation/washing with HCl solution, the solid was then washed with pure water for 10 times. The resulting solid was suspended in water under ultrasonication for at least 12 h to exfoliate graphite oxide until no visible particle was observed by native eyes. The brown solution was then centrifuged for 10 min to remove very small amount of visible particles. The final GO colloid in water was lyophilized to obtain fluey GO solid. The GO product was then resuspended in water (1 mg/mL), after ultrasonication for 2 h, the GO colloid in water with perfect dispersion can be reobtained.

For the preparation of rGO, a solution of GO in DMF (0.5 g/L) was prepared by ultrasonic treatment for 1 h. The solution was then reduced by hydrazine hydrate $H_2N\text{-}NH_2$ (4 times in mass) at 95 ^oC for 3 h. The precipitates can be obtained during the process. After washing by water for several times to remove the excess hydrazine and DMF, the product rGO was dried by lyophilization.

3.2.1.4 Modification of GO and rGO with IL: GO-IL and rGO-IL

In a typical synthesis, 0.5 mg/mL of GO colloid in water (4 mL) was prepared by ultrasonication for 20 min. The solution was alkalized by adding NaOH solution (0.1 M) till pH = 10. Two mL of IL-C8F13 solution in DMF (5 mg/mL) was then added dropwise under magnetic stirring (mass ratio of IL/GO = 5/1). The precipitant can be observed immediately. The solid was then separated by centrifugation and washed with water/DMF (2v/1v) 3 times and then water twice to remove the excess IL and DMF. The final product was obtained by freeze-drying denoted as GO-IL.

To prepare rGO-IL, a solution of GO-IL in DMF (0.5 g/L) was prepared by

ultrasonic treatment for 1 h. The solution was then reduced by hydrazine hydrate (4 times in mass) at 95 ^{o}C for 3 h. The homogenous black suspension was concentrated and then water was added into the flask to obtain precipitates. After washing withwater/DMF (2v/1v) and then water for several times to remove the excess hydrazine and DMF, the product rGO-IL was dried by lyophilization.

3.2.1.5 Characterizations

^{1}H, ^{13}C, ^{19}F and ^{31}P NMR spectra were recorded in $CDCl_3$ on a 400 MHz Bruker apparatus.

The X-ray diffraction (XRD) data were collected using a Bruker D8 Advance X-ray diffractometer. A bent quartz monochromator (before the sample) was used to select the Cu Kα_1 radiation (λ = 0.15406 nm) and run under operating conditions of 45 mA and 33 kV in a Bragg-Brentano geometry. The angle range scanned is $1^{o}< 2\theta<30^{o}$ for film composites and $1^{o}< 2\theta<50^{o}$ for graphite, GO and rGO powders at a scanning speed of 2^{o}/min with a step interval of 0.02^{o}.

Fourier transform infrared (FTIR) spectra were recorded at room temperature on a Nicolet iSO10 Thermo Scientific spectrometer. And the attenuated total reflectance (ATR) modes (a diamond crystal was used) were performed to determine each characteristic band. All spectra were recorded at 2 cm^{-1} resolution and 32 scans from 4000 to 650 cm^{-1} for ATR mode.

Thermogravimetric analysis (TGA) was performed on a Q500 thermogravimetric analyser (TA instruments). The samples were heated from RT to 1000 ^{o}C at 10 K min^{-1} under nitrogen flow.

Raman spectra were recorded on a DXR 532 nm Filter system spectrometer equipped with an integral microscope and He-Ne laser (532 nm) was used as the excitation source.

3.2.2 Results and discussion

3.2.2.1 Synthesis of fluorinated phosphonium IL (IL-C8F13)

The chemical structure and purity (~100%) of IL-C8F13 was confirmed by ^{1}H,

^{13}C, ^{19}F and ^{31}P NMR spectra in Figure 3-3. The results are shown in detail as follows.

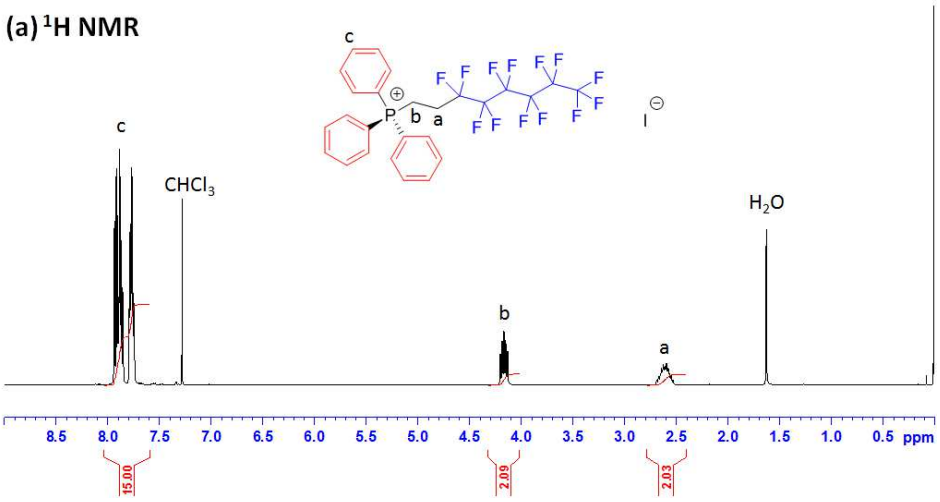

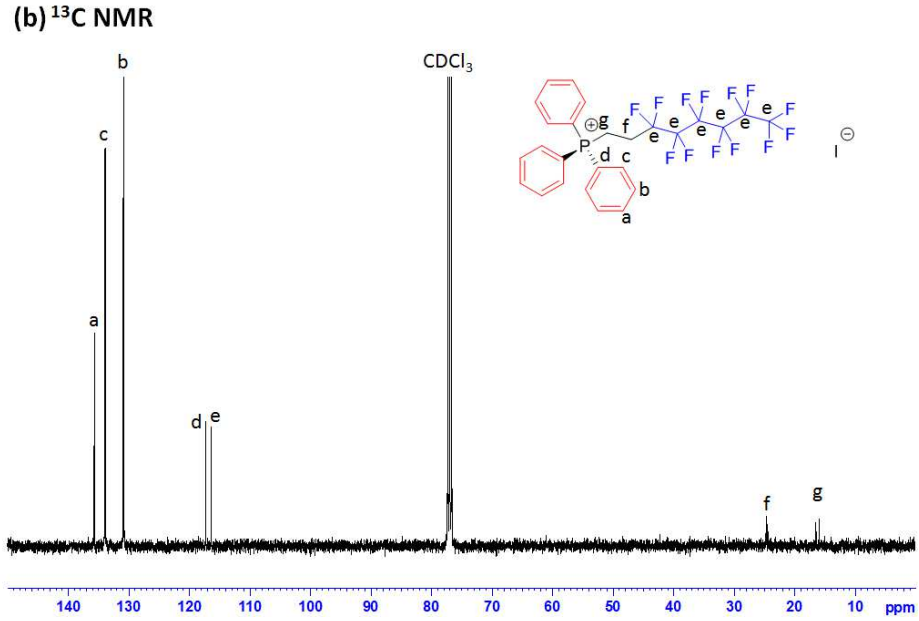

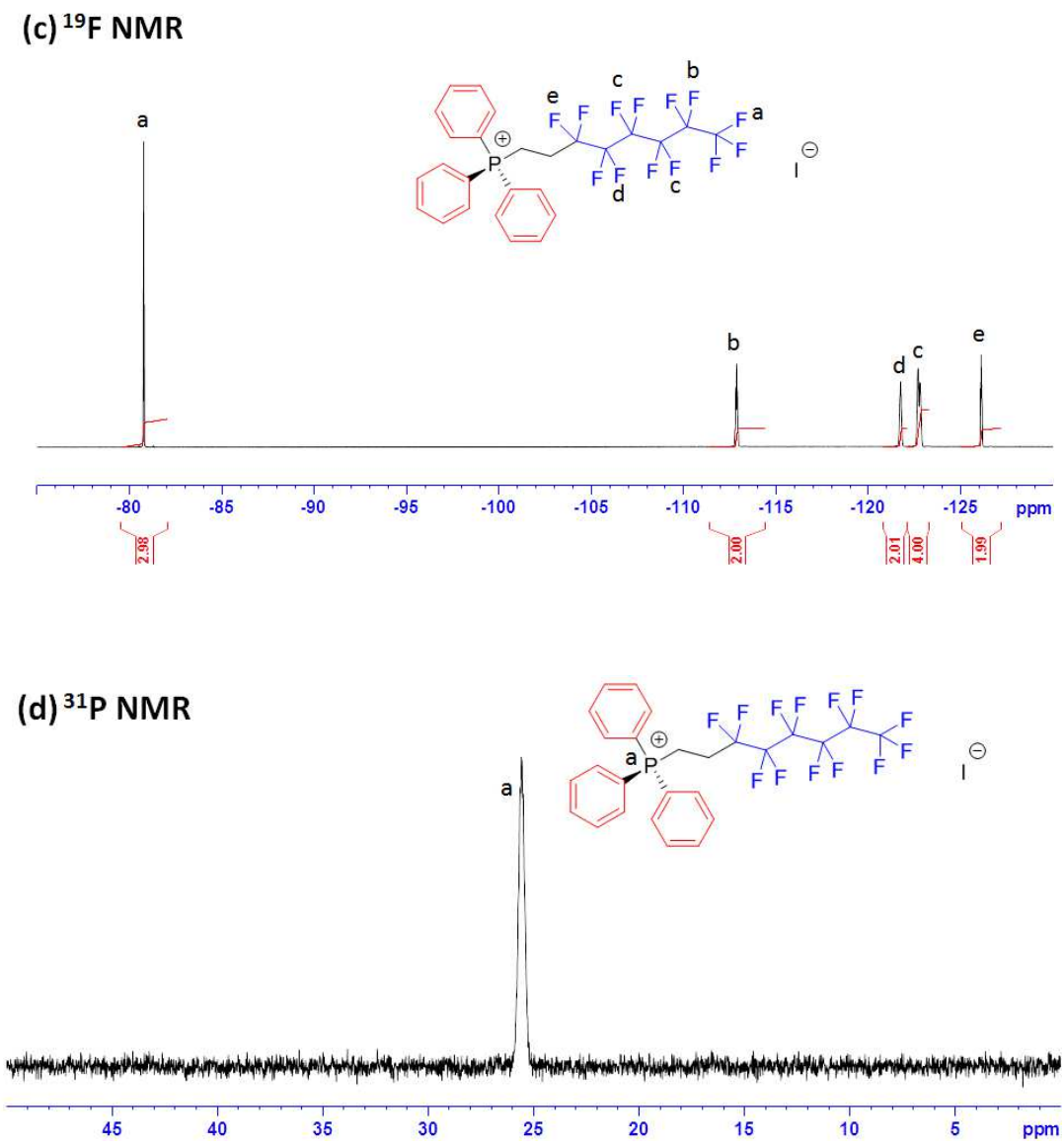

Figure 3-3: ^{1}H (a), ^{13}C (b), ^{19}F (c) and ^{31}P (d) NMR spectra of IL-C8F13

^{1}H NMR ($CDCl_3$, 400 MHz, ppm): δ = 2.52 ~ 2.73 (m, 2H, CH_2CF_2), 4.11 ~ 4.26 (m, 2H, CH_2P), 7.73 ~ 8.00 (m, 15H, aromatic H). ^{13}C NMR ($CDCl_3$, 400 MHz, ppm): δ = 135.73, 135.70, 133.94, 133.84, 130.92, 130.80 (C=C, aromatic C), 117.3 (aromatic C-P), 116.44 (CF_2, CF_3), 24.88, 24.65, 24.42 (CH_2CF_2), 16.49, 15.93 (CH_2P). ^{19}F NMR ($CDCl_3$, 400 MHz, ppm): δ = -80.70 ~ -80.83 (t, 3F, CF_3), -112.70 ~ -113.03 (m, 2F, $CF_2CF_2CF_2CF_2CF_2CF_3$), -121.57 ~ -121.92 (s, 2F, $CF_2CF_2CF_2CF_2CF_2CF_3$), -122.48 ~ -122.99 (m, 4F, $CF_2CF_2CF_2CF_2CF_2CF_3$), -125.96 ~ -126.25 (m, 2F, $CF_2CF_2CF_2CF_2CF_2CF_3$). ^{31}P NMR ($CDCl_3$, 400 MHz, ppm): δ = 25.61 (s).

3.2.2.2 Characterization of GO, rGO, GO-IL and rGO-IL

(1) TGA

Figure 3-4 presents the thermogravimetric (TG) plots of graphite, GO and rGO, together with their derivatives, *i.e.*, the so-called differential thermogravimetry (DTG) plots. There is only a very broad peak beginning from 700 ^{o}C in the DTG curve of graphite due to the pyrolysis of carbon backbone of graphite. However, for GO, it is easy to observe a gradual mass loss in the range from RT to 100 ^{o}C. One possibility is corresponding to the gradual removal of absorbed water because of the hydrophilic oxygen-containing functionalities covering surface of GO. Another possibility is due to the degradation of carboxylic acid on the edge of graphene plane. The maximum weight loss taking place around 175 ^{o}C in the DTG curve of GO is attributed to the decomposition of labile oxygen functional groups, and another relatively slow and steady mass loss beginning around 200 ^{o}C until 300 ^{o}C can be assigned to the elimination of more stable oxygen functionalities [16]. Moreover, the weight loss starting from 600 ^{o}C is ascribed to the carbon backbone sublimation [17,18]. After chemical reduction, the thermal stability of rGO has been improved compared to GO as represented in two aspects: (1) rGO did not show a gradual mass loss from RT to 100 ^{o}C because of the hydrophobic surface of rGO after reduction, and the peaks corresponding to the weight loss of oxygen functional groups become broader compared with those of GO due to the elimination of oxygenated groups by chemical reduction; (2) the carbon backbone decomposition of rGO initiates around 700 ^{o}C which shows 100 ^{o}C of retardance compared to GO.

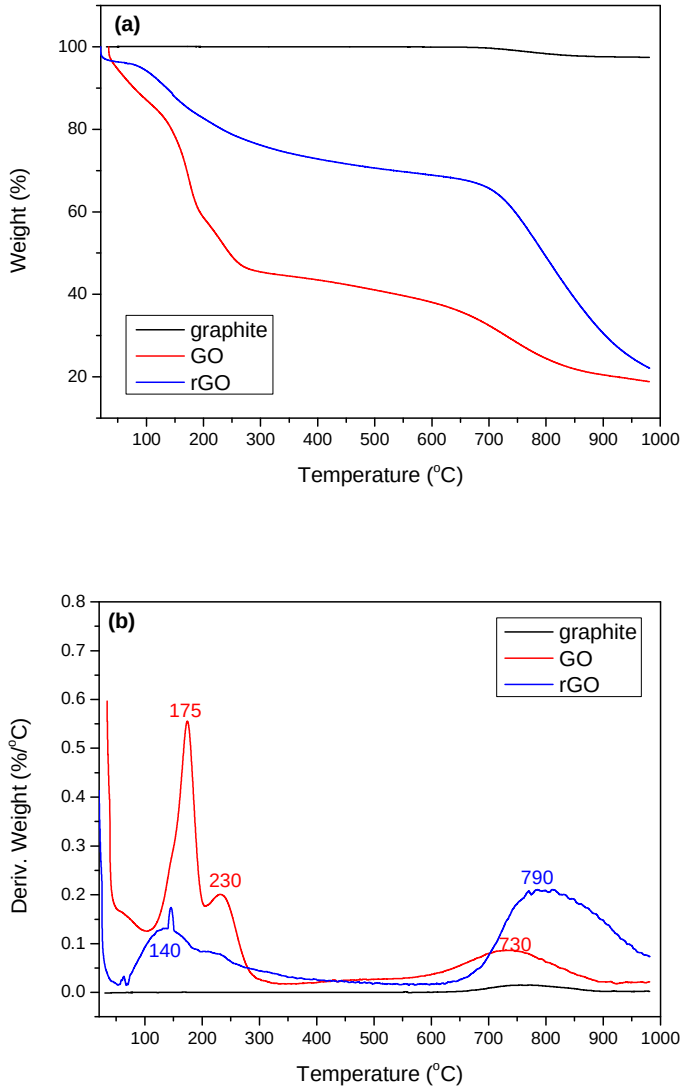

Figure 3-4: TGA (a) and DTG (b) thermograms of graphite, GO and rGO under N_2 atmosphere

Unfortunately, we cannot see the degradation peaks around 335 °C corresponding to ILs either from the DTG curves of GO-IL shown in Figure 3-5b or from rGO-IL shown in Figure 3-5d. One possible explanation is that the amount the ILs attached onto the graphene surface is so limited that the observations of their degradation peaks are difficult. Another possibility is that the degradation corresponding to IL could be accompanied with the degradation assigned to the GO and rGO in the range of temperature from 100 °C to 400 °C.

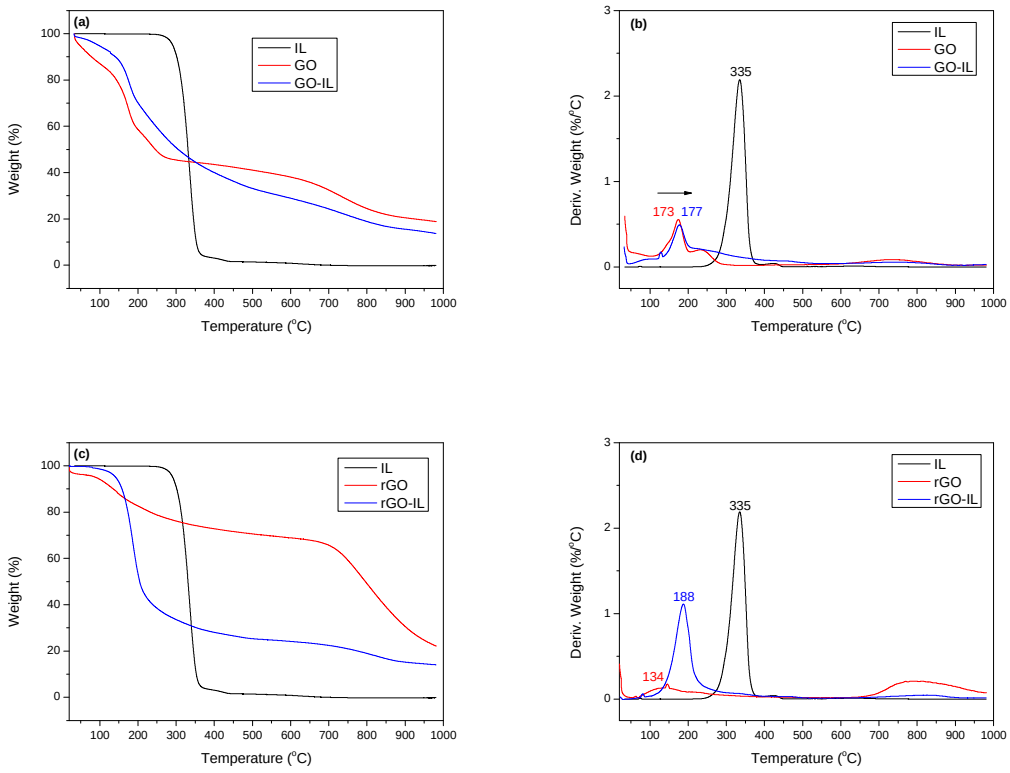

Figure 3-5: TGA (a) and DTG (b) curves of GO, IL, GO-IL; TGA (c) and DTG (d) curves of rGO, IL, rGO-IL under N_2 atmosphere

However, we could observe a slightly promoted influence of ILs on the thermostability of GO and rGO. As shown in the TGA and DTG curves in Figure 3-5, IL only shows a rapid weight loss process from 250 °C to 400 °C with a maximum weight loss at 335 °C. Moreover, it is interesting to see the higher-temperature shifting of the maximum weight loss in the DTG curves of GO-IL and rGO-IL compared with GO and rGO, respectively. On the one hand, this retardant effect of IL on the degradations of GO and rGO could reflect the interactions existing between IL and GO sheets or rGO ones. On the other hand, the fluorinated IL to some extent improves thermostabilities of GO-IL and rGO-IL due to the relatively thermally stable nature of phosphonium IL with fluorinated chains.

(2) XRD

The XRD patterns can be used to verify the preparation of GO, rGO, GO-IL and rGO-IL. As shown in Figure 3-6, the pattern of graphite displays a (002) peak at $2\theta = 26.5^{o}$ characterizing the π-stacking interlayer distance (d) of 3.4 Å, which is very

similar as reported one (d = 3.4 Å) in the literature[19,20,21,22,23].

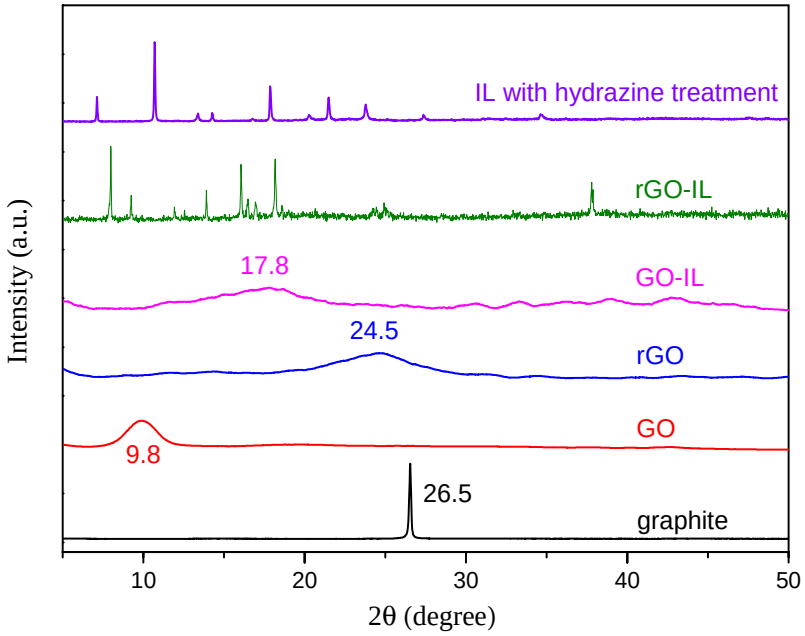

Figure 3-6: XRD patterns of graphite, GO, rGO, GO-IL, rGO-IL and IL.

Moreover, the average numbers of layers were calculated by the classic Debye-Scherrer equation:

$$t = \frac{0.89\lambda}{\beta\cos\theta}$$

$$n = \frac{t}{d}$$

where t = thickness of ordered stack of graphic sheets; λ = 1.5406 Å; β = full width at half maximum (FWHM) in radian; n = number of graphene layers; d = interlayer spacing. Around 158 layers of graphic sheets are assembled for graphite, which indicates a multi-layered stacking structure for pristine graphite (all parameters from XRD patterns are summarized in Table 3-1).

Table 3-1: Summary of parameters from XRD patterns

sample	2θ (°)	d (Å)	β (°)	t (Å)	n
graphite	26.5	3.4	0.15	538.3	158.3
GO	9.8	9.0	2.19	36.0	4.0
rGO	24.5	3.6	5.70	14.1	3.9
GO-IL	17.8	5.0	5.63	14.1	2.8

After oxidization-induced expansion, the pattern of GO exhibits a (002) peak at 9.8° corresponding to an interlayer spacing of 9.0 Å which is in good agreement with the reported ones in the literature (d = 9.1 Å) [20,21]) because oxygenated functional groups generated on the GO surface increase the interlayer distance. The numbers of graphic layers decreased dramatically as low as around 4 layers for GO, indicating a well exfoliated few-layer graphene structure. Nevertheless, the emergence of a new broad (002) peak at 24.5° in the XRD pattern of rGO indicates a reduced interlayer spacing of 3.6 Å (very similar as reported ones (d = 3.6 Å)) [19,22]) due to the elimination of most oxygen-containing functional groups. After reduction, rGO still exhibits an exfoliated few-layer state (around 4 graphic layers), which is also significantly different from the pristine graphite [22].

As shown in Figure 3-6, GO-IL has a weak and broad (002) peak at 17.8° with a decreased interlayer spacing of 5.0 Å in comparison with GO, and its decreased interlayer spacing could be ascribed to the ILs absorbed on the surface of GO. The graphic layers calculated for GO-IL further decreased to around 3, suggesting a positive influence of IL on the exfoliation. It is obvious to see a significantly different XRD pattern for rGO-IL: the broad diffraction of (002) peak of rGO at 24.5° disappeared but only some sharp peaks were observed. These sharp peaks, on the one hand, could be partially due to the ILs modified on the rGO. Note that the ILs in XRD experiments are with the same hydrazine reduction treatment (95 °C for 3 h in DMF) as the one used for rGO. One the other hand, the topology of exfoliated rGO-IL could

have become highly disordered during non-covalent functionalization with IL, thus, the typical XRD diffraction pattern of rGO cannot be observed anymore for rGO-IL [21].

TGA and XRD results can be used to verify the successful preparations of GO and rGO. However, we cannot use them to corroborate the attachement of ILs onto the surface of graphene. So, we expect to use the following techniques such as ATR-FTIR spectroscopy, Raman spectroscopy and solubility experiments to further prove it.

(3) ATR-FTIR

The spectrum of pristine graphite shown in Figure 3-7 has two vibration peaks at 1635 and 1577 cm^{-1} ascribed to the C=C skeletal vibrations [24]. After oxidative exfoliation, GO displays a new stretching vibration of epoxide at 1257 cm^{-1}, the carbonyl peak at 1732 cm^{-1}, the broad peak of hydroxyl around 3200 cm^{-1}, and the sp^2 hybridized C=C vibration band at 1626 cm^{-1}, definitely confirming the successful synthesis of GO. After the reduction by hydrazine, the epoxide peak at 1257 cm^{-1} was absent and the –OH peak around 3000 cm^{-1} has been weakened and much more broad than that of GO, but there still exist a weak peak at 1720 cm^{-1} corresponding to C=O whose intensity is much lower than that of GO. This result indicates that the hydrazine reduction can eliminate most of the oxygenated functionalities such as hydroxyls and epoxides, while leaving a number of carbonyl and carboxyl groups at the edges [25]. The relative intensity ratios of polar groups to C=C vibration (C=C peak is reasonably used as the reference for the normalization of all peaks because the sp^2 C=C skeleton is the primary structure for either GO or rGO and also keeps relatively more stable during the oxidation and reduction compared to those oxidative groups) are shown in Table 3-2. It is obvious to see the decreased intensity ratios of polar groups to C=C band for rGO compared to GO, indicating the largely reduced oxidation degree after the chemical reduction. Note that high-wavenumber shifting of C=C backbone from 1626 cm^{-1} to 1543 cm^{-1} after reduction is due to the transformation from C-sp^3 to C-sp^2 backbone, which was also observed in the literature [26].

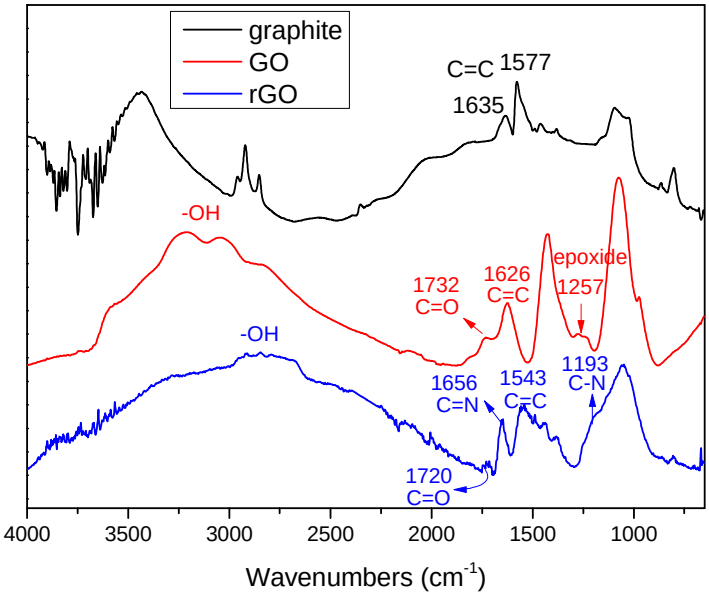

Figure 3-7: ATR FTIR spectra of graphite, GO and rGO

Table 3-2: Intensity ratios of polar groups to C=C band for GO and rGO

Sample	-OH/C=C	C=O/C=C
GO	3.9	2.2
rGO	1.8	0.2

The oxygen-containing functional groups of rGO were partially eliminated and nitrogen species were generated simultaneously during the hydrazine reduction process. A new band emerges at 1656 cm^{-1} in the FTIR spectrum of rGO in Figure 3-7 corresponding to C=N, indicating that covalent bond-forming reactions have occurred to give rise to hydrazone ($C=N-NH_2$) [27]. Additionally, the appearance of new peak at 1193 cm^{-1} which is the characteristic stretching vibration of C-N bond from aromatic amines indicates the formation of hydrazide ($-CONHNH_2$) obtained from the reaction between hydrazine and carboxyl. The weakened and broadened -OH peak also contributes the amidation process to partially modify the surface functionality from carboxyl (-COOH) to hydrazide ($-CONHNH_2$).

The modification of the surface of GO and rGO with ILs can be further confirmed by FTIR spectra in Figure 3-8. For both GO-IL and rGO-IL, the characteristic peaks at 1587, 1485, 1437, 1144, 810, 741, 725 and 688 cm^{-1} corresponding to IL alone can be found, indicating that ILs have been functionalized on the surfaces of GO or rGO. Moreover, the C=C backbone vibration shows an obvious blue-shifting from 1626 cm^{-1} to 1649 cm^{-1} for GO-IL in Figure 3-8(a) and from 1543 cm^{-1} to 1556 cm^{-1} for rGO-IL in Figure 3-8(b), respectively, further corroborating the successful modification of GO or rGO by ILs due to the specific interactions between ILs and GO or rGO.

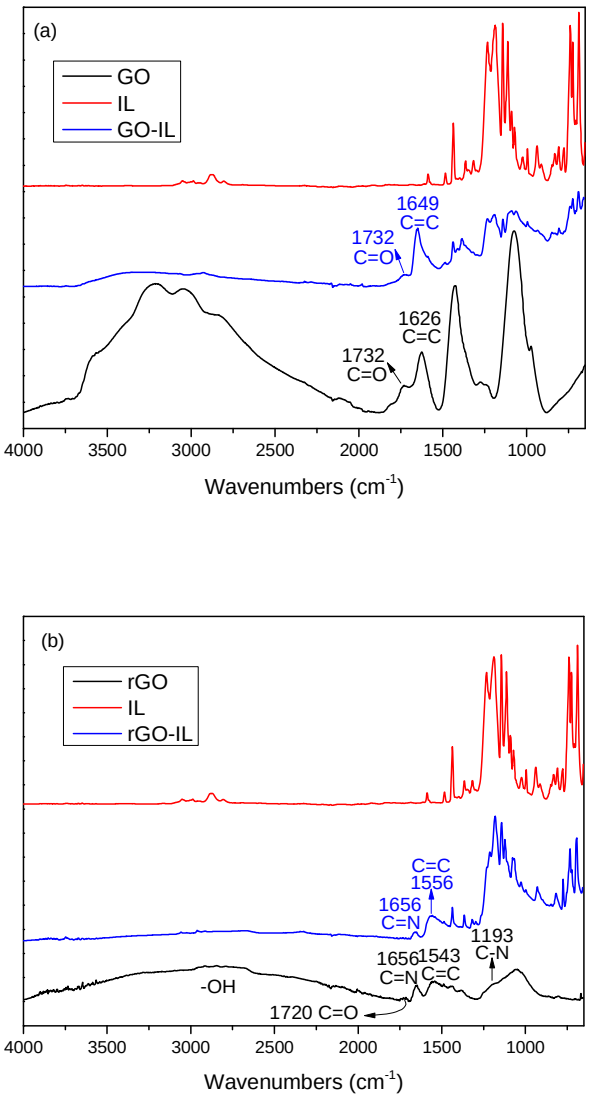

Figure 3-8: ATR FTIR spectra of GO, IL, GO-IL (a) and rGO, IL, rGO-IL (b)

(4) Raman spectroscopy

Figure 3-9 shows the Raman spectra of graphite, GO, rGO, GO-IL and rGO-IL. The D band at ~1340 cm^{-1} and G band at ~1580 cm^{-1} characteristic of graphene are evidenced. Generally, the D band corresponds to the first-order zone boundary phonons only observed in defected graphene, while G band associates with the in-plane optical vibration [28]. The intensity ratio (I_D/I_G) of the D band and G band is usually used to qualitatively characterize the defect density, namely, the lower value of I_D/I_G, the higher perfection of sp^2-hybridized structure. A strong G band at 1571 cm^{-1} and a weak D band at 1342 cm^{-1} can be found in the Raman spectrum of graphite with a very low I_D/I_G value of 0.069, indicating the primary sp^2-hybridized carbon atoms in graphite without a significant number of defects (summarized in Table 3-3).

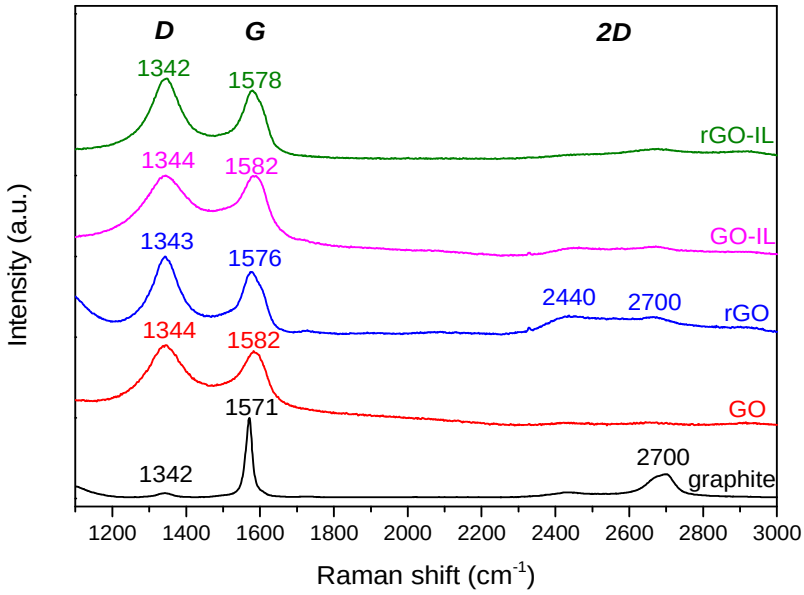

Figure 3-9: Raman spectra of graphite, GO, rGO, GO-IL and rGO-IL

Table 3-3: Raman shifts of D band, G band and 2D band for graphite, GO, rGO, GO-IL and rGO-IL

Sample	D band (cm^{-1})	G band (cm^{-1})	I_D / I_G	2D band (cm^{-1})
graphite	1342	1571	0.069	2700
GO	1344	1582	1.056	---
rGO	1343	1576	1.110	2440, 2700
GO-IL	1344	1582	1.003	---
rGO-IL	1342	1578	1.113	---

After oxidation, a very obvious D band appears at 1344 cm^{-1} for GO, whereas the G band of GO is broadened and shifted to a higher wavenumber position at 1582 cm^{-1}. The increase of the D band demonstrates the introduction of defect-like domains in graphene structures due to the oxidative groups, and thus the corresponding I_D/I_G ratio dramatically increases to 1.056. Further increased defect density with the I_D/I_G ratio of 1.110 was observed after reduction by hydrazine in the Raman spectrum of rGO. Moreover, the G band slightly moved to a lower wavenumber position, which means the recovery of sp^2 domain like graphite with a certain extent by eliminating oxidative groups. The increase in the defect density of rGO is ascribed to the fewer in-plane sp^2 domains upon the incorporation of nitrogen atoms on the edge of rGO after reduction by hydrazine [29]. The Raman spectra of GO-IL and rGO-IL show very similar D and G bands and I_D/I_G ratios very close to those of GO and rGO, respectively, indicating that no further defect structure incorporation in graphene sheets was highlighted after the modification of IL on the surface of GO and rGO.

In addition, another important profile of graphite in the Raman spectrum is the presence of a 2D band at 2700 cm^{-1}, which is used to evaluate the structural parameters of the c-axis orientation, since this band is very sensitive to the number of layers (<5 monolayers) and stacking order of the graphite along the c-axis [30]. In Figure 3-9, a visible single peak at 2700 cm^{-1} can be found for pristine graphite, indicative of stacking graphitic multilayers. However, after the chemical oxidation

process, GO shows no peaks in the 2D band at all because of the predominant structural changes in the graphite lattice due to the formation of different types of oxygenated functional groups intercalated between the graphitic layers at the basal plane and also at the edges, leading to the breaking of the stacking order [31,32]. When GO was reduced by hydrazine, rGO redisplays a very broad 2D band with a new generated lower-wavnumber peak at 2440 cm^{-1} except to 2700 cm^{-1} one. This reappearance of 2D band is due to the recovery of ordered graphitic stacking after eliminating the oxidative groups. Although the reaggregation of graphene sheets occurred for rGO, the number of layers still lower than 5, and the lower-wavenumber shifting indicates that the number of graphitic layers for rGO is lower than that of graphite, which has been accepted in the literature [33]. However, it is interesting to see the dramatic suppression of 2D band for rGO-IL. This behavior could suggest the successful modification of rGO by IL due to the breaking of the ordered multilayer structure along the c-axis, resulting in randomly dispersion of graphene sheets thanks to the specific interactions between IL and graphene.

(5) Solubility

The modification of GO by IL-C8F13 can be easily confirmed by the dispersion of GO-IL in different solvents (see photos in Figure 3-10). First, the solubility of IL in water and DMF was experimentally compared. Due to the hydrophobic nature of IL containing a fluorinated chain, IL was found to be not soluble in water but in DMF. Second, note that a mixed solvent water/DMF (2v/1v) was used to wash out of unmodified free IL during the modification because it was found that IL can be dissolved in this mixed solvent but not for GO-IL. After modification, GO-IL becomes precipitate in water due to the change of surface profile. It is very preferable that GO-IL can still form a good dispersion in DMF at nanoscale because DMF is also a good solvent for P(VDF-CTFE) at the concentration used in the following preparation of polymer composites by solution casting method.

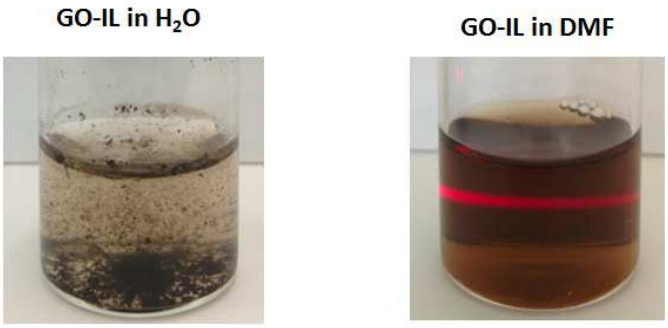

Figure 3-10: Dispersibility of GO-IL in water and DMF (c = 0.5 g/L at RT). Note that GO-IL cannot disperse in water even after 8 hours of ultrasonication treatment

It is well-known that the direct reduction of GO will result in inevitable aggregations due to the loss of polar groups on the surface, which is not expected to obtain a good dispersion in the polymer matrix within the cosolvent. Therefore, Poulin *et al.* used bile salts (BS) as surfactants to stabilize the rGO sheets against aggregation, still keeping the ability to form water-based liquid crystals of graphene [34]. Moreover, the authors also reported the use of a diblock copolymer polyaminopropylmethylsiloxane-*b*-polydimethylsiloxane (PAPMS-*b*-PDMS) as stabilizer to produce liquid crystals of GO in non-plar solvent (diethyl ether) *via* electrostatic attractions. This well-dispersed suspension can serve as the precursor to prepare composites with PDMS. The resulting composites were then thermally reduced to restore the electrical conductivity, which exihibits a very high dielectric constant with low loss (ε = 753, tanδ = 0.4 at 100 Hz) [35].

In this work, IL was modified on the surface of rGO, and thus, rGO-IL shows a very stable colloid dispersion in DMF even for a long time (~1 month), while the counterpart rGO one is hard to be dispersed well even under the same ultrasonic treatment and becomes total precipitates only in 1~2 h (see photos in Figure 3-11). This imperfect dispersion of rGO in DMF due to the absence of IL modification indicates that rGO cannot be used to prepare composites with P(VDF-CTFE) with a good distribution at nanoscale. Thus, IL modified on the surface of rGO plays a key role in the dispersion of rGO in a polar solvent. The perfect dispersion in a cosolvent (DMF) for both filler and polymer matrix is very important to the preparation of

conductive rGO fillers-incorporated polymer matrix P(VDF-CTFE) with a good dispersion. Therefore, in the following *subsection 3.3*, only P(VDF-CTFE) composites containing GO, GO-IL and rGO-IL as fillers are prepared but not for those containing rGO due to the bad dispersion of rGO in cosolvent DMF.

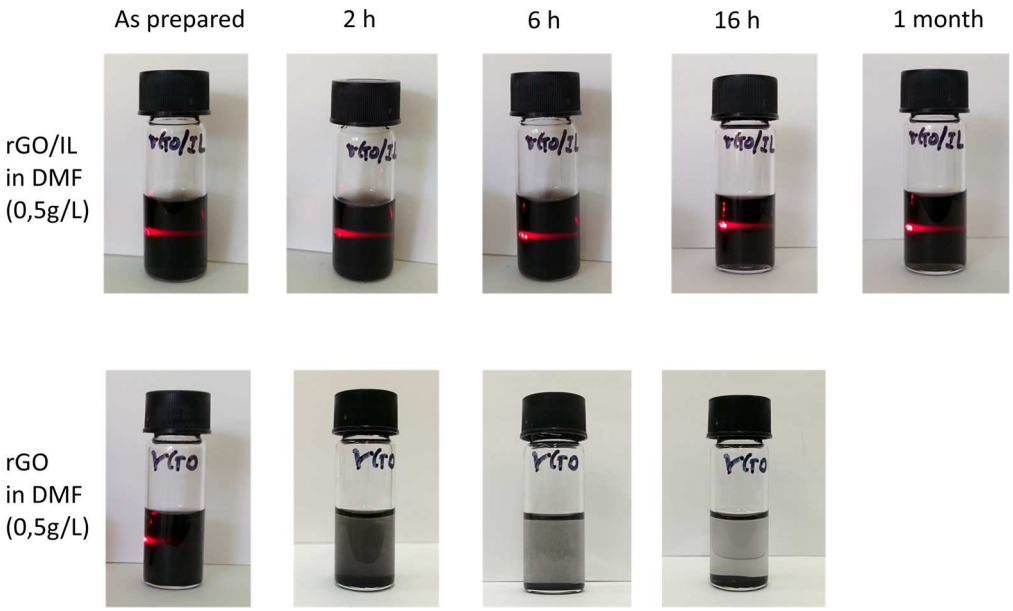

Figure 3-11: Dispersibility of GO in water and DMF (0.5 g/L at RT)

3.2.2.3 New interaction model: Hydrogen bond C-F…H-N between rGO and IL

As we mentioned in the FTIR spectroscopy above, the blue shifting of C=C vibration after IL modification confirms the interaction between IL and graphene which is the driving force to modify the surface of GO or rGO by IL. First, thanks to three phenyls in the cation structure of IL, the π-π or cation-π interaction between IL and GO or rGO is one of the interacting forces [10]. This π-π or cation-π interaction can be reflected by the blue shifting of breathing vibration of benzene rings of IL at 1436, 1485 and 1587 cm^{-1} as shown in Figure 3-12a to 1439, 1489, and 1592 cm^{-1} for GO-IL, and to 1438 and 1489 cm^{-1} for rGO-IL, respectively.

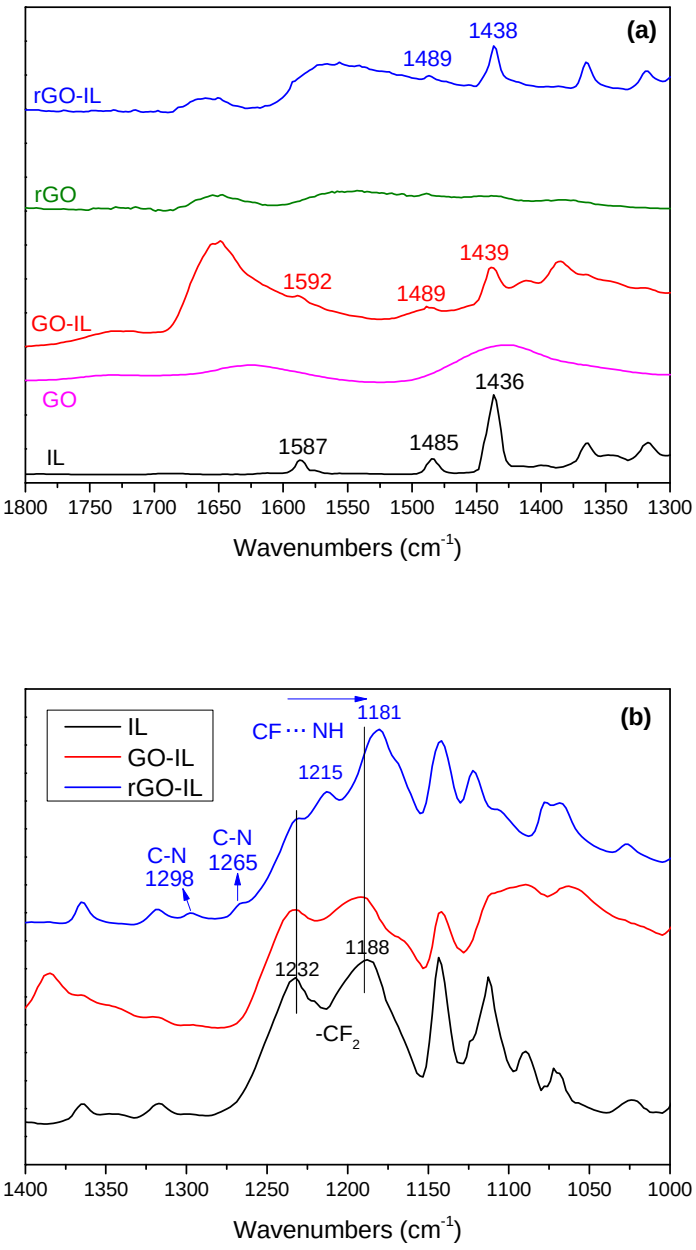

Figure 3-12: ATR FTIR spectra of IL, GO-IL and rGO-IL in the range of wavenumbers from 1300 to 1800 cm^{-1} (a) and from 1400 to 1000 cm^{-1} (b)

Second, the ionic interaction also contributes to the bonding between GO and IL. It is well-known that an alkaline solution adjusted by NaOH can capture protons of COOH groups on the edge of GO, generating negatively charged carboxylate COO^-. Through the following cation-exchange between Na^+ and cation of IL, IL is thus bonded on the surface of GO *via* ion interaction [36]. The ionic interaction between carboxylate and IL can be verified by the relative intensity attenuation of the broad –

OH band in COOH groups around 3000 cm^{-1} in Figure 3-8a after the IL modification onto the surface of GO.

However, once the chemical reduction of GO by hydrazine occurs, the interaction model between rGO and IL largely deviates from that between GO and IL because of the partially remaining oxygen functional groups and nitrogen doping of rGO surface after the oxygen removal process by hydrazine. On the one hand, as shown in Figure 3-8b, the very broad –OH band in COOH groups in the range of wavenumbers from 3300 to 3500 cm^{-1} in rGO become to be hardly observed in rGO-IL, indicating that there are some ILs interacting with residual COO^- groups at the edge of rGO *via* ionic interaction model. On the other hand, as we mentioned above, the surface of rGO became nitrogen doped: hydrazone and hydrazide were produced during the treatment of hydrazine reduction, and these two nitrogen-containing species can also be obtained during the preparation of rGO-IL. The newly generated hydrazone and hydrazide are expected to be responsible for the C=N vibration at 1656 cm^{-1} (in Figure 3-8b) and C-N bonds at 1265 cm^{-1} or 1298 cm^{-1} observed in FTIR spectra of rGO-IL in Figure 3-12b. What's more, we have carried out a parallel experiment to prove that IL-C8F13 is chemically stable under the reduction conditions by hydrazine (95 ^oC for 3 h in DMF with the same concentration), which can be confirmed by the identical NMR spectra before and after hydrazine treatment (see the ^1H, ^{13}C, ^{19}F, ^{31}P NMR spectra in Annexe). Therefore, the newly formed NH-containing groups after reduction is considered to be involved in the newly generated H-bond interaction with C-F bond of fluorinated IL, and this type of N-H…F-C H-bonding interaction has been confirmed by Chaudhari *et al* [37]. Moreover, two strong vibration bands at 1232 and 1188 cm^{-1} assigned to the asymmetric and symmetric stretch of $–CF_2$, respectively, [38] of IL alone show no change for GO-IL but a very obvious red-shifting to 1215 cm^{-1} and 1181 cm^{-1}, respectively for rGO-IL (see Figure 3-12b), confirming the H-bonding interaction of N-H…F-C experimentally. Consequently, the increased ratio of this new H-bonding model is accompanied with the decrease of ionic interaction one in the preparation of rGO-IL

in which the –COOH groups are partially reduced and graphene surfaces become nitrogen doped. It is the H-bonding interaction newly generated between rGO and IL combining the original ionic interaction that contribute the reliable and stable modification of IL on the surface of rGO which cannot be removed by washing for many times. The different interaction models of GO-IL and rGO-IL are generally presented in Scheme 3-2. In addition, the difference in the interaction model between GO-IL and rGO-IL could explain the phenomenon that the corresponding IL absorption peaks of rGO-IL is more obvious than those of GO-IL from FTIR results in Figure 3-8. The reduction treatment by hydrazine has converted the carbonyl and carboxyl groups into hydrazone and hydrazide, respectively, which increased interacting sites on the surface of rGO with IL, while for GO, only carboxyl groups on the edge of GO could supply interacting sites with IL.

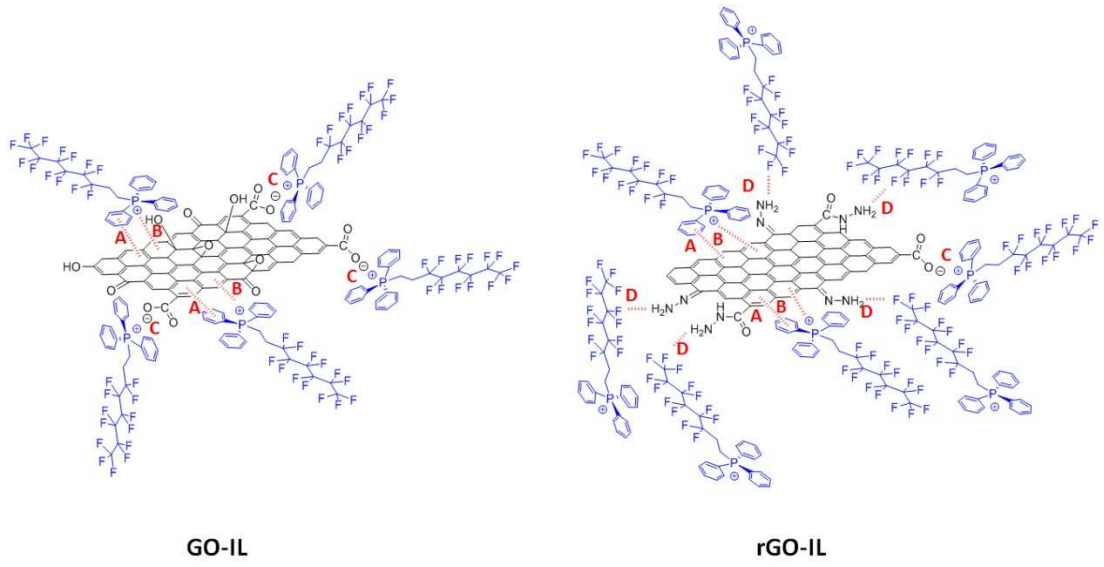

Scheme 3-2: Difference in the interaction model between GO-IL and rGO-IL with ILs: (A) π-π interaction; (B) cation-π interaction; (C) ionic interaction; (D) hydrogen bonding interaction

3.3 Preparation and characterization of P(VDF-CTFE) composite films containing GO, GO-IL and rGO-IL

3.3.1 Experimental section

3.3.1.1 Raw materials

P(VDF-CTFE) copolymer containing 8 wt% of CTFE was purchased from Arkema. The solvent DMF was provided by CARLO ERBA (France) and used as received.

3.3.1.2 Preparation of P(VDF-CTFE)/GO, P(VDF-CTFE)/GO-IL and P(VDF-CTFE)/rGO-IL composite films

A desired amount of GO, GO-IL or rGO-IL was ultrasonically dispersed in DMF for 1h, and then P(VDF-CTFE) was added into the suspension. After magnetic stirring for 1 h, and ultrasonication for more 2 h, the thin films were casted on a glass plate by doctor-blade. The resulting composite films were firstly dried at 60 ^{o}C in air oven overnight, and then under vacuum at 80 ^{o}C for 48 h to remove the residual solvent (no residual DMF shown in the ^{1}H NMR spectra of final films in Annexe). Composite films, denoted as P(VDF-CTFE)/GO, P(VDF-CTFE)/GO-IL and P(VDF-CTFE)/rGO-IL, with different compositions were prepared (see the compositions in Table 3-4). According to the litterature, the percolation threshold of 0.662 wt% is observed for phosphonium IL modified-rGO/PVDF composites [10], so the weight percentages of IL modified graphene incoporated within polymer matrix are finely adjusted from 0.27 wt% to 2.70 wt% in this work. In order to investigate the effect of IL-C8F13 on the copolymer alone, the composites containing 0.5, 1 and 2 wt% of IL-C8F13 were also prepared.

Table 3-4: Different compositions of P(VDF-CTFE) composites processed in this work

Sample	Filler content (wt%)						
P(VDF-CTFE)/IL	0.5	1	2				
P(VDF-CTFE)/GO	0.27	0.55	0.81				
P(VDF-CTFE)/GO-IL	0.27	0.55	0.81	1.08	1.36	2.16	2.70
P(VDF-CTFE)/rGO-IL	0.55	0.81	1.36	1.62	1.89	2.16	2.70

3.3.1.3 Characterizations

Differential scanning calorimetry (DSC) analyses were conducted on a thermoanalyzer system calibrated by In standard sample before each measurement, model Q20 (TA Co. Ltd., USA), under nitrogen atmosphere at a rate of 10 ^{o}C/min. Four scans (heating/cooling/heating/cooling, separated by a 10 min isotherm) were realized for each sample from -80 to 180 ^{o}C. All nonisothermal crystallization temperatures (T_c) from the first cooling run and melting temperatures (T_m) from the first and second heating run reported here correspond to the summit point of each peak.

Transmission electron microscopy (TEM) was performed at the Center of Microstructures (Universite de Lyon) using a Philips CM 120 field emission scanning electron microscope with an accelerating voltage of 80 kV. The samples were cut using an ultramicrotome equipped with a diamond knife to obtain 60 nm thick ultrathin sections. And the stained sections by RuO_4 were set on copper grids for observation.

Scanning electrical microscopy (SEM) was used to observe fractured cross-section morphologies of composite materials. The samples were fractured in liquid nitrogen, and thin gold layers were deposited on the fractured surfaces of the samples prior to observations.

Dynamic mechanical analysis (DMA) was investigated by a Rheometrics

Solid Analyzer RSA II at a frequency of 10 Hz. The heating rate was 3 K/min for the temperature range from -125 to 120 ^{o}C under a nitrogen atmosphere.

Dielectric analysis (DEA) measurements were performed using a Solartron Modulab XM analyser system. Circular Au electrodes with a diameter of 1cm were sputtered on thin films as 2×2 cm^2 with the thickness of 30-60 μm for the measurements. Measuring is done after heating steps of 3 °C under the frequency of 10^6~ 10^{-1} Hz in the temperature range from -80 to 120 ^{o}C and V_{RMS} = 1V. The model used for measurement is metal-insulator-metal capacitor.

The direct-current (DC) electrical conductivities of composites with GO or IL at different temperatures were measured with a Keithley 2636 electrometer, at least two parallel measurements for each composition were conducted to verify the reproducibility. The temperature of the sample was controlled by the air-circulationoven from room temperature (RT) to 100^{o}C, and a thermometer was used to monitor the temperature of air-circulation oven. The sample preparation is same as that used in DEA experiments.

3.3.2 Results and discussion

3.3.2.1 Dispersion morphology

The fractured cross-section morphologies of composite materials containing IL, GO, GO-IL and rGO-IL by SEM are shown in Figure 3-13. The tortuous morphology of each sample reveals a plastic deformation witnessing of the excellent adhesions of fillers with polymer matrix. Any fillers aggregates cannot be detected, highlighting a rather homogeneous dispersion state.

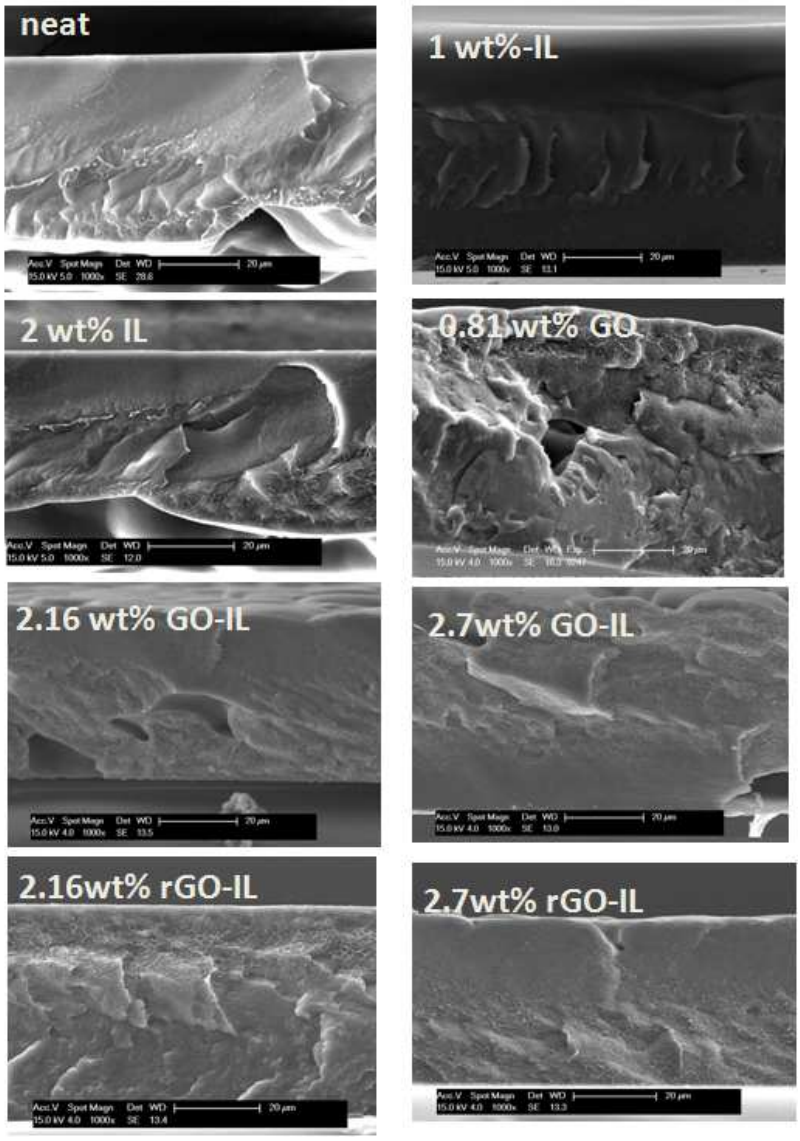

Figure 3-13: SEM images of fractured cross-section of composite films containing IL, GO, GO-IL and rGO-IL

However, we cannot see graphene sheets within polymer matrix by fractured cross-section images of SEM. To further evaluate the dispersion state of GO-IL and rGO-IL within polymer matrix, TEM study has been employed. In Figure 3-14(a) & (c), it is apparent that the GO-IL sheets are well individually and randomly dispersed in P(VDF-CTFE) matrix, whereas some aggregates of rGO-IL are observed within polymer matrix from TEM images shown in Figure 3-14(b) & (d) for composites with rGO-IL.

The formation of the enriched rGO-IL zones within polymer composites, on the one hand, could be due to the reduction of oxidative groups from GO-IL, which to

some extent induces more restackings of graphene layers between which there are almost no oxidative groups. On the other hand, it could be ascribed to the change of interaction model between graphene and IL during the reduction process. As mentioned before, a new H-bonding interaction model of rGO-IL through N-H…F-C association is different from that of GO-IL. In this way, when rGO-IL fillers are incorporated in the polymer matrix, for a given rGO-IL sheet, the IL bonded on the surface of one rGO sheet can also involved in other H-bonding interactions with neighboring graphene sheets, resulting in a morphology with enriched rGO-IL clusters within the polymer matrix shown in the TEM images.

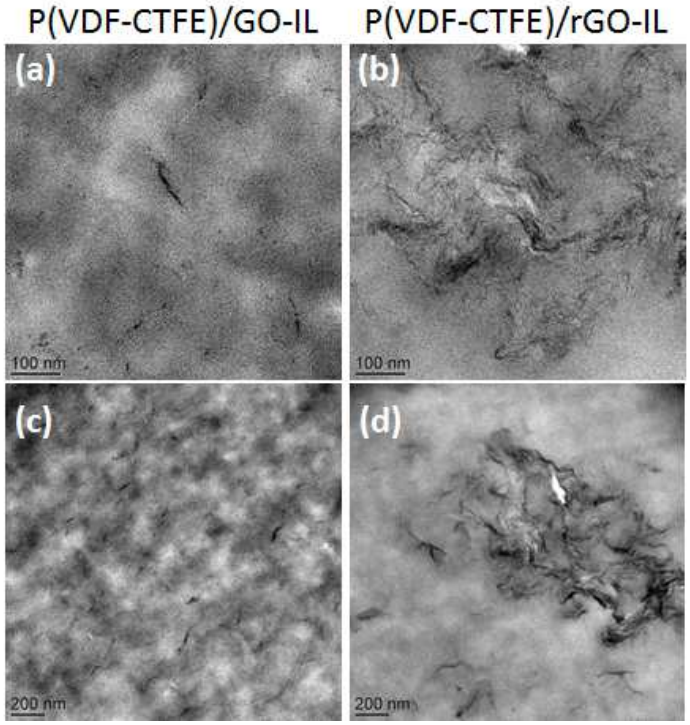

Figure 3-14: TEM images of P(VDF-CTFE)/GO-IL (a & c) and P(VDF-CTFE)/rGO-IL (b & d) with 2.70 wt% of fillers

3.3.2.2 Crystalline phase: total γ-phase transformation

The XRD pattern of neat P(VDF-CTFE) film from DMF in Figure 3-15 shows two characteristic diffraction peaks at $2\theta = 19.9^{o}$ and 26.6^{o} assigned to (110) and (021) reflections of α-phase crystal respectively, and the third peak at $2\theta = 18.3^{o}$ corresponds to (020) plane of γ-one. Moreover, the corresponding FTIR spectrum in ATR mode of neat P(VDF-CTFE) (Figure 3-16) displays the characteristic absorption peaks of α-

phase at 762, 796, 974 and 1383 cm^{-1}, and also the characteristic γ-phase peaks at 812, 834 and 1234 cm^{-1}. The XRD results combined with FTIR ones definitely corroborate the presence of α and γ-crystal mixture in neat copolymer. The crystalline pattern of P(VDF-CTFE) from DMF differs from one got from MEK in *Chapter 2*, in which the neat copolymer presents only α-phase because of the relatively lower polarity of MEK.

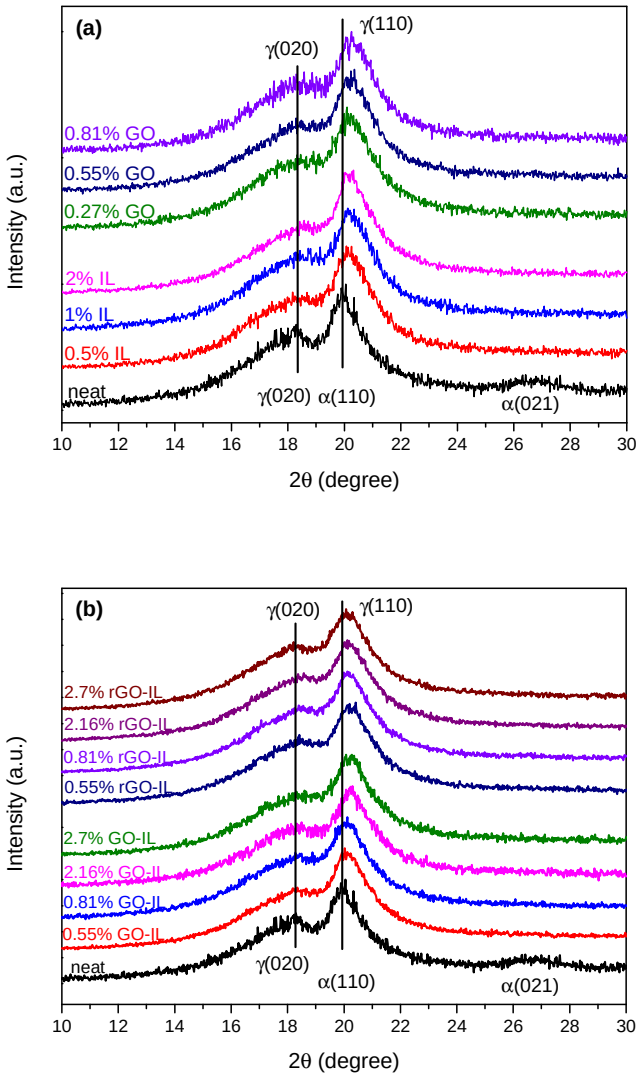

Figure 3-15: XRD patterns of neat P(VDF-CTFE) and composites with IL and GO (a); GO-IL and rGO-IL (b)

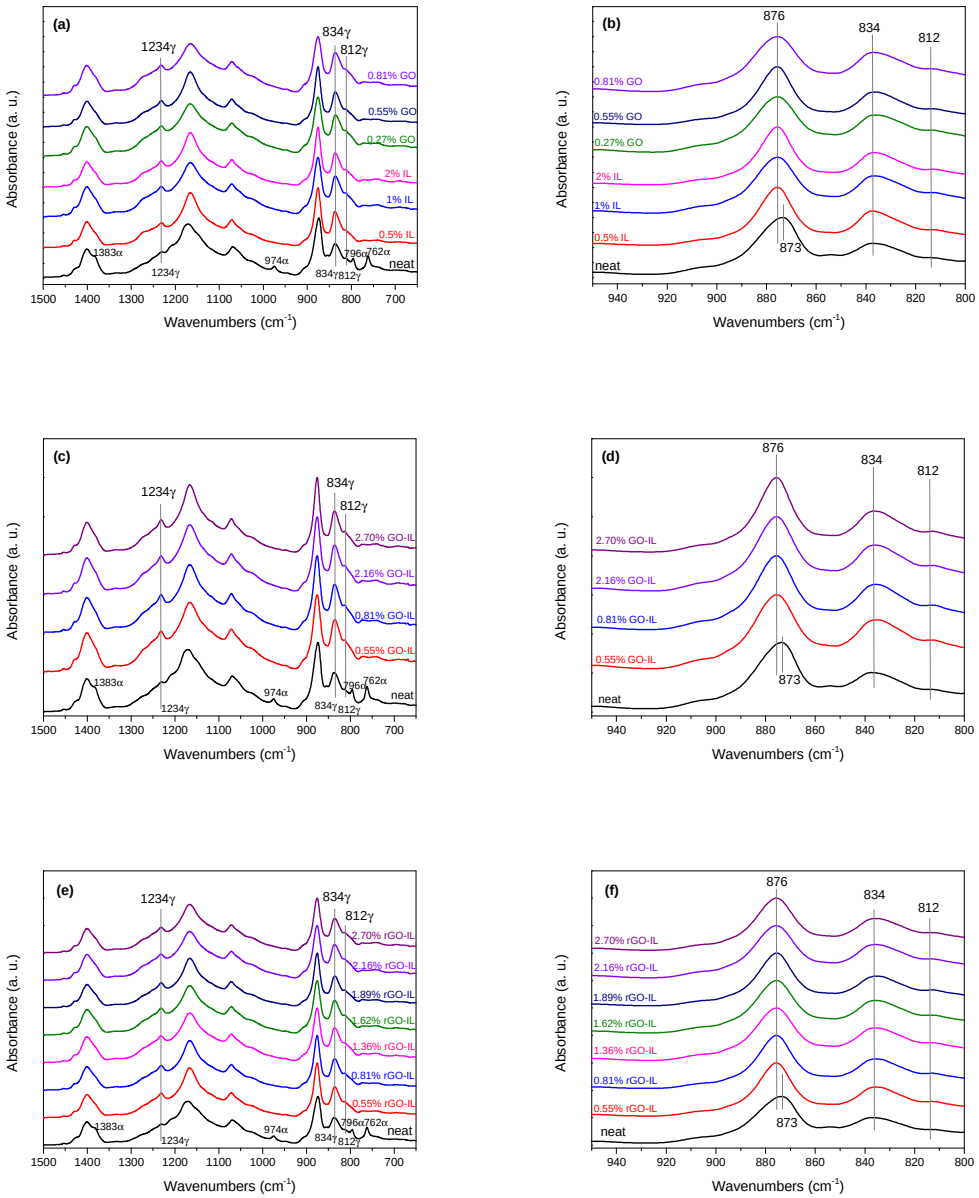

Figure 3-16: ATR FTIR spectra of neat P(VDF-CTFE) and composites with IL, GO (a) & (b); GO-IL (c) & (d); rGO-IL (e) & (f)

However, with adding all fillers, *i.e.*, IL-C8F13, GO, GO-IL, and rGO-IL in polymer matrix, the non-polar α-phase is completely transformed into polar γ-one regardless of the type and quantity of fillers incorporated in the polymer matrix. This entire transformation behavior from mixed α and γ-phase into pure γ-one is confirmed by the disappearance of diffraction peaks of α-phase and the observation of another new γ-phase peak at $2\theta = 20.1^{o}$ ascribed to γ(110) crystal plane in XRD patterns (shown in Figure 3-15), and also by the vanishing of α-phase characteristic peaks at

762, 796, 974, 1383 cm^{-1} but the emerging of typical bands of γ-phase at 812, 834 and 1234 cm^{-1} in FTIR spectra (shown in Figure 3-16(a), (c), (e)).

From XRD and FTIR results, it is easily found that both GO and IL can induce total crystalline phase transformation from α-phase to γ-one due to the 2D template effect of GO and dipolar interaction of IL with polymer chains respectively on the chain configuration of P (VDF-CTFE) to stabilize more TTT sequence[9,10,39,40]. Consequently, combining the crystal transformation effect induced from both graphene and IL, the fillers of GO-IL and rGO-IL can also induce thorough transformation of α-phase to γ-one.

Moreover, in the zoomed FTIR spectra of all composites in the range of 800 cm^{-1} to 900 cm^{-1} in Figure 3-16(b), (d) & (f), the peak at 873 cm^{-1} corresponding to amorphous $–CF_2-CH_2-$ bending vibration which is insensitive to crystalline phase transformation in P(VDF-CTFE) [41] shows a blue shift to 876 cm^{-1}, indicating the interactions of polymer matrix with fillers including IL, GO, GO-IL and rGO-IL. The interaction of IL with copolymer is ascribed to dipolar interactions of ions of ILs and C-F dipole from fluorinated short chain of cation with dipoles of C-F or C-Cl in the P(VDF-CTFE) copolymer. Note that the peak shifts of two vibration bands at 1232 and 1188 cm^{-1} assigned to the $–CF_2$ asymmetric and symmetric stretch in IL cation (if C-F dipoles in fluorinated short chain of cation in IL interact with polymer chains) cannot be seen in composites containing IL, GO-IL, or rGO-IL because of the superimposition of peaks in this zone for fluorinated copolymer matrix. The interactions of GO with polymer can be explained by the presence of oxygenated functional groups on the surface of GO with polymer matrix. Therefore, the dipolar interactions from both of IL and GO or rGO with polymer matrix induce a stronger interfacial interaction between the GO-IL or rGO-IL and the P(VDF-CTFE), subsequently stabilizing the dispersion of GO-IL or rGO-IL in polymer matrix.

3.3.2.3 Crystallization behavior: heterogeneous nucleation effect

It is well known that the fillers can significantly influence the crystallization behavior of a semi-crystalline polymer matrix, which is tightly linked with the

properties of composite materials. The values of T_c (the first cooling run—note that the values of T_c from the first cooling run are the same as those from the second cooling run), T_m and melting enthalpy (ΔH) (the first and second heating run) of neat P(VDF-CTFE) and composites containing either IL-C8F13 alone or modified graphene from DSC thermograms (see Figure 3-S3 in Annexe) are summarized in Table 3-5. Note that the values of T_m and ΔH from the first heating run vary those from the second heating run. It could result from that the first heating run reflect the properties of as-prepared films, namely, the crystallization process from solution during the film formation process. The results from the second heating run indeed illustrate the crystallization process from melting without the heat history of samples.

Table 3-5: T_c, T_m and ΔH of neat P(VDF-CTFE) and composites from DSC thermograms

Sample	Heating 1		Cooling 1	Heating 2	
	T_m (°C)	ΔH (J/g)	T_c (°C)	T_m (°C)	ΔH (J/g)
neat	152	32	114	147	30
0.5 wt% IL-C8F13	151	31	111	146	35
1 wt% IL-C8F13	152	34	111	151	35
2 wt% IL-C8F13	153	37	114	153	33
0.27 wt% GO	150	37	112	145	34
0.55 wt% GO	151	31	112	146	35
0.81 wt% GO	150	33	112	146	34
0.27 wt% GO-IL	152	37	121	153	35
0.55 wt% GO-IL	152	34	123	154	35
0.81 wt% GO-IL	152	37	122	155	34
2.16 wt% GO-IL	152	37	124	155	32
2.70 wt% GO-IL	152	40	123	154	34

0.55 wt% rGO-IL	151	33	120	153	32
0.81 wt% rGO-IL	151	35	122	153	32
1.62 wt% rGO-IL	152	32	123	155	30
1.89 wt% rGO-IL	152	35	122	155	30
2.16 wt% rGO-IL	152	30	123	154	30
2.70 wt% rGO-IL	151	31	123	154	30

(1) Effect of IL-C8F13

By increasing the amount of IL-C8F13 from 0.5 wt% to 2 wt% within P(VDF-CTFE) matrix, T_c displays no obvious change, while T_m from the second heating run and melting enthalpy in both first and second heating run show an increasing effect compared to the matrix. However, an opposite depression behavior (deceased T_c, T_m and melting enthalpy) has been demonstrated for the counterpart IL-C18 in *Chapter 2* in which a C18 alkyl substituent as well as three phenyls are on the cation. This difference can be ascribed to the functionality of cation structure: fluorinated C8F13 substituted chain (IL-C8F13) *versus* alkyl C18 (IL-C18) chain. A fluorinated short chain with regularly repeat C-F dipoles can be seen as a short-range order structure, and it can facilitate the orientation of polymer chains, inducing more perfect arrangement of polymer chains in crystallites with elevated T_m through dipole-dipole interaction with P(VDF-CTFE). This interaction should be overcome during the melting process, thus increased values of melting enthalpy are observed. Differing from IL-C8F13, IL-C18 possesses a long alkyl chain, because of the absence of repeat C-F unit it cannot supply the regular range order structure prompting the orientation of polymer chains to form crystals, thus, IL-C18 has been seen as an obstacle in the crystallization of P(VDF-CTFE) in *Chapter 2*, leading to the depression of crystallization behavior.

(2) Effect of GO

For GO incorporated composites, the values of T_c also show no clear change

as same as IL-C8F13, suggesting no heterogeneous nucleation effect which is distinguished to the extensively demonstrated 2D template heterogeneous nucleation effect of graphene on many semi-crystalline polymers [42]. This behavior can be rationally explained by the relatively weak oxidative groups on the surface of GO in our system which cannot provide enough interaction to absorb polymer chains on the 2D template structure and thus cannot become precursor to induce crystal growth. Besides the unchanged T_c, the values of T_m of GO/P(VDF-CTFE) from either first or second heating run are almost similar to the neat one, indicating no promotion effect on the perfect arrangement of polymer chains in crystals due to the random existence of oxidative groups on the surface unlike IL-C8F13 with so-called short-range order structure. Although the relatively weak interaction and random arrangement of oxidative groups of GO result in no effect on T_c and T_m significantly, the interaction between oxidative groups of GO and dipoles of P(VDF-CTFE) also contributes the energy requirement to disrupt the crystallites with increased values of melting enthalpy compared with neat one.

(3) Effect of GO-IL and rGO-IL

By combining both GO and IL or rGO and IL, it is remarkable to see the significant enhancement of T_c, indicating the strong nucleation effect for P(VDF-CTFE) crystallization in the presence of GO-IL and rGO-IL. IL modified graphene is therefore acting as nucleating agent to cause easier nucleation and crystal growth by combining the 2D template effect of graphene for absorption of polymer chains and fluorinated short chain of IL-C8F13 with short-range order structure and relatively strong dipole-dipole interaction. This synergistic effect also gives rise to elevated T_m values from the second heating run for GO-IL/P(VDF-CTFE) and rGO/P(VDF-CTFE) composites compared to the neat one due to the heterogeneously nucleated and more perfect crystals. However, note that the values of T_m of composites containing IL, GO-IL, and rGO-IL from the first heating run show comparable values with the neat P(VDF-CTFE). This behavior could be ascribed to the difference in the crystallization process, *i.e.*, IL, GO-IL and rGO-IL fillers do not affect the perfection of crystalline

domain or very weakly only through evaporating solvent to obtain films. Concerning the values of melting enthalpy, GO-IL/P(VDF-CTFE) also shows more energy requirement than neat one in the fully melting process to destroy the interactions including (1) IL with polymer and (2) oxidative groups with polymer. However, due to the reduction of partial oxidative groups for rGO-IL, the contribution from the interaction of oxidative groups with polymer is reduced, leading to a slight decrease of melting enthalpy for composites of rGO-IL/P(VDF-CTFE).

3.3.2.4 Relaxation behavior

The different effects of GO-IL and rGO-IL fillers on the polymer chain segmental relaxation can be reflected by dielectric analysis in Figure 3-17. For all composites containing GO, GO-IL and rGO-IL, the values of T_α at -17 ^oC corresponding to the relaxation in the mobile amorphous fraction (MAF) are the same as the neat P(VDF-CTFE) one determined from the imaginary part of relative permittivity (ε_r") as a function of temperature at 1 kHz in Figure 3-17(a), indicating that all fillers including GO, GO-IL and rGO-IL have no influence on the free volume of P(VDF-CTFE) in the MAF region. Moreover, the consistent values of T_α (MAF) for all composites compared to P(VDF-CTFE) matrix are also observed in the plot of imaginary part of dielectric modulus (M") as a function of temperature in Figure 3-17(b) in which the relaxation occurred at -26 ^oC. In addition, the DMA results shown in Annexe also demonstrated this behavior. The same values of T_α at -36 ^oC are shown for both neat matrix and all composites containing IL (Figure 3-S4(a)), GO (Figure 3-S4(b)), GO-IL (Figure 3-S4(c)) and rGO-IL (Figure 3-S4(d)). This behavior of unchanged T_α for all composites compared to neat P(VDF-CTFE) matrix indicates that the fillers have no plasticization effect on the P(VDF-CTFE) matrix.

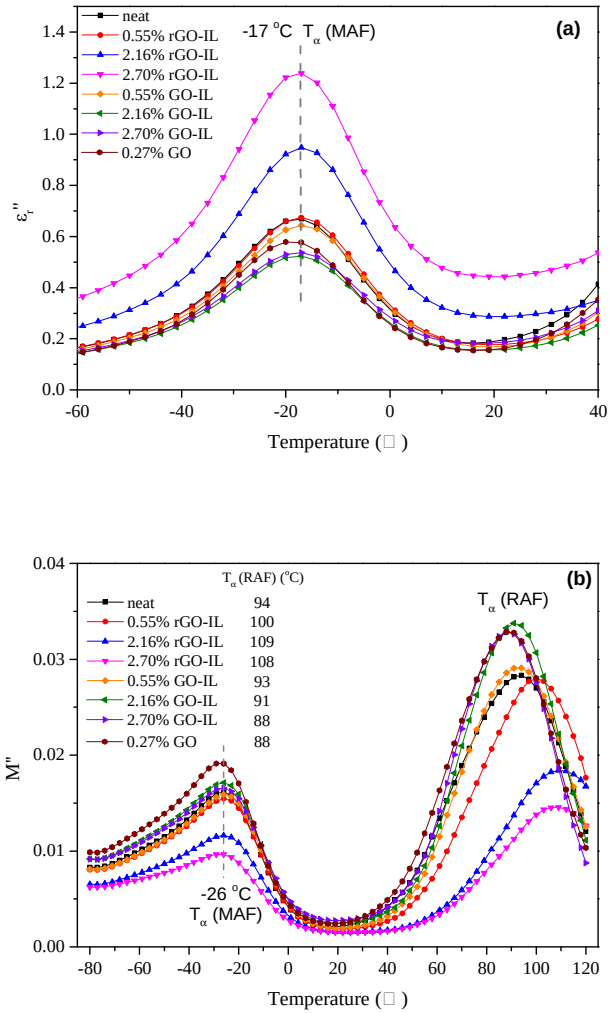

Figure 3-17: Imaginary part of relative permittivity (ε_r") (a) and dielectric modulus (M") (b) as a function of temperature of neat P(VDF-CTFE) and composites containing GO, GO-IL and rGO-IL (*f* = 1 kHz, the first heating run). Note that the peak position and intensity from the first heating run is the same as the one from the second heating run)

Nevertheless, the second T_α peak localized at higher temperature corresponding to defect movements in rigid amorphous region (RAF) regarded as the amorphous/crystalline interface with relatively immobile polymer chains confined between crystallites [43] shows shifting for all composites. The shift of relaxation peak in the RAF region for all the composites can be explained by the nucleation effect of GO-IL or rGO-IL which induces the crystal growth, and thus influences the chain segmental relaxation in this area. The relaxation of neat P(VDF-CTFE) in the RAF region occurs at 94 °C, while for composites containing GO and GO-IL, the values move to lower temperature. This lower-T shift is ascribed to the increased free

volume in the RAF region. The interaction between amorphous polymer chains in RAF region and either oxidative groups or IL on the surface of GO improves the dispersion of fillers in the matrix and also weakens the inter-chain affinity of P(VDF-CTFE), which facilitates the chain segmental movement with a lower-T shift of relaxation. However, it is interesting to find an opposite shift trend (higher-T) for all composites containing rGO-IL. The reduced free volume of polymer chain in the RAF region induced by rGO-IL accompanied with higher-T shift of relaxation could be due to the different dispersion morphologies induced by GO-IL and rGO-IL within polymer matrix which has been discussed in *subsection 3.3.2.1*. As shown in Figure 3-14, the composites with rGO-IL exhibit a morphology with rGO-IL enriched clusters within polymer matrix which to some extent constrains the polymer chains of P(VDF-CTFE) copolymer, leading to an increasd density of amorphous zone in the RAF. Thus, the chain segmental motion was hindered in the RAF, causing a difficulty in the relaxation process [44].

3.3.2.5 Electrical conductivity of P(VDF-CTFE)/GO composites

Figure 3-18(a) shows DC conductivity of P(VDF-CTFE)/GO as a function of temperature. It is obvious to see the conductive nature of composites containing GO alone from 0.27wt% (the composite with 0.27wt% GO act as a dielectric material, data not shown). The values of DC conductivity at RT with 0.55% and 0.81% of GO are 3.22×10^{-1} and 3.97×10^{-1} S/m, respectively. The DC conductivity of P(VDF-CTFE)/GO shows temperature stability in the range from RT to 70 ^{o}C, while starting from 70 ^{o}C, the DC conductivity presents a relatively sharp increase. This behavior is potentially related to the T_{α} (RAF) relaxation at around 70~80 ^{o}C for neat P(VDF-CTFE). Furthermore, the temperature dependences in two different temperature ranges (one case is from 20 ^{o}C to 70^{o}C, the other case is from 70 ^{o}C to 100^{o}C) of composites containing GO follow a Arrhenius type behavior as shown in Figure 3-18(b), and the calculated activation energy (Ea) are also given.

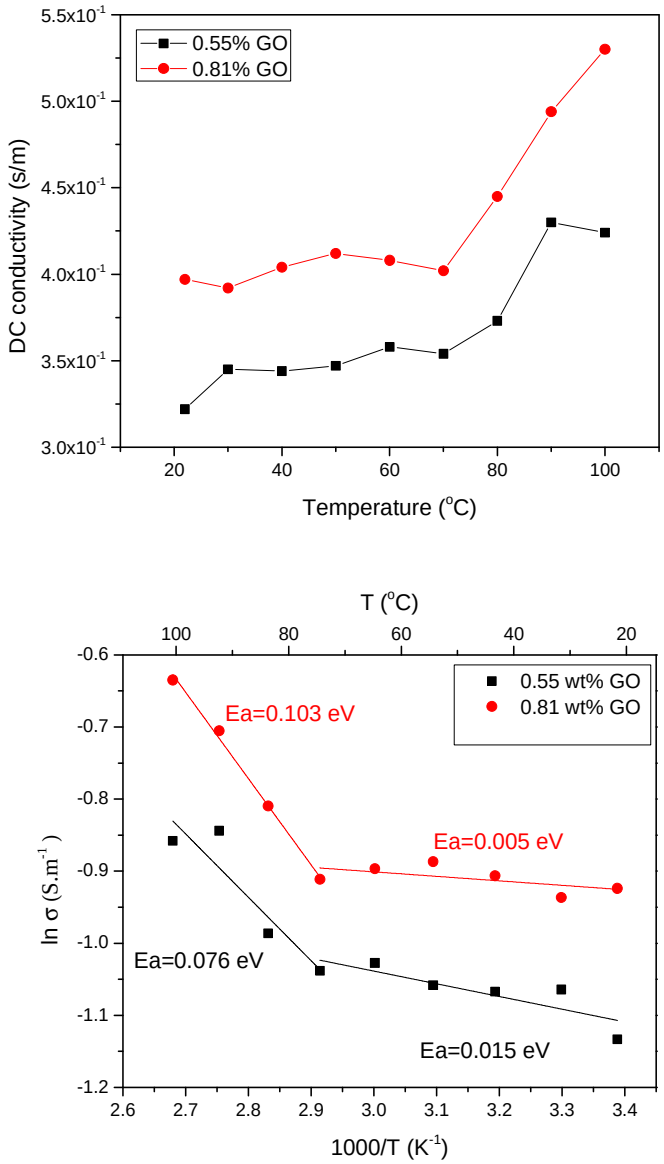

Figure 3-18: DC conductivity as a function of temperature of P(VDF-CTFE)/GO (a); temperature dependence of DC conductivity of composites containing GO (b). The solid lines represent Arrhenius equation linear fitting for each sample. The values of activation energy (Ea) obtained from Arrhenius type fitting applying in two different temperature ranges for each sample are given in the figure

3.3.2.6 Dielectric properties of P(VDF-CTFE)/IL-modified graphene composites

With the attachement of ILs onto the surface of graphene (rGO or GO), the composites act as dielectrics. The curves of dielectric permittivity (ε'), loss tangent (tan δ) and AC conductivity (σ') as a function of frequency at RT for P(VDF-CTFE)/rGO-IL composites with different compositions are plotted in Figure 3-19.

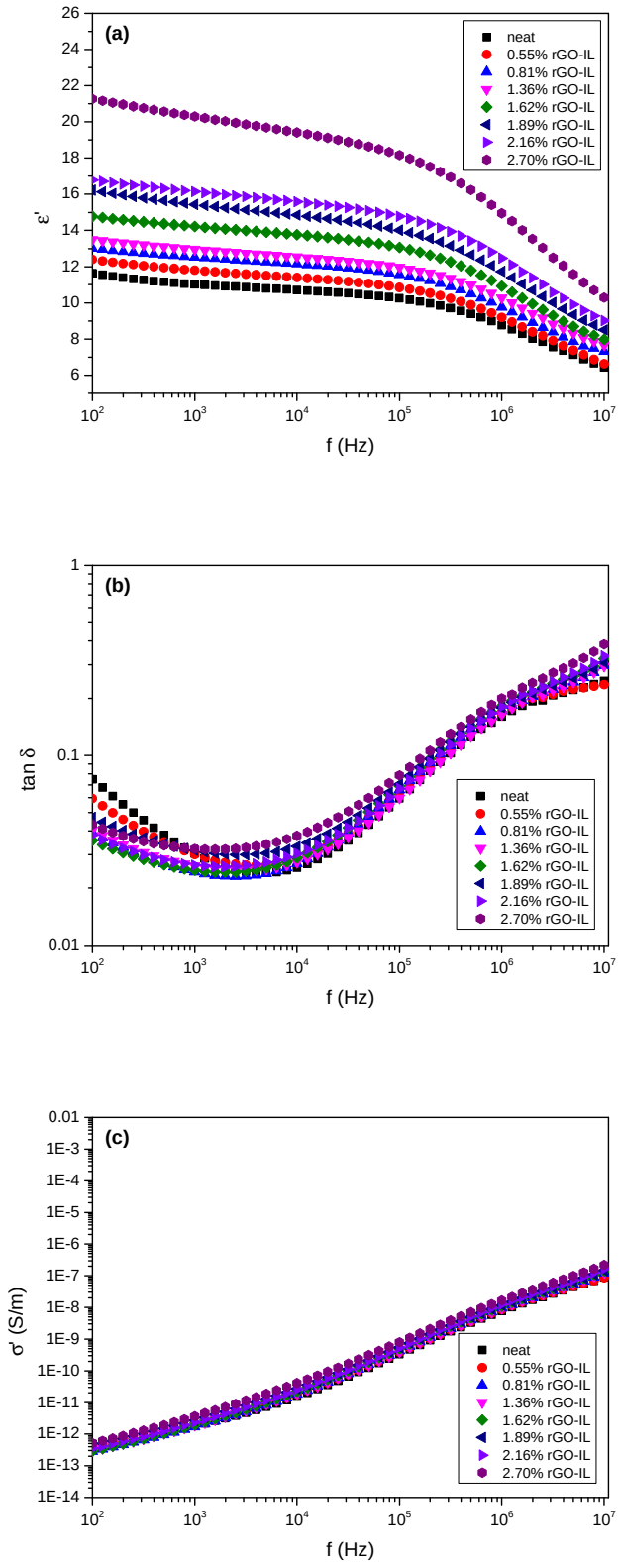

Figure 3-19: Relative dielectric permittivity (ε_r') (a), loss tangent (tan δ) (b) and AC conductivity (σ') (c) of P(VDF-CTFE)/rGO-IL composites as a function of frequency at RT with different compositions

It is obvious to see a gradual increasing behavior of permittivity with

increasing rGO-IL loading content, while the dielectric losses have almost no change in the whole frequency range, whose values at 1 kHz are listed in Table 3-6. For example, the permittivity at 1 kHz of composite with 2.70% of rGO-IL increases up to 20.30 compared with that of 11.02 for neat one, while tan δ is 0.032 which is almost the same with the value of neat one (tan δ = 0.030). The increase in dielectric constant is attributed to the good dispersion of rGO with the help of IL and subsequent the formation of so-called "microcapacitors" in P(VDF-CTFE) matrix, which has been widely reported in literatures [5,45,46,47,48].

Table 3-6: Relative dielectric permittivity (ε_r') and loss tangent (tan δ) of composites with different rGO-IL loadings at 1 kHz and RT

wt%	0	0.55%	0.81%	1.36%	1.62%	1.89%	2.16%	2.70%
ε_r'	11.0	11.8	12.5	13.0	14.2	15.4	16.1	20.3
tan δ	0.030	0.030	0.024	0.026	0.025	0.032	0.026	0.032

Moreover, the formation of clusters, *i.e.*, the zones rich in rGO-IL shown in Figure 3-14(b) & (d), which are close to a network dispersion morphology within polymer matix could be the second driving force to induce a regular increase of permittivity for P(VDF-CTFE)/rGO-IL. As a comparison, the permittivity of composites containing GO-IL displays an irregular evolution with the increase of the contents of fillers (see Figure 3-S5 in Annexe), and the permittivity of composites with GO-IL is similar to one of neat matrix. The phenomenon could be due to the random dispersion morphology within polymer matrix with GO-IL where GO-IL fillers are separated from each other in polymer matrix and the electrical properties of the composites are dominated by the matrix. Thus, the difference in the permittivity evolution behavior by using rGO-IL and GO-IL demonstrates the different effect of dispersion morphology of IL modified garphene used as fillers on the enhancement of permittivity of composites.

As mentioned above, the composites with GO display conductive characteristics. However, when ILs are anchored onto the surface of graphene through ionic and H-bonding interaction, the composites with rGO-IL and GO-IL show

dielectric behaviors. In this way, ILs not only play a role as interfacial agents to facilitate the dispersion of graphene in polymer matrix, but could also act as isolating shells to prevent the direct contact of the conductive graphene sheets, resulting in quite low dielectric losses for the composites with graphene compared to neat matrix. Although the P(VDF-CTFE)/IL modified graphene composites display a relatively high permittivity and a low dielectric loss compared with neat poymer marix, they can easily breakdown under a high electrical field (lower than 100 MV/m), which is detrimental to the application of this composite material.

For this type of conductive filler-based composites, accompanying with the increase of dielectric constant, the breakdown strength simultaneously decreases. When the filler content approaches the percolation threshold, the dielectric loss is normally high and the breakdown strength is also reduced. It is reported that P(VDF-TrFE-CTFE)/carbon black nanocomposites *via* a simple solution exhibit excellent mechanical properties and dielectric properties with a dielectric permittivity of 140 and a low dielectric loss of 0.05 at 100 Hz with an f_c = 4.68 wt% [49]. Nevertheless, the breakdown strength decreased simultaneously due to the enhanced local electric field induced by the thin insulating layer between CB fillers, which is not desirable to the practical applications. Although we are facing some issues to well utilize this kind of composites for applications, it is still promising to bring out the potentials in the high dielectric constant of these conductive filler-based composites but find an efficient way to reduce the dielectric loss.

Based on the considerations above, it should be interesting to pursue and to complete this work according to various directions. For example, the solution casting strategy to prepare composite films usually produces porous and defects structure within films due to the high evaporating temperature used for removing solvent DMF, which dramatically decreased the breakdown strength. This issue could be overcome by using melting blending methods such as hot-pressing and melting extrusion.

3.4 Conclusions

In this Chapter, a task-specific IL, IL-C8F13 with the cation structure combining three phenyls and a short fluorinated chain, was successfully synthesized and non-covalently modified on the surface of graphene (GO or rGO) due to the specific interactions between IL and GO or rGO. In particular, H-bonding interaction of N-H…C-F of IL with rGO because of the nitrogen doped surfaces of rGO by hydrazine reduction have emerged. These IL-modified graphene fillers were then incorporated into P(VDF-CTFE) matrix to prepare P(VDF-CTFE)/graphene composite materials in which IL played a key role in compatibilizing graphene fillers and matrix at the interface between them. The composites showed tortuous morphologies on fractured cross section thanks to the good dispersion and excellent adhesion of fillers in polymer matrix. The IL-modified graphene fillers worked as heterogeneous nucleating agents for polymer matrix with increased T_c due to the synergistic effects of fluorinated IL and graphene, and they also facilitated the total transformation of γ crystalline phases. More interestingly, rGO-IL imposed different effects on crystallization behavior, segmental chain relaxation behavior, and subsequent dielectric properties of composite materials compared to GO-IL because of different interactions of IL with GO or rGO. Finally, it is noticeable that these P(VDF-CTFE)/IL modified graphene composites exhibite relatively high dielectric permittivity and low dielectric loss, *e.g.*, the relative permittivity at 1 kHz of composite with 2.70% of rGO-IL increases up to 20.3 compared with that of 11.0 for neat one, while tan δ is 0.032 which is almost the same as the value of neat one (tan δ = 0.030).

3.5 References

[1] Kuilla T, Bhadra S, Yao D, et al. Recent advances in graphene based polymer composites. *Progress in Polymer Science*, 2010, 35(11): 1350-1375.
[2] Kim H, Abdala A A, Macosko C W. Graphene/polymer nanocomposites. *Macromolecules*, 2010, 43(16): 6515-6530.
[3] Hu K, Kulkarni D D, Choi I, et al. Graphene-polymer nanocomposites for structural and functional applications. *Progress in Polymer Science*, 2014, 39(11): 1934-1972.
[4] Layek R K, Nandi A K. A review on synthesis and properties of polymer functionalized graphene. *Polymer*, 2013, 54(19): 5087-5103.
[5] Stankovich S, Dikin D A, Dommett G H B, et al. Graphene-based composite materials. *Nature*, 2006, 442(7100): 282-286.
[6] Layek R K, Samanta S, Chatterjee D P, et al. Physical and mechanical properties of poly(methyl methacrylate)-functionalized graphene/poly(vinylidine fluoride) nanocomposites: Piezoelectric β polymorph formation. *Polymer*, 2010, 51(24): 5846-5856.
[7] Wang D, Bao Y, Zha J W, et al. Improved dielectric properties of nanocomposites based on poly(vinylidene fluoride) and poly(vinyl alcohol)-functionalized graphene. *ACS Applied Materials & Interfaces*, 2012, 4(11): 6273-6279.
[8] Han K, Li Q, Chen Z, et al. Suppression of energy dissipation and enhancement of breakdown strength in ferroelectric polymer–graphene percolative composites. *Journal of Materials Chemistry C*, 2013, 1(42): 7034-7042.
[9] Li Y, Xu J Z, Zhu L, et al. Role of ion–dipole interactions in nucleation of gamma poly(vinylidene fluoride) in the presence of graphene oxide during melt crystallization. *The Journal of Physical Chemistry B*, 2012, 116(51): 14951-14960.
[10] Wang J, Wu J, Xu W, et al. Preparation of poly(vinylidene fluoride) films with excellent electric property, improved dielectric property and dominant polar crystalline forms by adding a quaternary phosphorus salt functionalized graphene. *Composites Science and Technology*, 2014, 91: 1-7.
[11] Maity N, Mandal A, Nandi A K. Interface engineering of ionic liquid integrated graphene in poly(vinylidene fluoride) matrix yielding magnificent improvement in mechanical, electrical and dielectric properties. *Polymer*, 2015, 65: 154-167.
[12] Livi S, Duchet-Rumeau J, Gérard J F. Tailoring of interfacial properties by ionic liquids in a fluorinated matrix based nanocomposites. *European Polymer Journal*, 2011, 47(7): 1361-1369.
[13] Yang Y K, He C E, Peng R G, et al. Non-covalently modified graphene sheets by imidazolium ionic liquids for multifunctional polymer nanocomposites. *Journal of Materials Chemistry*, 2012, 22(12): 5666-5675.
[14] Livi S, Pham T N, Gérard J F, et al. Supercritical CO_2–ionic liquids: Green combination for preparing foams. *Chemical Engineering Journal*, 2014, 240: 534-540.
[15] Hummers Jr W S, Offeman R E. Preparation of graphitic oxide. *Journal of the American Chemical Society*, 1958, 80(6): 1339-1339.

[16] Paredes J I, Villar-Rodil S, Martinez-Alonso A, et al. Graphene oxide dispersions in organic solvents. *Langmuir*, 2008, 24(19): 10560-10564.
[17] Jeong H K, Lee Y P, Jin M H, et al. Thermal stability of graphite oxide. *Chemical Physics Letters*, 2009, 470(4): 255-258.
[18] Jeong H K, Lee Y P, Lahaye R J W E, et al. Evidence of graphitic AB stacking order of graphite oxides. *Journal of the American Chemical Society*, 2008, 130(4): 1362-1366.
[19] Wang D, Bao Y, Zha J W, et al. Improved dielectric properties of nanocomposites based on poly(vinylidene fluoride) and poly(vinyl alcohol)-functionalized graphene. *ACS Applied Materials &Interfaces*, 2012, 4(11): 6273-6279.
[20] Maity N, Mandal A, Nandi A K. Interface engineering of ionic liquid integrated graphene in poly(vinylidene fluoride) matrix yielding magnificent improvement in mechanical, electrical and dielectric properties. *Polymer*, 2015, 65: 154-167.
[21] Yang Y K, He C E, Peng R G, et al. Non-covalently modified graphene sheets by imidazolium ionic liquids for multifunctional polymer nanocomposites. *Journal of Materials Chemistry*, 2012, 22(12): 5666-5675.
[22] Wang S, Zhang Y, Abidi N, et al. Wettability and surface free energy of graphene films. *Langmuir*, 2009, 25(18): 11078-11081.
[23] Zhang K, Zhang Y, Wang S. Enhancing thermoelectric properties of organic composites through hierarchical nanostructures. *Scientific Reports*, 2013, 3, 3448.
[24] Khanra P, Lee C N, Kuila T, et al. 7, 7, 8, 8-Tetracyanoquinodimethane-assisted one-step electrochemical exfoliation of graphite and its performance as an electrode material. *Nanoscale*, 2014, 6(9): 4864-4873.
[25] Gao X, Jang J, Nagase S. Hydrazine and thermal reduction of graphene oxide: reaction mechanisms, product structures, and reaction design. *The Journal of Physical Chemistry C*, 2009, 114(2): 832-842.
[26] Tong W, Zhang Y, Yu L, et al. Novel Method for the Fabrication of Flexible Film with Oriented Arrays of Graphene in Poly(vinylidene fluoride-co-hexafluoropropylene) with Low Dielectric Loss. *The Journal of Physical Chemistry C*, 2014, 118(20): 10567-10573.
[27] Wang R, Wang Y, Xu C, et al. Facile one-step hydrazine-assisted solvothermal synthesis of nitrogen-doped reduced graphene oxide: reduction effect and mechanisms. *RSC Advances*, 2013, 3(4): 1194-1200.
[28] Zhu Y, Murali S, Cai W, et al. Graphene and graphene oxide: synthesis, properties, and applications. *Advanced Materials*, 2010, 22(35): 3906-3924.
[29] Almadhoun M N, Hedhili M N, Odeh I N, et al. Influence of stacking morphology and edge nitrogen doping on the dielectric performance of graphene–polymer nanocomposites. *Chemistry of Materials*, 2014, 26(9): 2856-2861.
[30] Pimenta M A, Dresselhaus G, Dresselhaus M S, et al. Studying disorder in graphite-based systems by Raman spectroscopy. *Physical Chemistry Chemical Physics*, 2007, 9(11): 1276-1290.
[31] Krishnamoorthy K, Veerapandian M, Yun K, et al. The chemical and structural analysis of graphene oxide with different degrees of oxidation. *Carbon*, 2013, 53: 38-

[32] Kaniyoor A, Ramaprabhu S. A Raman spectroscopic investigation of graphite oxide derived graphene. *AIP Advances*, 2012, 2(3): 032183.
[33] Ferrari A C, Meyer J C, Scardaci V, et al. Raman spectrum of graphene and graphene layers. *Physical Review Letters*, 2006, 97(18): 187401.
[34] Zamora-Ledezma C, Puech N, Zakri C, et al. Liquid crystallinity and dimensions of surfactant-stabilized sheets of reduced graphene oxide. *The Journal of Physical Chemistry Letters*, 2012, 3(17): 2425-2430.
[35] Yuan J, Luna A, Neri W, et al. Graphene liquid crystal retarded percolation for new high-*k* materials. *Nature Communications*, 2015, 6 : 8700.
[36] Balapanuru J, Yang J X, Xiao S, et al. A Graphene Oxide–Organic Dye Ionic Complex with DNA−Sensing and Optical−Limiting Properties. *Angewandte Chemie InternationalEdition*, 2010, 49(37): 6549-6553.
[37] Chaudhari S R, Mogurampelly S, Suryaprakash N. Engagement of CF_3 Group in N–H···F–C Hydrogen Bond in the Solution State: NMR Spectroscopy and MD Simulation Studies. *The Journal of Physical Chemistry B*, 2013, 117(4): 1123-1129.
[38] Gupta M, Gleason K K. Initiated chemical vapor deposition of poly (1H,1H,2H,2H-perfluorodecyl acrylate) thin films. *Langmuir*, 2006, 22(24): 10047-10052.
[39] Xing C, Zhao L, You J, et al. Impact of ionic liquid-modified multiwalled carbon nanotubes on the crystallization behavior of poly(vinylidene fluoride). *The Journal of Physical Chemistry B*, 2012, 116(28): 8312-8320.
[40] Mandal A, Nandi A K. Ionic liquid integrated multiwalled carbon nanotube in a poly(vinylidene fluoride) matrix: Formation of a piezoelectric β-polymorph with significant reinforcement and conductivity improvement. *ACS Applied Materials & Interfaces*, 2013, 5(3): 747-760.
[41] Sousa R E, Ferreira J C C, Costa C, et al. Tailoring poly(vinylidene fluoride-co-chlorotrifluoroethylene) microstructure and physicochemical properties by exploring its binary phase diagram with dimethylformamide. *Journal of Polymer Science Part B: Polymer Physics*, 2015, 53(11): 761-773.
[42] Xu J Z, Zhong G J, Hsiao B S, et al. Low-dimensional carbonaceous nanofiller induced polymer crystallization. *Progress in Polymer Science*, 2014, 39(3): 555-593.
[43] Mijovic J, Sy J W, Kwei T K. Reorientational dynamics of dipoles in poly(vinylidene fluoride)/poly(methyl methacrylate)(PVDF/PMMA) blends by dielectric spectroscopy. *Macromolecules*, 1997, 30(10): 3042-3050.
[44] Mandal A, Nandi A K. Ionic liquid integrated multiwalled carbon nanotube in a poly(vinylidene fluoride) matrix: Formation of a piezoelectric β-polymorph with significant reinforcement and conductivity improvement. *ACS Applied Materials &Interfaces*, 2013, 5(3): 747-760.
[45] Mack J J, Viculis L M, Ali A, et al. Graphite nanoplatelet reinforcement of electrospun polyacrylonitrile nanofibers. *Advanced Materials*, 2005, 17(1): 77-80.
[46] Chen G, Weng W, Wu D, et al. Preparation and characterization of graphite nanosheets from ultrasonic powdering technique. *Carbon*, 2004, 42(4): 753-759.
[47] Zheng G, Wu J, Wang W, et al. Characterizations of expanded graphite/polymer

composites prepared by in situ polymerization. *Carbon*, 2004, 42(14): 2839-2847.
[48] Kaczmarek H, Podgórski A. Photochemical and thermal behaviours of poly(vinyl alcohol)/graphite oxide composites. *Polymer Degradation and Stability*, 2007, 92(6): 939-946.
[49] Yin X, Capsal J F, Guyomar D. A comprehensive investigation of poly(vinylidene fluoride-trifluoroethylene-chlorofluoroethylene) terpolymer nanocomposites with carbon black for electrostrictive applications. *Applied Physics Letters*, 2014, 104(5): 052913.

3.6 Annexe

1. No residual DMF in the resulting composite films

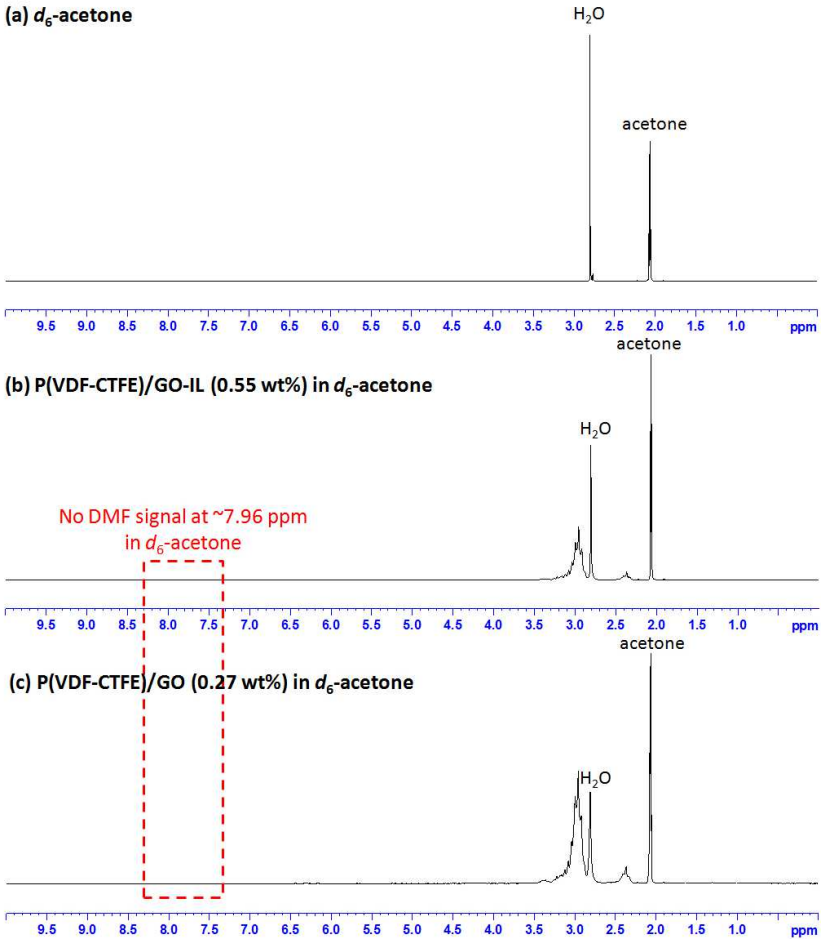

Figure 3-S1: ^{1}H NMR spectra of deuterated acetone (d_6-acetone) solvent (a), P(VDF-CTFE)/GO-IL (0.55 wt%) (b) and P(VDF-CTFE)/GO (0.27 wt%) composites in d_6-acetone. Note that the signal of DMF in d_6-acetone at around 7.96 ppm corresponding to $(CH_3)_2N$-C(O)***H*** (*J. Org. Chem.***1997**, *62*, 7512-7515) is not visible in the spectra of P(VDF-CTFE)/GO-IL and P(VDF-CTFE)/GO composites, suggesting total removing of DMF by using the drying conditions: first dried at 60 °C in air oven overnight, and then under vacuum at 80 °C for 48h.

2. Stability of IL-C8F13 during the chemical reduction by hydrazine

The IL-C8F13 is chemically stable under the reduction conditions by hydrazine (95 ºC for 3 h in DMF), which can be confirmed by NMR spectra of IL before and after hydrazine treatment.

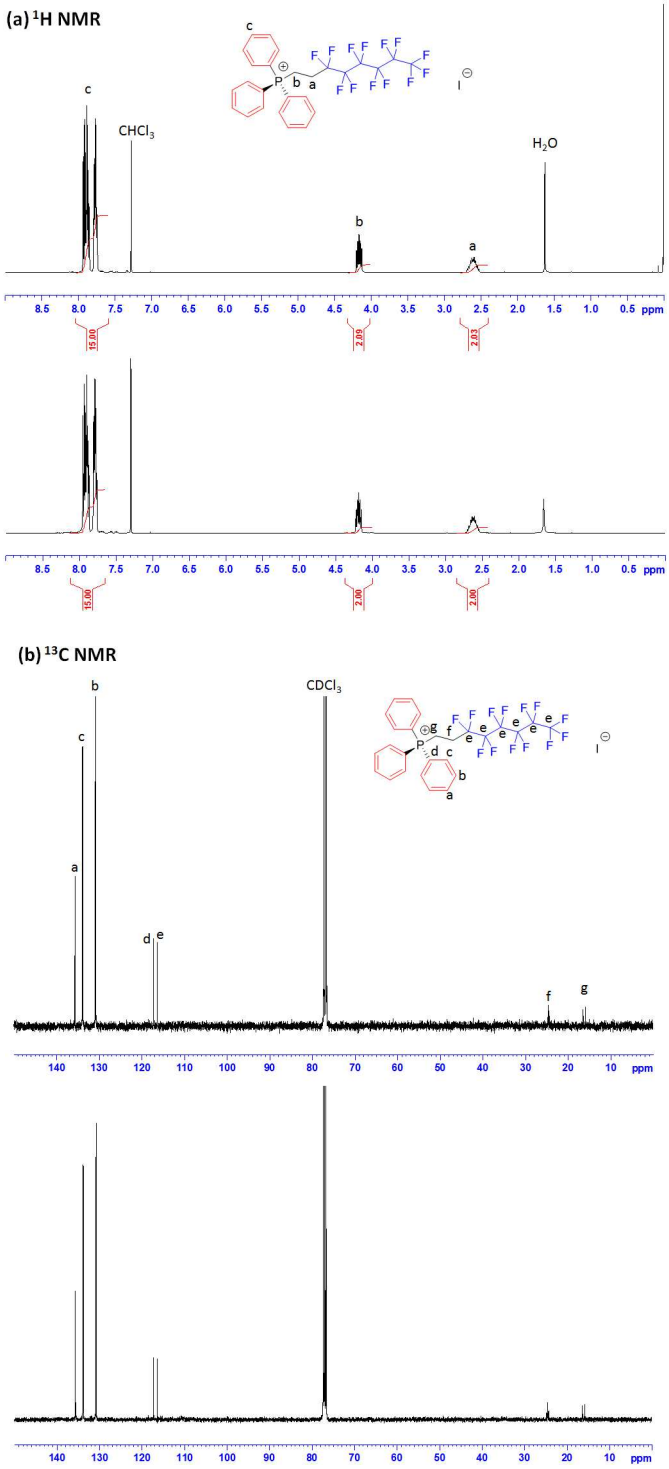

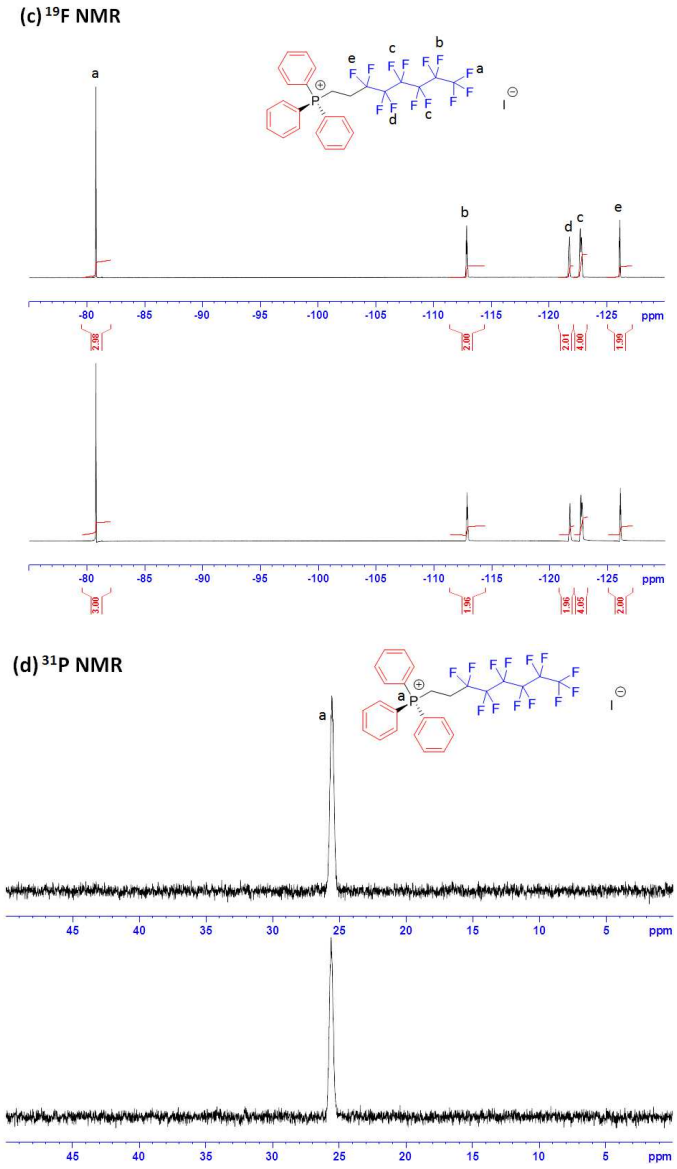

Figure 3-S2: ^{1}H, ^{13}C, ^{19}F and ^{31}P NMR spectra of IL-C8F13 before (upper) and after (lower) hydrazine treatment

3. DSC traces of neat P(VDF-CTFE) and its composites containing IL, GO, rGO, GO-IL, rGO-IL with different loading contents during heat/cool/heat runs

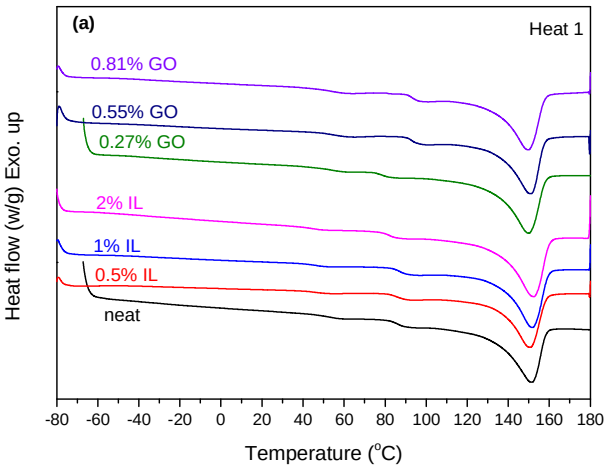

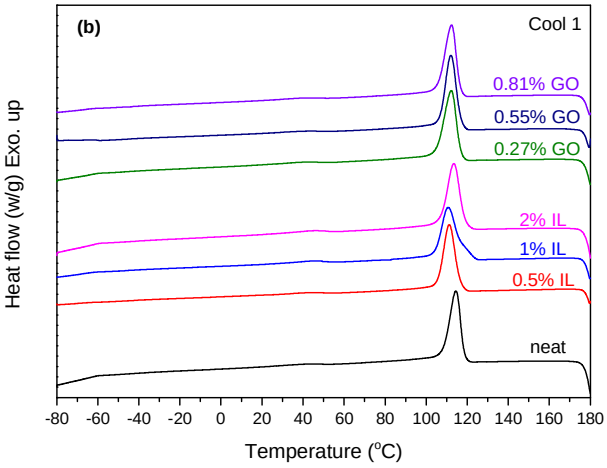

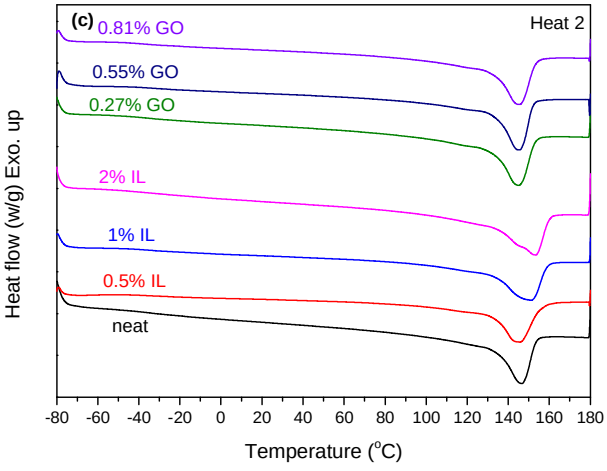

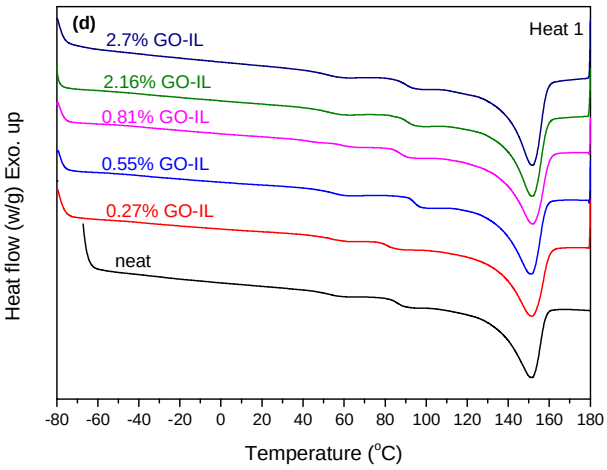

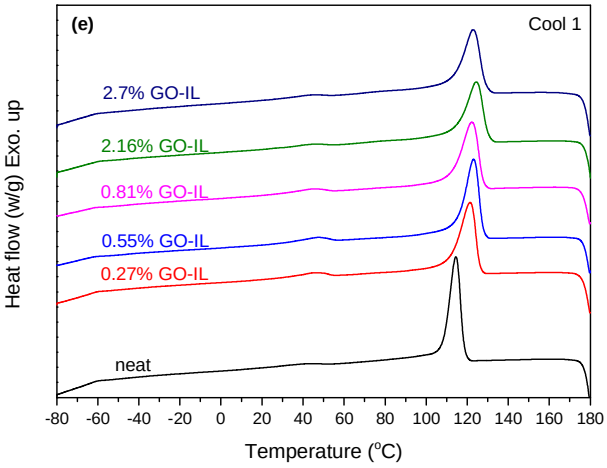

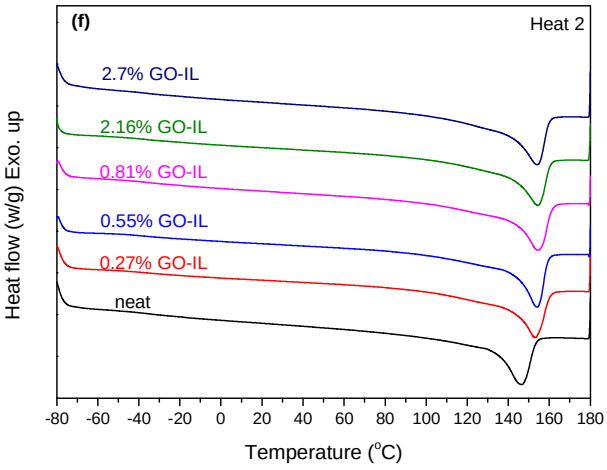

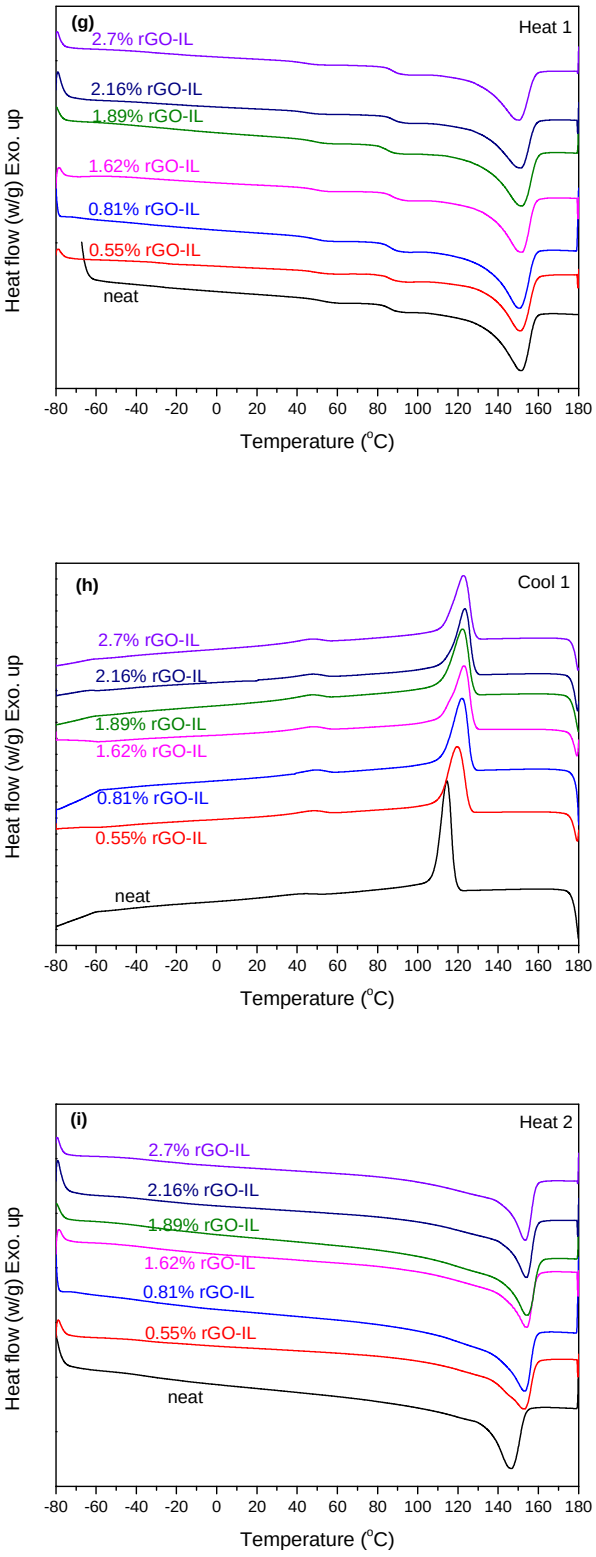

Figure 3-S3: DSC thermograms of neat P(VDF-CTFE) and its composites containing GO, GO-IL and rGO-IL during first and second heating run and the first cooling run.

4. DMA curves of neat P(VDF-CTFE) and its composites containing IL, GO, GO-IL and rGO-IL

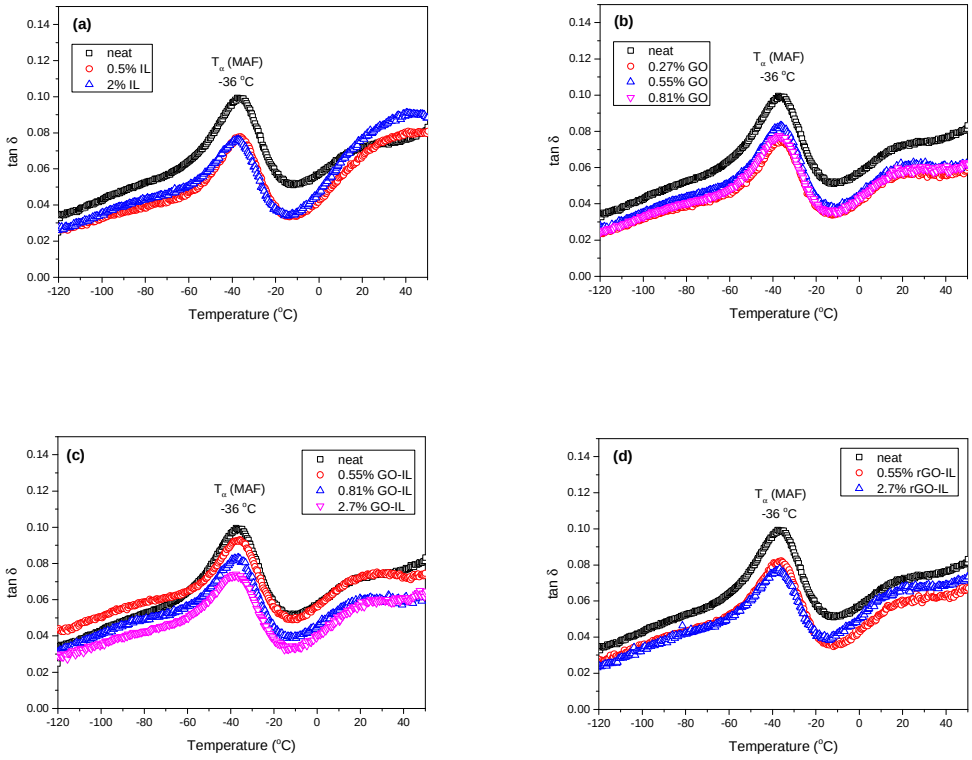

Figure 3-S4: Dynamic mechanical loss tangent (tan δ) as a function oftemperature for neat P(VDF-CTFE) and composites containing IL (a), GO (b), GO-IL (c) and rGO-IL (d)

5. Dielectric properties of P(VDF-CTFE)/GO-IL composites

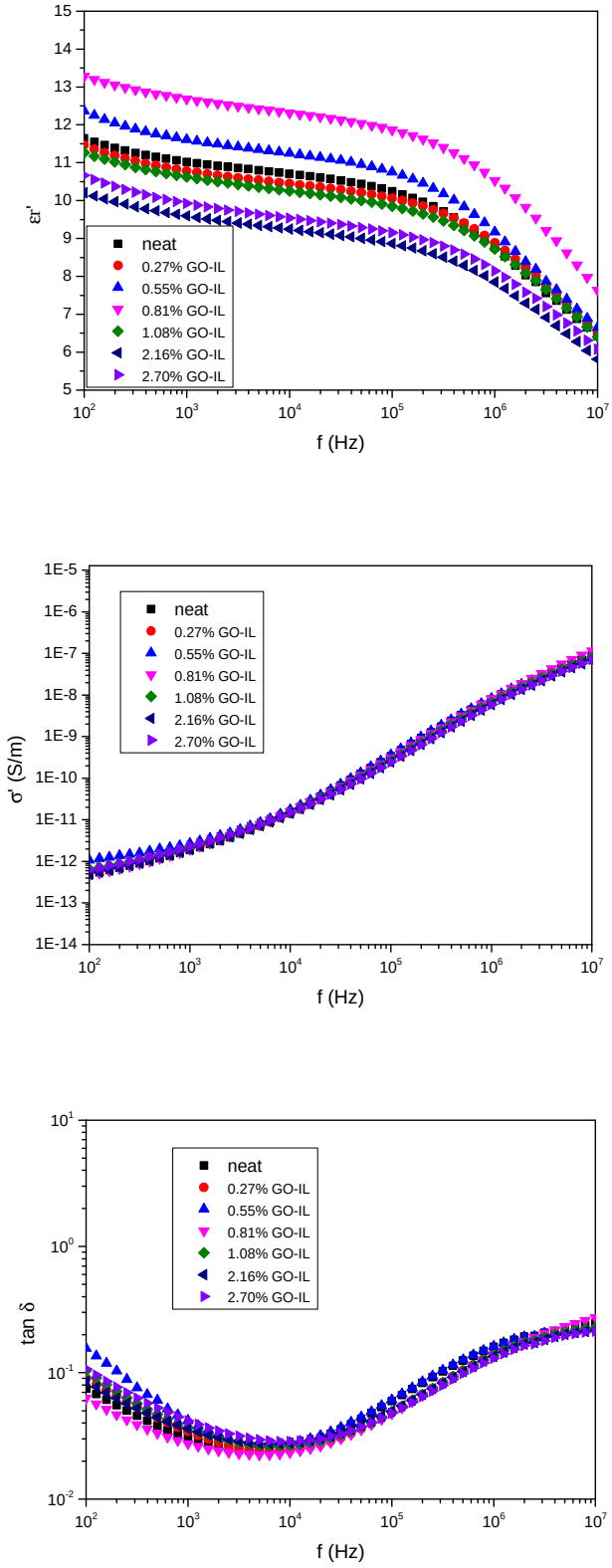

Figure 3-S5: Relative dielectric permittivity (ε_r') (a), loss tangent (tan δ) (b) and AC conductivity (σ') (c) of P(VDF-CTFE)/GO-IL composites as a function of frequency at RT with different compositions

General Conclusions and Perspectives

General Conclusions and Perspectives

The objective of this basic research work is to develop the understanding of versatile roles of phosphonium ionic liquids (ILs) as nanostructuration agents and interfacial agents in the fluorinated polymer matrix poly(vinylidene fluoride-chlorotrifluoroethylene) (PVDF-CTFE). It has been shown that tuning the chemical structure of ILs as well as the interaction with graphene fillers and/or polymer matrix is a efficient and powerful strategy to prepare functional fluorinated polymer composite films, which provides a platform to develop IL-based polymer composite materials with expected properties for applications through combining both merits from the physico-chemistry of ILs and polymer science communities.

The first bibliographic chapter focused on reviewing (1) the chemical structures and electroactive properties of PVDF-based polymer matrices; (2) the chemistry of ILs and its promising application as nanostructuration agents in polymer matrices; (3) the progress on the nanofiller-incorporated PVDF-based composites, especially on the graphene/PVDF composites, and the recent achievements on the IL-modified graphene as fillers in PVDF-based polymer matrix. Interestingly, the bibliographic survey emphasized the promising utilization of ILs as efficient nanostructuration and interfacial agents in polymer composite materials to develop more and more brilliant properties, which is a research-directed constituent to the following studies in this thesis.

The first part of this work – and the subject of *Chapter 2* of this thesis– was to develop a fundamental understanding of the versatile and tunable nanostructuration effect of two phosphonium ILs, IL-C18 and IL-108 with the differences in steric hindrance and extra dipolar groups, on P(VDF-CTFE). We suggested that the nanostructuration mechanism is very dependent on the diffusion and interacting abilities of ILs in matrix, which are determined by the chemical structures of ILs. Both ILs appear to diffuse and regularly assemble in the RAF of P(VDF-CTFE) between crystalline lamellae thanks to the “template” confinement effect of 2D structure. The assembled structure shows a gradually regular 1D to 2D geometric evolution with an increasing ILs amount. Simultaneously, these regularly assembled ILs in the RAF also act as “template” to efficiently induce a complete transition of nonpolar α-phase to polar γ- and/or β-phase with only a tiny amount of ILs (from 2

wt%). Moreover, the crystallization displays a depression behavior with reduced T_c, T_m, crystallinity and crystallite size due to the existence of ILs in the RAF seen as obstacle for the regular chain-folding and the dipolar interaction with P(VDF-CTFE). We proposed that the synergistic influence of mutual "templates" endues phosphonium ILs a versatile nanostructuration on the fluorinated matrix. Moreover, this versatile nanostructuration effect can be easily tuned by tailoring the chemical structures of ILs. Therefore, tailoring the chemical structures of phosphonium ILs based on the varied cation/anion combinations and small amount (from 2 wt%) in the PVDF-based matrix provides a facile and efficient pathway to adjust the profiles of blends through the tunable nanostructuration of ILs, which is of great potentiality for diverse applications of pyro-/ferro-/piezo-electric PVDF-based materials.

As the second part of this study, *Chapter 3* aims at evaluating the ability of ILs as interfacial agents to tune the interfacial properties between P(VDF-CTFE) matrix and graphene fillers. Thus, a task-specific IL, IL-C8F13 with the cation structure combining three phenyls and a short fluorinated chain, was synthesized and non-covalently modified on the surface of graphene (GO or rGO). These IL-modified graphene fillers were then incorporated into P(VDF-CTFE) matrix to compatibilize graphene fillers and P(VDF-CTFE) matrix at the interface between them. The crystalline phase structure, crystallization behavior, relaxation behavior, dispersion morphology and dielectric properties were found to be associated to the effects from both 2D graphene and IL decorated on the surface thereof. More interestingly, the newly formed hydrogen-bonding interaction between rGO and IL could be one driving force to induce a different network-like dispersion of graphene in the polymer matrix comparing with the GO/IL composites. Finally, the resulting P(VDF-CTFE)/rGO-IL composites showed increased dielectric constant up to 20.3 with low filler loading (2.7 wt%) compared to that of 11.0 for the neat copolymer, while the dielectric loss of composites remained the same level with that of polymer matrix. This research work promotes our understanding of the role of IL on the interfacial interaction between matrix and graphene, which facilitates the development of graphene/PVDF-based nanocomposites with tunable and enhanced properties through the versatile ILs as interfacial agents.

Although we have achieved some progresses on the structuration effect of ILs on composite films combining ILs and fluorinated polymer, it should be also interesting

and urgent to pursue and to complete this thesis work according to various directions in order to further deepen and broaden this newly developed topic.

(1) The emphasis of this thesis is the basic investigation of nanostructuration and interfacial effect mechanism of ILs on the polymer matrix, which is, of course, not the destination of the development of functional IL-based polymer composite materials. As one of ferroelectric polymer matrices, it is very interesting to investigate the electroactive properties of neat P(VDF-CTFE) and its composites containing ILs, and IL-modified graphene, however, this part of work is not mainly focused on in this thesis. Interestingly, neat P(VDF-CTFE) films from MEK were demonstrated to be very interesting materials with electrocaloric effects (ECE) in our tentative exploration based on the principle of differential detection of heat flow using Peltier cell heat flux sensors. The entropy change ΔS at 70 ^{o}C and 150 MV/m can even reach up to 4.8 $Jkg^{-1}K^{-1}$, which imposes potential applications in solid state refrigeration. Nevertheless, unfortunately, P(VDF-CTFE)/IL blends show negative factors to further improve the ECE in polymer blends with the addition of ILs, such as relatively higher dielectric conductivity and loss as well as lower breakdown strength (< 100 MV/m) compared to neat copolymer. It is potentially ascribed to that ILs present a free state in polymer matrix under AC or DC electric field because the dipolar interaction between ILs and P(VDF-CTFE) by physically blending cannot restrain their movements in domains, subsequently generating great conductivity and dielectric loss. This behavior is a negative factor for the dielectric applications because a large amount of heat energy can be produced from the movement of free ILs under electric field, and thus decreasing the breakdown strength of P(VDF-CTFE)/IL blends. Based on these analyses above, a continuous work should be focused on how to improve ECE for PVDF/IL blends. For example, there are several possibilities could be considered: *i)* fixing the ILs onto the polymer chains; *ii)* trapping ILs into so-called domains by chemical bonding; *iii)* adding the third filler to pin the movement of ILs in polymer blends. All possible solutions aim to improve the dielectric constant but restrain the dielectric loss, simultaneously maintain the breakdown strength of polymer matrix. Moreover, for P(VDF-CTFE)/graphene composites, accompanying with the increase of dielectric constant, the breakdown strength decreased simultaneously due to the enhanced local electric field induced by the thin insulating layer between conductive graphene fillers, which limits the dielectric applications like ECE materials. Thus,

further work should pay more attentions on the electroactive properties of resulting composite films. Only in this way, the interrelationship between structure and property can be advanced to facilitate the development of functional materials for the practical applications.

(2) As shown in the bibliographic chapter, the family of PVDF-based copolymers and terpolymers exhibits very interesting electroactive properties. In this thesis, only P(VDF-CTFE) was used as a model matrix for the research, thus more functional candidates of PVDF-based polymers, such as P(VDF-TrFE), P(VDF-HFP), P(VDF-TrFE-CTFE), should be introduced as the matrices to meet the different applied requirements. Moreover, it is well-known that the content of comonomer is related to the structure of semi-crystalline PVDF-based polymers but only one composition sample (containing 8 wt% of CTFE) was used in this thesis. Therefore, the content of comonomer should also be introduced as a factor to study the influence on the properties of composite films in future.

(3) Thanks to the growing development of the chemistry of IL, more and more functional ILs with task-directed properties are synthesized by organic chemists, which provides us a huge possibility to utilize these ILs as versatile building blocks in the development of IL-based polymer composite materials. Thus, one of important direction should be the designing and synthesis of application-directed ILs with task-specific structure. For example, as a modifier for graphene in this thesis, an IL possessing much stronger π-π interacting ability with large conjugate structure could enhance the bonding strength with graphene due to the larger sp^2 hybrid domain.

(4) Concerning the graphene as conductive fillers in polymer matrix, both covalent and non-covalent methods can be used to modify graphene by ILs. The interacting situation between ILs and graphene has been demonstrated very important to the final properties (*in Chapter 3*), thus different modification strategies could also change the interaction model of IL-modified graphene as well as the properties of its polymer composites. For example, “click” chemistry could be used in the modification of graphene by ILs due to the very high reaction efficiency, combining both merits of covalent strategy (stable covalent bond) and non-covalent one (simple experimental process).

(5) In view of the long-term progress of this topic, not only PVDF-based matrices and graphene fillers can be used as building elements, but also a large number of other functional polymers and fillers provides a huge potential ability to develop IL-based composite materials in which ILs act as a powerful and versatile additives to well tune the structure an properties of composite materials. The combination of polymers and ILs as well as other functional fillers generates a versatile platform to bring a brilliant future and theoretically infinite possibilities of advanced functional polymer/IL composite materials.

FOLIO ADMINISTRATIF

THESE SOUTENUE DEVANT L'INSTITUT NATIONAL DES SCIENCES APPLIQUEES DE LYON

NOM : YANG DATE de SOUTENANCE : 20/07/2016

Prénoms : Jing

TITRE :
PHOSPHONIUM IONIC LIQUIDS: VERSATILE NANOSTRUCTURATION AND INTERFACIAL AGENTS FOR POLY(VINYLIDENE FLUORIDE-CHLOROTRIFLUOROETHYLENE)

NATURE : Doctorat Numéro d'ordre : 2016LYSEI072

Ecole doctorale : Matériaux de Lyon

Spécialité : Matériaux Polymères

RESUME :

Ce travail de thèse porte sur la compréhension fuie du rôle polyvalent des liquides ioniques (LIs) phosphonium comme agents de nanostructuration et interfaciaux pour la matrice polymère fluorée poly(fluorure de vinylidène-chlorotrifluoroéthylène) (P(VDF-CTFE)). Dans un premier temps, deux LIs phosphonium avec des fonctionnalités différentes générant un encombrement stérique et des fontions dipolaire additionnelles sont tout d'abord incorporés dans la matrice P(VDF-CTFE) pour préparer des films de polymère additivés. La structure de la phase cristalline, la morpholigie issue de la dispersion et le comportement de cristallisation sont finement caractérisés dans le but de fournir une compréhension fuie et complète du rôle joué par le LI sur la nanostructuration. Dans un second temps, le rôle d'agent interfacial du LI est étudié avec un LI phosphonium fluoré comprenant un cation combinant trois phényles et une chaîne fluorée courte. Ce LI est utilisé pour modifier la surface de l'oxyde de graphène (GO) et de l'oxyde de graphène réduit (rGO) afin de rendre ces nanocharges fonctionnelles et les incorporer dans la matrice P(VDF-CTFE). Ainsi, des films composites de P(VDF-CTFE)/graphène avec differentes teneurs en nanocharges sont préparés et une caractérisation fuie de la structure et des propriétés est entreprise afin de mieux compendre les mécanisme d'interaction interfaciale et leurs influences sur les films composites, tels que la structure de la phase cristalline, le comportement de cristallisation, la relaxation des chaînes, la morphologie et les propriétés diélectriques finales.

MOTS-CLÉS : poly(fluorure de vinylidène-chlorotrifluoroéthylène); liquides ioniques phosphonium; nanostructuration; agent interfacial; graphène; films composites

Laboratoire (s) de recherche : Ingenierie des Matériaux Polymères (IMP) CNRS UMR 5223 INSA de Lyon

Directeurs de thèse: Prof. Jannick DUCHET-RUMEAU, Dr. Sébastien PRUVOST

Président de jury :

Composition du jury :

POULIN, Philippe	Directeur de Recherche	CRPP-CNRS	Rapporteur
MIRI, Valérie	Professeur des Universités	Université Lille 1	Rapportrice
BIZET, Stephane	Docteur	ARKEMA	Examinateur
GERARD, Jean-François	Professeur des Universités	INSA-Lyon	Examinateur
DUCHET-RUMEAU, Jannick	Professeur des Universités	INSA-Lyon	Directrice de thèse
PRUVOST, Sébastien	Maître de Conférences HDR	INSA-Lyon	Co-directeur de thèse